THESIS FOR THE DEGREE OF DOCTOR OF PHILOSOPHY

Spin and magneto transport in van der Waals heterostructures of graphene with ferromagnets

BOGDAN KARPIAK

Department of Microtechnology and Nanoscience (MC2)

Quantum Device Physics Laboratory

CHALMERS UNIVERSITY OF TECHNOLOGY

Göteborg, Sweden 2021

Spin and magneto transport in van der Waals heterostructures of graphene with ferromagnets

BOGDAN KARPIAK
Göteborg, Sweden 2021
ISBN 978-91-7905-473-1

Doktorsavhandlingar vid Chalmers tekniska högskola
Ny serie Nr 4940
ISSN 0346-718X

Quantum Device Physics Laboratory
Department of Microtechnology and Nanoscience (MC2)
Chalmers University of Technology
SE-412 96 Göteborg, Sweden
Telephone: +46 (0)31-772 1000

Cover
Schematic representation of the graphene-ferromagnet ($Cr_2Ge_2Te_6$) heterostructure. The brown, green blue and black balls correspond to Te, Ge, Cr and C atoms, respectively. The insets show the Dirac band structure of pristine graphene (left side) and ferromagnetic exchange splitting of graphene band in proximity with $Cr_2Ge_2Te_6$ (right side).

Printed by Chalmers Reproservice
Göteborg, Sweden 2021

Spin and magneto transport in van der Waals heterostructures of graphene with ferromagnets
Thesis for the degree of Doctor of Philosophy
BOGDAN KARPIAK
Quantum Device Physics Laboratory
Department of Microtechnology and Nanoscience (MC2)
Chalmers University of Technology

Abstract

The increasing demand for information and communication technologies has augmented the requirements of electronic devices with improved speed, sensitivity, and reduced power consumption. The utilization of novel electronic materials and the use of the spin degree of freedom as a state variable for information processing and storage are expected to fulfill these demands. In this direction, two-dimensional (2D) materials have attracted a significant research effort with the long-term goal of creating electronic devices with novel functionalities. Graphene has shown excellent potential for future device applications due to its outstanding electronic carrier mobility and spin coherence time at room temperature. Followed by the successful advent of graphene, a vast plethora of 2D materials with complementary electronic properties have been discovered, such as insulating hexagonal boron nitride (hBN), magnets and topological semimetals. We observed that engineering 2D material heterostructures by combining the best of different materials in one ultimate unit offers the possibility of the creation of new phases of matter and novel opportunities in device design. For example, graphene is shown to acquire magnetic properties because of proximity-induced interactions with a magnetic insulator in van der Waals heterostructure. On the other hand, topological semimetal candidates such as WTe_2 and $ZeTe_5$ allowed us to observe unconventional charge-to-spin conversion and anomalous Hall effects due to their enormous spin-orbit coupling, lower crystal symmetry, and larger fictitious magnetic field in the crystals. Furthermore, the performance of heterostructures comprised of graphene and hBN with one-dimensional ferromagnetic edge contacts and a path for optimizing such device geometry is outlined. These experimental findings on 2D materials and heterostructure device architectures can contribute to developing a new platform for spintronic as well as quantum science and technology.

Keywords: spintronics, graphene, topological semimetals, van der Waals magnets, magnetic proximity

List of publications

This thesis is mainly based on the work contained in the following papers:

[I] B. Karpiak, A. Dankert, and S. P. Dash, "Gate-tunable Hall sensors on large area CVD graphene protected by h-BN with 1D edge contacts", Journal of Applied Physics **122**, 054506 (2017).

[II] B. Karpiak, A. Dankert, A. W. Cummings, S. R. Power, S. Roche, and S. P. Dash, "1D ferromagnetic edge contacts to 2D graphene/h-BN heterostructures", 2D Materials **5**, 014001 (2018).

[III] A. Dankert*, B. Karpiak*, and S. P. Dash, "Hall sensors batch-fabricated on all-CVD h-BN/graphene/h-BN heterostructures", Scientific Reports **7**, 15231 (2017).

[IV] B. Karpiak, A. W. Cummings, K. Zollner, M. Vila, D. Khokhriakov, A. M. Hoque, A. Dankert, P. Svedlindh, J. Fabian, S. Roche, and S. P. Dash, "Magnetic proximity in a van der Waals heterostructure of magnetic insulator and graphene", 2D Materials **7**, 015026 (2020).

[V] B. Zhao, B. Karpiak, D. Khokhriakov, A. Johansson, A. M. Hoque, X. Xu, Y. Jiang, I. Mertig, and S. P. Dash, "Unconventional Charge-Spin Conversion in Weyl-Semimetal WTe_2", Advanced Materials **32**, 2000818 (2020).

* These authors contributed equally.

Dedicated to all those who bring value into the lives of others.

The world stands on your solid grounds!

Contents

Abbreviations and Symbols

Abbreviations

3D	Three-dimensional
2D	Two-dimensional
1D	One-dimensional
ARPES	Angle-resolved photoemission spectroscopy
STM	Scanning tunneling microscopy
MOKE	Magneto-optic Kerr microscopy
SdH	Shubnikov-de Haas
AFM	Antiferromagnetic
GPS	Global Positioning System
AHE	Anomalous Hall Effect
CVD	Chemical Vapour Deposition
SOC	Spin-orbit coupling
hBN	Hexagonal Boron Nitride
YIG	Yttrium iron garnet
F3GT	Fe_3GeTe_2
F5GT	Fe_5GeTe_2
CGT	$Cr_2Ge_2Te_6$

Mathematical symbols

T_c	Curie temperature
T	Temperature
B_c	Coercivity
R_{xy}	Transverse magneto resistance
R_{xx}	Longitudinal magneto resistance
g	g-factor
V_{NL}	Nonlocal voltage
R_{NL}	Nonlocal resistance
τ_s	Spin lifetime

Fundamental constants

$\hbar$	Reduced Planck constant ($\hbar = 1.054571817 \times 10^{-34}$ J·s)
k_B	Boltzman constant ($k_B = 1.38064852 \times 10^{-23}$ $m^2kg/(s^2K)$
q_e	Electron charge ($q_e = 1.60217662 \times 10^{-19}$ C)
μ_B	Bohr magneton ($\mu_B = 9.274009994 \times 10^{-24}$ $J{\cdot}T^{-1}$)
m_e	Electron rest mass ($m_e = 9.1093837015 \times 10^{-31}$ kg)

Acknowledgements

After over four years, this PhD journey has come to an end. It has been rich in new insights, including the scientific research developments. Reaching this far would not have been possible without the support from people at the department and outside.

First of all, I would like to acknowledge the support from my supervisor, Professor Saroj P. Dash. His patience, scientific advice and guidance have made this journey possible.

I would like to thank the current and former colleagues in the group, Anamul Md. Hoque, Dmitrii Khokriakov, Bing Zhao, Priyamvada Bhaskar, Linnea Andersson, Isabel H. Rodrigues. Thank you, André Dankert, your practical assistance and advices were of great aid at the beginning of this PhD. Additionally, I express my gratitude to all the other colleagues outside our group who made this journey pleasant. Particularly thanks, Silvia Ruffieux, for the nice QDP fika times, and Agin Vyas, for the company.

I acknowledge the support from our scientific collaborators Professor Stephan Roche, Professor Jaroslav Fabian, Professor Peter Svedlindh, Professor Ingrid Mertig, Associate Professor Annika Johansson as well as Dr. Aron W. Cummings, Dr. Marc Vila, Dr. Stephen R. Power, MSc Klaus Zollner.

Thank you, the staff at the Nanofabrication Laboratory, for the assistance with the practical matters related to the fabrication of devices.

My gratitude also goes to Linda Bråvell, Annika Holtringer, Debora Perlheden, Dag Winkler, Avgust Yurgens, Sergey Kubatkin, Samuel Lara Avila, Per Lundgren, Janine Splettstoesser, Lars Jönsson, Alexei Kalaboukhov, Thilo Bauch, Andrey Danilov for the assistance with administrative and other matters.

Thank you, Daphne Aldridge, Jonathan Aldridge, Marie Le May, Gurdeep Chahal, Victoria Mysdotter, Chatdanai Lumdee, Meihui Tao, Laure Charton, Victor Egerö, Simon Eriksson. You added color to these over four years here.

I should not forget Gustav Andersson, Ivo Cools, Nermin Trnjanin, Ragnar Ferrand-Drake del Castillo, Anamul Md. Hoque, Ananthu P. Surendran. Thanks for the badminton and padel games.

I would like to express my deep gratitude to my parents and sister, whose support was of great value.

Finally, I would like to acknowledge the funding support of the doctoral research from the Swedish Research council, Graphene Flagship, 2DTECH center as well as the scholarship funding provided by the European Commission within the framework of the EU Erasmus Mundus Master of Nanoscience and Nanotechnology programme, without which this doctoral study would not have been possible in the first place.

Gothenburg, 2021

1 Introduction

The modern electronic age is in full swing and the advancements in information technology stand behind the technological revolution that has touched upon all aspects of our lives. Whether it is social communication, medicine, rocket technologies, GPS navigation in the remote locations of our planet or simply ordering food delivery online from groceries store, none of this could have been possible without the rapid developments in the electronic devices.

A significant milestone on this path has been passed in 1947 when the first transistor with semiconducting channel material was invented by Bell Laboratories [1]. This was a big step forward in the semiconductor industry (accounting for the vast market of $\sim$ \$469b in 2021 [2]) as the vacuum tubes, utilized in place of transistors before their invention, were highly unreliable and energetically inefficient. Since 1960s, the constant strive for improvements in speed, energy consumption efficiency, portability and reduction of cost per functionality [3] gave rise to what is known as the Moore's law [4], a rule of thumb in the semiconductor industry according to which the amount of transistors on a microprocessor doubled every two years or so. This approach implied mainly scaling down device dimensions, but also engineering new ways and utilizing new materials to mitigate the increasing challenges posed by this trend. However, today the Moore's law approach is running out of space for further expansion in a conventional way [5] as the size of characteristic features is approaching fundamental limits of several atoms thick. Thus, at these size scales the gate current leakage and thermal dissipation are becoming a big challenge to cope with and, moreover, the quantum uncertainties start to govern the device behaviour making them unreliable [5]. The fundamental limitations have augmented the increasing demand for alternative ways for further device improvements beyond Moore's law [6]. One of such alternative approaches to operation of electronic devices is offered by spintronics [7].

Today most of the electronic devices utilized in practical applications are charge-based, i.e. they employ electrical charge of electron for information processing and storage. Spintronics introduces a different paradigm in device operation by utilizing another fundamental property of electron – its angular momentum or spin. This has the potential of further increase in speed and energy consumption efficiency in non-volatile devices as the manipulation of spin direction as a state variable requires less energy in comparison to rearranging charge carriers [8, 9]. The

spin-dependent charge carriers transport was first described in 1936 by Mott [10] and this concept was utilized much later in giant magnetoresistance and tunnel magnetoresistance devices [11–13] leading to a Nobel prize in 2007 [14]. The former phenomenon gave rise to magnetic hard disc drives that have been widely used for information storage for decades now. The proposal in 1976 to create non-equilibrium spin accumulation in nonmagnetic material [15] eventually led to the first experimental observation of spin injection into aluminum in 1987 [16, 17] and set the ground for spin-logic devices. In 1990 the first spin field effect transistor was proposed by Datta and Das [18].

A proper choice of functional materials is required for successful development of spintronic technologies. The extraordinary properties of graphene, a one-atom thin two-dimensional (2D) layer of carbon atoms arranged in a honeycomb lattice with semimetallic linear band structure near the Fermi level, were discovered in 2004 [19]. In spintronics today graphene is mainly utilized as a channel material since it allows for spin propagation without losing spin coherence over relatively large distances due to its low spin-orbit coupling. Following the successful advent of graphene, the field of 2D van der Waals heterostructures [20–27] has emerged and been extensively studied [28, 29]. A vast plethora of 2D materials with complementary electronic properties have been discovered, such as insulating hexagonal boron nitride (hBN), magnets and topological semimetals. These materials possess unique electronic properties which have focused significant amount of research efforts towards implementation of new generation of devices based on the heterostructures of atomically thin layered materials with the long-term goal of creating electronic devices with novel functionalities [9, 23, 30–34]. By assembling such layers of distinct 2D materials, one can tune the required functionality and combined properties of the assembled structures in one ultimate unit. This offers the possibility of creation of new phases of matter and novel opportunities in device design. For example, graphene is shown to be magnetic because of proximity-induced interactions, and topological semimetal candidates showed current-induced spin-polarization and anomalous Hall effects. This experimental progress contributed to developing 2D materials-based devices for spintronics and quantum technologies.

In this thesis, the research was focused on investigation of spin and magneto transport properties of graphene van der Waals heterostructures as well as other 2D materials that are promising for utilization in combination with graphene, particularly for spin injection and charge-to-spin conversion.

Chapter 2 will provide a brief overview of the state of the art of research fields studied in this thesis. These include the latest developments on graphene-based heterostructures for the prospect of spin injection into graphene through 1D ferromagnetic edge contact, recent advances on 2D magnetic materials-based devices and magnetic proximity effects in graphene and developments of topological semimetal candidates with strong spin-orbit coupling for anomalous magnetoresistance and

charge-spin conversion effects.

Chapter 3 presents spin transport in graphene and study of devices with one-dimensional (1D) ferromagnetic edge contacts to 2D graphene/hBN heterostructures. For optimization of heterostructures and devices, Hall sensors are investigated with CVD graphene and hBN capping layer [Paper I]. While aiming to explore spin injection/detection with 1D ferromagnetic edge contacts, a local Hall effect in graphene due to fringe fields from ferromagnetic edge contact is also detected [Paper II]. We further investigated such 1D edge contacts in all-CVD hBN/graphene heterostructures and characterized the device parameters and its Hall sensitivity [Paper III]. These studies are useful for the optimization of spin injection and detection in 2D material heterostructures through 1D edge contacts, which remains a challenging task.

Engineering 2D material heterostructures by combining the best of different materials in one ultimate unit can offer many opportunities in condensed matter physics. In chapter 4, in the van der Waals heterostructures of the ferromagnetic insulator $Cr_2Ge_2Te_6$ and graphene, our observations indicate an out-of-plane proximity-induced ferromagnetic exchange interaction in graphene. The perpendicular magnetic anisotropy of $Cr_2Ge_2Te_6$ results in significant modification of the spin transport and precession in graphene, which can be ascribed to the proximity-induced exchange interaction [Paper IV]. Furthermore, the observation of a larger lifetime for perpendicular spins in comparison to the in-plane counterpart suggests the creation of a proximity-induced anisotropic spin texture in graphene. This chapter will also present magneto transport characterization of van der Waals metallic ferromagnets Fe_3GeTe_2 and Fe_5GeTe_2, with high Curie temperatures that are potential 2D magnetic materials for spin injection and detection into the graphene channel, which remains to be observed in the future. These experimental results open opportunities for the realization of proximity-induced magnetic interactions and spin filters in van der Waals material heterostructures and can form the basic building blocks for all-2D spintronics as well as topological quantum devices.

The discovery of topological semimetals has revealed the opportunities to realize several extraordinary physical phenomena in condensed matter physics. In chapter 5, we will present the electronic and magnetotransport properties of topological semimetal WTe_2 and candidate in this material class $ZrTe_5$ exhibiting large magnetoresistance, Shubnikov de Haas oscillations and anomalous Hall effect. We further utilized semimetal WTe_2 to demonstrate a large current-induced spin polarization up to room temperature. We also observed unconventional charge-spin conversion effects in WTe_2 in different device geometries because of the broken crystal symmetry of the material [Paper V]. Our measurements show an out-of-plane electrical field-induced spin polarization in WTe_2, which could be injected and detected in the graphene channel in the non-local measurement geometries (Appendix A). These findings open opportunities for spin-orbit based

spintronic technologies and open possibilities for the detection of charge-spin conversion in other topological semimetal candidates with novel spin textures.

The last chapter 6 provides a summary of the experimental results presented in the thesis and discusses the future outlook for the research in these directions.

2 State of the art

Since the advent of graphene the van der Waals materials and their heterostructures are under intense investigations. This is, in particular, due to a wide range of layered materials already discovered with different topological, magnetic, electrical transport properties owing to a spectrum of band structure configurations. In this chapter, the main developments in graphene as well as van der Waals magnets and some of the layered topological semimetals and candidates are discussed. These highlights demonstrate their unique properties and application potential for spintronic studies.

2.1 Spin transport in graphene

For operation of spintronic logic devices and implementation of spin-based circuits, one needs a way to inject, detect and manipulate non-equilibrium spin accumulations in an appropriate nonmagnetic channel. Such channels should allow for sufficiently long spin communication without losing non-equilibrium distribution over relatively large distances. Over time the main focus of research on spin transport shifted from metallic channels such as Al or Cu [7, 35], to semiconductors such as GaAs [36] and Si [37–42] at room temperature. Today, graphene is mainly utilized for this purpose in spintronic devices, where long-distance spin transport is observable at room temperature [25, 43, 44]. Additionally, utilization of 2D graphene as a channel material allows for benefiting from its heterostructures with other 2D materials with complementary electronic properties. However, being atomically thin, this material is highly sensitive to environmental influences such as e.g. charge doping and contamination by impurities. Therefore, the substrate material and possible capping layer can have significant impact on the quality of graphene channel properties. Another factor that impacts the quality is the growth and transfer method on the target substrate for device fabrication.

The first time spin transport in graphene was demonstrated in 2007, in exfoliated layer placed onto SiO_2 substrate with spin relaxation lengths λ_s of several micrometers at room temperature [45]. The typical spin lifetimes for such channels τ_s are several hundreds of ps [45–48]. The best way to avoid substrate-induced effects is to suspend graphene channel. Such devices showed very high mobilities $\mu \sim 10^5$ $\mathrm{cm^2V^{-1}s^{-1}}$ [49] and spin transport with $\tau_s \sim 130$ ps and

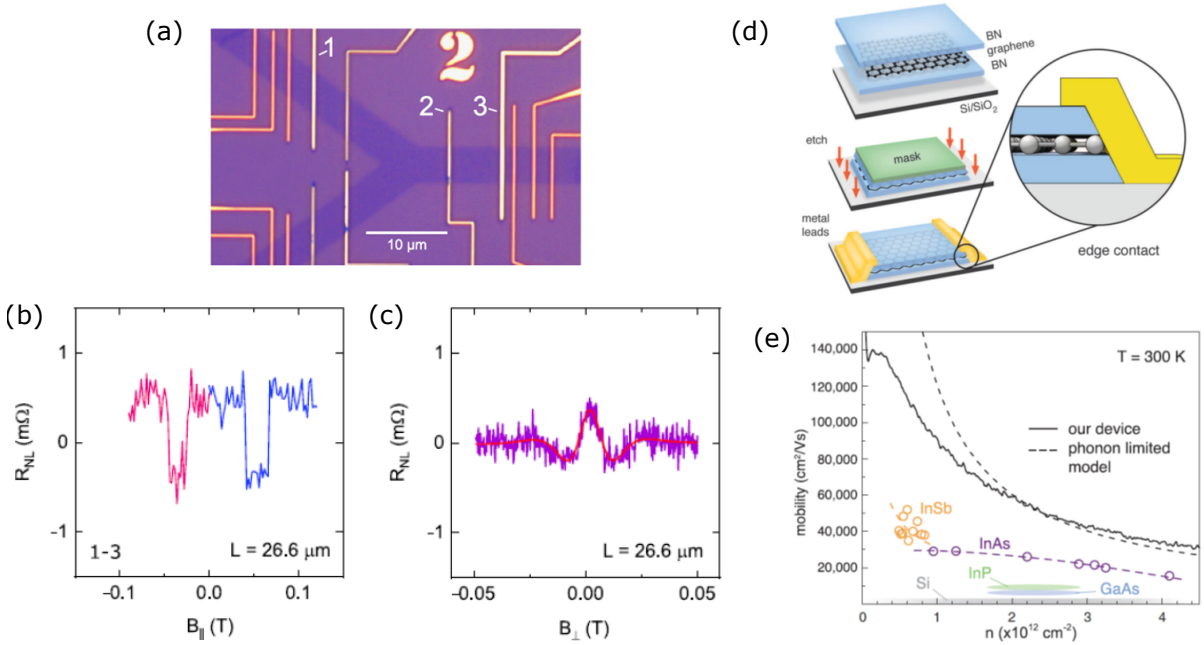

Figure 2.1: (a) Optical microscope picture of the nanofabricated device with CVD graphene channel on Si/SiO_2 substrate. (b),(c) Spin-valve and Hanle nonlocal measurements at room temperature between ferromagnetic contacts 1 and 3, respectively. The nonlocal channel length is ~ 27 µm. (a)-(c) is adapted from [55]. (d) Schematics of the hBN/graphene/hBN heterostructure after assembly, etching and fabrication of 1D contacts. (e) The corresponding mobility of encapsulated graphene as a function of carrier density in comparison to other materials, as indicated. (d),(e) is adapted from [60].

$\lambda_s \sim 3$ µm [47, 50, 51]. However, fabrication of suspended channels is challenging and they are not viable for practical applications.

Although exfoliated graphene is useful for scientific research as it provides better quality of the material with less grain boundaries and higher mobility, for commercialization purposes scalable CVD-grown layers and transfer methods from growth substrate are required. Spin transport in CVD graphne has been demonstrated [52–54]. Recently, spin communication at room temperature has been observed in commercially available CVD graphene on SiO_2 substrate over long distances of up to ~ 27 µm (Fig. 2.1a-c) with estimated possible increase of this parameter to ~ 34 µm [55].

Insulating hexagonal boron nitride (hBN) is known to have good interface properties with graphene [47]. Its utilization as a substrate material in stacks of exfoliated hBN/graphene allows for reduction of charge impurities in graphene [56] and higher mobilities of tens of thousands [57] or even above 10^5 $cm^2V^{-1}s^{-1}$ [58] (in contrast to typical few thousands with SiO_2 substrate [45, 55, 59]). Spin transport in such channels was observed at room temperature with $\lambda_s \sim 5$ µm [57] and similar values of τ_s to devices with SiO_2 substrate despite higher mobility [47].

The hBN dielectric substrate provides improved bottom interface quality of

graphene, but leaves the top surface exposed to the environment, e.g. contamination by polymer residues during the lithographic steps of device fabrication. Although annealing can improve the material quality after exposure to organic residues, it does not remove the residues completely or restore the initial graphene characteristics [61]. Therefore, flakes of hBN are sometimes used to pick up and dry transfer graphene onto the pre-fabricated ferromagnetic contacts to avoid its exposure to polymer residues and solvents. This allowed for observation of spin transport with $\tau_s \sim 12.6$ ns at room temperature [62]. Moreover, top hBN capping is additionally beneficial for protection of post-fabricated graphene devices from environmentally-induced degradation over time.

To mitigate the conductivity mismatch issue [63, 64], i.e. backscattering of spin-polarized charge carrier after injection into the graphene channel, conventionally TiO_2 [53, 65–71], Al_2O_3 [45] or MgO [62] tunnel barriers are utilized together with ferromagnetic contacts. However, these barriers are prone to have pinholes, which contribute to increased spin dephasing in the channel underneath the contacts [72]. Employing atomically smooth single- to few-layer thin hBN as a tunnel barrier material [73, 74] mitigates the issue with barrier roughness and provides better interface quality with graphene. Spin transport in such devices revealed inversion of spin signal with hBN thickness and spin filtering [75].

An ultimate approach towards graphene protection for preservation of its outstanding intrinsic properties could be in full encapsulation by hBN with utilization of 1D edge contacts to graphene channel (Fig. 2.1d), as it has been demonstrated for the first time by Wang et. al. in 2013 [60]. This allowed for observation of very high mobilities of up to $\sim$ 140000 $cm^2V^{-1}s^{-1}$ (Fig. 2.1e). In ultra-clean stacks of hBN/graphene/hBN ballistic transport has been probed with 1D edge contacts over 28 µm distance at 1.8 K, where channel mobility was reaching up to three million $cm^2V^{-1}s^{-1}$ [76]. Motivated by these developments, we investigated ferromagnetic 1D edge contacts to graphene structures as presented in Chapter 3 of this thesis. Spin transport studied in hBN-encapsulated graphene channels with 1D ferromagnetic edge contacts revealed gate-tunable inversion of the nonlocal spin signal [77].

There is additional utility to employing graphene as a channel material with long distance spin communication for spintronic applicaitons. Being atomically smooth and thin, it allows for additional benefit of making heterostructure devices with other 2D materials that possess complementary electronic properties for spin injection, detection, manipulation. Thus, ferromagnetic van der Waals metals such as Fe_3GeTe_2 and Fe_5GeTe_2 could be employed instead of thin films of traditional 3D ferromagnetic metals or alloys such as e.g. Co or permalloy for spin injecion and detection with graphene channels. Layered topological semimetals and candidates such as WTe_2 and $ZrTe_5$ are promising for charge-to-spin conversion due to non-trivial spin textures and strong spin-orbit coupling. Additionally, heterostructures of 2D materials could be utilized for creation of new phases of matter such as

e.g. proximity-induced magnetic interactions in graphene placed in contact with magnetic insulators.

2.2 Developments with layered van der Waals magnets and proximity-induced magnetism in graphene

To utilize magnetism in low dimensions, for decades epitaxial thin films of 3D magnetic materials have been under investigation [13, 23, 78, 79]. However, they suffer from e.g. nonhomogeneous surface (formation of islands), irregular shapes, interfacial hybridization and their properties are difficult to reproduce [23]. In contrast, van der Waals magnets are mainly devoid of these limitations and they can be naturally made atomically thin. The field of research in magnetic layered 2D materials recently has quickly gained tremendous interest within scientific community investigating van der Waals materials. Atomically thin magnets open opportunities for both fundamental studies as well as design of flexible magnetooptic and magnetoelectric devices and heterogeneous integration with complementary materials [23]. It has long been thought that intrinsic magnetism in two dimensions is not possible as it would be disrupted by thermal fluctuations [80]. However, as recently demonstrated [81–83], long-range magnetic ordering can persist in atomically thin materials due to magnetic anisotropy that opens spin-wave excitation gap [81].

2.2.1 Discovery of intrinsic magnetism in two dimensions in layered materials

Among the first reports demonstrating magnetic properties in van der Waals magnets that boosted research in this field were published in 2017-2018 (Fig. 2.2) [81–83]. Thus, insulating layered $Cr_2Ge_2Te_6$ was demonstrated to possess out-of-plane ferromagnetic ordering (Fig. 2.2a) through ferromagnetic loops measured by magneto-optic Kerr rotation microscopy (MOKE) with minor reminiscent magnetization values [81]. The magnetism was shown to persist down to bilayers of $Cr_2Ge_2Te_6$ with Curie temperature (~ 65 K for bulk) dependent on the thickness for thin samples. Layered semiconductor CrI_3 with out-of-plane anisotropy is ferromagnetic in bulk and possesses layer-dependent magnetic properties in thin flakes (Fig. 2.2b). Thus, atomically thin flakes of CrI_3 demonstrate ferromagnetic loops for odd number of layers and antiferromagnetic behaviour for even layer number. Itinerant ferromagnetism in two-dimensional metallic Fe_3GeTe_2 with strong out-of-plane anisotropy persists up to ~ 230 K (Fig. 2.2c) [82] and observable down to monolayer samples (Fig. 2.2d) [84]. By applying electric fields the Curie temperature can be tuned in thin flakes of Fe_3GeTe_2 [84].

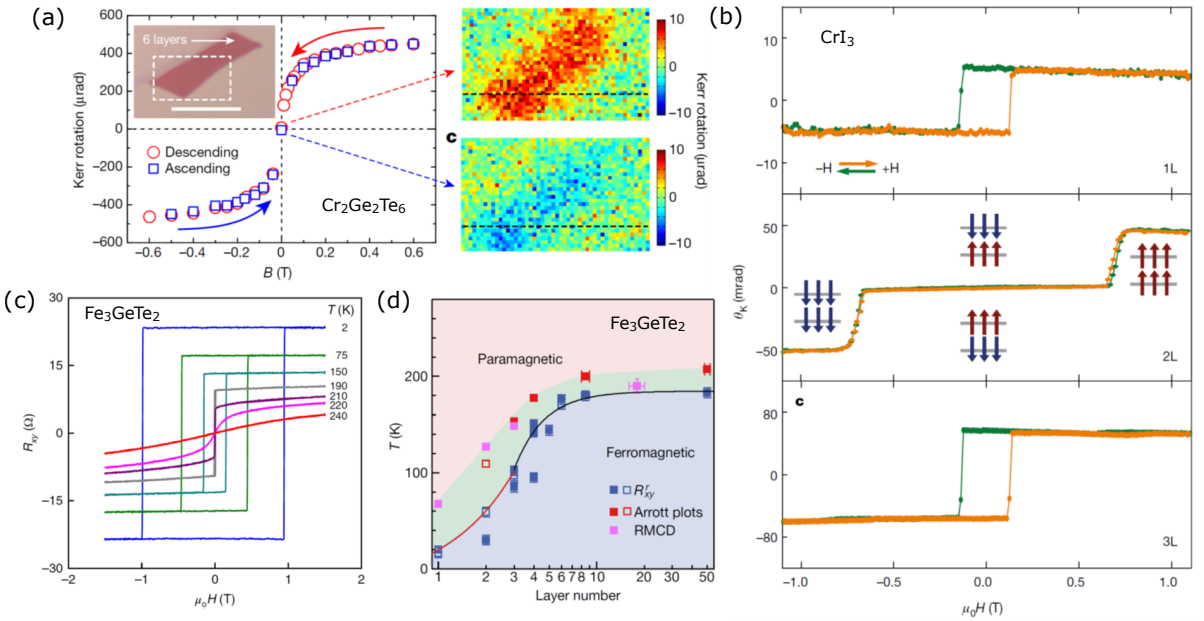

Figure 2.2: The first reports on 2D magnetism in van der Waals layered materials. (a) Ferromagnetic hysteresis loop (left) and spatial scans at zero field after withdrawing preliminary applied field of 0.6 T (top right) and -0.6 T (bottom right) in six-layer-thick flake of $Cr_2Ge_2Te_6$ obtained by MOKE measurement at 4.7 K. Scale bar in the inset is 10 µm. Adapted from [81]. (b) MOKE signal measured in monolayer (1L), bilayer (2L) and trilayer (3L, as indicated) flakes of CrI_3 as a function of applied perpendicular magnetic field. The 1L and 3L flakes show ferromagnetic loops, while 2L flake demonstrates antiferromagnetic response. The insets indicate magnetization directions in each layer of the 2L flake at different applied field values. Adapted from [83]. (c) Temperature dependence of ferromagnetic loops obtained by electric transport measurements in 12 nm thick flake of Fe_3GeTe_2. The magnetic ordering is persistent up to at least 220 K. Adapted from [82]. (d) Different phases of Fe_3GeTe_2 as a function of number of layers and temperature. The dots represent magnetic ordering temperatures as obtained by magneto resistance measurements (blue), Arrott plots (red) and refractive magnetic circular dichroism measurements (pink). Adapted from [84].

Today, the range of discovered layered magnetic materials includes a number of compounds [23, 33, 34, 85] with different conduction properties, i.e. metals [82, 84, 86], insulators [81, 87–89], semiconductors [83, 90–92] and dissimilar magnetic ordering states such as ferromagnetism [81, 82, 84, 86, 90, 92] and antiferromagnetism [83, 87–89, 91]. Additional class of van der Waals 2D magnets, intrinsic multiferroics that combine properties of ferromagnetism and ferroelectricity, are theoretically predicted [93, 94], but yet remain to be experimentally realized.

2.2.2 Magnetic tunnel junctions and nontrivial magneto resistance

The data storage technologies have greatly benefited from advances in fabrication and growth methods of magnetic ultrathin films and barriers for utilization in magnetic tunnel junctions (MTJs) [95, 96]. However, the traditional films, grown by epitaxy, sputtering or pulsed laser deposition [24], suffer from interdiffusion, disorder present in the electrodes and barrier roughness that affects the quality of the interfaces, spin-dependent conductance and eventually degrades the operation of MTJs [97–99].

Heterostructures of van der Waals materials comprised of 2D layered magnets allow to mitigate the issues accompanying conventional magnetic thin films leading to extremely large values of tunneling magneto resistance (TMR). Thus, utilizing antiferromagnetic CrI_3 as a tunnel barrier in combination with graphene electrodes led to observation of TMR of up to $\sim 19000\%$ (Fig. 2.3a) [100, 103], where four-layer CrI_3 acts as a multi-spin-filter. With applied field of sufficient strength all layers become saturated in the same direction and tunneling current increases, while for lower fields the conduction is hindered due to spin-dependent scattering.

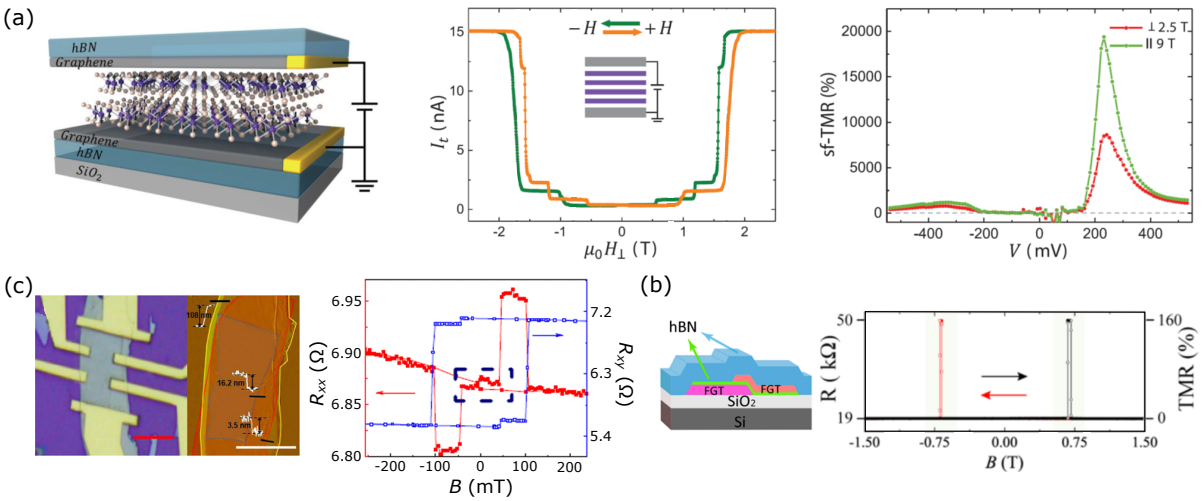

Figure 2.3: Magnetic tunnel junctions with van der Waals magnets and nontrivial magneto resistance. (a) From left to right: schematics of the vertical tunneling devices with CrI_3 barrier, tunneling current as a function of perpendicular field in the corresponding device at 2 K and the calculated spin-flip TMR as a function of bias voltage for perpendicular (red) and in-plane (green) applied magnetic field of 2.5 T and 9 T, respectively. Adapted from [100]. (b) Schematic of vertical tunneling junction with Fe_3GeTe_2 electrodes and hBN tunnel barrier (left) and the magneto resistance measured in such junction (right). Adapted from [101]. (c) Left: optical and atomic force microscope pictures of the device with trilayer Fe_3GeTe_2/graphite/Fe_3GeTe_2 heterostructure channel. Scale bars are 5 µm. Right: Longitudinal (R_{xx}) and transverse (R_{xy}) magneto resistances in the corresponding device at 50 K. Adapted from [102].

This demonstrated the tremendous potential of van der Waals magnets for data storage applications. An alternative approach to designing MTJs was undertaken in ref. [101] (Fig. 2.3b), where hBN is utilized as tunnel barrier in a heterostructure with magnetic Fe_3GeTe_2 electrodes. Here, TMR of up to 160% was observed.

In addition to large TMR ratios obtained by employing layered magnets in tunneling junctions, a nontrivial antisymmetric magneto resistance response was measured in heterostructures of Fe_3GeTe_2/graphite/Fe_3GeTe_2 (Fig. 2.3c), although with significantly lower TMR ratio of $\sim 1\%$. The origin of such magneto resistance behaviour was attributed to spin-polarized current that arise due to spin-momentum locking in the SOC-split 2D electron gas at the Fe_3GeTe_2/graphite interfaces. This result highlights the rich physics that could be accompanying conventional magnetism in the van der Waals magnetic materials (e.g. topological nodal lines reported in Fe_3GeTe_2 [104]) and heterostructures.

2.2.3 Magnetic proximity effects in graphene

Spin injection plays an important role in operation of spintronic devices. A number of ways exist to achieve this, e.g. through electrical injection, optical injection, spin-orbit coupling effect. A different path implies inducing magnetism in intrinsically nonmagnetic medium. Many approaches to create magnetism in graphene as a promising spin transport material for spintronics have been investigated. It was predicted that graphene nanoribons with zigzag edges host spin polarized states [109–111] and lattice imperfections such as vacancies [112–114] or adatoms [112, 115–117] create local magnetic moments by introducing unpaired electrons [23, 27, 32]. However, these approaches are difficult to controllably engineer. Moreover, defects would degrade graphene properties, e.g. mobility.

An alternative solution could be in inducing spin-polarized states in graphene by placing it in close proximity to magnetic materials (hence proximity effect). An atomically thin nature of graphene is beneficial for achieving this goal, as proximity-induced interactions strongly decay with distance. Additionally, the possibility of obtaining smooth van der Waals interfaces in heterostructures with layered magnets further facilitates observation of proximity magnetism in graphene. By placing graphene in contact with magnetic materials, it can acquire exchange gap due to spin-splitting of normally spin-degenerate Dirac cones. Thus, in heterostructures of graphene with magnetic insulator EuS, induced exchange interactions led to observation of Zeeman spin Hall effect (Fig. 2.4a) [105]. Measurements of transverse magneto resistance in graphene on YIG (ferrimagnetic insulator) substrate displayed presence of Anomalous Hall effect (AHE) in magnetized channels (Fig. 2.4b) [106, 118]. Additonally, spin injection into graphene on YIG was observed via spin pumping [119, 120]. Since the induced exchange fields in graphene are a consequence of exchange interactions at the graphene/magnet interface, by modulating this coupling one can tune the physical phenomena in the

channel that are affected by the exchange splitting. Thus, a shift in Landau levels in graphene on antiferromagnetic CrSe substrate was observed to be tunable by different strength of magnetic fields applied during field cooling (Fig. 2.4c) [107]

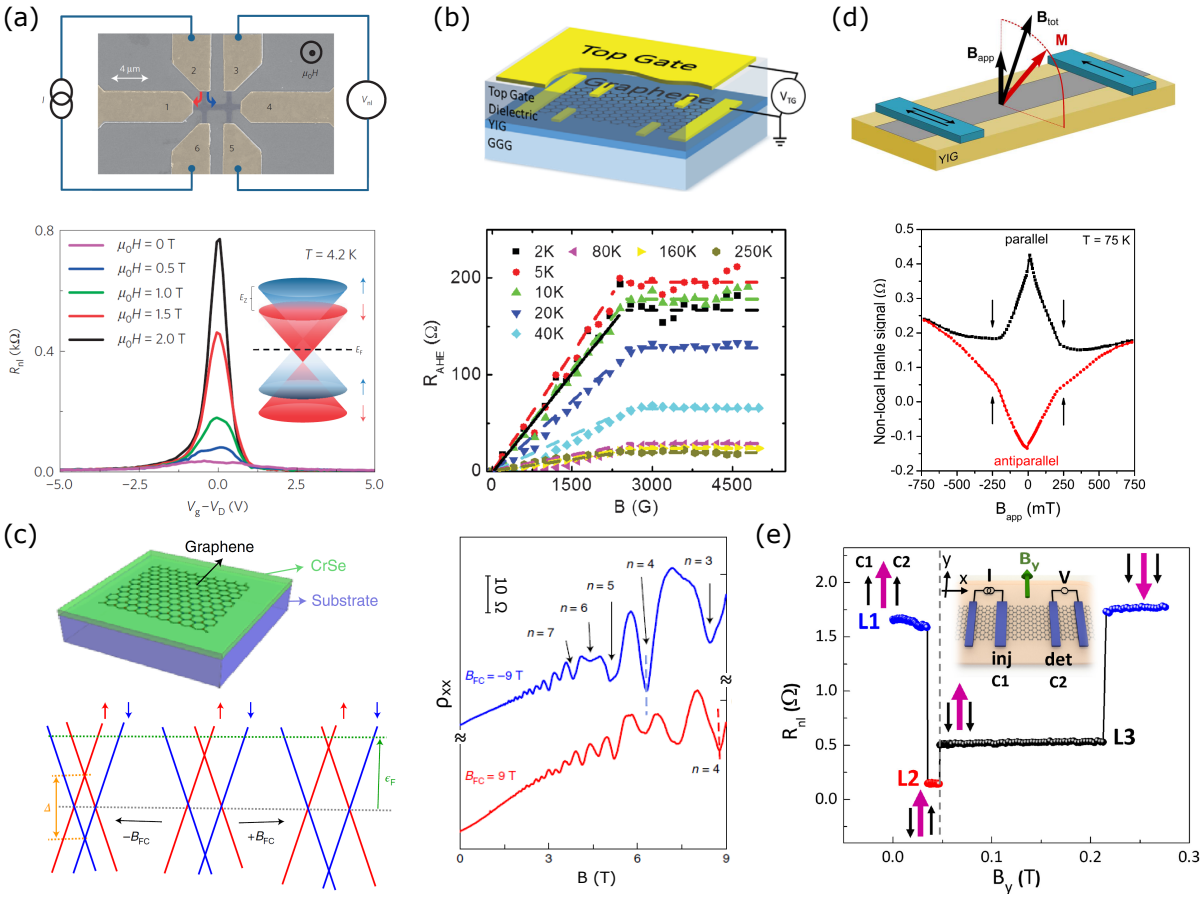

Figure 2.4: Proximity-induced magnetic interactions in graphene. (a) False-colored scanning electron microscope image of the device (top) for measurements of Zeeman spin Hall effect as shown below in graphene/EuS heterostructure. The inset indicates exchange splitting of normally spin-degenerage Dirac cones in graphene. Adapted from [105]. (b) Schematics of the graphene device placed on YIG substrate (top) and the measured AHE in this device at different temperatures as indicated (bottom). Adapted from [106]. (c) Proximity effects probed in graphene placed on antiferromagnetic substrate of CrSe. Shifts in Landau levels (n indicates index) are observed that are tunable by the strength of magnetic field B_{FC} applied during cooling. Adapted from [107] with ρ_{xx} vs B curves at intermediate values of B_{FC} removed. (d) Schematics of device with graphene channel placed on YIG with ferromagnetic contacts (top) and the measured Hanle spin precession signal in this device (bottom) with kinks characteristic of complete rotation of YIG magnetization from in-plane to perpendicular direction. Adapted from [108]. (e) Nonlocal spin valve measurement in graphene on antiferromagnetic substrate of CrSBr with three resistance levels that correspond to different magnetization directions of the Co injector (C1), detector (C2) indicated by black arrows and CrSBr susbtrate indicated by purple arrow. Adapted from [91].

with increased (decreased) value of exchange gap for applied positive (negative) fields during cooling.

A different approach to probing magnetic proximity effects in graphene channels is by investigating spin transport in such channels (Fig. 2.4d,e). The internal exchange field contributes to modified Hanle spin precession measurements, manisfested e.g. in graphene on YIG substrate through appearance of kinks in the Hanle signal at the values of external magnetic field corresponding to the complete rotation of YIG magnetization from in-plane to out-of-plane direction (Fig. 2.4d) [108]. Similarly, modulation of the nonlocal spin transport signals in graphene on YIG was observed in the presence of fluctuating proximity exchange fields [121]. These reports, in addition to several others [122–125], demonstrated induced magnetic ordering in graphene in contact with non-van der Waals magnets. Recently, three studies showed proximity magnetism in graphene with all-van der Waals heterostructures through Zeeman spin Hall effect utilizing magnetic $CrBr_3$ [126], AHE utilizing $Fe_xSn_{1-x}S_2$ [127] and modified spin transport utilizing CrSBr substrate [91]. In the latter report, the nonlocal spin-valve signals measured in proximitized graphene channel led to observation of additional resistance states that were correlated to the direction of magnetization of the magnetic substrate (Fig. 2.4e) [91]. These reports demonstrate the potential of atomically thin graphene for fundamental studies of proximity-induced magnetism towards advancements in spintronics.

2.3 Topological semimetals and candidates

Since the theoretical prediction [128] and experimental discovery [129, 130] of 2D topological insulators, topological materials have been under intense investigation for over a decade [131–137]. Particularly, Weyl semimetals have attracted recently significant research focus [138] as they present rich ground for investigation of fundamental physical phenomena. For spintronics, particularly, topological semimetals are interesting due to large intrinsic spin-orbit coupling and bulk spin textures, which are beneficial for charge-spin conversion effects.

A representative material that falls under topological semimetals classification is WTe_2. Its band structure contains Weyl nodes in the bulk with additional nearly-compensated electron and hole pockets at the Fermi level that allowed observation of extremely large nonsaturating magneto resistance in bulk crystals reaching up to 13×10^6 % at 60 T, 0.53 K (Fig. 2.5a). Monolayer flake of WTe_2 was shown to open a bulk gap with edge conduction [139], thus leading to observation of quantum spin Hall effect at temperatures up to 100 K (Fig. 2.5b) [140], while at higher temperatures the bulk was contributing to conduction. Due to large Berry curvature, the nonlinear anomalous Hall effect was also observed in flakes of WTe_2 [141].

Another layered van der Waals material, $ZrTe_5$, has been shown to possess

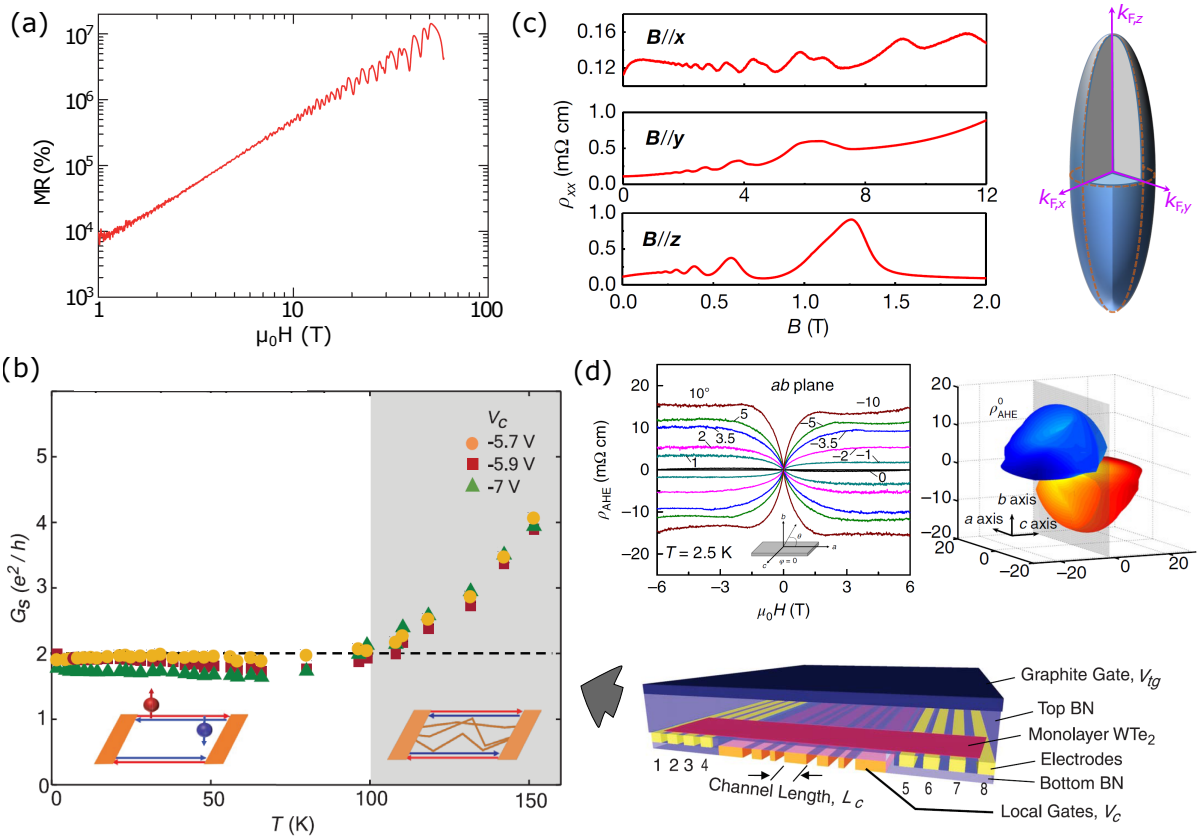

Figure 2.5: (a) magneto resistance (MR) in bulk WTe_2 as a function of magnetic field up to 60 T at 0.53 K. Adapted from [147]. (b) Quantum spin Hall effect measured in monolayer WTe_2 up to $\sim$ 100 K. The plot shows temperature dependence of edge conductance at three gate voltages, as indicated. Bottom right schematics depicts the device design with hBN/WTe_2/hBN/graphite heterostructure. Adapted from [140]. (c) 3D quantum Hall effect measured in bulk crystal of $ZrTe_5$. The plots show Shubnikov de Haas oscillations along three perpendicular crystal axes, as indicated. Right schematic depicts the Fermi surface. Adapted from [145]. (d) Representative angle dependence of the Anomalous Hall effect in $ZrTe_5$ with subtracted linear ordinary contribution (left) and 3D polar plots of the anomalous Hall resistivity ρ^0_{AHE}, representing the Berry curvature (right). Adapted from [146].

topological features [142–144], although the exact topological classification is still not defined. The temperature dependence of resistivity in $ZrTe_5$ demonstrates a peak at intermediate temperature (resistivity anomaly), which is related to temperature-induced band structure change and topological Lifshitz transition [142]. Quantum Hall effect oscillations have been observed in this material along all crystal axes leading to conclusion about ellipsoidal shape of the Fermi surface and 3D nature of the system (Fig. 2.5c) [145]. Similarly to WTe_2, $ZrTe_5$ also possesses large Berry curvature, which led to observation of AHE (Fig. 2.5d) and negative magneto resistance [146].

The studies on topological semimetals have a short history, but they have

already demonstrated reach fundamental intrinsic properties. Additional interest in the van der Waals materials from this classification is due to possibility of easy integration into heterostructures with other 2D materials such as e.g. graphene for spin injection and detection without the need for external magnetic fields. This is due to their large charge-to-spin conversion efficiencies. Investigations in this direction are being undertaken.

3 One-dimensional edge contacts to graphene

Conventional approach to study spin transport in graphene utilizes top ferromagnetic contacts. However, they are prone to increased spin dephasing at the interface due to roughness of oxide tunnel barrier. Additionally, fabrication of top contacts is not a viable approach if one wants to benefit from high-quality fully-encapsulated graphene with hexagonal Boron Nitride (hBN). This chapter characterizes 1D edge contacts to graphene with top exfoliated hBN capping layer and all-CVD batch-fabricated hBN/graphene/hBN heterostructures. While aiming to study spin injection/detection with 1D edge contacts, a contribution from spurious magnetoresistance signal is revealed, which is found to originate from the local Hall effect in graphene due to fringe fields from ferromagnetic edge contacts and in the presence of charge current spreading in the nonlocal measurement configuration. Calculations for optimization of the contacts geometry for reduction of the influence of stray fields are provided.

Motivation

Graphene has been shown to be a promising material for spin-polarized electron transport due to its low spin-orbit coupling and negligible hyperfine interactions [29, 44, 148]. Long-distance spin transport and electrical control over spin signal and lifetimes have been achieved in graphene at room temperature [44, 53, 55, 62, 70, 75, 148, 149]. These experiments have shown that the performance of graphene spintronic devices is significantly affected by the quality of the contacts to the graphene channel [148]. Conventional spin transport experiments, such as spin-valve and Hanle spin precession measurements (Fig. 3.1 and Appendix A), use top ferromagnetic metal/tunnel barrier contacts of micrometer width on graphene channels for the purpose of spin injection and detection [29, 44, 148]. However, the fabrication of atomically smooth oxide tunnel barriers is challenging, as they usually contain pinholes, roughness, and defects [46, 72, 150]. The use of such wide contacts is known to limit the device performance due to inhomogeneous injection and detection of spins, and due to interface-induced spin dephasing under the contacts [46, 72, 150]. Additionally, at the nanoscale graphene edges can become

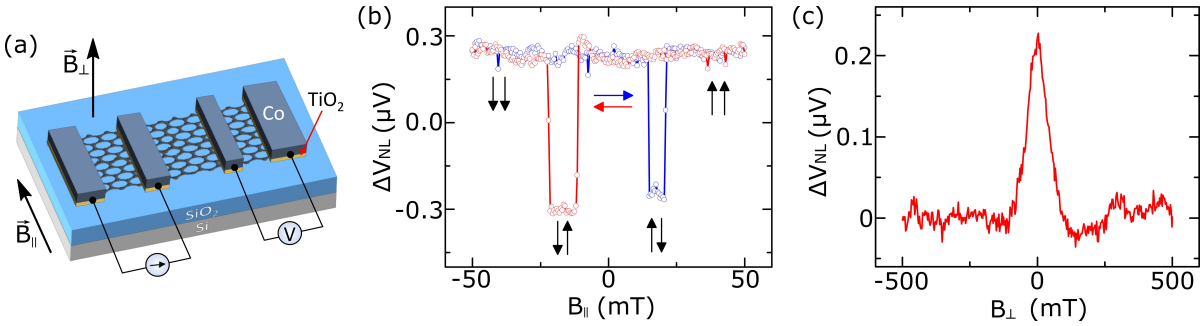

Figure 3.1: A representative spin transport measurements in nonlocal configuration in graphene channel with top ferromagnetic contacts. (a) Device schematic and measurement configuration. (b) Measured nonlocal voltage V_{NL} as a function of external in-plane field ($B_{\parallel}$) sweep. The magnetic field sweep directions are indicated by the red and blue arrows. Black arrows indicate alignment of ferromagnetic contacts. (c) Hanle spin precession signal V_{NL} as a function of an out-of-plane magnetic field ($B_{\perp}$) sweep.

important and are predicted to host spin-polarized edge states, giving rise to spin filtering [111, 151]. Such spintronic properties are also predicted to be tunable by external electric fields [111, 151]. If realized, this would add the spin degree of freedom to graphene-based devices and circuits, where spin currents can be generated and injected from zigzag nanoribbons to graphene without the need of ferromagnetic spin injectors.

Additionally, atomically thin graphene sheet is prone to degradation of its properties when exposed to the environment, e.g. from disorder and impurities caused by conventional SiO_2 substrate. Therefore, encapsulation of graphene by material that would preserve its properties is necessary for high-quality devices. Van der Waals wide-bandgap (~ 5.7 eV) insulator hBN can be utilized for this purpose, particularly as a substrate and top protection layer in graphene spin transport devices with mobility reaching several millions $\mathrm{cm^2V^{-1}s^{-1}}$ [60, 76, 152] and spin lifetimes ~ 12 ns [47]. Moreover, the ultra-clean encapsulated graphene devices set the ground for the study of ballistic spin transport, theoretically described [153] but not yet realized experimentally. However, this would require utilization of 1D edge contacts instead of traditional top contacts to the sandwiched stack of graphene and hBN for efficient fabrication of devices.

3.1 Characterization of ferromagnetic 1D edge contacts

The ferromagnetic 1D edge contacts were characterized in a device fabricated on commercially available CVD graphene after it was transferred onto Si/SiO_2 substrate [Paper I]. The schematic illustration and an optical image of the investigated sample are shown in Fig. 3.2a and Fig. 3.2b, respectively. The micro-fabrication

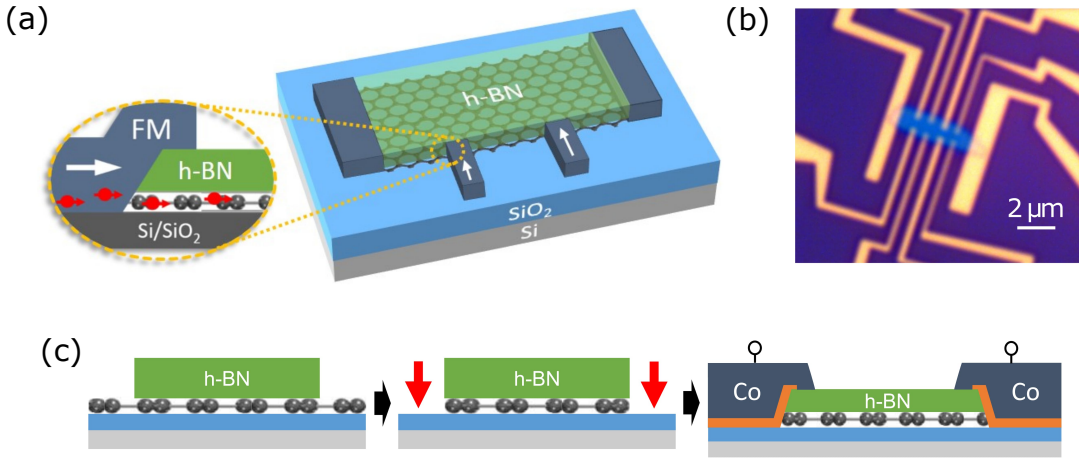

Figure 3.2: (a) Schematic representation and (b) optical microscope picture of the fabricated device. (c) Schematics of the fabrication process steps from left to right: the preparation of graphene/h-BN heterostructures; patterning by oxygen plasma; and deposition of 1D edge contacts.

process steps are depicted in Fig. 3.2c. The hBN was exfoliated from bulk crystal and transferred onto graphene. The unprotected graphene regions were etched away with oxygen plasma.The 1D edge contacts [60] were fabricated by means of electron beam lithography and electron beam evaporation of metals (TiO_2/Co).

The Raman spectrum of CVD graphene/hBN heterostructure [154, 155] is shown in Fig. 3.3a. The absence of a band splitting of the 2D peak and its higher intensity compared to the G peak indicate that the graphene in the heterostructure is a monolayer [154]. The CVD graphene used here has grain sizes of 1-3 µm.

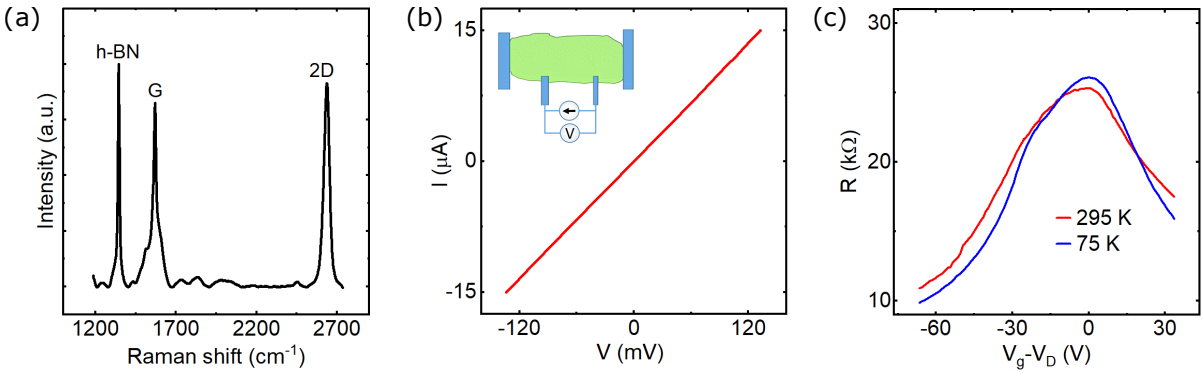

Figure 3.3: (a) Raman spectrum of graphene/h-BN heterostructure. (b) Typical two-terminal I-V characteristic of the 1D edge contacts to graphene at room temperature. Inset: two-terminal measurement configuration. (c) Graphene channel resistance as a function of the back gate voltage (V_g) at 295 K (red) and 75 K (blue) for a local measurement configuration (inset). The horizontal axis is centered around the charge neutrality point V_D

The typical two-terminal current-voltage (I-V) characteristic at room temperature (Fig. 3.3b) shows a linear behaviour and the contact resistances, estimated from the analysis of data from local four- and two-terminal measurements, are reproducible in several devices. The estimated sheet resistance $R_{\square} \approx 6\,\mathrm{k\Omega}/\square$. The back gate dependence of graphene channel resistance (Fig. 3.3c) reveals the charge neutrality (Dirac) point V_D of graphene in the range of $V_D \sim -5$ to $+26$ V for different channels measured in local or nonlocal configurations between different contacts due to variations of doping levels within the graphene sheet.

Fig. 3.4a shows the Hall measurements performed using the measurement configuration depicted in the inset. The Hall voltage (V_H) response of investigated samples obtained during the perpendicular magnetic field (B) sweep at applied current bias $I = 15\,\mu\mathrm{A}$ is fitted with [156, 157]

$$\frac{\partial V_H}{\partial B} = \frac{1}{q_e n_{2D}} I, \tag{3.1}$$

where q_e is the elementary electron charge and n_{2D} is the charge carrier density. Graphene was found to show hole conduction at zero back gate voltage with a sheet charge carrier concentration of $n_{2D} \approx 1.75 \times 10^{12}\,\mathrm{cm}^{-2}$ and background voltage offset of 3 mV, which has been subtracted from the measured raw data. The extracted estimate of the Hall mobility $\mu = {}^{1}/_{q_e n_{2D} R_{\square}} \approx 120\ \mathrm{cm^2 V^{-1} s^{-1}}$. The linearity errors [157–159] were found to be within ± 3.1 % with an average absolute value of 1.3 % over a large magnetic field range from $-760\,\mathrm{mT}$ to $780\,\mathrm{mT}$ at room temperature. From the measured Hall voltage response as a function of time at different perpendicular magnetic fields (Fig. 3.4b) one can estimate the minimum resolvable magnetic field of $\sim 20\,\mathrm{mT}$ at room temperature. The

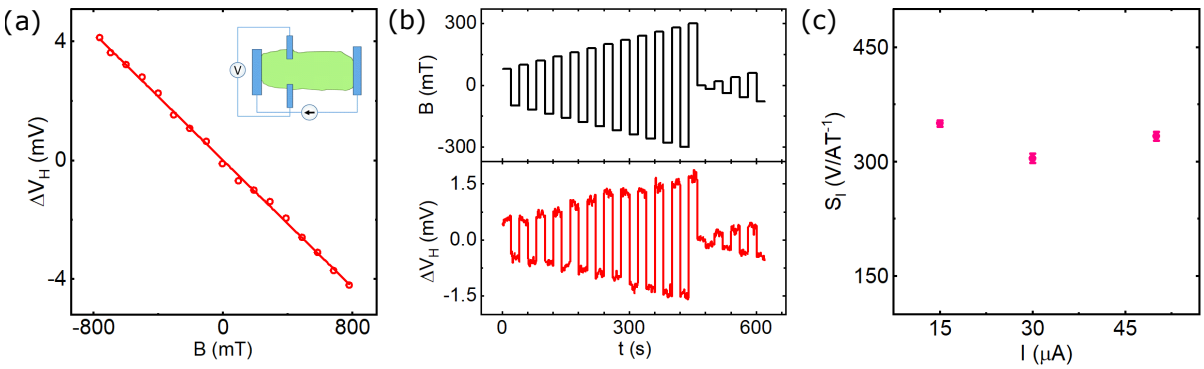

Figure 3.4: (a) Output Hall voltage as a function of perpendicular magnetic field measured at $I = 15\,\mu\mathrm{A}$ at room temperature (circles) with linear fitting (solid line) according to equation 3.1. Inset: Hall measurement configuration. (b) Output Hall voltage as a function of time at different applied magnetic fields measured at $I = 15\,\mu\mathrm{A}$ and at room temperature. (c) Current-related sensitivity as a function of current bias.

calculated current-related Hall sensitivity

$$S_I = \frac{1}{I}\frac{\partial V_H}{\partial B}\bigg|_{I=const} \tag{3.2}$$

did not show significant bias-related change in the bias current range from 15 µA to 50 µA at room temperature (Fig. 3.4c).

The Hall sensitivity of graphene for different carrier concentrations in electron- and hole-doped regimes is shown in Fig. 3.5. Graphene has the unique property that its charge carrier type and concentration can be tuned continuously by applying gate voltage. Fig. 3.5a shows the Hall measurements with application of gate voltages $V_g = \pm 40$ V, where a sign change is observed in the slope of Hall response for electron- and hole-doped regimes. From the back gate dependence of the graphene resistance the charge neutrality point was found at $V_g = 26$ V. Such full gate-dependent Hall effect measurements were performed by sweeping the back gate voltages from electron to hole type of conduction across the Dirac point in the presence of different perpendicular magnetic fields (bottom panel of Fig. 3.5b). To reduce the influence of the device geometry, the Hall response at different magnetic fields ($V_H(B)$) is subtracted from measured response at 0 T magnetic field (V_{H0}): $\Delta V_H = V_H(B) - V_{H0}$ [160]. Here, a change in the amplitude and sign of ΔV_H is observed when sweeping the gate voltage. Using equation. 3.2 the current-related sensitivity is extracted by fitting the ΔV_H-B dependencies. It is plotted in Fig. 3.5c as a function of gate voltage at room temperature. This dependence reveals the gate tuning of the sensitivity with maxima (up to 345 V/(AT)) close to the graphene Dirac point. Such tunability of Hall response stems from gate voltage-induced change of the carrier concentration in the graphene sheet yielding a change of the current-related sensitivity and the

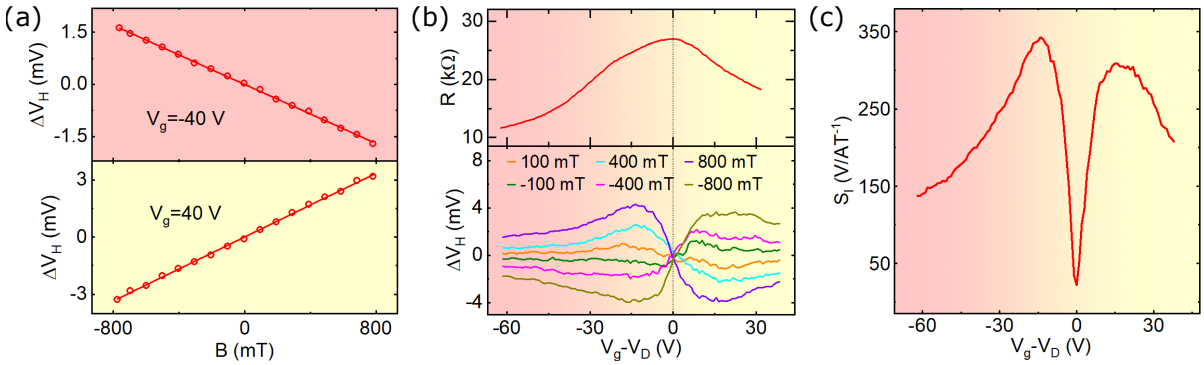

Figure 3.5: (a) Output Hall voltage as a function of perpendicular magnetic field at gate voltages of ±40 V. (b) Back gate dependence of graphene resistance (top) and Hall voltage response at different perpendicular magnetic fields (bottom). V_D is the gate voltage corresponding to the Dirac point. (c) Absolute value of current-related sensitivity calculated from Hall voltage response as a function of gate voltage according to equation 3.2.

output Hall voltage (equations 3.1 and 3.2).

These sensitivities of the large area CVD graphene/h-BN heterostructures are at least three times higher than current silicon-based devices [157, 161]. Previous studies reported on the performance of unencapsulated graphene Hall devices [159, 162, 163] with sensitivities up to 2093 V/(AT). Such unprotected devices are known to be extremely sensitive to environmental parameters and degrade rapidly. Consequently, an insulating barrier is required to protect the graphene layer. Even though studies on Al_2O_3 show very promising results on easily scalable and reproducible device fabrication techniques [164], the close nature of insulating h-BN demonstrated outstanding electronic properties when encapsulating graphene [58]. Such exfoliated h-BN/graphene/h-BN heterostructure Hall devices showed sensitivities 15 times higher than in hBN capped CVD graphene described here [160]. This can be attributed to growth quality of CVD graphene, presence of grain boundaries and charge doping from SiO_2 substrate as well as contaminations introduced during wet transfer of the CVD graphene. Contaminations and grain boundaries are also likely reasons behind the observed low mobility and high sheet resistance of graphene.

3.2 Influence of stray fields and local Hall effect

To investigate the possibility of spin injection and detection with 1D edge contacts to the graphene channel, the heterostructure graphene/hBN device (Fig. 3.2) was utilized. The nonlocal magnetoresistance measurements were carried out as shown in Fig. 3.6a. The nonlocal voltage V_{NL} was observed with single switching and hysteresis behavior while sweeping the in-plane magnetic field aligned with the contacts at fixed bias currents (Fig. 3.6b). By changing the current direction, a similar switching signal with opposite sign was observed. The complete bias dependence of the signal is presented in Fig. 3.6c, which shows a linear dependence in the measured bias range. The observed signal of the switching amplitude $\Delta V_{\uparrow\downarrow}$ decayed with increasing temperature and vanished at $\sim$200 K [Paper II].

The presence of only one step of magnetoresistance for each sweep direction is not typical for spin signals that arise from spin injection and detection [45, 46, 165]. For comparison, a typical spin-valve signal for top ferromagnetic contacts to graphene is shown in Fig. 3.1b. In the latter case, at least two steps are usually visible for each sweep direction, when both injector and detector contacts switch their magnetization direction [45, 46, 165]. The coercivity values of the ferromagnetic contacts used here are within the typical sweeping field range, which has been verified with higher field sweep ranges [Paper II]. A single-step switching signal can arise if the graphene edge itself generates a spin current; however, such effects are only expected in graphene nanoribbons and not in the micrometer-scale devices used here [111, 151]. The quantum spin Hall effect is also unlikely to be responsible for the observed signal considering the negligible spin-orbit coupling in

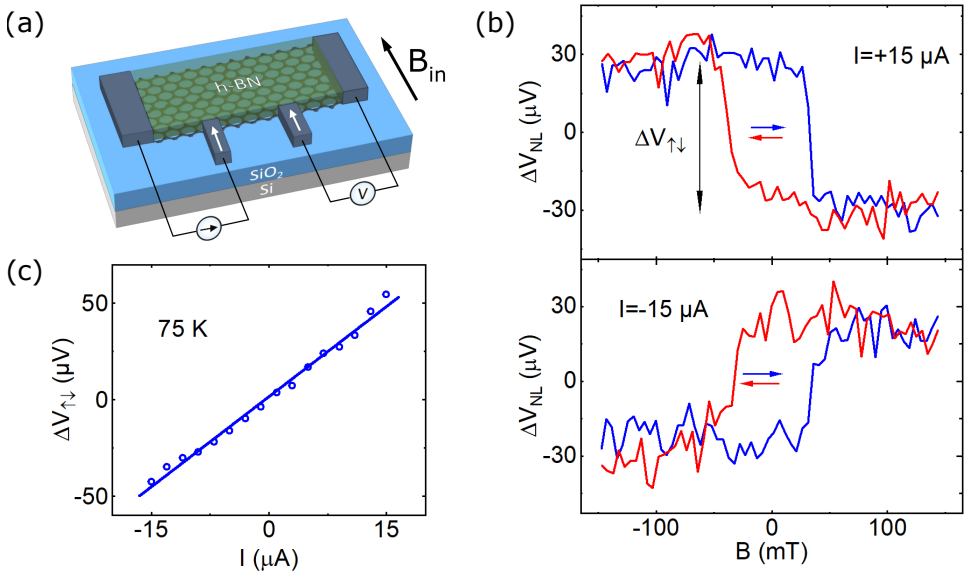

Figure 3.6: (a) Schematic of the nonlocal measurement configuration. (b) Measured nonlocal voltage V_{NL} as a function of external in-plane magnetic field ($B_{||}$) at $I = \pm 15$ μA at 75 K. The $B_{||}$ sweep directions are indicated by red and blue arrows. A baseline linear background voltage is subtracted from the measured data. (c) Current bias dependence of the magnetoresistance switching amplitude $\Delta V_{\uparrow\downarrow}$ at 75 K.

graphene. Additional confirmation of the absence of spin transport in the measured 1D contact device comes from the out-of-plane field sweeps, where no Hanle spin precession signal was observed [Paper II]. Therefore, the observed single-switching magnetoresistance with 1D ferromagnetic contacts could be due to the local Hall effect in the graphene in the presence of stray magnetic fields emanating from the edges of ferromagnetic contacts [150, 166–169].

In order to further clarify the origin of the magnetoresistance, gate-dependent measurements were carried out, where the concentration and type of the charge carriers in graphene is tuned. Fig. 3.7a shows the magnetoresistance switching with the application of $V_g = \pm 30$ V, where a change in the sign of the $\Delta V_{\uparrow\downarrow}$ is observed due to electron or hole conduction of the graphene channel. The complete gate dependence of $\Delta V_{\uparrow\downarrow}$, along with the channel resistance is shown in Fig. 3.7b, revealing a correlation between the sign of $\Delta V_{\uparrow\downarrow}$ and type of charge carrier in graphene. The absolute value of $\Delta V_{\uparrow\downarrow}$ is found to have two maxima near the charge neutrality point in graphene, where the charge density n_{2D} is minimal. These results support the argument in favor of a local Hall effect-dominated magnetoresistance switching. At the same time, this gives additional evidence to rule out any spin-related nature of the observed switching, since the spin signal should not change sign with a change of charge carrier type [45]. One can notice a clear similarity between the V_g dependence of the magnetoresistance signal $\Delta V_{\uparrow\downarrow}$ (Fig. 3.7b) and the regular Hall voltage V_H (Fig. 3.4b). This similarity is justified due to the similar origin of the local Hall magnetoresistance and the regular Hall

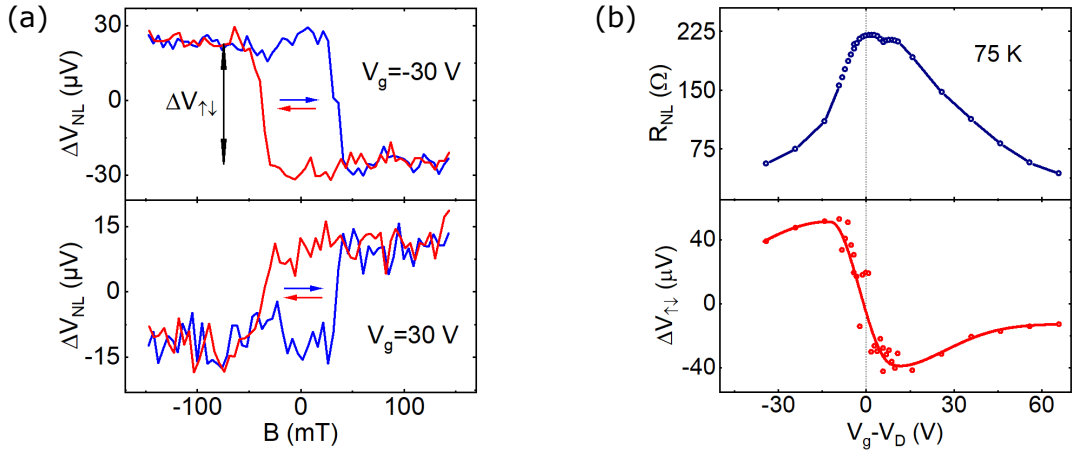

Figure 3.7: (a) Nonlocal magnetoresistance voltage V_{NL} as a function of the in-plane external magnetic field sweeps at $V_g = -30$ V (top panel) and $V_g = 30$ V (bottom panel), measured with $I = 15$ μA at 75 K. A linear baseline offset voltage is subtracted from the raw data. (b) Dependence of the nonlocal graphene resistance $R_{NL} = \Delta V_{NL}/I$ on the back gate voltage $V_g - V_D$ (top panel) and the nonlocal voltage step $\Delta V_{\uparrow\downarrow}$ (bottom panel). V_D is the charge neutrality point of graphene.

effects, which are due to stray magnetic fields from the ferromagnetic contacts, or the Lorentz force acting on moving charges in the presence of a perpendicular external magnetic field, respectively.

In order to quantify the impact of the local Hall effect on the magnetoresistance signal, the Biot-Savart law was employed to numerically calculate the stray magnetic fields that can arise from the 1D edge contacts [Paper II]. The considered contact geometry is shown in Fig. 3.8a. Away from the sloped region, the cobalt magnetizes along the y-axis. In the sloped region, the magnetization yields an out-of-plane component to the stray fields. For metal surfaces parallel to the principal axes, the stray magnetic field can be calculated analytically [170], while the sloped portion of the contact requires a numerical solution.

In Fig. 3.8b the spatial distribution of the perpendicular component of the stray magnetic field B_z is shown within the graphene layer, using the experimental contact geometry (with $t_{hBN,lower} = 0$ and the rest of the parameters listed in the caption of Fig. 3.8). The black dashed lines indicate the contact metal edges. The stray field can reach more than 600 mT at the graphene edge. In addition, the end of the top portion of the ferromagnetic contact also induces a strong perpendicular stray field on the order of 350 mT. Near the 1D edge contact to graphene, the stray field decays from 600 mT to zero over a distance of 50 nm. This average field of 300 mT corresponds to an average magnetic length of ~ 50 nm, indicating that the stray field can indeed induce a significant Hall effect at the charge injection/detection point. In Fig. 3.8c the B_z is plotted along the middle of the contact, indicated by the white dashed line in Fig. 3.8b. This plot shows that by increasing the thickness of the bottom hBN layer, the magnitude of the stray

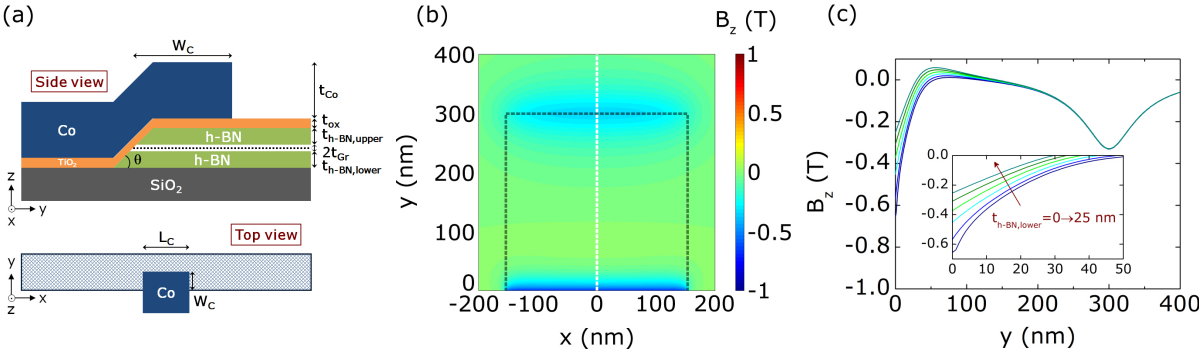

Figure 3.8: (a) Contact geometry considered for the stray field calculations. (b) Profile of the perpendicular stray field B_z within the graphene layer, assuming $L_C = 310$ nm, $W_C = 300$ nm, $t_{Co} = 65$ nm, $t_{ox} = 1$ nm, $t_{hBN,upper} = 25$ nm, $t_{Gr} = 0.35$ nm, $t_{hBN,lower} = 0$, and $\Theta = 45°$. (c) Stray magnetic field along the center of the contact ($x = 0$) for different thicknesses of $t_{hBN,lower}$, where the y-position is relative to the graphene edge.

field at the graphene edge can be reduced by nearly a factor of three for a typical set of experimental parameters. This reduction occurs because the stray fields due to the top and bottom surfaces of the contact tend to cancel one another as the vertical position of the graphene layer increases. While the perpendicular stray field at the injection edge is still relatively large, ~ 250 mT, further optimization of the contact geometry can reduce this, e.g. by tuning the ratio of $t_{hBN,upper}/t_{hBN,lower}$ [Paper II]. A shallower etching angle Θ could also reduce the stray fields at the graphene edge [Paper II]. Additionally, thicker top hBN layer can significantly reduce the stray fields at the contact edge corresponding to $y = 300$ nm [Paper II].

3.3 All-CVD batch-fabricated fully-encapsulated graphene devices with 1D edge contacts

The graphene quality could be further increased in comparison to graphene-hBN heterostructure by improving the CVD graphene mobility via reducing the SiO_2 substrate-induced doping and graphene-substrate interactions [159, 171] by fully encapsulating CVD graphene in h-BN. Utilizing high-quality, large-grain graphene growth would also allow to significantly improve graphene characteristics and spin transport performance. Furthermore, as a next step fully-scalable fabrication approach should be considered with utilization of only all-CVD h-BN/graphene/h-BN stacks patterned on large area. In this section characterization of fully-encapsulated by hBN all-CVD graphene devices with Ti and Cr 1D edge contacts is investigated in Hall bar-geometry devices.

The samples were prepared using a scalable fabrication process. An optical picture and schematic representation of a chip-size batch-fabricated graphene Hall bar devices with 1D edge contacts are shown in Fig. 3.9a and Fig. 3.9b, respectively. Each device consists of CVD graphene sandwiched between multilayer CVD hBN.

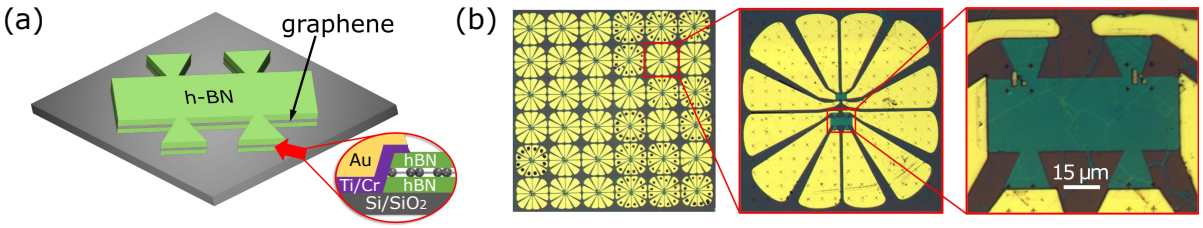

Figure 3.9: (a) The schematic representation of the fabricated CVD graphene encapsulated in CVD hBN Hall-bar devices on Si/SiO_2 substrate with 1D edge contacts. (b) Optical microscope picture of the batch-fabricated chip and the individual graphene Hall bar device.

The 2D material heterostructure was prepared on a Si/SiO_2 wafer by large-area PMMA-supported wet-transfer technique and Ar/H_2 annealing for each layer. Next, they were patterned to Hall bar structures by using an Al (20 nm) hard mask for etching with CHF_3 and O_2 gas. The Al hard mask was removed by wet chemical etching. The 1D edge contacts were fabricated by means of photo-lithography and electron beam evaporation of metals (Ti/Au or Cr/Au).

Fig. 3.10a shows the prepared all-CVD hBN/graphene/hBN heterostructures on a 4-inch SiO_2/Si wafer. The grain size of the CVD graphene is mostly between $1-5$ µm range. The thickness of the CVD hBN used in the heterostructures was measured by AFM ($\sim 10-13$ nm, as shown in Fig. 3.10b). The rms roughness of the hBN films were found to be $1-2$ nm on SiO_2 substrate. Although the organic contamination introduced on hBN from the transfer and device fabrication process could be removed by annealing in Ar/H_2, the roughness remains at similar values.

The electrical characteristics of 1D edge contacts with Cr/Au and Ti/Au metals to graphene are shown in Fig. 3.10c–e. As observed from the current-voltage (IV) characteristics, the Cr/Au contacts provide a low-resistive linear behavior, while Ti/Au contacts show a high-resistive non-linear tunneling behavior. The weak temperature dependence of the resistance for the Cr/Au contacts at zero bias and at 0.5 V bias (Fig. 3.10d) indicates high quality interfaces [172]. However, the high resistance and tunneling behavior of the Ti/Au edge contact to graphene (Fig. 3.10e) could be due to interfacial species, such as oxidation at the interfaces. The encapsulated CVD graphene is found to be hole-doped with sheet resistances $R_\square \approx 520-870\ \Omega/\square$.

The Hall measurements on the hBN/graphene/hBN heterostructure devices with Cr/Au and Ti/Au edge contacts at ambient conditions are presented in Fig. 3.11. The Hall signal V_H, measured at a constant applied current while sweeping a perpendicular magnetic field $B_\perp$ at bias current $I = 90$ µA, is shown in Fig. 3.11b. A background voltage offset, due to a misalignment between Hall probe contacts, has been subtracted. Fitting the Hall response with equation 3.1, the Hall mobilities were obtained $\mu = 1/(q_e n_{2D} R_\square) \approx 1200\ \mathrm{cm^2/Vs^{-1}}$ with carrier concentrations $n_{2D} \approx 8 \times 10^{12}\ \mathrm{cm^{-2}}$. The high charge doping is most likely due to

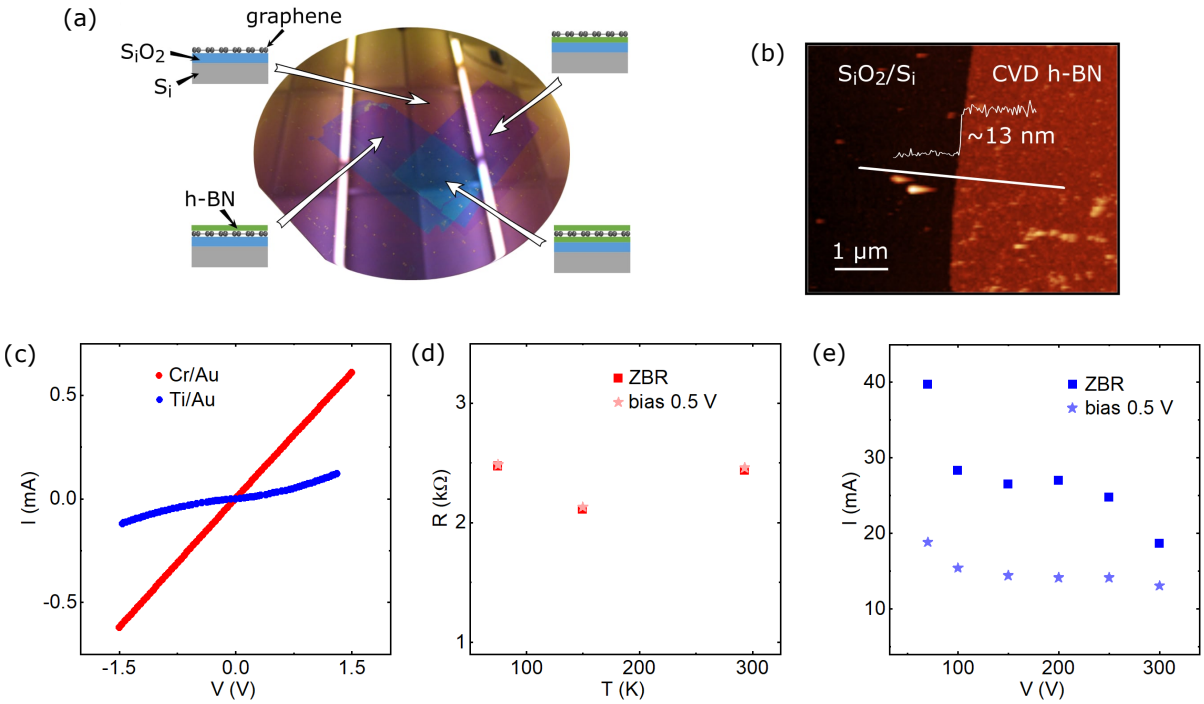

Figure 3.10: (a) The prepared hBN/graphene/hBN heterostructures using all-CVD 2D materials on a 4-inch SiO_2/Si wafer by layer transfer method. Different regions containing 2D layers and heterostructures are indicated by schematics. (b) AFM image and thickness profile of CVD hBN on SiO_2/Si wafer. (c) Two-terminal IV characteristics of the device with Cr/Au (red) and Ti/Au (blue) edge contacts to graphene at 293 K. (d),(e) Cr/Au and Ti/Au edge contact resistances at 0.5 V bias (asterisks) and zero bias voltage (squares) as a function of temperature, respectively.

the wet transfer process that might have trapped impurities at the hBN/graphene interfaces. The Hall bar samples with Cr/Au contacts showed stable performance and good response to magnetic field changes in time (Fig. 3.11c), while Ti/Au contacts revealed much higher noise (Fig. 3.11d). This shows that Cr/Au edge contacts perform better in terms of higher linearity of the Hall response and lower noise compared to Ti/ Au. The extracted current-related Hall sensitivities (equation 3.2) S_I were found in the range $60-100$ V/(AT), similar for both Cr/Au and Ti/Au contacts and of comparable amplitude to Si-based Hall sensitivities [157]. Measurements up to 190 days after fabrication showed little degradation of the contacts and graphene channel over time, in contrast to unencapsulated graphene devices [Paper III].

The utilized h-BN encapsulation is imperative step forward towards protection of graphene for practical applications in ambient environment. The performance of devices would greatly benefit from improved CVD growth methods of graphene and multi-layer hBN, as well as large-area layer transfer techniques for fabrication of heterostructures. Furthermore, development of methods for in-situ growth [173–175] of high-quality hBN/graphene/hBN van der Waals heterostructures on large

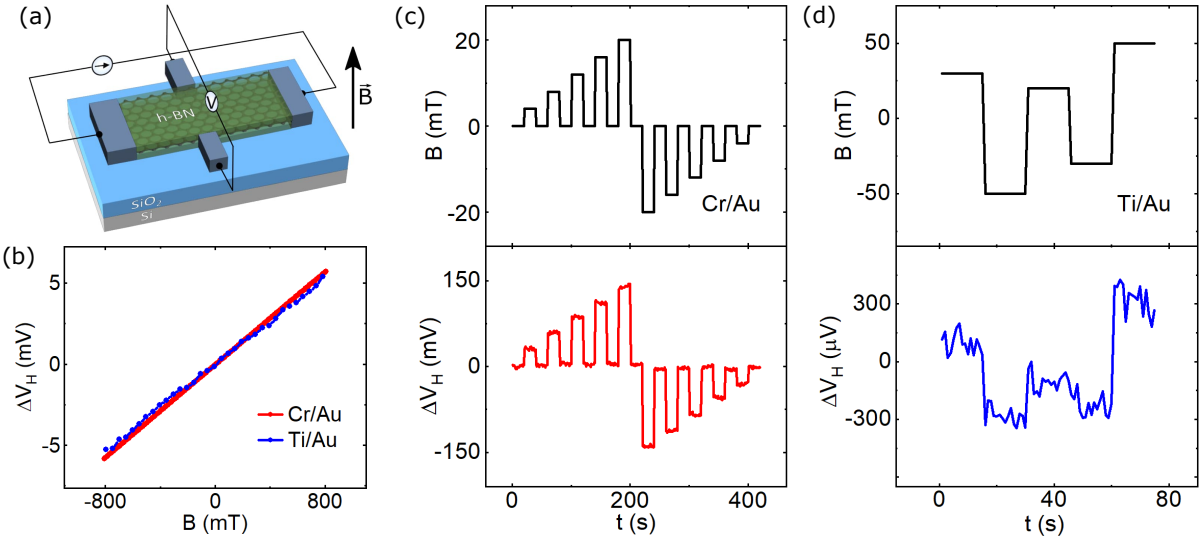

Figure 3.11: (a) The schematic configuration for the Hall measurements. (b) Hall voltage as a function of perpendicular magnetic field at 293 K for Cr/Au (red) and Ti/Au (blue) contacts. (c),(d) Hall voltage as a function of time at different applied magnetic fields at 293 K for Cr/Au and Ti/Au contacts, respectively. Measurements are shown for a bias current of $I = 90$ µA and the background offset voltage is subtracted from the measured data.

areas would by-pass fabrication-related problems and allow for higher Hall sensitivities with lower graphene doping levels. Further investigations are required on the performance of all-CVD fully-encapsulated graphene devices with ferromagnetic 1D edge contacts and spin transport in such graphene devices. To be noted, as revealed from the calculations on the stray fields from ferromagnetic contacts in the 2D graphene channels contacted by 1D contacts, the presence of additional bottom hBN layer would benefit the performance of such devices in terms of reducing fringe fields and possibly allowing for observation of spin injection/detection with 1D edge contacts. Additionally, modifying the contacts outline to make them cross the channel completely along its width has been reported to be beneficial for injection and detection of spins with 1D edge contacts, where spin transport was observed in all-exfoliated hBN/graphene/hBN heterostructure device in nonlocal measurement geometry [77].

4 Van der Waals magnetism and magnetic proximity effect in graphene

The field of two-dimensional magnetic materials has been thriving since 2017 when first experimental reports on atomically thin 2D magnets were published. The availability of a range of such atomically thin van der Waals materials already discovered, and many more to come in the future, hold promise for making new heterogeneous devices in combination with other 2D materials for pushing the frontiers of the state of the art in the field of spintronics. This chapter provides a characterization of Fe-based metallic van der Waals ferromagnets and magnetic insulator $Cr_2Ge_2Te_6$ with perpendicular magnetic anisotropy. The measured data are analyzed and discussed in the context of the present state of the art in the field. The latter was studied in heterostructure with graphene, where proximity magnetic order was induced leading to modified Hanle spin precession signals and increased spin relaxation anisotropy.

4.1 Ferromagnetic insulator $Cr_2Ge_2Te_6$

Although the first studies on bulk crystals of the Heisenberg ferromagnet CGT have appeared decades ago [176, 177], an active research on this material started in 2017, sparked by the interest in two-dimensional magnets [81]. The lattice structure of the CGT (schematically shown in Fig. 4.1a) consists of van der Waals layers of magnetic ions of Cr sandwiched by Te and Ge with a thickness of ~ 6.9 Å per layer [178] and lattice constants $a = b = 6.83$ Å, $c = 20.6$ Å [176, 179, 180]. The Raman spectrum of the CGT flake of ~ 30 nm in thickness (Fig. 4.1b) contains pronounced E_g^3 and A_g^1 phonon modes at 108 cm^{-1} and 134 cm^{-1}, respectively, which is characteristic of a CGT sample with more than one layer [179, 181]. In the freshly cleaved flake no broad peak at 121 cm^{-1} is observed, which can appear in case of formation of any TeO_x on the surface [181].

In contrast to Fe-based ferromagnets, CGT has semiconducting or Mott insulator-type temperature dependence of resistivity [182, 183] with different reported bulk bandgap ranging between ~ 0.38 eV measured by ARPES [184],

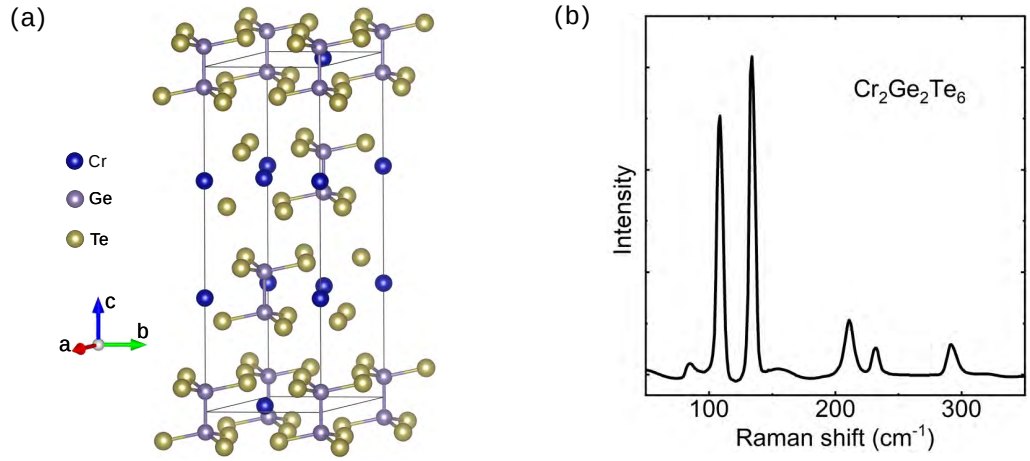

Figure 4.1: Crystal structure (a) and Raman spetrum of $Cr_2Ge_2Te_6$ flake (b).

$\sim$ 0.74 eV as obtained from optical transmission experiments [185] and tunneling spectroscopy [186], $\sim$ 0.2 eV as activation energy extracted from temperature dependence of resistivity [176, 183]. The resistance exponentially increases as the temperature approaches Curie point and below, giving rise to insulating charge transport properties in the ferromagnetic state. The transition from paramagnetism to ferromagnetism occurs at Curie temperature of $\sim$ 65 K in the bulk sample as obtained from temperature dependence of magnetic moment of bulk CGT crystal that was measured by SQUID (Fig. 4.2a), in agreement with reports in literature [81, 176, 178, 182, 187, 188]. As the thickness of flakes reduces below $\sim$ 5 nm, presumably below the range of spin-spin interactions in CGT [189]

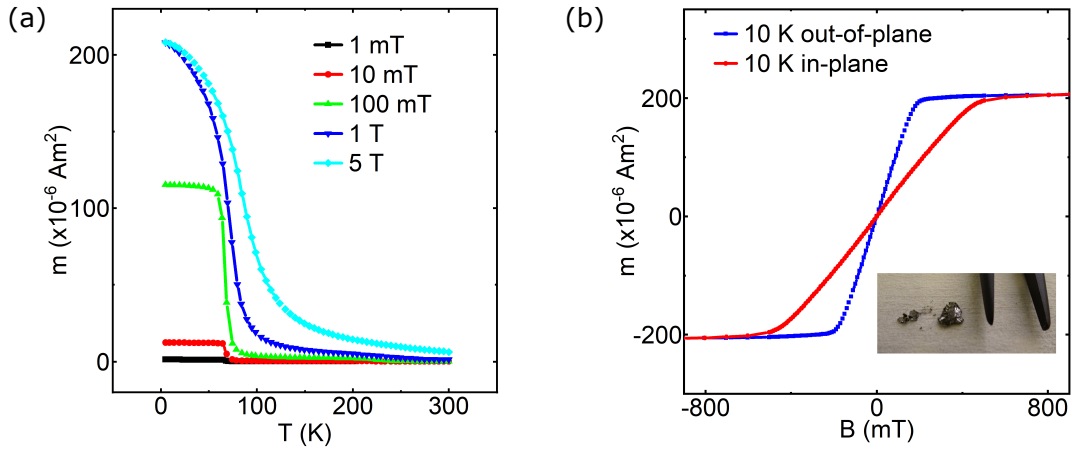

Figure 4.2: Magnetic characterization of bulk $Cr_2Ge_2Te_6$. (a) Magnetic moment m measured as a function of temperature with different applied magnetic fields. (b) Field dependence of m as a function of magnetic field at 10 K for both in-plane and out-of-plane magnetic field directions. Inset picture shows bulk CGT crystal next to tweezers for scale reference.

after dimensional crossover from 3D to 2D system [78], the magnetic ordering temperature drops and reaches a value of $\sim$ 30 K in bilayer as shown experimentally by MOKE measurements [81] and confirmed by calculations [190]. The magnetic field dependence of magnetic moment of bulk CGT (Fig. 4.2b) do not show any visible remanence and magnetic saturation state onsets easier when magnetic field is applied along the c-axis. This confirms the out-of-plane magnetic anisotropy, in accordance with other reports [81, 182, 183]. By application of electric field through gating in thin flakes of CGT the channel conductivity was tuned by an order of magnitude below Curie temperature and the AHE was observed [178]. Lorentz transmission electron microscopy [191] study of the magnetic domain structure of CGT revealed formation of non-trivial magnetic textures (skyrmions) in thin flakes of $\sim$ 20 nm below Curie temperature when the sample was cooled under small applied perpendicular magnetic field or moderate-magnitude (below saturation value) perpendicular fields were applied [192], similar to F3GT [193, 194]. Under applied elevated pressures the lattice constants can be modified, leading to decrease of Curie temperature [187], switching to easy-plane magnetic anisotropy [183], semiconductor-to-metal transition [195, 196].

4.2 Magnetic proximity in graphene/$Cr_2Ge_2Te_6$ heterostructures

Topological quantum states of matter and spintronics have considerable interest in the field of condensed matter physics for applications in low-power electronics without the application of an external magnetic field [197, 198]. The generation of magnetic exchange interaction and strong spin-orbit coupling in 2D Dirac materials such as graphene is expected to result in the emergence of quantum anomalous Hall state and topologically protected chiral spin textures [199, 200]. Graphene, having excellent charge and spin transport properties, is a suitable atomically-thin 2D material to create proximity-induced effects when placed in heterostructures with other functional materials [148, 201–203]. Inducing magnetism in graphene through proximity effects, in contrast to functionalization with adatoms and vacancies [44, 112, 115], allows to reduce the disorder, which in terms of energy scale must be smaller than exchange splitting gap. Magnetic proximity effects have been investigated in graphene in heterostructures with ferromagnetic semiconductor $CrBr_3$ [90, 126], antiferromagnetic semiconductors CrSe [107], CrSBr [91], 3D ferromagnetic metals Co and Ni [204], magnetic oxides $BiFeO_3$ [124, 125], YIG [106, 108, 118, 121, 122, 205], EuO [123] and other magnetic insulators such as EuS [105]. Atomically-flat nature of 2D material-based van der Waals heterostructures is beneficial for a good interfacial contact for proximity interactions. Theoretical predictions indicate that heterostructures of 2D magnetic materials with graphene are expected to produce a large exchange splitting in the graphene layer, enabling the emergence of a topological quantum phase [206–208], which is switchable by

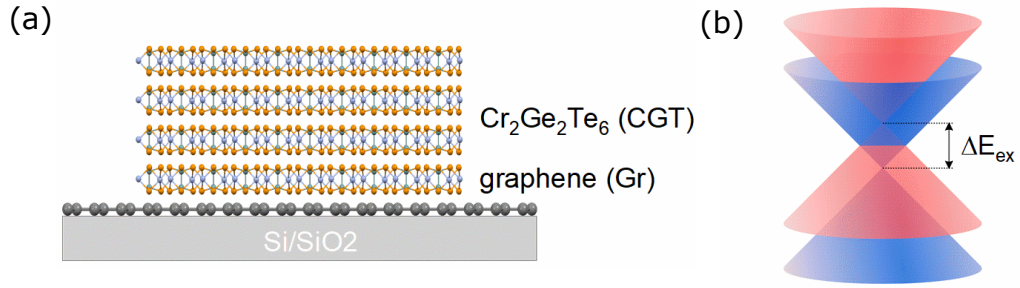

Figure 4.3: (a) Schematic of atomic structure of CGT/graphene heterostructure. (b) Graphene band structure in proximity with CGT in the vicinity of the Dirac point. Graphene can acquire magnetic order with a splitting of spin-degenerate bands by an exchange gap ΔE_{ex}.

electric field valley splitting [209].

In the present work, the magnetic exchange splitting in graphene was induced through proximity to a flake ($\sim$ 30 nm in thickness) of ferromagnetic insulator $Cr_2Ge_2Te_6$ (Fig. 4.3) [Paper IV] and studied by employing nonlocal spin transport and Hanle spin precession measurements (section A and Fig. 4.4a) in graphene/CGT heterostructure channel. The choice of CGT is motivated by its layered structure and insulating behavior at low temperature ($\sim$ 60 MΩfor CGT [Paper IV]). The device (Fig. 4.4b) was nanofabricated on Si/SiO_2 substrate with pre-transferred CVD graphene on it. After patterning graphene into stripes with electron beam lithography and oxygen plasma etching, the exfoliated flakes of CGT were dry-transferred on top, followed by another series of lithography steps for electron beam evaporation of TiO_2/Co contacts.

The spin valve and Hanle precession measurements at room temperature

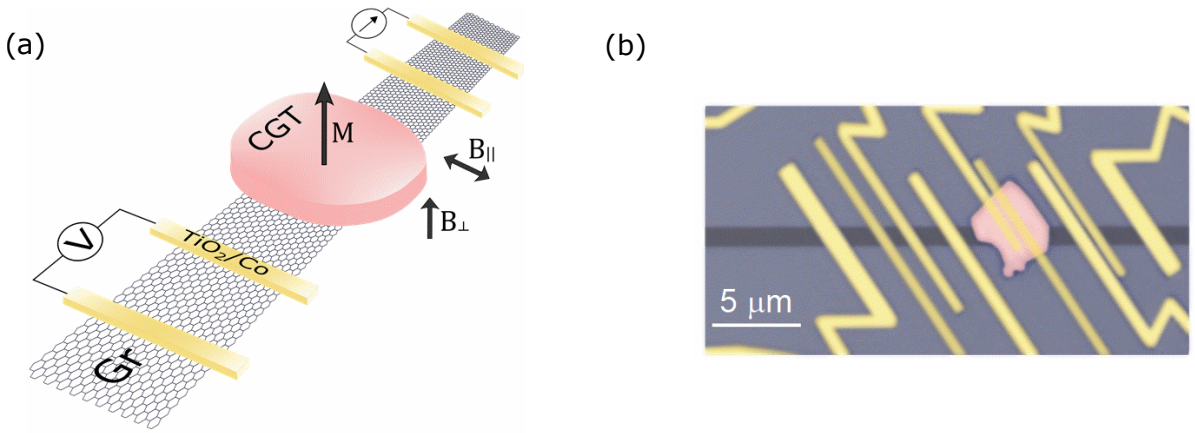

Figure 4.4: (a) The nonlocal spin transport measurement configuration with graphene/CGT channel. (b) False-color optical microscope picture of the nanofabricated device.

(300 K), well above the T_c of CGT (Fig. 4.5a,b), demonstrated signals that are representative of pure graphene channels for both up and down magnetic field sweeps (Fig.3.1). By fitting the signal with equation A.2 the spin lifetime $\tau_s = 244 \pm 32$ ps, diffusion coefficient $D_s = 0.019 \pm 0.005$ m^{2}s^{-1} and diffusion length $\lambda = \sqrt{D\tau_s} = 2.1 \pm 0.4$ µm were obtained. At low temperatures (50 K), below the Curie point of CGT (Fig. 4.5c), one can notice two distinctive features of the measured Hanle signal: a shift of the two Hanle peaks with respect to each other and asymmetry of the Hanle peaks. Such observations are indicative of an out-of-plane magnetism induced in the graphene by proximity to CGT.

These features are also seen in simulations (Fig. 4.6) obtained from the solution of the Bloch equation that considers spatially inhomogeneous spin transport properties due to the influence of the CGT flake, which was derived in supplementary material of [210]. The expression is given by

$$R_{NL} = \frac{C}{I} \cdot \mathrm{Re}\left\{ \frac{\lambda e^{-(L_{ch}-L_H)/\lambda}}{\frac{(\lambda_H+\lambda)^2}{\lambda_H\lambda} e^{L_H/\lambda_H} - \frac{(\lambda_H-\lambda)^2}{\lambda_H\lambda} e^{-L_H/\lambda_H}} \right\} \tag{4.1}$$

where $\lambda = \sqrt{D\tau_s/(1+i\omega\tau_s)}$ is the spin relaxation length in the uncovered graphene region, modified by the magnetic field. The Larmor precession frequency (equation A.1) is given by ω. In the graphene/CGT region, these parameters are given by $\lambda_H = \sqrt{D_H\tau_H/(1+i\omega_H\tau_H)}$, where Larmor frequency ω_H is modified by substitution $B_\perp \to B_\perp + B_{ex}$ and B_{ex} is the perpendicular exchange field induced in the graphene by the CGT. The channel length is given by L_{ch} and the length of the graphene/CGT region is L_H, C denotes the ampliude of the Hanle signal. The parameters used in simulation of Fig. 4.6a are $L_{ch} = 6.95$ µm, $L_H = 4.3$ µm, $\tau_s = 340$ ps, $\tau_H = 100$ ps, $D = D_H = 0.05$ m^2/s and $C = 3.4$ mΩ. The form of B_{ex} as a function of $B_\perp$ is shown in the inset of Fig. 4.6a. In the Fig. 4.6b the Hanle signal is simulated for a different value of $L_H = L_{ch}$ that corresponds to

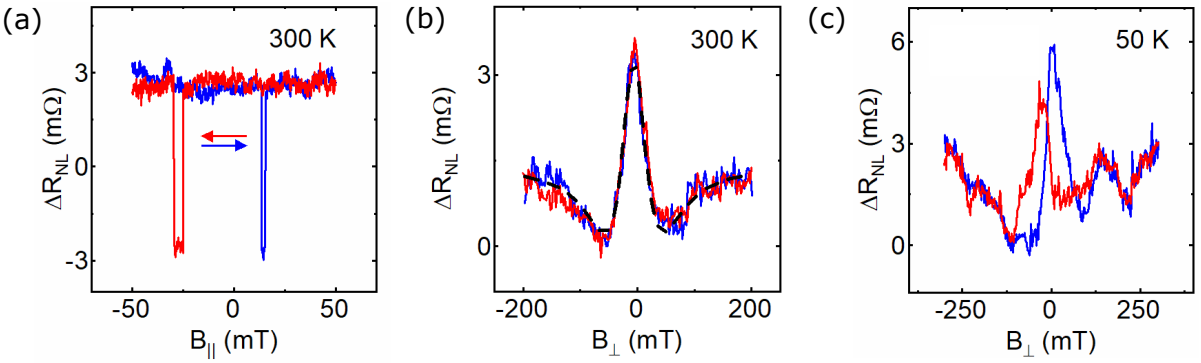

Figure 4.5: (a) Spin valve and (b) Hanle measurements at room temperature in graphene/CGT heterostructure channel with black dashed line fitting according to equation A.2. (c) Hanle spin precession signal at 50 K in the same channel.

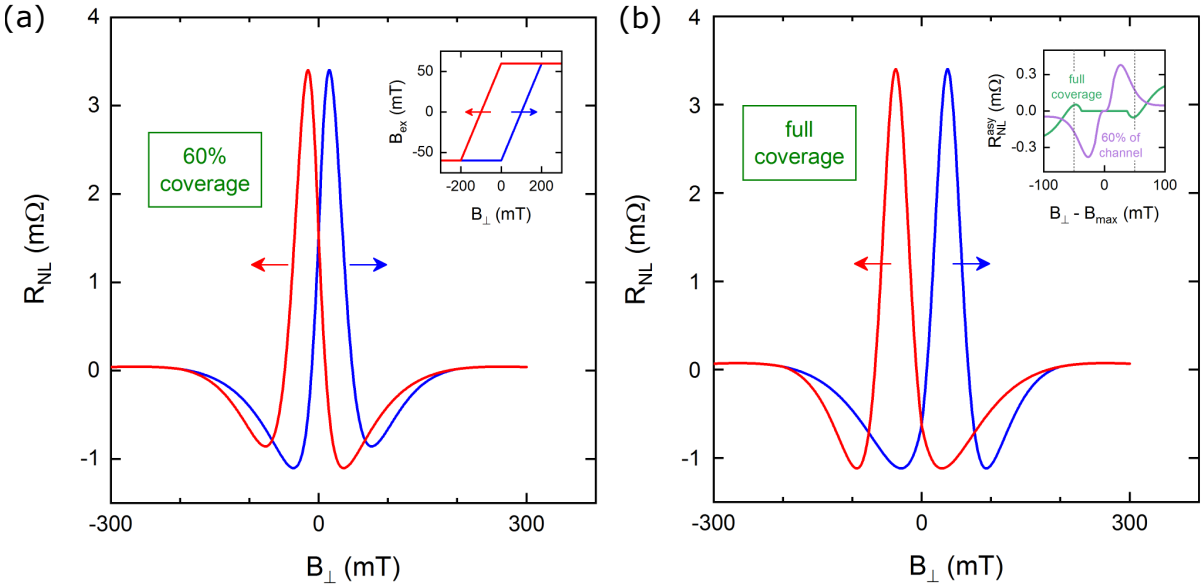

Figure 4.6: Simulated Hanle curves. (a) The case when the CGT flake covers ∼60% of the graphene channel, with the inset showing the assumed behavior of B_{ex}. (b) The case when the CGT flake uniformly covers the entire graphene flake. The inset shows the asymmetric portion of the forward sweep curve for each case, indicating that asymmetry in the central Hanle peak arises from the nonuniformity of the proximity-induced exchange field. B_{max} denotes magnetic field at the peak position [Paper IV].

full coverage of the nonlocal graphene channel by the CGT, in contrast to 60% coverage in Fig. 4.6a. The inset in Fig. 4.6b shows the asymmetric component of the forward sweep in each case. Here it is evident that the asymmetry of the central Hanle peak (between the dashed lines in the inset) arises from the finite extent of the proximity-induced exchange field, and this asymmetry disappears in the limit of full coverage by the CGT. In the experimental sample perpendicular component of the stray fields B_s from the CGT flake do contribute to the spin precession in the channel by adding to the external field $B_\perp \rightarrow B_\perp + B_{ex} + B_s$. However, the observed Hanle signals are mainly shaped by the contributions from externally applied and exchange fields as shown in Supplementary note 2 of [Paper IV]. The peak splitting between the two Hanle sweeps can then originate from hysteretic behavior [211] of the proximity-induced magnetic exchange fields in graphene. This alters the position of the Hanle peak corresponding to zero total field, which, due to hysteresis, is obtained at different values of the applied magnetic field depending on the sweep direction.

The Hanle spin precession measurements performed at several different temperatures further elucidate the proximity-induced magnetic interaction in graphene-CGT heterostructures (Fig. 4.7). The measured data reveal a rapid decrease of the nonlocal spin signal amplitude (R_{NL}) with increasing temperature in comparison to the temperature dependence of pristine graphene (Fig. 4.7b) [53], followed by

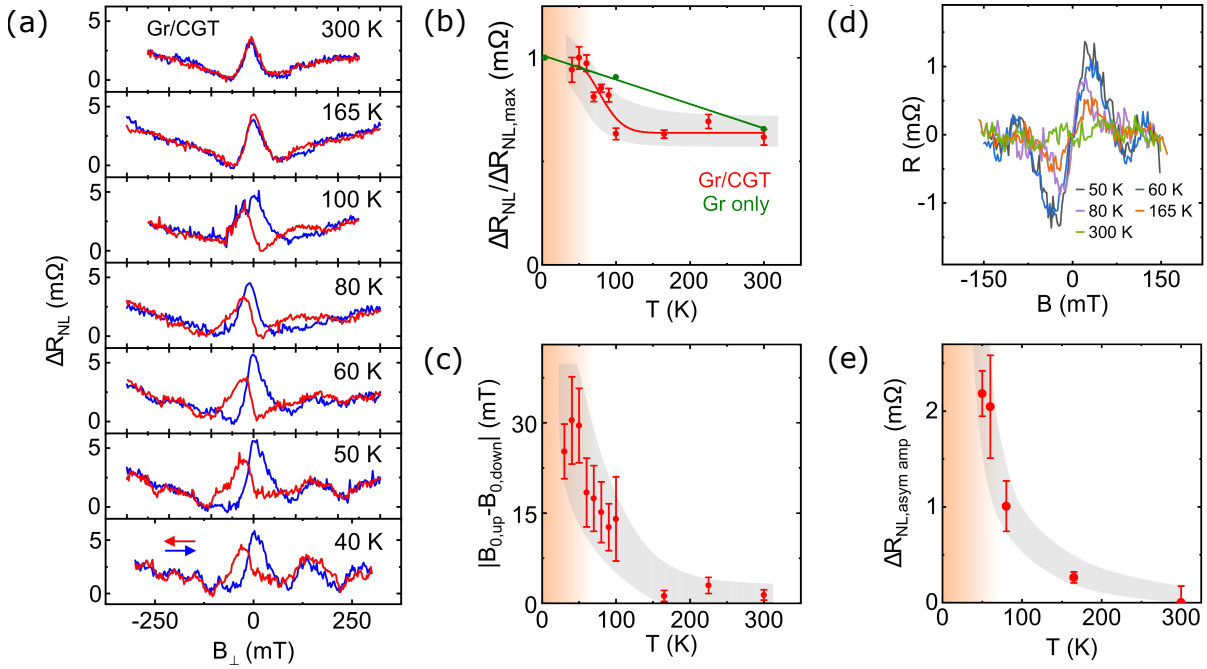

Figure 4.7: Temperature dependence of spin signal in graphene/CGT heterostructures. (a) Nonlocal Hanle spin precession measurements as a function of perpendicular magnetic field for up (blue) and down (red) sweeps at different temperatures. (b) Normalized nonlocal Hanle signal amplitudes (R_{NL}) as a function of temperature for a graphene/CGT device (red) and for a 4 µm CVD graphene channel (green) [53]. (c) Magnitude of the horizontal separation between positions of nonlocal Hanle signal peaks for up ($B_{0,up}$) and down ($B_{0,down}$) sweeps as a function of temperature. (d) Asymmetric part of the measured Hanle signal at different temperatures. (e) Amplitude of the asymmetric signal from (d) as a function of temperature. The solid lines in (b) and grey regions in (b), (c) and (e) are guides to the eye.

a saturation of the signal above the Curie temperature of the CGT. The rapid spin signal amplitude decay with temperature in the range of $T < T_c$, compared to pristine graphene, can be attributed to fluctuating proximity-induced magnetic exchange fields due to random fluctuations of the magnetization of the CGT flake, which become more pronounced approaching the magnetic ordering temperature of CGT [121]. Such fluctuations cause random changes of the proximity-induced exchange field and, hence, the effective field that acts on the propagating spins, leading to enhanced spin relaxation [212, 213]. Furthermore, the separation between the peaks for opposite Hanle sweeps vanishes at elevated temperatures (Fig. 4.7c).

The presence of Hanle peak shifts indicates that the proximity-induced exchange field in graphene persists above the Curie temperature for bulk CGT [123, 214–218] ($\sim$ 65 K) up to at least 100 K. Possible factors that lead to such enhancement of Curie temperature at the interace are e.g. interface charge transfer, interface built-in electric field, interfacial orbital hybridization, strain, band renor-

malization [85]. Additionally, one can deconvolute the measured Hanle signal into symmetric and asymmetric components, where the latter contains information on additional rotation of spins in the channel [219] with respect to normal precession caused by the applied perpendicular magnetic field. Such rotation can originate e.g. from the modified spin texture of graphene under the CGT flake caused by the proximity to the latter. From Fig. 4.7d,e one can see that the asymmetric contribution to the signal also vanishes with increasing temperature in a comparable way as in Fig. 4.7c. This suggests the same origin for peak splitting and asymmetry: both can arise from the proximity-induced exchange field in the graphene channel under the flake, which persists at $T > T_c$ of bulk CGT and decays with increasing temperature, while being completely absent at temperatures above 165 K. Fitting the symmetric component of the Hanle signal with the solution of the Bloch equation for spin diffusion in a homogeneous channel gives values of the in-plane spin lifetimes $\tau_{\parallel}$ in the range of $90 - 280$ ps; the comparably large spread of values results due to a large number of free fitting parameters (supplementary note 4 in [Paper IV]). However, most fits resulting in reasonable spin transport parameters yielded an exchange field on the order of a few tens of mT.

The spin transport measurements in the graphene-based hetero-structures revealed also the spin relaxation anisotropy, as observed by employing the same nonlocal Hanle measurement configuration (Fig. 4.8). However, here the field sweep range is broader, allowing for injection and detection of both in-plane and out-of-plane spins in different field ranges. In-plane spins are injected and detected at low field values when the contacts are magnetized in-plane at magnetic fields $B_{\perp} < 0.2$ T (Fig. 4.8a). With increasing out-of-plane field the magnetization of the contacts starts to rotate to the out-of-plane direction, reaching saturation at $B_{\perp} > 2$ T(Fig. 4.8b). When spins relax with different rates in the in-plane or out-of-plane direction, different amplitudes of the signal are observed for the corresponding magnetic field ranges (Fig. 4.8c). Therefore, the in-plane spin lifetime $\tau_{\parallel}$ is estimated from low $B_{\perp}$-field Hanle data, while the out-of-plane spin lifetime $\tau_{\perp}$ is extracted from large out-of-plane $B_{\perp}$-field measurements. As shown in Fig. 4.8d, in the graphene/CGT heterostructure the spin signal magnitudes at $B_{\perp} = 0$ for in-plane spins ($\Delta R_{NL}^{\parallel}$) and at $B_{\perp} = 2.5$ T for spins perpendicular to the plane ($\Delta R_{NL}^{\perp}$) show strong anisotropy, with $\Delta R_{NL}^{\perp} > \Delta R_{NL}^{\parallel}$ and with a ratio $\Delta R_{NL}^{\perp}/\Delta R_{NL}^{\parallel} \sim 10$. The spin lifetime anisotropy $r \equiv \tau_{\perp}/\tau_{\parallel}$ is obtained from $\Delta R_{NL}^{\perp}/\Delta R_{NL}^{\parallel} = \sqrt{r}e^{-(L/\lambda_{\parallel}(1/\sqrt{r}-1)}$, where L is the channel length and $\lambda_{\parallel}$ is the spin diffusion length for in-plane spins [220]. From this expression we find a strong anisotropy, with r being 3.9 times the value of $\tau_{\parallel} \sim 150$ ps (assuming homogeneous channel characteristics). Such observations are in contrast with the isotropic spin relaxation in pristine graphene channels, which have a value of r close to 1 (0.94 ± 0.01 in Fig. 4.8e).

While the increase of SOC, particularly Valley-Zeeman type, in the proximitized graphene can generate an out-of-plane spin texture and increase spin

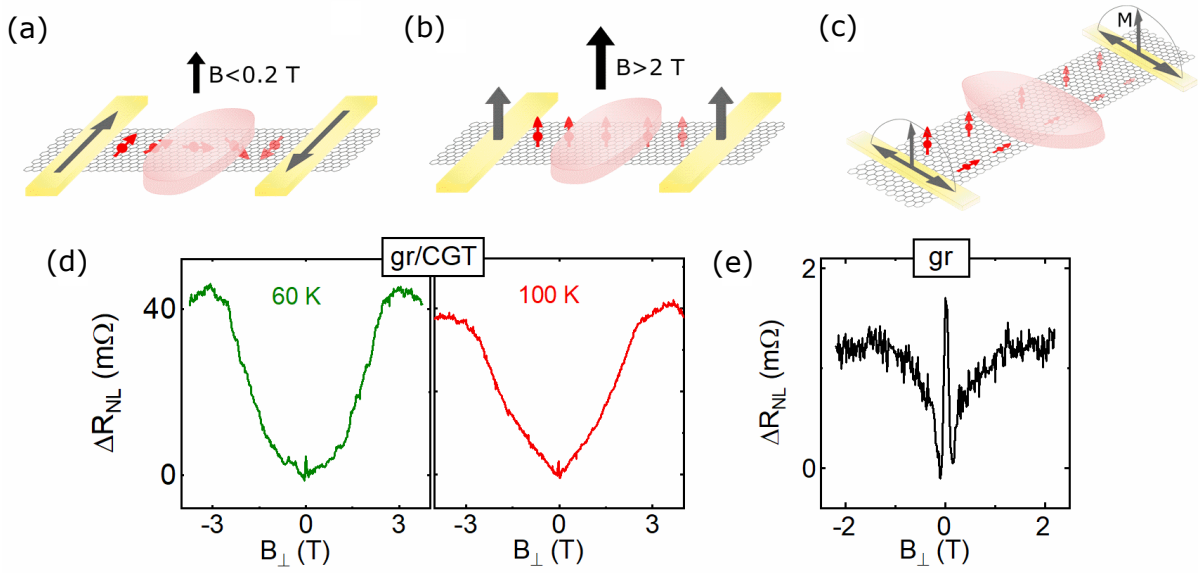

Figure 4.8: Anisotropic spin relaxation in graphene/CGT heterostructure. (a) Measurement geometry with small perpendicular magnetic field $B_\perp < 0.2$ T, where the magnetization of the ferromagnetic Co contacts and injected spin polarization are inplane, resulting in Hanle spin precession. (b) Measurement geometry with large perpendicular magnetic field $B_\perp > 2$ T, where the magnetization of the ferromagnets and injected spin polarization are out of plane, resulting in no Hanle precession. (c) The measurements of graphene/CGT channels indicate anisotropic relaxation with faster rates of spin relaxation for in-plane spins, as shown in the schematic. (d) Experimental nonlocal measurements in a channel with $\sim 60\%$ flake overlap at 60 K and 100 K. A parabolic magnetoresistance background is subtracted from the measured data. (e) The reference measurement in pristine CVD graphene showing very low anisotropy with almost similar signal for in-plane and perpendicular spins.

relaxation for in-plane spins leading to spin relaxation anisotropy $r > 1$ as shown in CGT/graphene [Paper IV] and TMDC/graphene [221, 222] heterostructures, the temperature dependence of the spin signal in Fig. 4.7b suggests that magnetic exchange fluctuations are playing a role in the spin relaxation. In this scenario, an apparent spin relaxation anisotropy can also emerge. In case of the exchange fluctuation mechanism the spins are dephased by the fluctuations, but if magnetic field is applied the fluctuations are suppressed. This is different for spins parallel and perpendicular to the applied magnetic field, which results in an increase of anisotropy with increasing out-of-plane magnetic field $B_\perp$. Assuming that exchange fluctuations are the sole source of spin relaxation in the graphene/CGT devices, the spin relaxation is nearly completely isotropic ($r \approx 1.002$) at $B_\perp = 0$ and becomes anisotropic with increasing values of $B_\perp$ (supplementary note 6 in [Paper IV]). This analysis indicates that if the spin relaxation is dominated by exchange fluctuations, the large anisotropy seen in Fig. 4.8d can be driven by the external field $B_\perp$ and may not be intrinsic to the graphene/CGT interface. This is

because the perpendicular proximity-induced exchange field B_{ex}, while sufficiently large to see in Hanle measurements, is not large enough to suppress exchange fluctuations in graphene. It is still unclear whether spin relaxation is dominated by SOC, exchange fluctuations, or a combination of the two. However, considering that according to DFT calculations [Paper IV] the exchange splitting is expected to be an order of magnitude stronger than SOC, one can expect the origin of the experimentally observed anisotropy of spin relaxation to be mainly caused by the exchange fluctuations. The temperature dependence data in Fig. 4.7b points to at least some contribution of exchange fluctuations, while the anisotropy measurement in Fig. 4.8d can be explained by either of the mechanisms.

These findings on proximity-induced magnetism in graphene demonstrate the potential of proximity effects in graphene for spin injection. An alternative approach implies direct injection of spin polarized carriers from ferromagnets, either conventional 3D metals and alloys such as e.g. Co, permalloy or from van der Waals metallic magnets, which provide a smoother interface with graphene.

4.3 Metallic ferromagnets Fe_3GeTe_2 and Fe_5GeTe_2

The layered magnetic materials Fe_3GeTe_2 and Fe_5GeTe_2 are exfoliable van der Waals metallic itinerant ferromagnets. The crystal structures (Fig. 4.9a and Fig. 4.9b) consist of two layers of alternating Te-Fe-Ge(Fe)-Fe-Te for Fe_3GeTe_2 (F3GT) and 3 layers for Fe_5GeTe_2 (F5GT) in the unit cell. For the latter, each layer consist of 3 Fe atoms, whilst Fe at site 1 is a split-site that is located either above or below the Ge atoms. Hence, Ge site is also a split-site that adjust to the position of Fe atom to maintain the proper bond length. The layers are kept together by the weak van der Waals interactions with gaps in between them. The

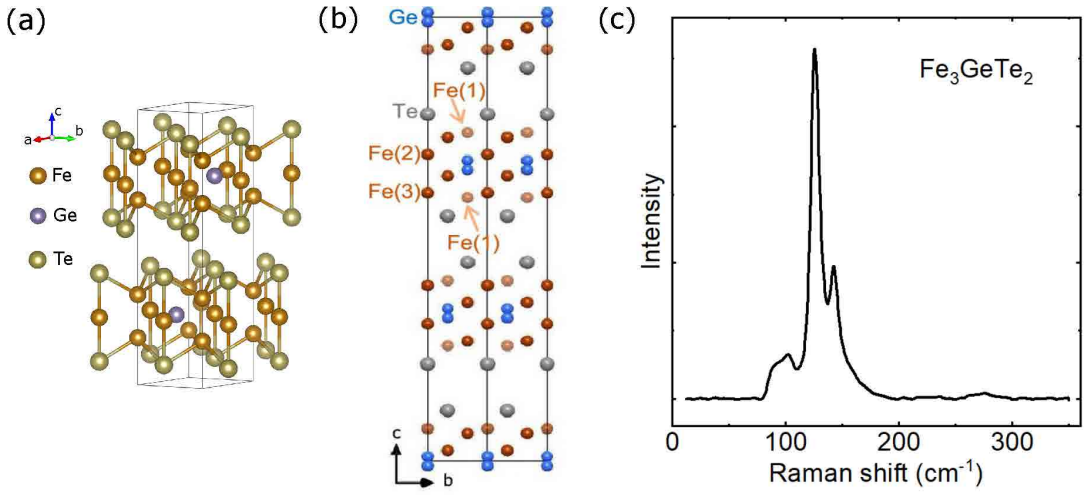

Figure 4.9: Crystal structures of (a) F3GT and (b) F5GT [223]. (c) Raman spectrum of F3GT.

lattice parameters are $a = b = 4.00$ Å($a = b = 4.04$ Å), $c = 16.28$ Å($c \sim 29.1$ Å) for F3GT (F5GT) [86, 223–227]. The Raman spectrum of bulk F3GT at room temperature (Fig. 4.9c) shows a pronounced A_{1g} symmetry mode peak at 125 cm^{-1} related to vibrations of Fe and Te atoms along the interlayer direction [228].

To investigate electronic and magnetotransport properties, samples of F3GT and F5GT were nanofabricated on Si/SiO_2 substrate by means of mechanical exfoliation, electron beam lithography and electron beam evaporation of contacts made of Cr/Au. The temperature dependence of the representative F3GT flake (thickness $\sim$ 20 nm) resistance (Fig. 4.10a) reveals a metallic behavior with a gradual drop of resistance with decreasing temperature. This was observed for F3GT flakes with thicknesses of 4 layers and more [84]. The resistance shows an upward increase below 20 K. The fit of the low-temperature resistance data according to 2D Mott variable range hopping model (top inset in Fig. 4.10a) gives $Ln(R) \sim T^{-1/3}$, suggesting that at low temperatures the carrier transport is dominated by localized states. This is in accordance with previous observations in F3GT [82, 84, 229–231] and other materials such as metallic Tl_4S_3Se [229], semiconducting $MoTe_2$, $MoSe_2$ [232], magnetically doped topological insulator $Cr_xBi_{2-x}Te_3$ [233]. There is a kink in resistance at $\sim$ 170 K, which is clearly visible in the first derivative $\partial R/\partial T$. The kink indicates the Curie Temperature with phase transition from a paramagnetic to a ferromagnetic state of F3GT.

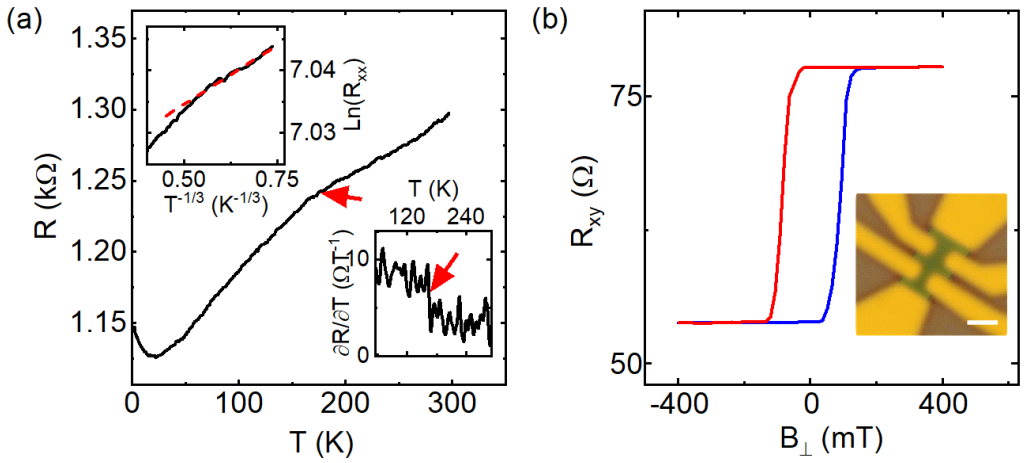

Figure 4.10: (a) Temperature dependence of longitudinal two-terminal resistance of F3GT. (b) Transverse magneto resistance measured at 4 K in a Hall bar device as shown in a false-colored optical picture in the inset. Scale bar is 1 µm. Insets in (a) are a fit according to the variable range hopping model (bottom right) and a smoothed first derivative of resistance $\partial R/\partial T$ (bottom right). The red arrow indicates the T_c ~170 K for the F3GT flake.

Anomalous Hall effect and magnetism

AHE measurements were performed in nanofabricated Hall bar devices with Cr/Au contacts to characterize the magnetic properties of the materials. The presence of long-range magnetic order at low temperature and the perpendicular magnetic anisotropy allows for observation of AHE, as shown in Fig. 4.10b for F3GT. It has been measured while sweeping the out-of-plane magnetic field and measuring transverse magnetoresistance R_{xy}, which consists of the ordinary and AHE components. The latter component stems from inherent ferromagnetism. Since F3GT is highly conductive with a high concentration of carriers, the ordinary Hall contribution is small compared to the anomalous component within the measured field range, giving a flat magnetic field dependence after each switching. The hysteresis loop reveals an abrupt jump of magnetoresistance for the two opposite perpendicular magnetic field sweeps at 4 K, indicating near-single magnetic domain in the F3GT flake at this temperature for the flake lateral dimensions of ~ 3 µm.

As the magnetic order in F3GT changes with temperature, so does the AHE response (Fig. 4.11). The magnetic field sweeps start to acquire loop shape at temperatures below 150 K, while the width of the loops increases when the temperature drops (Fig. 4.11a). The jumps of magnetoresistance at the switching fields change from gradual (low temperatures) to sharp (intermediate temperatures $50 - 130$ K) and eventually smooth out with the loss of magnetic structure. The Curie point was obtained by Arrot plots analysis method [234, 235] (Fig. 4.11b). The value of Rxy^2 is plotted against B/R_{xy} at different temperatures. The intercept of the straight line fittings, which changes from positive to negative when magnetic order transforms from ferromagnetic to paramagnetic state [236], is shown in the inset. It crosses zero at 149.5 ± 8.0 K, suggesting this value of the Curie temperature in the F3GT flake. It is less than reported for bulk samples of FGT (with T_c of around 200 K [82, 84]). Such a reduction of T_c is known to be present in thin flakes with a thickness below 20 nm [82, 84, 231] and also can be indication of reduced Fe content with distorted stoichiometry and presence of Fe vacancies.

To obtain the critical exponent β, the temperature dependence of the anomalous Hall resistance $\Delta R_{xy,sat}$ can fitted according to $\Delta R_{xy,sat} \sim (1 - T/T_c)^{\beta}$ [78]. The value of $\Delta R_{xy,sat}$ is the transverse resistance obtained after subtraction of the linear contribution from the ordinary Hall effect and it is proportional to the saturation magnetization of the F3GT flake [231]. From the fitting (top panel in Fig. 4.11c) the value of $\beta = 0.34 \pm 0.06$ is obtained with T_c fixed at 155 K. This value of the critical exponent is characteristic of a 3D system (either Heisenberg, XY or Ising model which all have very close values of β) [78, 237, 238]. One could expect this for a flake of > 20 nm in thickness, as the dimensional crossover to 2D system (consequently, reduction of β value) appears when T_c starts to drop with

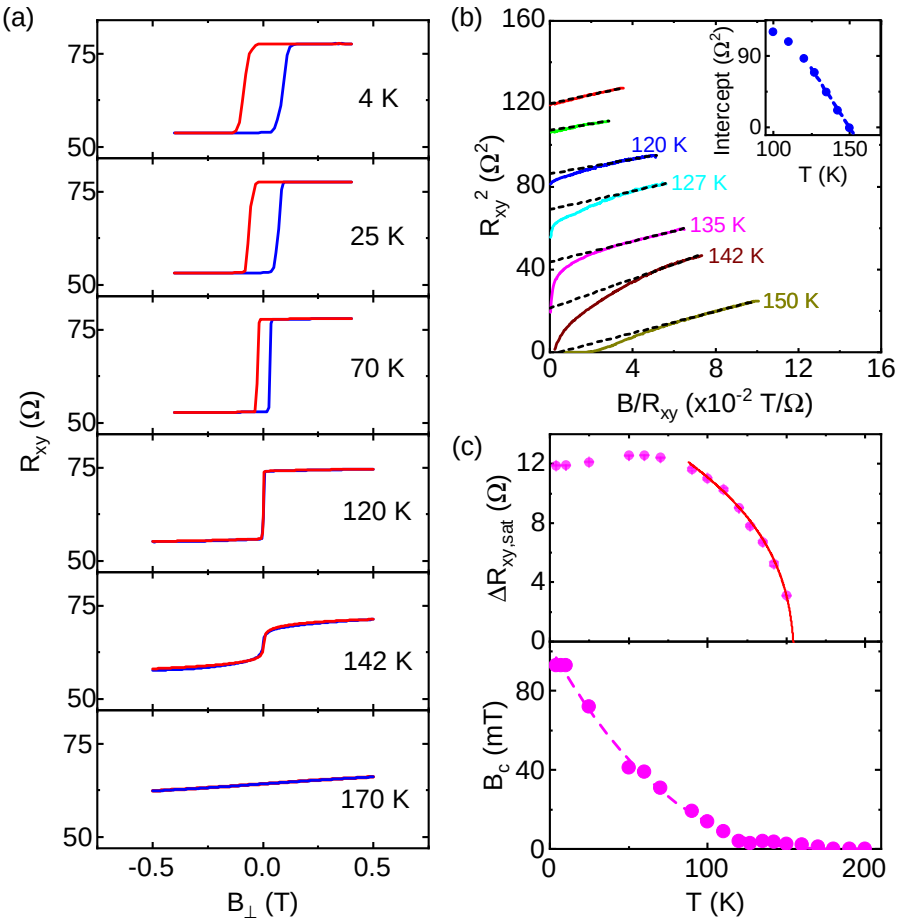

Figure 4.11: Temperature dependence of the AHE in Fe_3GeTe_2. (a) AHE data measured in the Fe_3GeTe_2 Hall-bar device at different temperatures, as indicated. (b) Arrot plots of the AHE data. The inset shows the temperature dependence of the intercept. (c) Top panel: transverse resistance at saturation $\Delta R_{xy,sat}$, obtained after subtraction of the linear component. The red solid line is a fitting according to $\Delta R_{xy,sat} \sim (1 - T/T_c)^{\beta}$. Bottom panel: coercivity B_c as a function of temperature. The dashed line is a guide to the eye.

thickness, which occurs once the range of spin-spin interactions becomes larger than the sample thickness [189]. In F3GT it was demonstrated for thicknesses below 6 monolayers [84, 231], for CGT in flakes thinner than 6 monolayers as well [81] and other magnetic thin films at few monolayers thicknesses [78, 189]. Considering such value of β one can conclude that T_c in the sample is determined by exchange interactions primarily, rather than by the excitation gap in 2D that results from magnetic anisotropy [81]. The value of the coercivity B_c (bottom panel in Fig. 4.11c) decreases with temperature and already at $T > 140$ K nears zero, while the transverse magneto resistance field sweeps remain highly nonlinear. This again suggests formation of many small domains near the Curie point, giving rise to nonlinearity. The transition persists up to about 170 K (Fig. 4.11a), when the R_{xy} dependence becomes linear. In the paramagnetic state, above the Curie tem-

perature, the carrier sheet density (2.5×10^{14} cm^{-2}) and mobility (20.4 cm^{2}V^{-1}s^{-1}) were extracted at 180 K by fitting the R_{xy} versus B data according to the ordinary Hall effect.

To investigate the magnetic anisotropy of the F3GT flake sample, the angle dependence of the AHE was measured (Fig. 4.12). The transverse R_{xy} (Fig. 4.12a) and longitudinal R_{xx} (Fig. 4.12b) magneto resistances were obtained while sweeping the magnetic field at different angles from perpendicular to flake ($\psi = 0$) to in-plane directions. The angle dependence reveals the presence of sharp hysteresis loops at perpendicular field direction. The width of the loops, or coercive field B_c, increases as the angle is tilted towards the in-plane direction (Fig. 4.12c), while the

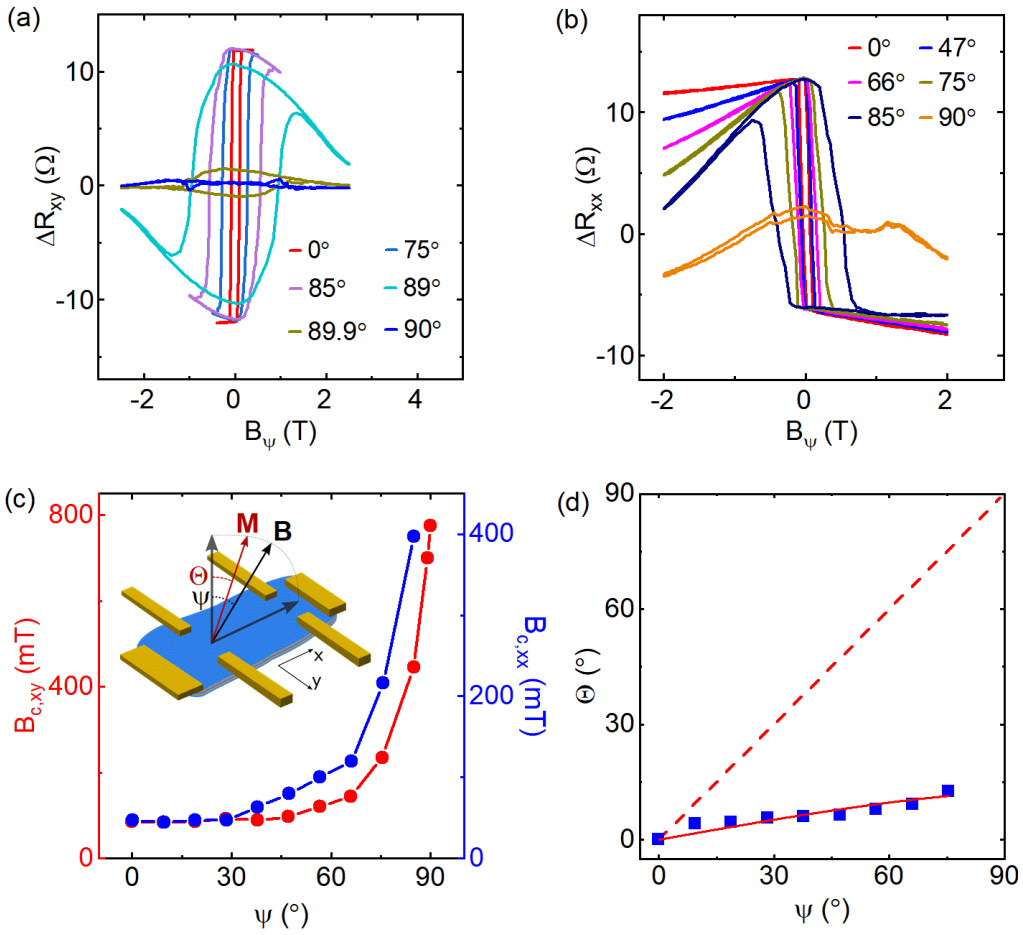

Figure 4.12: Angle dependence of the AHE in Fe_3GeTe_2. (a),(b) AHE measured for transverse (R_{xy}) and longitudinal (R_{xx}) magnetoresistance at different angles. The data is shifted vertically. (c) Coercivity as a function of angle ψ obtained from (a) ($B_{c,xy}$, red) and (b) ($B_{c,xx}$, blue), respectively. Inset: schematics of the device configuration with noted angles between the out-of-plane direction and magnetization M (angle Θ) and magnetic field B (angle ψ). (d) Θ as a function of ψ (blue squares). The red dashed line represents the isotropic case $\Theta = \psi$ while solid red line is a fitting according to Stoner-Wohlfarth model.

amplitude of the magnetoresistance jumps is reduced since it is caused only by the perpendicular component of the magnetic field. With a large enough in-plane field of about 2 T the magnetic domains in F3GT are forced in the in-plane direction. The observation of the AHE for the longitudinal magnetoresistance is not trivial and arises due to imperfections in the shape of the Hall bar, where side contacts, used for measuring R_{xy}, overlap the channel. This allows for measurement of the transverse charge separation with Hall bar contacts on one side of the flake. Previously it has been shown that etching the flake into a perfect Hall bar shape can eliminate the AHE signal for R_{xx} [102]. Taking into account that the R_{xy} is proportional to the out-of-plane component of the magnetization M, the angle Θ between M and perpendicular direction was extracted as a function of ψ using equation $\Theta = \arccos(R_{xy,\psi}/R_{xy,\perp})$, where $R_{xy,\psi}$ is an amplitude of the transverse magnetoresistance jump at an angle ψ and magnetic field of 500 mT (Fig. 4.12d). The Stoner-Wohlfarth model was used to fit the data [239]. According to the model, in equilibrium state the Zeeman energy is minimal with respect to the magnetization angle Θ, giving rise to $K_u sin(2\Theta) = M_s B \sin(\psi - \Theta)$. Here, M_s and K_u are the magnetic moment and magnetic anisotropic energy per unit volume, respectively. Considering M_s to be 1.625 μB per atom of Fe [224], the fitting gives an estimation of $K_u = 2.1 \times 10^5$ J/m^3. This value is similar to previous reports in F3GT flakes of up to 10 nm in thickness [84, 231] and slightly above the value of 0.5×10^5 J/m^3 reported for $Cr_2Ge_2Te_6$ [240]. Fig. 4.12d shows that the magnetization angle changes with delay with respect to the magnetic field direction, tending to tilt closer to the out-of-plane direction. This confirms the perpendicular anisotropy of F3GT.

In comparison to F3GT, F5GT has larger Fe content and increased Curie temperature, which in bulk crystals was reported to be 310 K [86]. The material possesses very little anisotropy in bulk samples, especially at high T, with prevailingly reported preferred out-of-plane magnetization direction [86, 241], except one study that claims in-plane preffered direction [242]. Such discrepancy in anisotropy could be related to different content of Fe and its vacancies [225]. As the thickness of F5GT flakes reduces, material demonstrates increasing tendency towards out-of-plane magnetic ordering as revealed by the AHE measurements with sharper R_{xy} switching and increase in coercivity [223, 243]. The domain dynamics with change of temperature appears to be complex in F5GT and not completely understood yet. It is believed to be related to tunable iron content and vacancies as well as fluctuating moments on the Fe-1 split-site location in the lattice [86, 225, 241, 242] that remains magnetically disordered down to $T \sim 110$ K. Around this temperature the lattice constants slightly change [86]. Several reports suggest formation of ferrimagnetic ground state or spin canting at intermediate temperatures ($\sim 100 - 270$ K) in F5GT [86, 223, 225, 242, 243], possibly due to antiparalell or canted alingment of spins at Fe-1 sublattice. It has been demostrated in literature that magnetic properties in F5GT can be significantly modified with

substitution of Fe atoms by Co in $(Fe_{1-x}Co_x)_5GeTe_2$ [241, 244]. Thus, increasing Co substitution to 20% enhances anisotropy and Curie temperature, while further increase up to $\sim 50\%$ leads to formation of AFM ground state.

AHE in Fe_5GeTe_2 flake of ~ 30 nm thickness at several distinct temperatures is shown in Fig. 4.13. At room temperature the signal remains nonlinear, indicating slight presence of magnetic ordering. In contrast, at 50 K abrupt jumps in R_{xy} suggest fully ordered magnetic state with a single domain behavior. More interesting Hall signal is obtained at intermediate temperature of 250 K. Here, as the magnetic field is swept with increase in amplitude, the R_{xy} response gradually transitions to intermediate value forming a plateau. With further increase of magnetic field magnitude the gradual transition in R_{xy} continues until saturation is reached. Similar transitions of the AHE signal were reported in ferromagnetic thin films of $SrRuO_3$ [245], ferromagnetic semiconductor trilayers of GaMnAsP/GaAs:Be/GaMnAsP [246], trilayer structures of F3GT/graphite/F3GT [102], ferrimagnetic insulator YIG [247], 2D ferromagnet $CrBr_3$ [248]. The physical origin of this effect comes from domain magnetization dynamics in the measured sample. The presence of one plateau in R_{xy} for each sweep direction at intermediate value between the two saturation levels suggests formation of the two parallel transport channels in the flake [245]. The AHE signal can be decomposed into two signals of the same sign, each one corresponding to one channel, as shown schematically in the inset of middle panel in Fig. 4.13. The nature of such channels is in formation of two magnetically different spatial regions in the sample. Each region as a whole behaves as one domain that corresponds to one transport channel that switch at specific coercive field characteristic to that domain. Each of these two domains, when considered separately, can be spatially continuous and interrupted only by one domain wall when it meets with the other domain of the same type of spatial arrangement [247, 248]. Another possibility is formation of e.g. stripe-like multidomain patterns in F5GT at intermediate temperatures, where two-step AHE is observed. Such behavior has in fact been demonstrated in literature in nanoflake (~ 70 nm thickness) of F5GT at temperature range of $110 - 210$ K [242], where stripe-shaped magnetic domains of $1.5 - 2$ µm width appeared. Each of the two sets of such stripes were aligned in opposite directions. Assuming that each set of stripes behaves magnetically as a single domain gives rise to the two AHE transport channels that switch separately, which has been observed in $SrRuO_3$ [245]. One can expect a correlation between the number of channels and, consequently, the shape of the AHE signal transitions, on one side, and thickness, lateral dimensions of the sample, temperature, on the other side. Similar correlation has been shown in F3GT [82], but due to more complex magnetic behavior that is observed in F5GT owing to increased Fe content and fluctuating moments in Fe-1 sublattice at intermediate temperatures, this dependence could be more intricate.

Another feature that one can observe in Fig. 4.13 is how the AHE amplitude

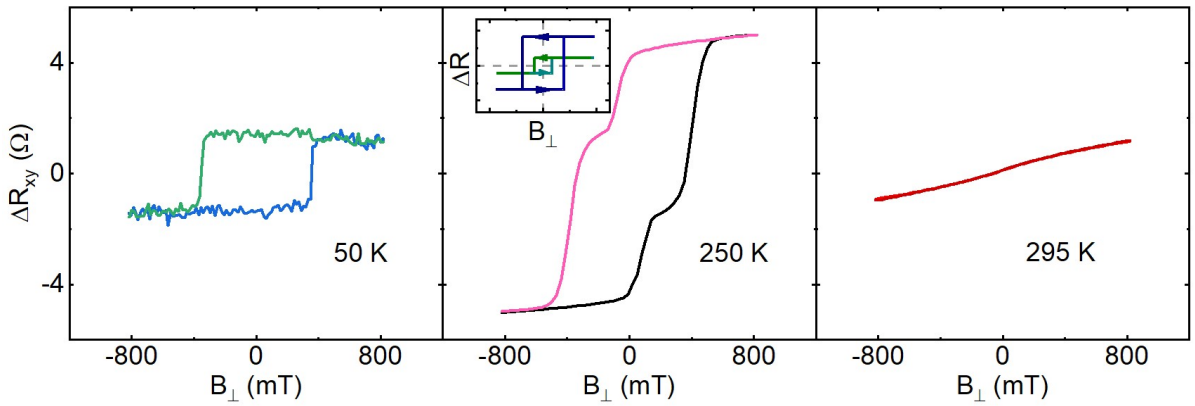

Figure 4.13: Temperature dependence of the AHE in Fe_5GeTe_2. From left to right: AHE at temperatures of 50, 250 and 295 K, respectively. Inset in the middle panel: schematic plot of a two-channel AHE. Different colors at each temperature indicate opposite magnetic field sweep directions.

changes with temperature. It is evident that at 250 K the amplitude is larger than at 50 K, suggesting a presence of a peak at intermediate temperature. This has been confirmed before [223, 225, 243] and is attributed to a decrease of anomalous Hall coefficient below $\sim$ 100 K, when Fe-1 sublattice orders leading to a change in the band structure [225]. Such behavior of AHE amplitude with temperature points also to a possibility of presence of ferrimagnetic state in F5GT [86, 223, 225, 243].

Layered magnets for spin injection and detection

Considering that F3GT and F5GT both are van der Waals magnets with metallic charge transport behavior and perpendicular magnetic anisotropy, they are potential candidates for spin injection into graphene. The traditional contacts made of thin ferromagnetic films of e.g. Co with tunnel barriers contain pinholes that contribute to spin dephasing. The potentially atomically flat interface between graphene and van der Waals metallic magnets could provide a solution to mitigate this issue. Additionally, the perpendicular magnetic anisotropy is desirable in microelectronics industry for high density spintronic devices [96, 249]. Spin transport measurements in the device with F3GT/graphene channel (Fig. 4.14) reveal that the spin signal amplitude ΔR_{NL} (obtained from spin-valve measurements in Fig. 4.14b,d,f) is reduced when spin transport is measured in the heterostructure channel (ch3) in comparison to only graphene channels (ch1 and ch2) in the same device. However, the reduction of ΔR_{NL} can be due to the longer channel length of ch3 (4.3 µm), compared to pristine graphene channels (3 µm and 3.3 µm). The estimated spin lifetimes τ_s (Fig. 4.14h) are obtained from fitting of the Hanle spin precession signals according to equation A.2 for the respective channels. Here, the spin lifetimes is also found to be slightly lower in the heterostructure channel

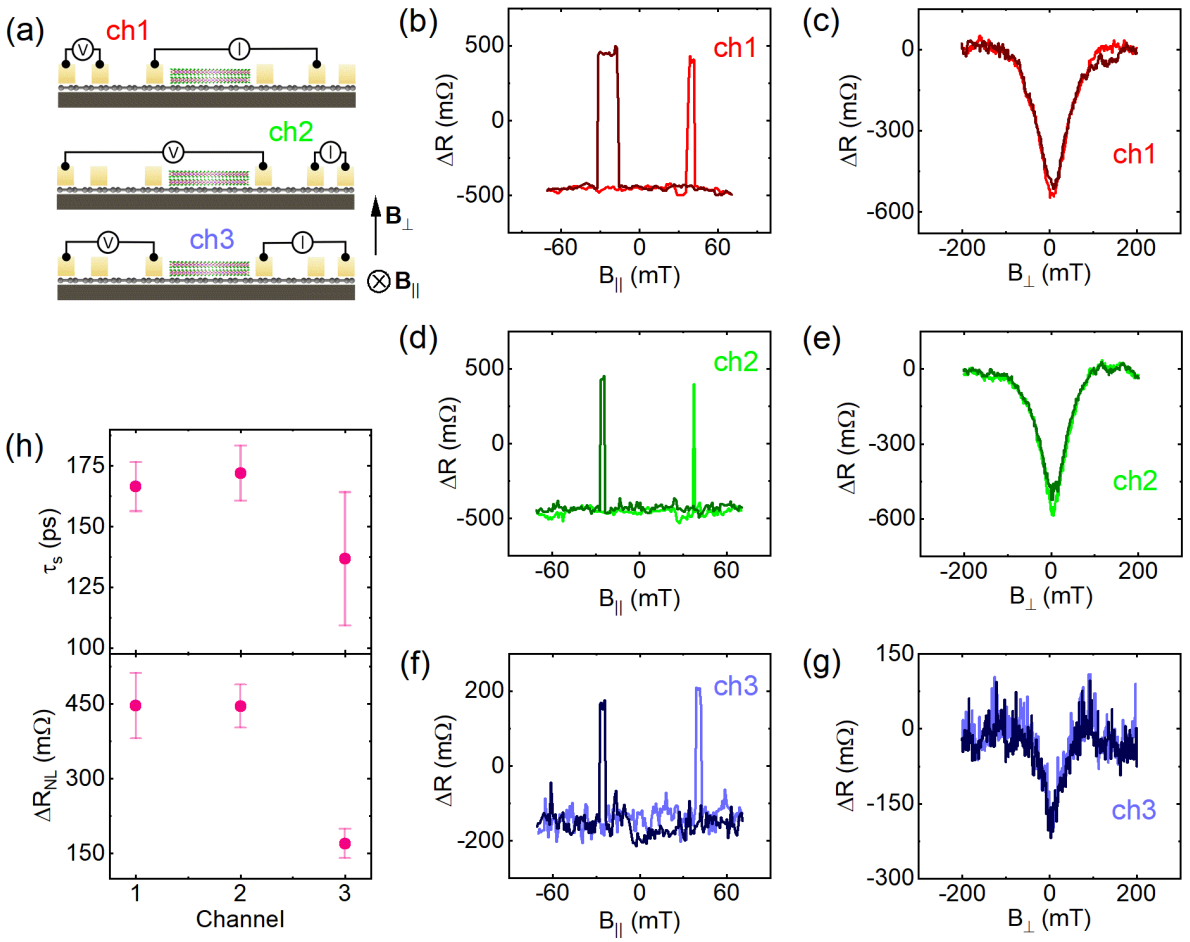

Figure 4.14: Spin transport in graphene/F3GT heterostructure. (a) Schematics of the side view of the graphene/F3GT device with Co/TiO_2 contacts and nonlocal measurement schematics for three channels ch1 (3 µm), ch2 (3.3 µm), ch3 (4.5 µm), as indicated. (b),(d),(f) The spin valve and (c),(e),(g) Hanle measurements in the three channels ch1, ch2, ch3, respectively. (h) The spin lifetimes τ_s in the three channels as obtained from fitting of the Hanle signals. The data is obtained at 50 K.

compared to pristine graphene channel. Therefore, the presence of F3GT flake on the graphene can be viewed as a parallel transport channel. Thus, one of the possible scenarios is that part of the spins accumulated in the heterostructure channel are absorbed by the F3GT flake, leading to reduced spin transport parameters in comparison to pristine graphene channels. The efficiency of such absorption is dependent on the relative orientation between the spins in the channel and the direction of magnetization in F3GT below Curie temperature [250]. Further experiments are required with injection and detection of out-of-plane spin polarization from Co electrodes at high magnetic fields > 2 T to investigate the spin absorption anisotropy. The van der Waals heterostructure of F3GT/graphene is interesting for spin injection/detection in the graphene channels. A representative device for such measurements is shown in Fig. 4.15a, while schematic nonlocal

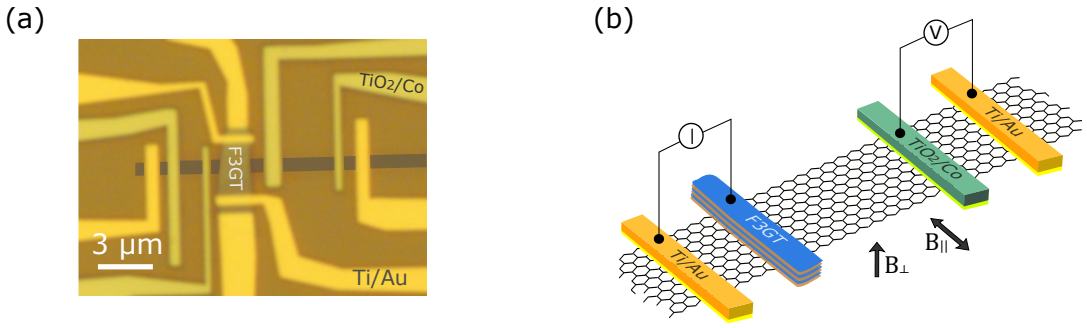

Figure 4.15: (a) Optical microscope picture of the Fe_3GeTe_2/graphene heterostructure device. The graphene stripe is false-colored for clarity. (b) Schematics of the nonlocal measurement configuration for spin injection from the F3GT flake into the graphene channel and subsequent detection of spin current by conventional Co contacts.

configuration is shown in Fig. 4.15b. After numerous attempts the experimental observation of spin injection/detection with an F3GT flake instead of one of the traditional Co contacts has been elusive so far. A main reason for this is the quality of the interface obtained during the exfoliation and flake transfer process onto the graphene channel. Although the experimentally observed interface resistance is comparable in magnitude to that of Co/TiO_2 contacts, this is not sufficient. Presence of interface contamination, although not affecting significantly the resistance, could reduce the spin injection and accumulation in the channel and be responsible for the challenging character of such measurements. Further experiments with improved interface optimization can provide conclusive spin injection and detection in van der Waals heterostructures.

5 Magneto and spin transport in van der Waals semimetals and candidates

Topological quantum materials present an attractive ground in spintronics studies owing to their strong spin-orbit coupling with unique band structures and topologically protected spin textures that can give rise to charge-to-spin conversion. Concurrently, graphene is utilized in spintronics as a long-distance spin channel due to its low spin-orbit coupling strength. Combining these van der Waals materials together in a heterostructure is promising for future all-electrical spin-circuit devices that utilize charge-to-spin conversion without the need for external magnetic fields. In this chapter, magneto transport studies are discussed in topological van der Waals semimetals WTe_2 and $ZrTe_5$ and unconventional charge-to-spin conversion is demonstrated in WTe_2 hybrid device.

5.1 Weyl semimetal WTe_2

In the last decade topological materials have attracted significant research interest due to their unique band structures and new topological states of matter were discovered. Previously overlooked type-II Weyl semimetallic states were found in WTe_2 [251]. Its crystal lattice (Fig. 5.1a) has orthorhombic structure and is arranged in layers bonded by weak van der Waals forces that stack along the c-axis with interlayer distance of ∼0.8 nm [252]. Along the a-axis within the a-b crystal plane the W atoms form quasi-1D chains that are surrounded by Te atoms [253]. The crystal structure has a nonsymmorphic symmetry with only one mirror plane (bc plane), a glide mirror plane (ac plane with translation of (a+c)/2), and a screw axis || c. Neither twofold rotational invariance nor inversion symmetry is present in this system [254]. Monolayer WTe_2 was shown to host quantum spin Hall state [255], while bulk crystal is a type-II Weyl semimetal with tilted Weyl cones in 3D momentum space in the bulk Brillouin zone (BZ) [251, 256] that are connected by Fermi arcs in the surface BZ (Fig. 5.1b) [257–261]. The Fermi surface in the bulk contains electron and hole pockets (Fig. 5.1c) [262–264], giving rise to multi-carrier conduction [147, 252, 265].

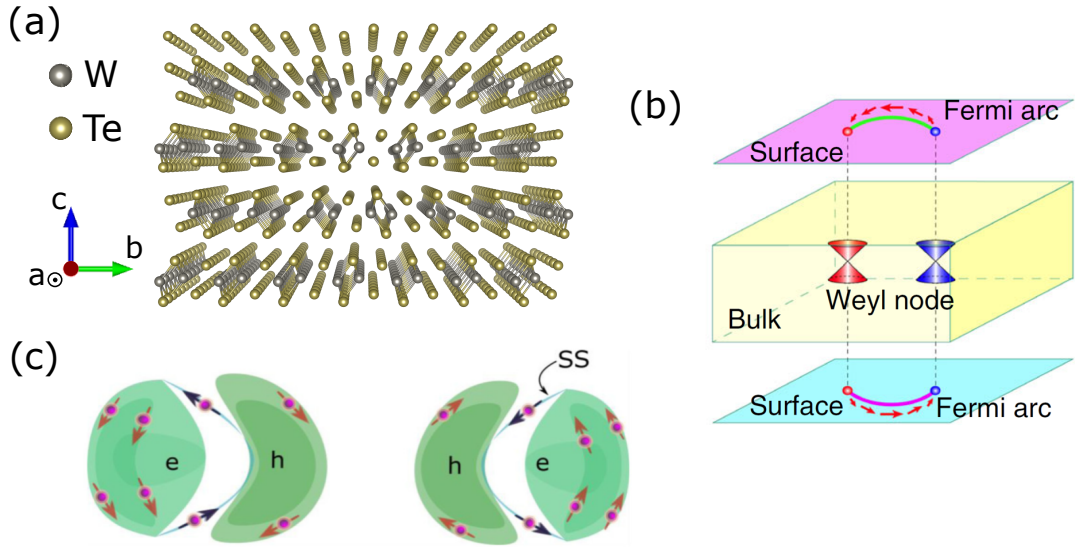

Figure 5.1: (a) Crystal lattice of T_d phase of WTe_2. (b) Schematics of the Brillouin zone for Weyl semimetal. Adapted from ref. [261]. (c) Schematics of the Fermi surface of WTe_2 with electron, hole pockets and surface states (SS). Arrows indicate a peculiar spin texture. Adapted from ref. [264].

The electrical transport measurements were investigated in bulk WTe_2 sample and 10 nm flake (as obtained from the AFM scan of the topography). The measurements in the bulk WTe_2 are summarized in Fig. 5.2. The field dependence of bulk channel resistance (Fig. 5.2a) shows very large magneto resitance MR of up to $\sim 7500\%$ when the magnetic field $B_\perp$ is applied along the c-axis of the lattice, which is a consequence of a peculiar band structure with nearly compensated electron-hole two-band conduction [147]. The magneto resistance in another bulk channel reveals Shubnikov de Haas (SdH) oscillations (Fig. 5.2b,c). Analysis of these oscillations allows to extract a number of the transport parameters in WTe_2. Thus, by fitting the Landau fan diagram (Fig. 5.2d) according to $N = B \cdot B_F + \beta$ [266], the frequency of the oscillations $B_F \approx 141 \pm 1$ T can be extracted as well as the phase factor $\beta \approx 0.53 \pm 0.11$. This value of β agrees well with 0.5 that is expected for Dirac fermions [137], which could arise in WTe_2 from the Weyl nodes. Next, from the Onsager's relation [137], the carrier concentration $n_{2D} = eB_F/h \sim 3.4 \times 10^{12}$ cm^{-2}, the Fermi momentum $k_F = \sqrt{4\pi q_e B_F/h} = 0.065$ Å^{-1} are obtained and the cross-sectional area of the Fermi surface S_F that is normal to the field direction $S_F = \pi k_F^2 = 2\pi e B_F/\hbar = 1.3 \times 10^{-2}$ Å^{-2} [145]. By fitting the temperature dependence of the SdH oscillations amplitude ΔR_{xx} with [266]

$$\Delta R_{xx} \propto \frac{\lambda(T)}{sinh(\lambda(T))} \tag{5.1}$$

as shown in Fig. 5.2e, where $\lambda(T) = 2\pi^2 k_B T/\hbar\omega_c$ and ω_c is cyclotron frequency, the electron effective mass is obtained $m_{eff} = q_e B/\omega_c = 0.39 m_e$. Here B is the

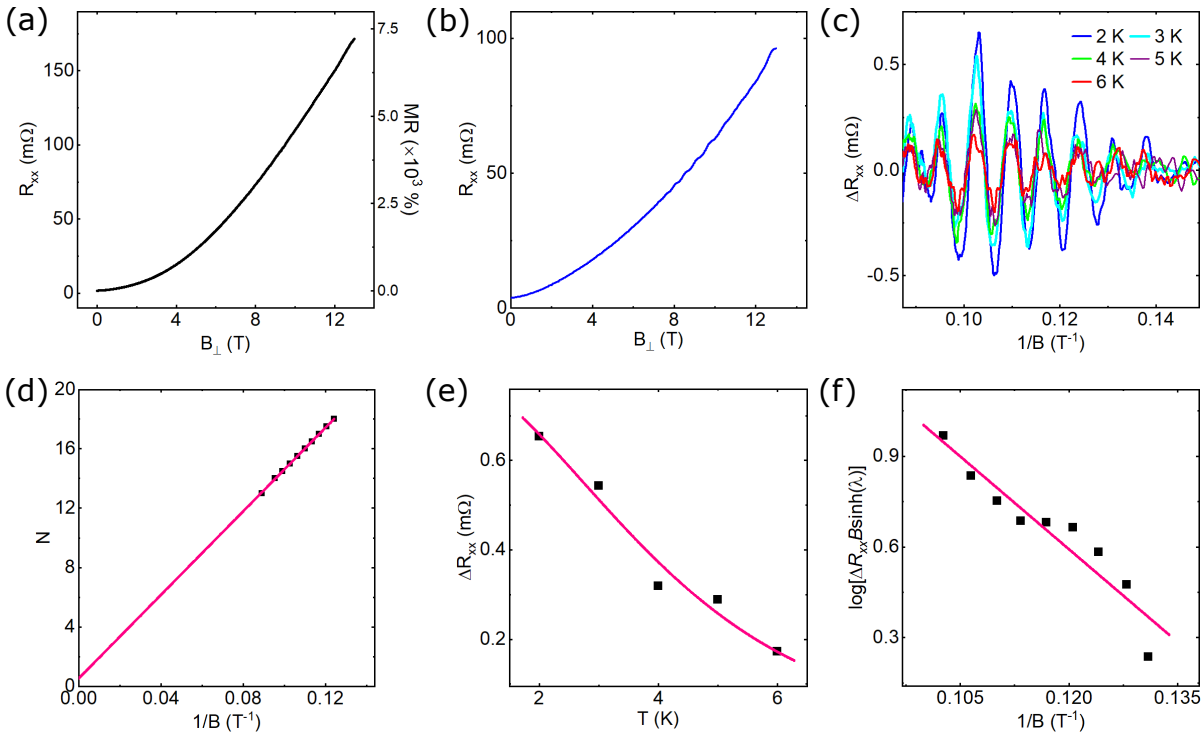

Figure 5.2: Electrical transport measurements in bulk WTe_2 sample. (a) Four-terminal resistance of the bulk channel R_{xx} and magneto resistance $MR = {}^{R_{xx}(B_\perp) - R_{xx}(0)}/_{R_{xx}(0)}$ as a function of magnetic field $B_\perp$ applied along the c-axis of the lattice at 2 K. (b) Magneto resistance with SdH oscillations at 2 K for another bulk channel. (c) Temperature dependence of the SdH oscillations in WTe_2 obtained from (a) after subtraction of the background signal. (d) Landau fan diagram of the Landau index N versus 1/B in the a-c plane. (e) Amplitude of the SdH oscillations ΔR_{xx} as a function of temperature. The solid line is a fitting according to the equation 5.1. (f) Dingle plot at 2 K with fitting (solid line) according to the equation 5.2.

magnetic field that corresponds to the position of the fitted oscillation amplitude. Taking into account the linear dispersion near the Fermi level, the Fermi velocity is obtained by $\upsilon_F = \hbar k_F / m_{eff} = 2.0 \times 10^5$ m/s and Fermi energy $E_F = \hbar k_F \upsilon_F \sim$ 84 meV. The transport lifetime τ can be estimated from the Dingle plot [266, 267]:

$$log\left(\Delta R_{xx} B sinh\left(\frac{2\pi^2 k_B T}{\hbar\omega_c}\right)\right) \approx \frac{2\pi^2 E_F}{\tau q_e \upsilon_F^2} \cdot \frac{1}{B}. \tag{5.2}$$

Fitting of the electrical transport data according to equation 5.2 (Fig. 5.2f) yields $\tau \sim 2.1 \times 10^{-12}$ s. Therefore, the mean free path $l = \upsilon_F \tau \sim 417$ nm and mobility $\mu = q_e \tau / m_{eff} \sim 9760$ $cm^2 V^{-1} s^{-1}$.

The 10 nm flake device (inset in Fig. 5.3a) was nanofabricated by means of exfoliation, electron beam lithography and electron beam evaporation of Cr/Au contacts. The temperature dependence of resistivity (main panel of Fig. 5.3a) shows metallic behavior, in accordance with previous reports [147, 252, 262, 268,

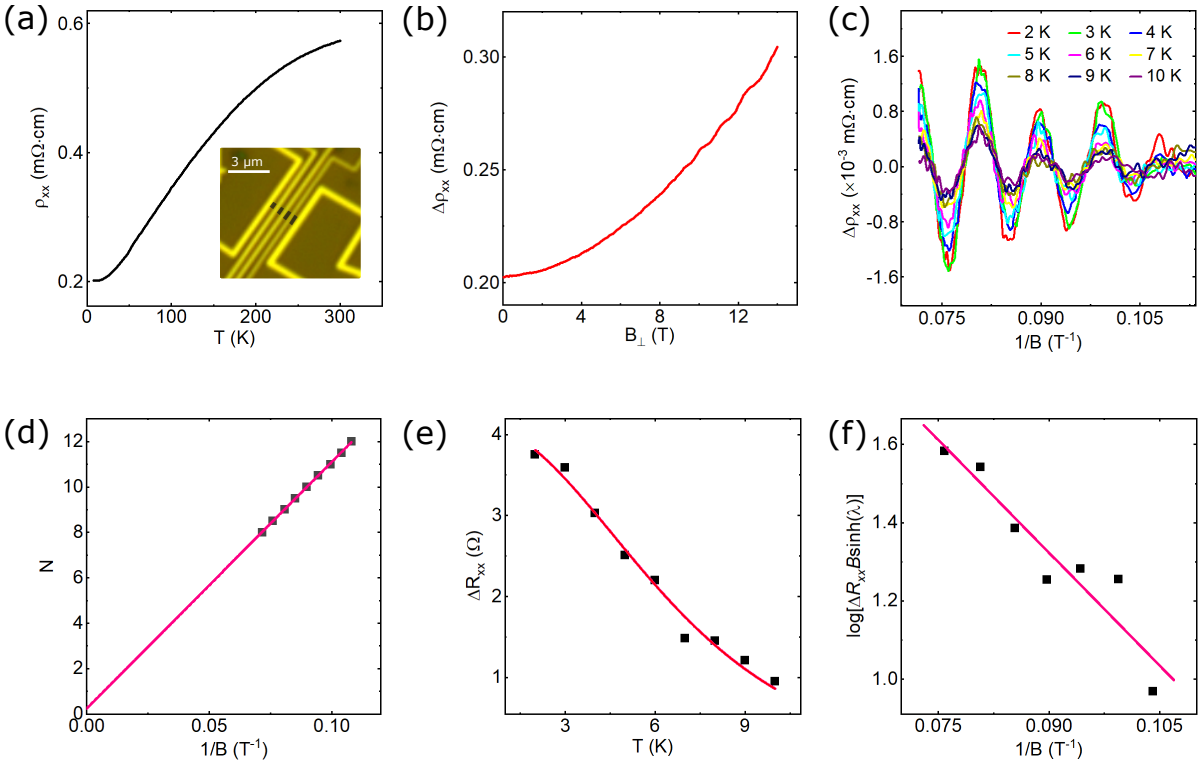

Figure 5.3: Electrical transport measurements in 10 nm WTe_2 flake. (a) Temperature dependence of resistivity ρ_{xx}. Inset: optical microscope picture of the nanofabricated device. The flake is false-colored for clarity. (b) Magneto resistivity with SdH oscillations at 2 K. (c) Temperature dependence of the SdH oscillations in WTe_2 flake sample. Magnetic field $B_\perp$ is applied along the c-axis of the lattice. (d) Landau fan diagram of the Landau index N versus 1/B in the a-c plane. (e) Amplitude of the SdH oscillations ΔR_{xx} as a function of temperature. The solid line is a fitting according to the equation 5.1. (f) Dingle plot at 2 K with fitting (solid line) according to the equation 5.2.

269]. The SdH oscillations are also observed here (Fig. 5.3b,c). At 10 K the oscillations remain discernible after subtraction of the background signal. Analysis of these oscillations in the same way as for the bulk sample yields transport parameters for the 10 nm WTe_2 flake, which are summarized in Table 5.1.

The value of phase factor β obtained in the flake device is 0.25 ± 0.05, which

	B_F (T)	β	n_{2D} (10^{12} cm^{-2})	m_{eff} (m_e)	k_F (Å^{-1})	v_F (10^5 m/s)	E_F (meV)	τ (10^{-12} s)	l (nm)	μ (cm^2/(Vs))
flake (10 nm)	109	0.25	2.6	0.32	0.057	2.1	79	1.8	380	10060
bulk	141	0.53	3.4	0.39	0.065	2.0	84	2.1	417	9760

Table 5.1: Estimated parameters from the SdH oscillations for WTe_2.

differs from the bulk sample value of 0.53 ± 0.11. This indicates a different Berry phase in the flake $\phi = 2\pi\beta \sim \pi/2$ (in comparison to $\sim \pi$ in the bulk) and slight deviation of the band structure at the Fermi level from linear dispersion [137], which could be due to a different position of the Fermi level (79 meV in the flake and 84 meV in the bulk samples) and is in agreement with a claim about sensitivity of the Fermi surface to small shifts in E_F that can lead to topological Lifshitz transition [251, 265, 270]. To be noted, the SdH oscillations amplitude in bulk WTe_2 (Fig. 5.2c) is decreasing when magnetic field is increased beyond certain high-field value ($1/B < 0.1$ T^{-1}). This could be due to presence of additional oscillation frequency, indicative of contributions from additional Fermi pockets. However, the observed dominant oscillation frequencies B_F of $\sim$ 109 T and $\sim$ 141 T for the flake and the bulk indicate that electron pockets provide the main contribution to conduction at the extracted Fermi level positions [265, 271].

5.2 Charge-spin conversion in WTe_2

It has been shown that WTe_2 hosts spin polarization of Fermi pockets in bulk bands and Fermi arc surface states [272, 273]. In such semimetals, the application of an electric field is expected to induce a macroscopic spin polarization, known as the Edelstein effect [274], that can be utilized to generate and detect spin currents efficiently. Moreover, in crystals with lower or broken symmetry compared to conventional metals [254], unconventional spin conductivity components can exist [275]. Additionally, in the search for spin-polarized current sources in topological quantum materials, various experiments have been reported on topological insulators (TIs) [131]. However, a reliable nonlocal measurement for spin polarization in TIs and its utilization for spin injection into non-magnetic materials are so far limited to cryogenic temperatures (below 20 K) [276, 277] because of the interference from nontrivial bulk bands [131]. Therefore, finding a highly efficient spin-polarized topological material for charge-spin conversion (CSC) at room temperature is indispensable for practical applications in spintronics and quantum technologies.

The CSC in WTe_2 was investigated in a hybrid device structure with graphene channel and ferromagnetic tunnel contacts (FM) in a nonlocal device geometry (Fig. 5.4a and section A). The device was nanofabricated by means of exfoliation of WTe_2 flakes and transfer on pre-patterned CVD graphene stripes, followed by fabrication of ferromagnetic tunnel contacts (Co/TiO_2) by a series of electron beam lithography steps and electron beam evaporation of metals. For the measurement of the CSC effects, an electric current is applied vertically through the WTe_2 flake, which generates and injects a spin current into the graphene channel. After propagation through the nonlocal channel, the spin-polarized current is detected by the ferromagnetic contacts. The nonlocal spin-valve resistance $R_{CSC} = V_{CSC}/I$ with an in-plane magnetic field (B_y) sweep at room temperature changes upon

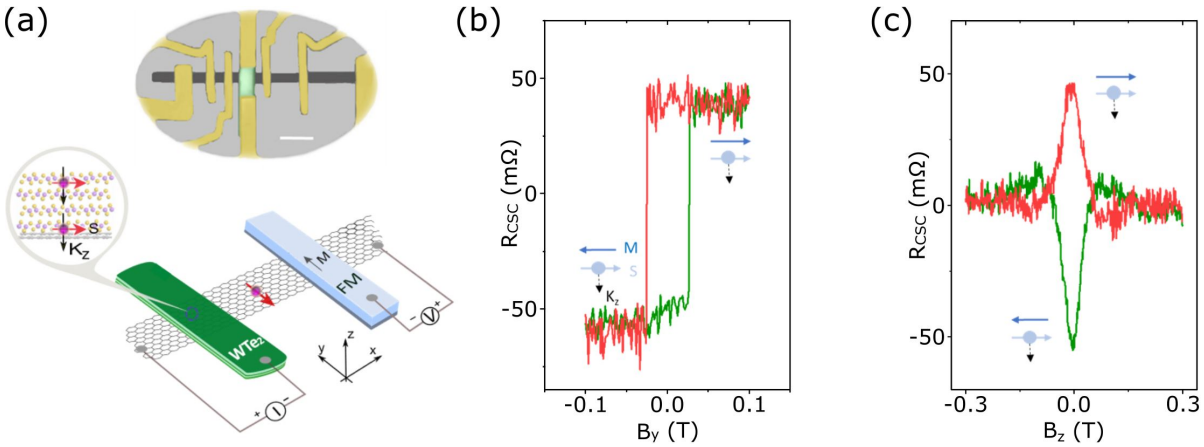

Figure 5.4: (a) Schematic of measurement geometry and false-colored device picture (the scale bar is 5 µm) for electrical detection of charge-spin conversion in WTe_2. The inset in the schematic show the spin polarization due to perpendicular current component K_z. (b) The nonlocal spin-valve measurement ($R_{CSC} = V_{CSC}/I$, I is the bias current across the WTe_2/graphene junction). (c) The corresponding Hanle spin precession signal observed for parallel and anti-parallel orientation of the injected spin (s) from WTe_2 and magnetization of ferromagnet (M) with positive and negative magnetic field B sweep directions at 300 K [Paper V].

reversing the magnetization M direction of the FM detector with respect to the directions of the injected spins (s) from the WTe_2 (Fig. 5.4b). The Hanle spin precession signal is also observed in the same nonlocal configuration (Fig. 5.4c). The observation of both the spin-valve and Hanle signal provide the direct and unambiguous evidence of the creation of current-induced spin polarization in WTe_2 and subsequent spin current injection and transport in the graphene channel at room temperature.

In a WTe_2-graphene hybrid device, the source of the spin polarization can have several origins, such as the spin Hall effect (SHE) and Edelstein effect (EE) from the bulk WTe_2, Rashba-Edelstein effect (REE) from the surface states [264] and proximity-induced SHE and REE in graphene [278–280]. Moreover, some of these effects can induce the in-plane spin polarization and can be entangled with each other [264]. To distinguish different sources of the spin polarization, and to identify the origin of the induced spin current in the WTe_2 device, control experiments with geometrical dependence were performed (Fig. 5.5). The charge current (I) applied in WTe_2 can have three components, i.e., K_x, K_y, and K_z, that can possibly induce the spin polarization. The control experiments performed by reversing the bias current polarity along different directions to check the polarity of the CSC signals reveal that the switching directions of the CSC signal (R_{CSC}) remain the same with the reversal of bias currents along both sides of the WTe_2 flake, i.e., the K_x and $-K_x$ directions (Fig. 5.5a). Therefore, the bias current component in K_x direction is not the source for the current-induced spin polarization. Consequently,

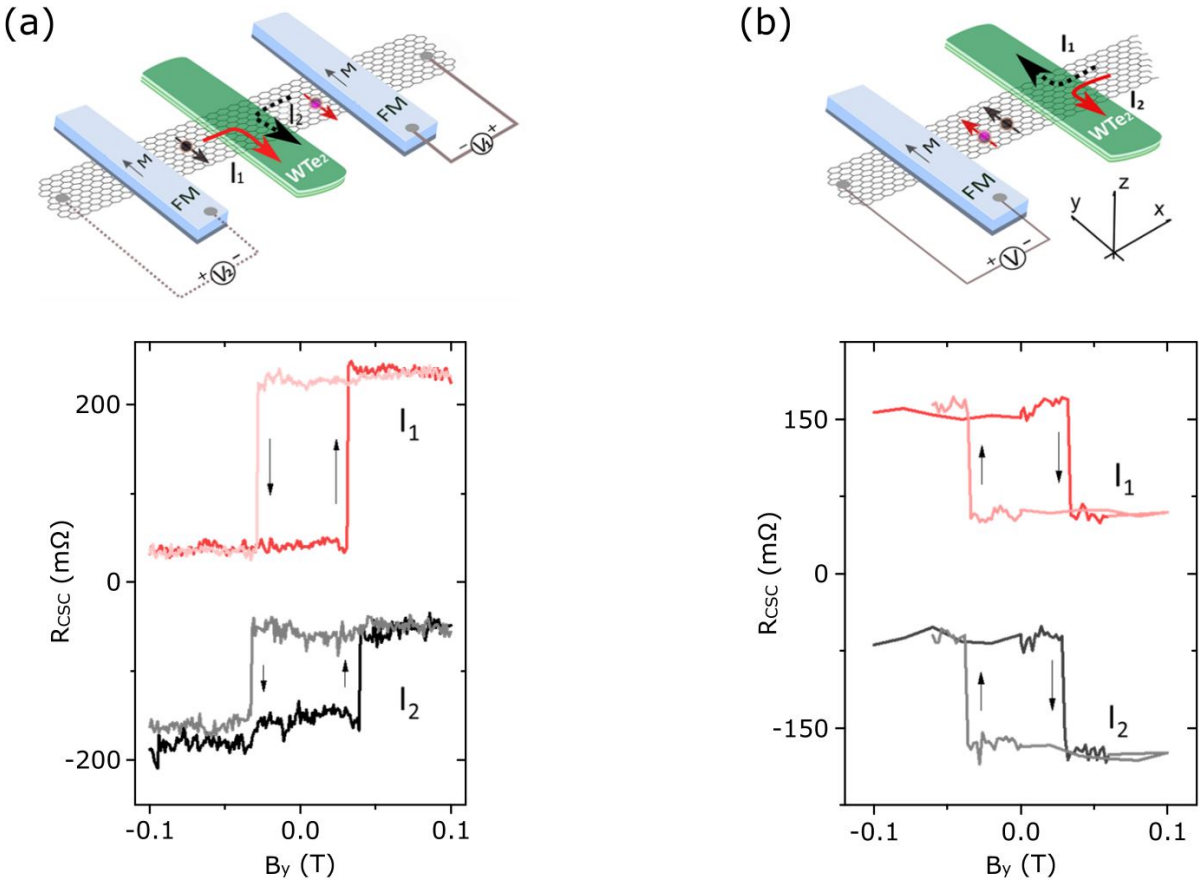

Figure 5.5: (a) Schematics of the measurement geometry with bias current (represented by solid and dashed arrows) applied at both sides of the WTe_2 flake and the corresponding spin valve signals measured. This measurement creates a reversal of the component K_x of the bias current. (b) Schematics of the measurement with bias current applied at both terminals of the WTe_2 flake and the corresponding spin valve signals measured in another device. This measurement creates a reversal of the component K_y of the bias current. A shift in the Y-axis is added for the sake of clarity [Paper V].

we can rule out the origins of spin polarizations entangled to K_x-direction, like SHE and REE effect in WTe_2 [264] and also proximity-induced SHE and REE in graphene [278, 279, 281, 282]. Second, when the bias current was applied either to one or the opposite terminals (K_y and $-K_y$ directions) of WTe_2 (Fig. 5.5b), the R_{CSC} signal switching directions remain the same. This rules out the contribution to the spin polarization from the current component in K_y direction. To be noted, the switching direction of the spin-switch signal is observed to be different for different devices as shown in Fig. 5.5a and Fig. 5.5b. This can be due to the uncertainty in different crystal orientations (±a, ±b axis) of the exfoliated WTe_2 flakes relative to the detector FM.

All these control experiments indicate that the current component in K_z direction in WTe_2 is the primary source for the generation of spin polarization in the measurement geometry of WTe_2/graphene devices. Therefore, the origin of the

spin signal can be attributed to the out-of-plane current-induced spin momentum locking of the spin-polarized Fermi states at room temperature [272, 273]. To be noted, here the charge current along k_z that give rise to the spin-polarized current (j_s) are both collinear with each other, which is unconventional CSC that does not follow the right-hand rule with $j_s \perp k_z$. This could be possible due to reduced symmetry in WTe_2 induced by e.g. strain [283, 284] arising in the devices with metal contacts.

5.3 Topological semimetal candidate $ZrTe_5$

The research on $ZrTe_5$ has started nearly four decades ago [285–287], but a new push towards more investigations was sparked recently by prediction of topological properties in the material [288–291], signatures of which have been demonstrated experimentally by a number of studies [142–146, 292–309]. The crystal structure of $ZrTe_5$ is shown in Fig. 5.6. The material consists of weakly bonded van der Waals layers that stack along the b-axis of the lattice with interlayer distance of ~ 0.8 nm [310]. The sheets consist of quasi-1D chains of $ZrTe_5$ prisms along a-axis. Each chain is bonded with the neighbouring ones in the same layer by one Te-Te bond for each adjacent chain along the c-axis. In this direction (in addition to stacking b-axis) the flakes are easily cleavable [294, 309], which often leads to formation of elongated shapes during exfoliation with high length to width ratio.

The nanofabricated device for magneto transport measurements is shown in Fig. 5.7a. The sample consists of thin flake of $ZrTe_5$ (~ 60 nm in thickness) obtained by exfoliation method and transferred onto Si/SiO_2 substrate. Contacts were fabricated by means of electron beam lithography and electron beam evaporation of Cr/Au metals.

The temperature dependence of longitudinal channel resistivity (Fig. 5.7b)

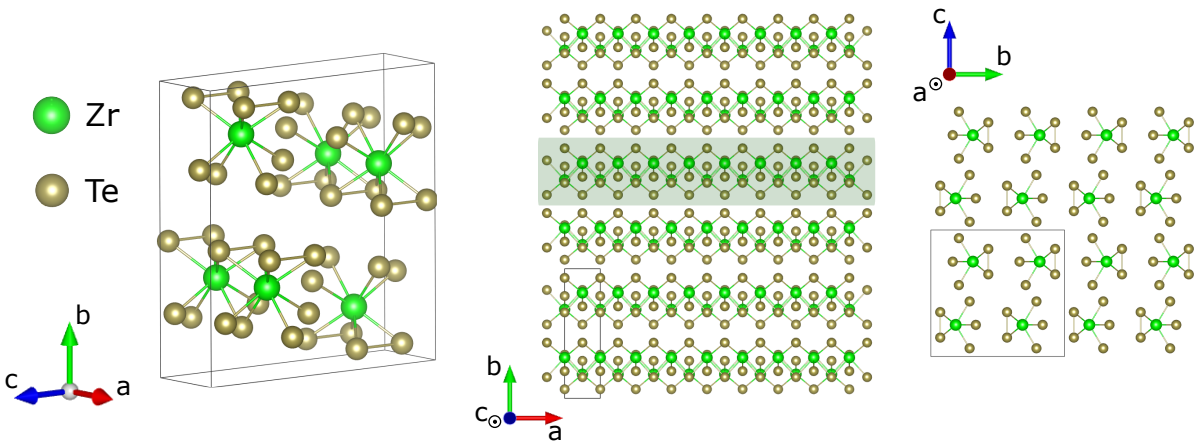

Figure 5.6: The crystal structure of ZrTe5. The solid line rectangulars and shaded region indicate single unit cells and quasi-1D chains, respectively.

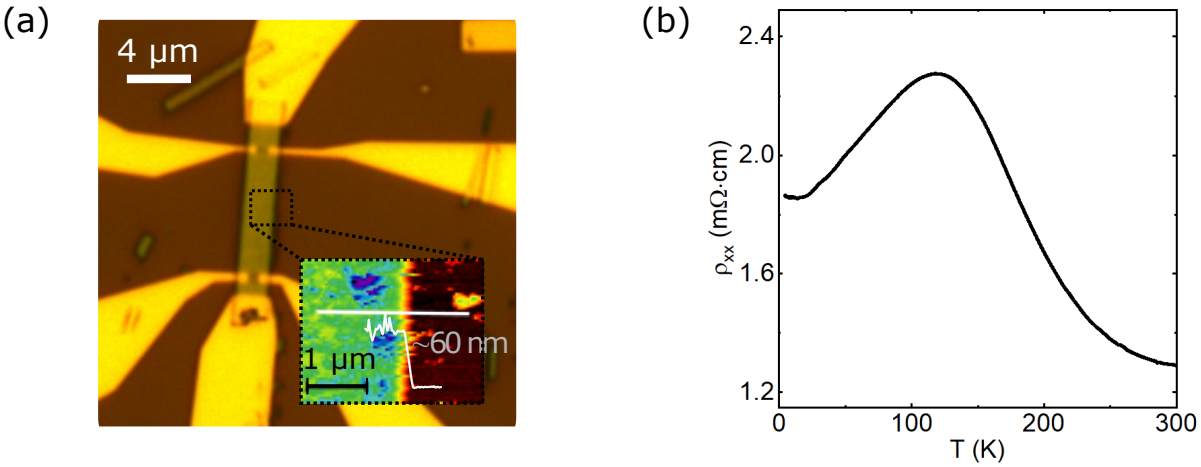

Figure 5.7: (a) Optical microscope picture of the $ZrTe_5$ device. Inset: atomic force microscope scan of the device region as highlighted by the dashed lines. (b) Temperature dependence of longitudinal resistivity ρ_{xx}.

reveals a peak at intermediate temperature value of $T_p \sim 121$ K. Thus, during a cooling process, as the temperature is reduced from 300 K, the channel resistance first increases showing a semiconducting behavior. After passing the peak position T_p, the trend changes to metallic behavior and the resistance drops with further cooling. Such temperature dependence has been well reported in literature [142, 144, 146, 297, 299, 305, 308, 310–319], including in the first studies several decades ago [285, 287], and is referred to as resistivity anomaly. Its position is known to change depending on the crystal growth method, which is attributed to density of impurities and defects in the sample [297, 318]. In the case when the Fermi level is located deep in the valence band, the peak position might not be observable even at $T = 0$ K [146, 297, 299, 318]. T_p is also known to be dependent on flake thickness t (for $t < 60$ nm) and can even be located above room temperature (when $t < 20$ nm) [310, 317]. Position of T_p and its amplitude is tunable by electric fields in thin flakes [310]. Around temperature T_p the carrier type changes from holes at $T > T_p$ to electrons at $T < T_p$ as shown below and reported in literature [146, 310, 311]. Additionally, the reported Seebeck coefficient that is related to thermopower changes sign as well at T_p [305, 311, 318].

The appearance of resistivity anomaly is believed to be originated from the band structure evolution with temperature as experimentally demonstrated by ARPES [142, 315, 319] and infrared spectroscopy [144] measurements in $ZrTe_5$ samples. Thus, as the temperature is reduced, the electronic structure near the Fermi level tends to shift towards lower energies and bandgap changes. Therefore, the material undergoes Lifshitz phase transition [320, 321] with change of Fermi surface topology. Additionally, this explains the change of carrier type conduction from holes to electrons. During cooling process, first at high temperatures $T > T_p$, the Fermi level crosses valence band, giving rise to hole conduction, and

shifts towards electron conduction as Fermi level changes its position to above conduction band minimum at low temperatures below T_p. The temperature-driven bandgap change explains also the wide range of gap values reported in literature, specifically 20-100 meV measured by ARPES and STM [142, 301, 303, 304] as well as 10 meV by magneto-spectroscopy measurements [302]. This picture becomes even more puzzling when one takes into account the thickness dependence of bandstructure [310] with reported two-band conduction model, one of semimetallic (Dirac) and another of semiconducting type [310, 311]. Despite the many studies performed, there is no consensus by now regarding the temperature-dependent electronic structure in $ZrTe_5$ and its topological classification. Regarding the latter, the material was reported to be a weak topological insulator [208, 322], strong topological insulator [323], 3D Dirac semimetal [308, 324], Weyl semimetal [146, 300], while several reports contradict the existence of 3D Dirac fermions [325] and strong topological insulator phase [301, 304] in $ZrTe_5$. Such discrepancy in classification could be due to thickness variations and high sensitivity of topological phase in the material on slight changes in the lattice constants [288, 289, 292]. The strong dependence on lattice constants has been confirmed experimentally by inducing strain [322] and pressure [298, 299, 326].

The longitudinal magneto resistance (MR) R_{xx} measurements in $ZrTe_5$ flake are shown in Fig. 5.8. The resistivity values are obtained by $\rho_{xx} = R_{xx}wt/L$, where w, L are the width and length of the transport channel, respectively. One can observe a decrease of MR when the magnetic field is tilted in the a-b plane by an angle α (Fig. 5.8a) towards a-axis direction. To obtain an insight into the dimensionality of the fermions that contribute to the magneto transport, the resistivity ρ_{xx} is plotted against projection of magnetic field $Bcos(\alpha)$ on the b-axis (Fig. 5.8b). The curves measured at different angles α overlap each

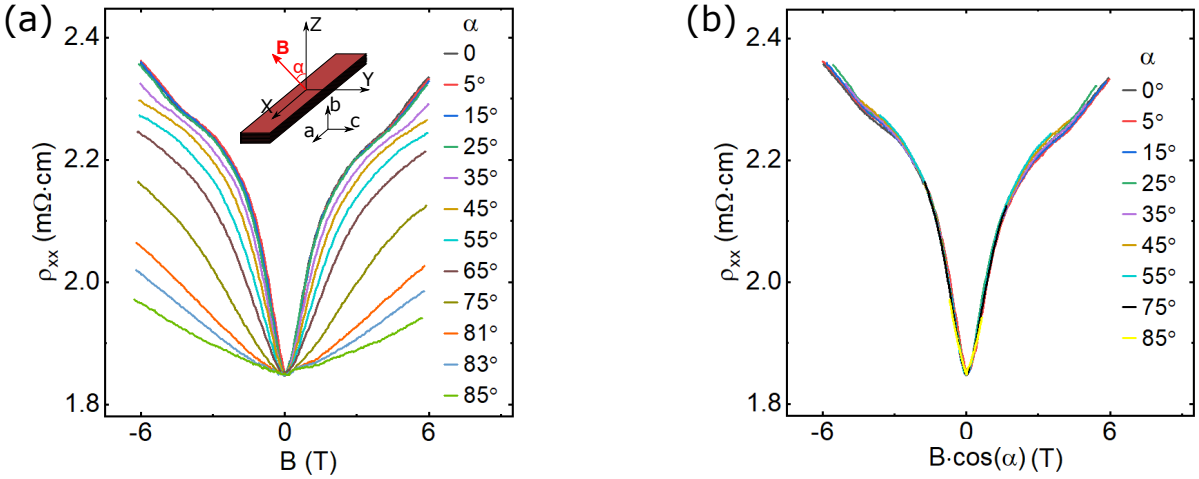

Figure 5.8: (a) Angle dependence of longitudinal resistivity ρ_{xx} in $ZrTe_5$ at 4 K. Inset: Schematic of the flake. The angle α is swept in the a-b plane. (b) Data from (a) with magnetic field values changed to projection $Bcos(\alpha)$ on the Z axis.

other, indicating a 2D-type behavior of the system [294]. Previous investigations of the Fermi surface shape by SdH oscillations, as measured with application of magnetic fields along different crystallographic planes and angles in $ZrTe_5$, reported ellipsoid-type shape that is highly elongated along k_b in the reciprocal space both in exfoliated flakes [294] and bulk crystals [145, 292, 307]. Thus, the material behaves as quasi-2D system, although with a closed (that is characteristic of 3D system) and elongated Fermi surface along the stacking direction. Such behavior in bulk crystals could originate from weak interlayer bonding along b-axis that leads to formation of parallel 2D electron channels within layers, giving rise to 2D-type system [292].

As the temperature evolution of the band structure defines the change of electrical transport properties, the dependence of Hall magneto resistivity $\rho_{xy} = R_{xy}wt/L$ (R_{xy} is the transverse resistance) on temperature can provide insight into such evolution. As revealed from the measurements (Fig. 5.9a), the Hall signals significantly change with temperature and magnetic fields. At $T < T_p$ the ρ_{xy} demonstrates strongly nonlinear dependence on magnetic field, which gradually changes to linear-type as the temperature approaches the resistivity anomaly peak position T_p. At $T > T_p$ the signals become increasingly nonlinear again as the temperature increases towards 190 K. With further increase the ρ_{xy} dependence on magnetic field flattens out and becomes nearly linear at 300 K. As the Hall coefficient R_H (obtained from Fig. 5.9a as a first derivative at zero magnetic field $R_H = (L/w)\partial\rho_{xy}/\partial B_\perp|_{B=0}$ [311]) changes sign around $T \sim T_p$ (Fig. 5.9b), the carrier type changes from electrons at $T < T_p$ to holes at $T > T_p$, in accordance with previous reports [146, 310, 311]. The high nonlinearity of ρ_{xy} signals with

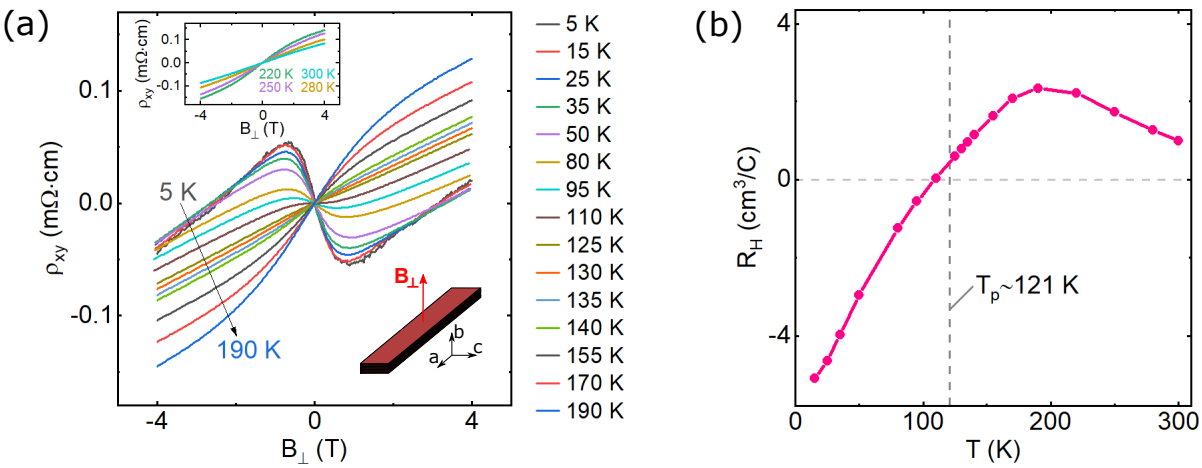

Figure 5.9: (a) Temperature dependence of the Hall resistivity ρ_{xy} in $ZrTe_5$ in the range of 5-190 K (main panel) and 220-300 K (top inset). Bottom inset indicates direction of applied magnetic field with respect to the flake crystal axes. (b) Hall coefficient R_H as a function of temperature. The vertical dashed line marks the position T_p of the resistivity anomaly peak.

magnetic fields at certain temperatures indicates that two bands near the Fermi level contribute to carrier transport [252, 310, 311, 318]. Previous reports have shown that with a temperature sweep the chemical potential changes position [142, 311, 315], giving rise to change of carrier concentrations and types in each band as well as the observed ρ_{xy} magneto resistivity evolution with temperature.

An alternative approach to look into the origin of the nonlinear ρ_{xy} signals is in considering Berry curvature that acts as intrinsic magnetic field in momentum space. Thus, the Hall signals are composed of two components $\rho_{xy} = \rho_{xy,ord} + \rho_{xy,AHE}$, where $\rho_{xy,ord}$ is the linear contribution from the ordinary Hall effect and $\rho_{xy,AHE}$ is the anomalous component, the amplitude of which is proportional to the Berry curvature [146]. The ordinary component can be excluded by subtracting a linear background from the raw ρ_{xy} signals as shown in Fig. 5.10a with dependence of the signal on the tilt angle of magnetic field in the a-b plane. The anomalous component is antisymmetric with respect to magnetic field, which is characteristic of the origin due to Berry curvature [146]. The amplitude of this component at saturation with field $\rho^0_{xy,AHE}$ is highly sensitive to change of the angle when magnetic field approaches the direction along the a-axis, in contrast to other angles closer to the b-axis direction (Fig. 5.10b). This hints to a circular dependence of the Berry curvature on the the angle within $0 - 70°$ and sharp decrease for angles in the range $70 - 90°$ in the $k_a - k_b$ plane in reciprocal space, in accordance with ref. [146]. The Berry curvature in $ZrTe_5$ might arise from field-induced Lifshitz transition when Weyl points appear due to Zeeman splitting larger than the bandgap [146, 327, 328], which is possible considering large reported g factor of ~ 35 [304, 329]. Another possibility is that high doping in the material shifts the

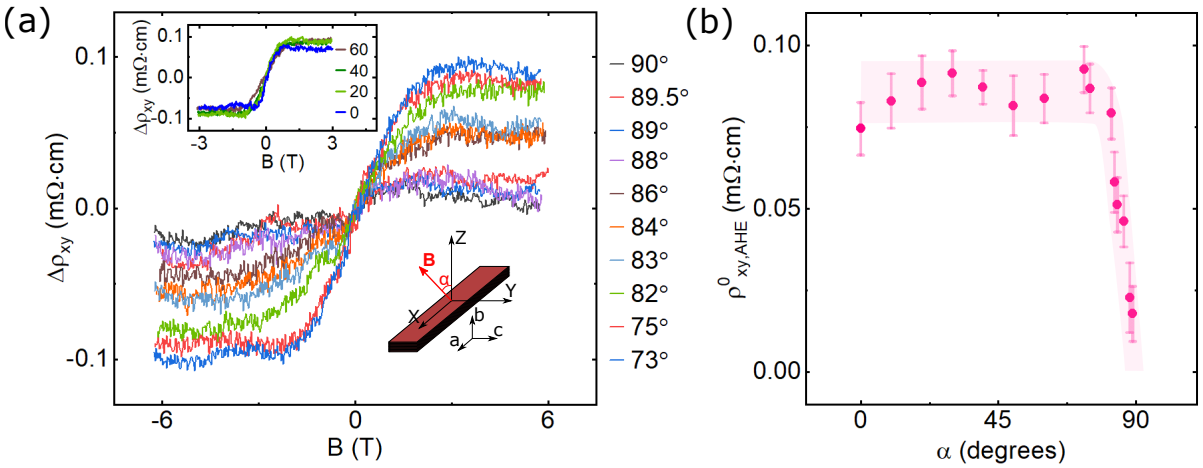

Figure 5.10: (a) Angle dependence of the Hall magneto resistivity ρ_{xy} in $ZrTe_5$ with angle range 73-90° (main panel) and 0-60° (top inset) at 4 K. The angle alpha is swept in the a-b plane as shown in the bottom inset. The linear background contribution from the ordinary Hall effect is subtracted. (b) Angle dependence of the anomalous Hall contribution $\rho^0_{xy,AHE}$. The colored background region is a guide to the eye.

chemical potential above the conduction band minimum, giving rise to non-zero Berry curvature effects when the magnetic field is applied [330].

The appearance of nonlinear AHE in $ZrTe_5$ presents its potential for observation of charge-to-spin conversion, as both effects have the same origin and usually accompany each other [331–333]. Therefore, $ZrTe_5$ is interesting for investigation of spin injection into graphene by means of charge-to-spin conversion, which has not been reported with this material so far. Attempts to experimentally observe this effect have been undertaken. However, improved interface quality is required as this effect is yet to be observed.

6 Summary & Outlook

Layered van der Waals materials and their heterostructures have proven to provide a versatile ground for fundamental studies with an outlook for practical applications. This work focused on investigations of both intrinsic properties of such layered materials as well as the physical phenomena that can arise when distinct van der Waals materials with complementary properties are placed in contact with each other. Additionally, unconventional device architecture for spin transport in graphene was explored.

Graphene is an excellent material for charge and spin-polarized electron transport; however, it lacks magnetic properties. We created a magnetic proximity effect in graphene in a van der Waals heterostructure with ferromagnetic insulator $Cr_2Ge_2Te_6$. This phenomenon was probed by means of spin transport studies in the heterostructure channel, where nontrivial Hanle spin precession features appeared below the Curie temperature. Furthermore, magnetic properties in thin layers of metallic ferromagnets Fe_3GeTe_2 and Fe_5GeTe_2 were investigated using anomalous Hall effect measurements, which can be useful as spin-polarized current source and drain contacts in spintronic devices.

To create and utilize the spin-polarized currents in strong spin-orbit coupling materials, we investigated the magnetotransport and charge-spin conversion properties of topological semimetal WTe_2 and $ZrTe_5$. We observed large magnetoresistance and Shubnikov de Haas oscillations providing insight into the Fermi surface properties in WTe_2, whereas $ZrTe_5$ revealed an anomalous Hall effect. An unconventional charge-to-spin conversion was observed in WTe_2, which was probed electrically using graphene spin-valve device. Contrary to conventional bulk spin Hall effect and Rashba-Edelstein effect, the charge-spin conversion is shown here to be created in WTe_2 due to unconventional nature due to lower crystal symmetry of the materials. The spin polarization created in WTe_2 is utilized for spin injection and detection in a graphene channel in an all-electrical van der Waals heterostructure spintronic device. While aiming for study of spin transport in unconventional device architechture with injection and detection of spin signals in graphene channel with one-dimensional ferromagnetic edge contacts, we revealed the contribution from the stray magnetic fields emanating from the edges of ferromagnets. A path towards elimination of these spurious signals was outlined and the electrical characterization of the device with full encapsulation of

the graphene channel with edge contacts, which is the next step on this path, was provided.

Regarding future perspectives, the development of reproducible 1D ferromagnetic edge contacts to graphene devices can be useful for investigating spin transport in high-quality encapsulated graphene and exploring spin interactions in the heterostructures. 2D magnetic materials and their hybrid devices with other layered materials can be useful not only for fundamental studies but also for practical spintronic and quantum applications. Whereas the insulating ferromagnets can be helpful for magnetic proximity effects, the metallic ferromagnets can be utilized as spin polarization current sources in hybrid devices. Development of 2D ferromagnets with magnetic ordering present above room temperature with perpendicular magnetic anisotropy can open the path for various magnetoresistive and spin-valve device applications. For example, 2D metallic magnets can be used for spin injection and detection in graphene spin-valves instead of traditional ferromagnetic metals. The perpendicular magnetic anisotropy of the 2D magnets and their electric field control and switching properties can boost application in data storage and memory technologies.

Charge-to-spin conversion effects in topological semimetal candidates such as WTe_2 and $ZrTe_5$ have excellent potential to be employed as a non-magnetic spin-polarized current source. Recently, WTe_2 is proved to be a potential candidate for field-free switching of ferromagnets due to its perpendicular spin-orbit field compotent and is a suitable material for spin-orbit torque technologies. The intrinsic spin-orbit coupling and observation of Anomalous Hall effect in $ZrTe_5$ give a hint about its potential charge-spin conversion effects, as both share the same origin [331–333]. The presence of spin-polarized electronic states in such topological material candidates can be further explored by tuning the Fermi level close to the topological bands. Finding a suitable topological material that can efficiently transform the electric current into a large spin polarization and its integration with 2D magnetic materials in a large scale is highly desirable for energy-efficient spintronic memory and information processing technologies.

A

Nonlocal spin transport

To separate spin currents from local charge transport, nonlocal spin transport configuration is utilized as shown in Fig. A.1. Spin injection and detection circuits are separated spatially. The injector contact made of magnetic material such as e.g. Co creates non-equilibrium spin population under it in the channel. The chemical potentials μ corresponding to the two opposite spin populations change towards equilibrium as spins diffuse along the channel. The reduction of spin coherence is characterized by spin lifetime τ_s. The magnetic contact in the voltage sensing circuit detects chemical potential that corresponds to spins that are aligned with

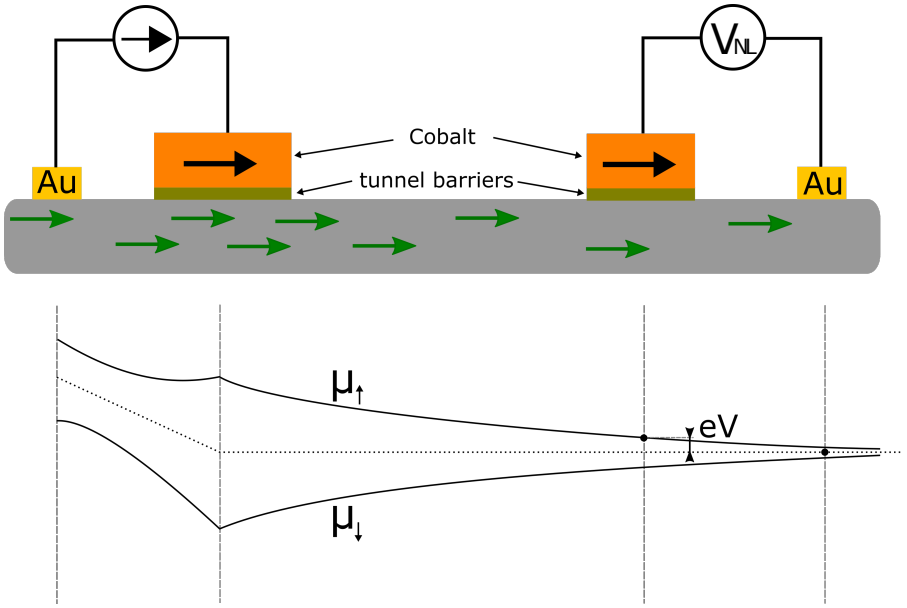

Figure A.1: Nonlocal spin transport configuration. Spins are injected into spin transport channel, where they propagate with decaying amplitude of chemical potential for each population of spins of opposite directions. At the detection circuit, spatially separated from the injecting circuit, the voltage V is measured between chemical potentials corresponding to the spin direction aligned with magnetization direction of the detector contact and neutral chemical potential (middle dashed line) that is sensed by the non-magnetic Au contact. Adapted from [334].

the magnetization direction of that contact. Thin tunnel barriers such as TiO_2 are utilized to reduce backscattering of spins into the contacts. Their magnetization direction can be manipulated by external magnetic field and the coercivity tuned due to shape anisotropy by changing the width of the contacts.

The spin transport in such nonlocal channel configuration is studied by sweeping the magnetic field and the resulting signal depends on the direction (Fig. 3.1). For spin-valve measurement (Fig. 3.1b), as the in-plane magnetic field is swept, one of the two magnetic contacts (injector or detector, depending on the width) switch the direction of magnetization. This results in change of detected resistance. As the field magnitude is increased further and reaches the value of the coercivity of the other contact, it switches its magnetization direction as well and the resistance level returns to the original level. In another type of experiment (Fig. 3.1c), magnetic field is applied in the out-of-plane direction. The presence of magnetic field that is perpendicular to the spin polarization in the channel causes precession of spins as they propagate along the channel, known as Hanle effect. The precession occurs with Larmor frequency that is defined as

$$\omega_L = \frac{g\mu_B B_\perp}{\hbar}. \tag{A.1}$$

It leads to dephasing of spins and, consequently, modulation of the nonlocal voltage V_{NL} with the magnetic field amplitude. This signal can be fitted with [334]

$$V_{NL} = \pm\frac{P_1 P_2 R_\square I}{W} \cdot \mathrm{Re}\left(\frac{exp\left(-L\sqrt{\frac{\omega}{D}}\right)}{2\sqrt{D\omega}}\right) \tag{A.2}$$

to obtain spin polarizations at the contact interfaces P_1 and P_2 as well as spin lifetime τ_s. Here $R_\square$, I, W, L, D are square resistance of the channel, current bias, channel width, length, diffusion constant, respectively, and $\omega = \frac{1}{\tau_s} - i\omega_L$. The nonlocal voltage V_{NL} can be converted into nonlocal resistance $R_{NL} = V_{NL}/I$.

Bibliography

[1] https://ethw.org/Bell_Demonstrates_Transistor.

[2] Semiconductor market size worldwide from 1987 to 2021, https://www.statista.com/statistics/266973/global-semiconductor-sales-since-1988/.

[3] The International Technology Roadmap for Semiconductors published by the Semiconductor Industry Association, http://www.itrs.net.

[4] G. M. Moore, "Cramming more components onto integrated circuits With unit cost", Electronics **38**, 114 (1965).

[5] M. M. Waldrop, "The chips are down for Moore's law", Nature **530**, 145 (2016).

[6] J. Shalf, "The future of computing beyond Moore' s Law", Philosophical Transactions Royal Society A **378**, 20190061 (2020).

[7] I. Žutić, J. Fabian, and S. D. Sarma, "Spintronics: Fundamentals and applications", Reviews of Modern Physics **76**, 323–410 (2004).

[8] H. Dery, H. Wu, B. Ciftcioglu, M. Huang, Y. Song, R. K. Kawakami, J. Shi, I. N. Krivorotov, D. A. Telesca, I. Žutić, and L. J. Sham, "Reconfigurable nanoelectronics using graphene based spintronic logic gates", SPIE **8100**, 81000W (2011).

[9] X. Lin, W. Yang, K. L. Wang, and W. Zhao, "Two-dimensional spintronics for low-power electronics", Nature Electronics **2**, 274–283 (2019).

[10] N. F. Mott, "The electrical conductivity of the transition metals", Proc. R. Soc. Lond. A **153**, 699–717 (1936).

[11] M. Julliere, "Tunneling between ferromagnetic films", Physics Letters A **54**, 225–226 (1975).

[12] J. S. Moodera, L. R. Kinder, T. M. Wong, and R. Meservey, "Large Magnetoresistance at Room Temperature in Ferromagnetic Thin Film Tunnel Junctions", Phys. Rev. Lett. **74**, 3273–3276 (1995).

[13] M. N. Baibich, J. M. Broto, A. Fert, F. N. Van Dau, F. Petroff, P. Eitenne, G. Creuzet, A. Friederich, and J. Chazelas, "Giant magnetoresistance of (001)Fe/(001)Cr magnetic superlattices", Physical Review Letters **61**, 2472–2475 (1988).

[14] E. Gerstner, "Nobel Prize 2007: Fert and Grünberg", Nature Physics **3**, 754–754 (2007).

[15] A. G. Aronov, "Spin injection in metals and polarization of nuclei", JETP Letters **24**, 37–39 (1976).

[16] M. Johnson and R. H. Silsbee, "Thermodynamic analysis of interfacial transport and of the thermomagnetoelectric system", Phys. Rev. B **35**, 4959–4972 (1987).

[17] M. Johnson and R. H. Silsbee, "Interfacial charge-spin coupling: Injection and detection of spin magnetization in metals", Phys. Rev. Lett. **55**, 1790–1793 (1985).

[18] S. Datta and B. Das, "Electronic analog of the electro-optic modulator", Applied Physics Letters **56**, 665–667 (1990).

[19] I. V. G. K. S. Novoselov, A. K. Geim, S. V. Morozov, D. Jiang, Y. Zhang, S. V. Dubonos and A. A. Firsov, "Electric Field Effect in Atomically Thin Carbon Films", Science **306**, 666–669 (2004).

[20] Y. Liu, N. O. Weiss, X. Duan, H.-C. Cheng, Y. Huang, and D. Xiangfeng, "Van der Waals heterostructures and devices", Nature Reviews Materials **1**, 16042 (2016).

[21] K. S. Novoselov, A Mishchenko, A Carvalho, and A. H. C. Neto, "2D materials and van der Waals heterostructures", Science **353**, 461 (2016).

[22] A. K. Geim and I. V. Grigorieva, "Van der Waals heterostructures", Nature **499**, 419 (2013).

[23] C. Gong and X. Zhang, "Two-dimensional magnetic crystals and emergent heterostructure devices", Science **363**, 706 (2019).

[24] J. F. Dayen, S. J. Ray, O. Karis, I. J. Vera-Marun, and M. V. Kamalakar, "Two-dimensional van der Waals spinterfaces and magnetic-interfaces", Applied Physics Reviews **7**, 011303 (2020).

[25] A. Avsar, H. Ochoa, F. Guinea, B. Zyilmaz, B. J. Van Wees, and I. J. Vera-Marun, "Colloquium: Spintronics in graphene and other two-dimensional materials", Reviews of Modern Physics **92**, 021003 (2020).

[26] M Gibertini, M Koperski, A. F. Morpurgo, and K. S. Novoselov, "Magnetic 2D materials and heterostructures", Nature Nanotechnology **14**, 408–419 (2019).

[27] M. C. Wang, C. C. Huang, C. H. Cheung, C. Y. Chen, S. G. Tan, T. W. Huang, Y. Zhao, Y. Zhao, G. Wu, Y. P. Feng, H. C. Wu, and C. R. Chang, "Prospects and Opportunities of 2D van der Waals Magnetic Systems", Annalen der Physik **532**, 1900452 (2020).

[28] K. S. Novoselov, V. I. Fal'ko, L. Colombo, P. R. Gellert, M. G. Schwab, and K. Kim, "A roadmap for graphene", Nature **490**, 192–200 (2012).

[29] A. C. Ferrari et al., "Science and technology roadmap for graphene, related two-dimensional crystals, and hybrid systems", Nanoscale **7**, 4598–4810 (2015).

[30] S. Wei, X. Tang, X. Liao, Y. Ge, H. Jin, W. Chen, H. Zhang, and Y. Wei, "Recent progress of spintronics based on emerging 2D materials: CrI_3 and Xenes", Materials Research Express **6**, 122004 (2019).

[31] E. C. Ahn, "2D materials for spintronic devices", npj 2D Materials and Applications **4**, 17 (2020).

[32] Y. Liu, C. Zeng, J. Zhong, J. Ding, Z. M. Wang, and Z. Liu, "Spintronics in Two-Dimensional Materials", Nano-Micro Letters **12**, 1–26 (2020).

[33] V. P. Ningrum, B. Liu, W. Wang, Y. Yin, Y. Cao, C. Zha, H. Xie, X. Jiang, Y. Sun, S. Qin, X. Chen, T. Qin, C. Zhu, L. Wang, and W. Huang, "Recent Advances in Two-Dimensional Magnets: Physics and Devices towards Spintronic Applications", Research **2020**, 1768918 (2020).

[34] P. Huang, P. Zhang, S. Xu, H. Wang, X. Zhang, and H. Zhang, "Recent advances in two-dimensional ferromagnetism: Materials synthesis, physical properties and device applications", Nanoscale **12**, 2309–2327 (2020).

[35] H. Idzuchi, Y. Fukuma, and Y. Otani, "Spin transport in non-magnetic nanostructures induced by non-local spin injection", Physica E: Low-Dimensional Systems and Nanostructures **68**, 239–263 (2015).

[36] X. Lou, C. Adelmann, S. A. Crooker, E. S. Garlid, J. Zhang, K. S. Reddy, S. D. Flexner, C. J. Palmstrøm, and P. A. Crowell, "Electrical detection of spin transport in lateral ferromagnet-semiconductor devices", Nature Physics **3**, 197–202 (2007).

[37] R. Ishihara, Y. Ando, S. Lee, R. Ohshima, M. Goto, S. Miwa, Y. Suzuki, H. Koike, and M. Shiraishi, "Gate-Tunable Spin xor Operation in a Silicon-Based Device at Room Temperature", Physical Review Applied **13**, 044010 (2020).

[38] A. Spiesser, H. Saito, S. Yuasa, and R. Jansen, "Tunnel spin polarization of Fe/MgO/Si contacts reaching 90% with increasing MgO thickness", Physical Review B **99**, 224427 (2019).

[39] T. Suzuki, T. Sasaki, T. Oikawa, M. Shiraishi, Y. Suzuki, and K. Noguchi, "Room-temperature electron spin transport in a highly doped Si channel", Applied Physics Express **4**, 023003 (2011).

[40] T. Sasaki, Y. Ando, M. Kameno, T. Tahara, H. Koike, T. Oikawa, T. Suzuki, and M. Shiraishi, "Spin Transport in Nondegenerate Si with a Spin MOSFET Structure at Room Temperature", Physical Review Applied **2**, 034005 (2014).

[41] S. P. Dash, S. Sharma, R. S. Patel, M. P. de Jong, and R. Jansen, "Electrical creation of spin polarization in silicon at room temperature", Nature **462**, 491–494 (2009).

[42] A. Dankert, R. S. Dulal, and S. P. Dash, "Efficient spin injection into silicon and the role of the schottky barrier", Scientific Reports **3**, 3196 (2013).

[43] P. Miró, M. Audiffred, and T. Heine, "An atlas of two-dimensional materials", Chemical Society Reviews **43**, 6537–6554 (2014).

[44] W. Han, R. K. Kawakami, M. Gmitra, and J. Fabian, "Graphene spintronics", Nature Nanotechnology **9**, 794–807 (2014).

[45] N. Tombros, C. Jozsa, M. Popinciuc, H. T. Jonkman, and B. J. van Wees, "Electronic spin transport and spin precession in single graphene layers at room temperature", Nature **448**, 571–574 (2007).

[46] W. Han, K. Pi, K. M. McCreary, Y. Li, J. J. I. Wong, A. G. Swartz, and R. K. Kawakami, "Tunneling spin injection into single layer graphene", Physical Review Letters **105**, 167202 (2010).

[47] M. Gurram, S. Omar, and B. J. Van Wees, "Electrical spin injection, transport, and detection in graphene-hexagonal boron nitride van der Waals heterostructures: Progress and perspectives", 2D Materials **5**, 032004 (2018).

[48] M. Shiraishi, M. Ohishi, R. Nouchi, N. Mitoma, T. Nozaki, T. Shinjo, and Y. Suzuki, "Robustness of spin polarization in graphene-based spin valves", Advanced Functional Materials **19**, 3711–3716 (2009).

[49] X. Du, I. Skachko, A. Barker, and E. Y. Andrei, "Approaching ballistic transport in suspended graphene", Nature Nanotechnology **3**, 491–495 (2008).

[50] M. H. Guimarães, A. Veligura, P. J. Zomer, T. Maassen, I. J. Vera-Marun, N. Tombros, and B. J. Van Wees, "Spin transport in high-quality suspended graphene devices", Nano Letters **12**, 3512–3517 (2012).

[51] I. Neumann, J. Van De Vondel, G. Bridoux, M. V. Costache, F. Alzina, C. M. Torres, and S. O. Valenzuela, "Electrical detection of spin precession in freely suspended graphene spin valves on cross-linked poly(methyl methacrylate)", Small **9**, 156–160 (2013).

[52] A. Avsar, T. Y. Yang, S. Bae, J. Balakrishnan, F. Volmer, M. Jaiswal, Z. Yi, S. R. Ali, G. Guöntherodt, B. H. Hong, B. Beschoten, and B. Özyilmaz, "Toward wafer scale fabrication of graphene based spin valve devices", Nano Letters **11**, 2363–2368 (2011).

[53] V. M. Kamalakar, C. Groenveld, A. Dankert, and S. P. Dash, "Long distance spin communication in chemical vapour deposited graphene", Nature Communications **6**, 6766 (2015).

[54] Z. M. Gebeyehu, S. Parui, J. F. Sierra, M. Timmermans, M. J. Esplandiu, S. Brems, C. Huyghebaert, K. Garello, M. V. Costache, and S. O. Valenzuela, "Spin communication over 30-µm long channels of chemical vapor deposited graphene on SiO_2", 2D Materials **6**, 034003 (2019).

[55] D. Khokhriakov, B. Karpiak, A. M. Hoque, and S. P. Dash, "Two-dimensional spintronic circuit architectures on large scale graphene", Carbon **161**, 892–899 (2020).

[56] D. Van Tuan, F. Ortmann, A. W. Cummings, D. Soriano, and S. Roche, "Spin dynamics and relaxation in graphene dictated by electron-hole puddles.", Scientific reports **6**, 21046 (2016).

[57] P. J. Zomer, M. H. Guimarães, N. Tombros, and B. J. Van Wees, "Long-distance spin transport in high-mobility graphene on hexagonal boron nitride", Physical Review B **86**, 161416(R) (2012).

[58] C. R. Dean, a. F. Young, I Meric, C Lee, L Wang, S Sorgenfrei, K Watanabe, T Taniguchi, P Kim, K. L. Shepard, and J Hone, "Boron nitride substrates for high-quality graphene electronics", Nature nanotechnology **5**, 722–726 (2010).

[59] D. Khokhriakov, B. Karpiak, A. M. Hoque, B. Zhao, S. Parui, and S. P. Dash, "Robust spin interconnect with isotropic spin dynamics in chemical vapor deposited graphene layers and boundaries", ACS Nano **14**, 15864–15873 (2020).

[60] L Wang, I Meric, P. Y. Huang, Q Gao, Y Gao, H Tran, T Taniguchi, K Watanabe, L. M. Campos, D. a. Muller, J Guo, P Kim, J Hone, K. L. Shepard, and C. R. Dean, "One-dimensional electrical contact to a two-dimensional material", Science **342**, 614 (2013).

[61] Y. C. Lin, C. C. Lu, C. H. Yeh, C. Jin, K. Suenaga, and P. W. Chiu, "Graphene annealing: How clean can it be?", Nano Letters **12**, 414–419 (2012).

[62] M. Drögeler, C. Franzen, F. Volmer, T. Pohlmann, L. Banszerus, M. Wolter, K. Watanabe, T. Taniguchi, C. Stampfer, and B. Beschoten, "Spin lifetimes exceeding 12 ns in graphene nonlocal spin valve devices", Nano Letters **16**, 3533–3539 (2016).

[63] A. T. Filip, B. H. Hoving, F. J. Jedema, and B. J. V. Wees, "Experimental search for the electrical spin injection in a semiconductor", Physical Review B **62**, 9996–9999 (2000).

[64] W. Han, K. Pi, W. Bao, K. M. McCreary, Y. Li, W. H. Wang, C. N. Lau, and R. K. Kawakami, "Electrical detection of spin precession in single layer graphene spin valves with transparent contacts", Applied Physics Letters **94**, 2007–2010 (2009).

[65] D. Khokhriakov, A. W. Cummings, K. Song, M. Vila, B. Karpiak, A. Dankert, S. Roche, and S. P. Dash, "Tailoring emergent spin phenomena in Dirac material heterostructures", Science Advances **4**, 1–9 (2018).

[66] A. M. Hoque, D. Khokhriakov, B. Karpiak, and S. P. Dash, "Charge-spin conversion in layered semimetal $TaTe_2$ and spin injection in van der Waals heterostructures", Physical Review Research **2**, 33204 (2020).

[67] B. Zhao, D. Khokhriakov, B. Karpiak, A. M. Hoque, L. Xu, L. Shen, Y. P. Feng, X. Xu, Y. Jiang, and S. P. Dash, "Electrically controlled spin-switch and evolution of Hanle spin precession in graphene", 2D Materials **6**, 035042 (2019).

[68] D. Khokhriakov, A. M. Hoque, B. Karpiak, and S. P. Dash, "Gate-tunable spin-galvanic effect in graphene-topological insulator van der Waals heterostructures at room temperature", Nature Communications **11**, 3657 (2020).

[69] A. Dankert, J. Geurs, M. V. Kamalakar, S. Charpentier, and S. P. Dash, "Room Temperature Electrical Detection of Spin Polarized Currents in Topological Insulators", Nano Letters **2**, Article ASAP (2015).

[70] A. Dankert and S. P. Dash, "Electrical gate control of spin current in van der Waals heterostructures at room temperature", Nature Communications **8**, 16093 (2017).

[71] A. Dankert, P. Bhaskar, D. Khokhriakov, I. H. Rodrigues, B. Karpiak, M. V. Kamalakar, S. Charpentier, I. Garate, and S. P. Dash, "Origin and evolution of surface spin current in topological insulators", Physical Review B **97**, 125414 (2018).

[72] S. P. Dash, S. Sharma, J. C. Le Breton, J. Peiro, H. Jaffrès, J. M. George, A. Lemaître, and R. Jansen, "Spin precession and inverted Hanle effect in a semiconductor near a finite-roughness ferromagnetic interface", Physical Review B **84**, 054410 (2011).

[73] M. V. Kamalakar, A. Dankert, J. Bergsten, T. Ive, and S. P. Dash, "Spintronics with graphene-hexagonal boron nitride van der Waals heterostructures", Applied Physics Letters **105**, 212405 (2014).

[74] M. V. Kamalakar, A. Dankert, J. Bergsten, T. Ive, and S. P. Dash, "Enhanced tunnel spin injection into graphene using chemical vapor deposited hexagonal boron nitride.", Scientific reports **4**, 6146 (2014).

[75] V. M. Kamalakar, A. Dankert, P. J. Kelly, and S. P. Dash, "Inversion of Spin Signal and Spin Filtering in Ferromagnet|Hexagonal Boron Nitride-Graphene van der Waals Heterostructures", Scientific reports **6**, 1–9 (2016).

[76] L. Banszerus, M. Schmitz, S. Engels, M. Goldsche, K. Watanabe, T. Taniguchi, B. Beschoten, and C. Stampfer, "Ballistic transport exceeding 28 µm in CVD grown graphene", **16**, 1387–1391 (2015).

[77] J. Xu, S. Singh, J. Katoch, G. Wu, T. Zhu, I. Žutić, and R. K. Kawakami, "Spin inversion in graphene spin valves by gate-tunable magnetic proximity effect at one-dimensional contacts", Nature Communications **9**, 2869 (2018).

[78] Y. Li and K. Baberschke, "Dimensional Crossover in Ultrathin Ni(111) Films on W(110)", Physical review letters **68**, 1208–1212 (1992).

[79] S. S. Parkin, N. More, and K. P. Roche, "Oscillations in exchange coupling and magnetoresistance in metallic superlattice structures: Co/Ru, Co/Cr, and Fe/Cr", Physical Review Letters **64**, 2304–2307 (1990).

[80] N. D. Mermin and H. Wagner, "Absence of ferromagnetism or antiferromagnetism in one- or two-dimensional isotropic Heisenberg models", Physical Review Letters **17**, 1133–1136 (1966).

[81] C. Gong, L. Li, Z. Li, H. Ji, A. Stern, Y. Xia, T. Cao, W. Bao, C. Wang, Y. Wang, Z. Q. Qiu, R. J. Cava, S. G. Louie, J. Xia, and X. Zhang, "Discovery of intrinsic ferromagnetism in two-dimensional van der Waals crystals", Nature **546**, 265–269 (2017).

[82] Z. Fei, B. Huang, P. Malinowski, W. Wang, T. Song, J. Sanchez, W. Yao, D. Xiao, X. Zhu, A. F. May, W. Wu, D. H. Cobden, J.-h. Chu, and X. Xu, "Two-dimensional itinerant ferromagnetism in atomically thin Fe_3GeTe_2", Nature Materials **17**, 778–782 (2018).

[83] B. Huang, G. Clark, E. Navarro-Moratalla, D. R. Klein, R. Cheng, K. L. Seyler, D. Zhong, E. Schmidgall, M. A. McGuire, D. H. Cobden, W. Yao, D. Xiao, P. Jarillo-Herrero, and X. Xu, "Layer-dependent ferromagnetism in a van der Waals crystal down to the monolayer limit", Nature **546**, 270–273 (2017).

[84] Y. Deng, Y. Yu, Y. Song, J. Zhang, N. Z. Wang, Z. Sun, Y. Yi, Y. Z. Wu, S. Wu, J. Zhu, J. Wang, X. H. Chen, and Y. Zhang, "Gate-tunable room-temperature ferromagnetism in two-dimensional Fe_3GeTe_2", Nature **563**, 94–99 (2018).

[85] W. Zhang, P. Kwan, J. Wong, R. Zhu, and A. T. S. Wee, "Van der Waals magnets: Wonder building blocks for two-dimensional spintronics?", InfoMat **1**, 479–495 (2019).

[86] A. F. May, D. Ovchinnikov, Q. Zheng, R. Hermann, S. Calder, B. Huang, Z. Fei, Y. Liu, X. Xu, and M. A. McGuire, "Ferromagnetism Near Room Temperature in the Cleavable van der Waals Crystal Fe_5GeTe_2", ACS Nano **13**, 4436–4442 (2019).

[87] X. Cai, T. Song, N. P. Wilson, G. Clark, M. He, X. Zhang, T. Taniguchi, K. Watanabe, W. Yao, D. Xiao, M. A. Mcguire, D. H. Cobden, and X. Xu, "Atomically Thin $CrCl_3$: An In-Plane Layered Antiferromagnetic Insulator", Nano Letters **19**, 3993–3998 (2019).

[88] J. U. Lee, S. Lee, J. H. Ryoo, S. Kang, T. Y. Kim, P. Kim, C. H. Park, J. G. Park, and H. Cheong, "Ising-Type Magnetic Ordering in Atomically Thin $FePS_3$", Nano Letters **16**, 7433–7438 (2016).

[89] A. R. Wildes, K. C. Rule, R. I. Bewley, M. Enderle, and T. J. Hicks, "The magnon dynamics and spin exchange parameters of FePS 3", Journal of Physics Condensed Matter **24**, 416004 (2012).

[90] D. Ghazaryan, M. T. Greenaway, Z. Wang, V. H. Guarochico-Moreira, I. J. Vera-Marun, J. Yin, Y. Liao, S. V. Morozov, O. Kristanovski, A. I. Lichtenstein, M. I. Katsnelson, F. Withers, A. Mishchenko, L. Eaves, A. K. Geim, K. S. Novoselov, and A. Misra, "Magnon-assisted tunnelling in van der Waals heterostructures based on $CrBr_3$", Nature Electronics **1**, 344–349 (2018).

[91] T. S. Ghiasi, A. A. Kaverzin, A. H. Dismukes, D. K. de Wal, X. Roy, and B. J. van Wees, "Electrical and Thermal Generation of Spin Currents by Magnetic Graphene", arXiv:2007.15597 (2020).

[92] L. D. Casto, A. J. Clune, M. O. Yokosuk, J. L. Musfeldt, T. J. Williams, H. L. Zhuang, M. W. Lin, K. Xiao, R. G. Hennig, B. C. Sales, J. Q. Yan, and D. Mandrus, "Strong spin-lattice coupling in $CrSiTe_3$", APL Materials **3**, 041515 (2015).

[93] J. Qi, H. Wang, X. Chen, and X. Qian, "Two-dimensional multiferroic semiconductors with coexisting ferroelectricity and ferromagnetism", Applied Physics Letters **113**, 043102 (2018).

[94] W. Luo, K. Xu, and H. Xiang, "Two-dimensional hyperferroelectric metals: A different route to ferromagnetic-ferroelectric multiferroics", Physical Review B **96**, 235415 (2017).

[95] C. Chappert, A. Fert, and F. N. Van Dau, "The emergence of spin electronics in data storage", Nature materials **6**, 813–823 (2007).

[96] J. G. J. Zhu and C. Park, "Magnetic tunnel junctions", Materials Today **9**, 36–45 (2006).

[97] S. Cardoso, P. P. Freitas, C. De Jesus, P. Wei, and J. C. Soares, "Spin-tunnel-junction thermal stability and interface interdiffusion above 300Â°C", Applied Physics Letters **76**, 610–612 (2000).

[98] W. Shen, D. Mazumdar, X. Zou, X. Liu, B. D. Schrag, and G. Xiao, "Effect of film roughness in MgO-based magnetic tunnel junctions", Applied Physics Letters **88**, 182508 (2006).

[99] E. Y. Tsymbal and D. Pettifor, "Spin-polarized electron tunneling across a disordered insulator", Physical Review B **58**, 432–437 (1998).

[100] T. Song, X. Cai, M. W. Y. Tu, X. Zhang, B. Huang, N. P. Wilson, K. L. Seyler, L. Zhu, T. Taniguchi, K. Watanabe, M. A. McGuire, D. H. Cobden, D. Xiao, W. Yao, and X. Xu, "Giant tunneling magnetoresistance in spin-filter van der Waals heterostructures", Science **360**, 1214–1218 (2018).

[101] Z. Wang, D. Sapkota, T. Taniguchi, K. Watanabe, D. Mandrus, and A. F. Morpurgo, "Tunneling Spin Valves Based on Fe_3GeTe_2/hBN/Fe_3GeTe_2 van der Waals Heterostructures", Nano Letters **18**, 4303–4308 (2018).

[102] S. Albarakati, C. Tan, Z.-j. Chen, J. G. Partridge, G. Zheng, L. Farrar, E. L. H. Mayes, M. R. Field, C. Lee, Y. Wang, Y. Xiong, M. Tian, F. Xiang, A. R. Hamilton, O. A. Tretiakov, D. Culcer, Y.-j. Zhao, and L. Wang, "Antisymmetric magnetoresistance in van der Waals Fe_3GeTe_2/graphite/Fe_3GeTe_2 trilayer heterostructures", Science Advances **5**, eaaw0409 (2019).

[103] D. R. Klein, D. MacNeill, J. L. Lado, D. Soriano, E. Navarro-Moratalla, K. Watanabe, T. Taniguchi, S. Manni, P. Canfield, J. Fernández-Rossier, and P. Jarillo-Herrero, "Probing magnetism in 2D van der Waals crystalline insulators via electron tunneling", Science **360**, 1218–1222 (2018).

[104] K. Kim, J. Seo, E. Lee, K. T. Ko, B. S. Kim, B. G. Jang, J. M. Ok, J. Lee, Y. J. Jo, W. Kang, J. H. Shim, C. Kim, H. W. Yeom, B. Il Min, B. J. Yang, and J. S. Kim, "Large anomalous Hall current induced by topological nodal lines in a ferromagnetic van der Waals semimetal", Nature Materials **17**, 794–799 (2018).

[105] P. Wei, S. Lee, F. Lemaitre, L. Pinel, D. Cutaia, W. Cha, F. Katmis, Y. Zhu, D. Heiman, J. Hone, J. S. Moodera, and C. T. Chen, "Strong interfacial exchange field in the graphene/EuS heterostructure", Nature Materials **15**, 711–716 (2016).

[106] Z. Wang, C. Tang, R. Sachs, Y. Barlas, and J. Shi, "Proximity-induced ferromagnetism in graphene revealed by the anomalous Hall effect", Physical Review Letters **114**, 016603 (2015).

[107] Y. Wu, G. Yin, L. Pan, A. J. Grutter, Q. Pan, A. Lee, D. A. Gilbert, J. A. Borchers, W. R. Ii, A. Li, X.-d. Han, and K. L. Wang, "Large exchange splitting in monolayer graphene magnetized by an antiferromagnet", Nature Electronics **3**, 604–611 (2020).

[108] J. C. Leutenantsmeyer, A. A. Kaverzin, M. Wojtaszek, and B. J. Van Wees, "Proximity induced room temperature ferromagnetism in graphene probed with spin currents", 2D Materials **4**, 014001 (2016).

[109] O. V. Yazyev and M. I. Katsnelson, "Magnetic correlations at graphene edges: Basis for novel spintronics devices", Physical Review Letters **100**, 047209 (2008).

[110] J. Jung, T. Pereg-Barnea, and A. H. MacDonald, "Theory of interedge superexchange in zigzag edge magnetism", Physical Review Letters **102**, 227205 (2009).

[111] Y.-W. Son, M. L. Cohen, and S. G. Louie, "Half-Metallic Graphene Nanoribbons", Nature **444**, 347–342 (2006).

[112] O. V. Yazyev and L. Helm, "Defect-induced magnetism in graphene", Physical Review B **75**, 125408 (2007).

[113] R. R. Nair, M. Sepioni, I. L. Tsai, O. Lehtinen, J. Keinonen, A. V. Krasheninnikov, T. Thomson, A. K. Geim, and I. V. Grigorieva, "Spin-half paramagnetism in graphene induced by point defects", Nature Physics **8**, 199–202 (2012).

[114] J. Červenka, M. I. Katsnelson, and C. F. Flipse, "Room-temperature ferromagnetism in graphite driven by two-dimensional networks of pointdefects", Nature Physics **5**, 840–844 (2009).

[115] K. M. McCreary, A. G. Swartz, W. Han, J. Fabian, and R. K. Kawakami, "Magnetic moment formation in graphene detected by scattering of pure spin currents", Physical Review Letters **109**, 186604 (2012).

[116] A. J. Giesbers, K. UhlíÅ™ová, M. Konečný, E. C. Peters, M. Burghard, J. Aarts, and C. F. Flipse, "Interface-induced room-temperature ferromagnetism in hydrogenated epitaxial graphene", Physical Review Letters **111**, 166101 (2013).

[117] D. W. Boukhvalov, M. I. Katsnelson, and A. I. Lichtenstein, "Hydrogen on graphene: Electronic structure, total energy, structural distortions and magnetism from first-principles calculations", Physical Review B - Condensed Matter and Materials Physics **77**, 035427 (2008).

[118] C. Tang, B. Cheng, M. Aldosary, Z. Wang, Z. Jiang, K Watanabe, T Taniguchi, M. Bockrath, and J. Shi, "Approaching quantum anomalous Hall effect in proximity-coupled YIG/graphene/h-BN sandwich structure", APL Materials **6**, 026401 (2018).

[119] S. Dushenko, H. Ago, K. Kawahara, T. Tsuda, S. Kuwabata, T. Takenobu, T. Shinjo, Y. Ando, and M. Shiraishi, "Gate-Tunable Spin-Charge Conversion and the Role of Spin-Orbit Interaction in Graphene", Physical Review Letters **116**, 166102 (2016).

[120] R. Ohshima, A. Sakai, Y. Ando, T. Shinjo, K. Kawahara, H. Ago, and M. Shiraishi, "Observation of spin-charge conversion in chemical-vapor-deposition-grown single-layer graphene", Applied Physics Letters **105**, 162410 (2014).

[121] S. Singh, J. Katoch, T. Zhu, K. Y. Meng, T. Liu, J. T. Brangham, F. Yang, M. E. Flatté, and R. K. Kawakami, "Strong Modulation of Spin Currents in Bilayer Graphene by Static and Fluctuating Proximity Exchange Fields", Physical Review Letters **118**, 187201 (2017).

[122] Y. Li, M. Amado, T. Hyart, G. P. Mazur, V. Risinggård, T. Wagner, L. McKenzie-Sell, G. Kimbell, J. Wunderlich, J. Linder, and J. W. Robinson, "Transition between canted antiferromagnetic and spin-polarized ferromagnetic quantum Hall states in graphene on a ferrimagnetic insulator", Physical Review B **101**, 241405(R) (2020).

[123] D. V. Averyanov, I. S. Sokolov, A. M. Tokmachev, O. E. Parfenov, I. A. Karateev, A. N. Taldenkov, and V. G. Storchak, "High-Temperature Magnetism in Graphene Induced by Proximity to EuO", ACS Applied Materials and Interfaces **10**, 20767–20774 (2018).

[124] H.-D. Song, Y.-F. Wu, X. Yang, Z. Ren, X. Ke, M. Kurttepeli, G. V. Tendeloo, D. Liu, H.-C. Wu, B. Yan, X. Wu, C.-G. Duan, G. Han, Z.-M. Liao, and D. Yu, "Asymmetric Modulation on Exchange Field in a Graphene/$BiFeO_3$ Heterostructure by External Magnetic Field", Nano Letters, 2435–2441 (2018).

[125] Y. F. Wu, H. D. Song, L. Zhang, X. Yang, Z. Ren, D. Liu, H. C. Wu, J. Wu, J. G. Li, Z. Jia, B. Yan, X. Wu, C. G. Duan, G. Han, Z. M. Liao, and D. Yu, "Magnetic proximity effect in graphene coupled to a $BiFeO_3$ nanoplate", Physical Review B **95**, 195426 (2017).

[126] C. Tang, Z. Zhang, S. Lai, Q. Tan, and W.-b. Gao, "Magnetic Proximity Effect in Graphene/$CrBr_3$van der Waals Heterostructures", Advanced Materials **32**, 1908498 (2020).

[127] H. D. Song, P. F. Zhu, J. Fang, Z. Zhou, H. Yang, K. Wang, J. Li, D. Yu, Z. Wei, and Z. M. Liao, "Anomalous Hall effect in graphene coupled to a layered magnetic semiconductor", Physical Review B **103**, 125304 (2021).

[128] B. A. Bernevig, T. L. Hughes, and S.-C. Zhang, "Quantum Spin Hall Effect and Topological Phase Transition in HgTe Quantum Wells", Science **314**, 1757–1762 (2006).

[129] A. Roth, C. Brüne, H. Buhmann, L. W. Molenkamp, J. Maciejko, X.-L. Qi, and S.-C. Zhang, "Nonlocal Transport in the Quantum Spin Hall State", Science **325**, 294–297 (2009).

[130] M. König, S. Wiedmann, C. Brüne, A. Roth, H. Buhmann, L. W. Molenkamp, X.-L. Qi, and S.-C. Zhang, "Quantum Spin Hall Insulator State in HgTe Quantum Wells", Science **318**, 766–770 (2007).

[131] M. Z. Hasan and C. L. Kane, "Colloquium: Topological insulators", Reviews of Modern Physics **82**, 3045–3067 (2010).

[132] X. L. Qi and S. C. Zhang, "Topological insulators and superconductors", Reviews of Modern Physics **83**, 1057 (2011).

[133] J. E. Moore, "The birth of topological insulators", Nature **464**, 194–198 (2010).

[134] N. P. Armitage, E. J. Mele, and A. Vishwanath, "Weyl and Dirac semimetals in three-dimensional solids", Reviews of Modern Physics **90**, 15001 (2018).

[135] Q. D. Gibson, L. M. Schoop, L. Muechler, L. S. Xie, M. Hirschberger, N. P. Ong, R. Car, and R. J. Cava, "Three-dimensional Dirac semimetals: Design principles and predictions of new materials", Physical Review B **91**, 205128 (2015).

[136] H. Wang and J. Wang, "Electron transport in Dirac and Weyl semimetals", Chinese Physics B **27**, 107402 (2018).

[137] Y. Ando, "Topological Insulator Materials", Journal of the Physical Society of Japan **82**, 102001 (2013).

[138] B. Yan and C. Felser, "Topological Materials : Weyl Semimetals", Annual Review of Condensed Matter Physics **8**, 337–354 (2017).

[139] Z. Fei, T. Palomaki, S. Wu, W. Zhao, X. Cai, B. Sun, P. Nguyen, J. Finney, X. Xu, and D. H. Cobden, "Edge conduction in monolayer WTe_2", Nature Physics **13**, 677–682 (2017).

[140] S. Wu, V. Fatemi, Q. D. Gibson, K. Watanabe, T. Taniguchi, R. J. Cava, and P. Jarillo-herrero, "Observation of the Quantum Spin Hall Effect up to 100 Kelvin in a Monolayer", Science **359**, 76–79 (2018).

[141] K. Kang, T. Li, E. Sohn, J. Shan, and K. F. Mak, "Nonlinear anomalous Hall effect in few-layer WTe_2", Nature Materials, 324–328 (2019).

[142] Y. Zhang et al., "Electronic evidence of temperature-induced Lifshitz transition and topological nature in $ZrTe_5$", Nature Communications **8**, 15512 (2017).

[143] G. Zheng, X. Zhu, Y. Liu, J. Lu, W. Ning, H. Zhang, W. Gao, Y. Han, J. Yang, H. Du, K. Yang, Y. Zhang, and M. Tian, "Field-induced topological phase transition from a three-dimensional Weyl semimetal to a two-dimensional massive Dirac metal in $ZrTe_5$", Physical Review B **96**, 121401(R) (2017).

[144] B. Xu, L. X. Zhao, P. Marsik, E. Sheveleva, F. Lyzwa, Y. M. Dai, G. F. Chen, X. G. Qiu, and C. Bernhard, "Temperature-Driven Topological Phase Transition and Intermediate Dirac Semimetal Phase in $ZrTe_5$", Physical Review Letters **121**, 187401 (2018).

[145] F. Tang, Y. Ren, P. Wang, R. Zhong, J. Schneeloch, S. A. Yang, K. Yang, P. A. Lee, G. Gu, Z. Qiao, and L. Zhang, "Three-dimensional quantum Hall effect and metal-insulator transition in $ZrTe_5$", Nature **569**, 537–541 (2019).

[146] T. Liang, J. Lin, Q. Gibson, S. Kushwaha, M. Liu, W. Wang, H. Xiong, J. A. Sobota, M. Hashimoto, P. S. Kirchmann, Z. X. Shen, R. J. Cava, and N. P. Ong, "Anomalous Hall effect in $ZrTe_5$", Nature Physics **14**, 451–455 (2018).

[147] M. N. Ali, J. Xiong, S. Flynn, J. Tao, Q. D. Gibson, L. M. Schoop, T. Liang, N. Haldolaarachchige, M. Hirschberger, N. P. Ong, and R. J. Cava, "Large, non-saturating magnetoresistance in WTe_2", Nature **514**, 205–208 (2014).

[148] S. Roche, J. Åkerman, B. Beschoten, J.-C. Charlier, M. Chshiev, S. Prasad Dash, B. Dlubak, J. Fabian, A. Fert, M. Guimarães, F. Guinea, I. Grigorieva, C. Schönenberger, P. Seneor, C. Stampfer, S. O. Valenzuela, X. Waintal, and B. van Wees, "Graphene spintronics: the European Flagship perspective", 2D Materials **2**, 030202 (2015).

[149] J. Ingla-Aynés, M. H. D. Guimarães, R. J. Meijerink, P. J. Zomer, and B. J. Van Wees, "24-μm spin relaxation length in boron nitride encapsulated bilayer graphene", Physical Review B **92**, 201410 (2015).

[150] P. K. Muduli, J Barzola-Quiquia, S Dusari, A Ballestar, F Bern, W Böhlmann, and P Esquinazi, "Large local Hall effect in pin-hole dominated multi-graphene spin-valves", Nanotechnology **24**, 015703 (2013).

[151] M. Wimmer, I. Adagideli, S. Berber, D. Tománek, and K. Richter, "Spin currents in rough graphene nanoribbons: Universal fluctuations and spin injection", Physical Review Letters **100**, 177207 (2008).

[152] M. Yankowitz, Q. Ma, P. Jarillo-Herrero, and B. J. LeRoy, "van der Waals heterostructures combining graphene and hexagonal boron nitride", Nature Reviews Physics **1**, 112–125 (2019).

[153] M. Vila, J. H. Garcia, A. W. Cummings, S. R. Power, C. W. Groth, X. Waintal, and S. Roche, "Nonlocal Spin Dynamics in the Crossover from Diffusive to Ballistic Transport", Physical Review Letters **124**, 196602 (2020).

[154] A. Ferrari, J. Meyer, C. Scardaci, C. Casiraghi, and M. Lazzeri, "Raman Spectrum of Graphene and Graphene Layers", Physical review letters **97**, 187401 (2006).

[155] R. V. Gorbachev, I. Riaz, R. R. Nair, R. Jalil, L. Britnell, B. D. Belle, E. W. Hill, K. S. Novoselov, K. Watanabe, T. Taniguchi, A. K. Geim, and P. Blake, "Hunting for monolayer boron nitride: Optical and raman signatures", Small **7**, 465–468 (2011).

[156] J Heremans, "Solid state magnetic field sensors and applications", Journal of Physics D: Applied Physics **26**, 1149–1168 (1993).

[157] R. S. Popovic, *Hall Effect Devices*, Second (Institute of Physics, 2003).

[158] T. Hara, M. Mihara, N. Toyoda, and M. Zama, "Highly Linear Gaas Hall Devices Fabricated By Ion Implantation", IEEE Transactions on Electron Devices **ED-29**, 78–82 (1982).

[159] H. Xu, Z. Zhang, R. Shi, H. Liu, Z. Wang, S. Wang, and L.-M. Peng, "Batch-fabricated high-performance graphene Hall elements", Scientific reports **3**, 1207 (2013).

[160] J. Dauber, A. A. Sagade, M. Oellers, K. Watanabe, T. Taniguchi, D. Neumaier, and C. Stampfer, "Ultra-sensitive Hall sensors based on graphene encapsulated in hexagonal boron nitride", Applied Physics Letters **106**, 193501 (2015).

[161] K. Vervaeke, E. Simoen, G. Borghs, and V. V. Moshchalkov, "Size dependence of microscopic Hall sensor detection limits", Review of Scientific Instruments **80**, 074701 (2009).

[162] Z. Wang, M. Shaygan, M. Otto, D. Schall, and D. Neumaier, "Flexible Hall sensors based on graphene", Nanoscale **8**, 7683–7687 (2016).

[163] L. Huang, Z. Zhang, B. Chen, X. Ma, H. Zhong, and L. M. Peng, "Ultra-sensitive graphene Hall elements", Applied Physics Letters **104**, 183106 (2014).

[164] J. A. Alexander-Webber, A. A. Sagade, A. I. Aria, Z. A. V. Veldhoven, P. Braeuninger-Weimer, R. Wang, A. Cabrero-Vilatela, M.-B. Martin, J. Sui, M. R. Connolly, and S. Hofmann, "Encapsulation of graphene transistors and vertical device integration by interface engineering with atomic layer deposited oxide", 2D Materials **4**, 011008 (2017).

[165] H. M. Gon, "Quantum Effects for Spintronic Devices Optimization", Physics (2009).

[166] F. G. Monzon, D. S. Patterson, and M. L. Roukes, "Characterization of individual nanomagnets by the local Hall effect", Journal of Magnetism and Magnetic Materials **195**, 19–25 (1999).

[167] F. G. Monzon, M. Johnson, and M. L. Roukes, "Strong Hall voltage modulation in hybrid ferromagnet/semiconductor microstructures", Applied Physics Letters **71**, 3087–3089 (1997).

[168] M. Hara, A. Endo, S. Katsumoto, and Y. Iye, "Transport in ferromagnet/semiconductor 2DEG hybrid network structure", Physica E **22**, 345–348 (2004).

[169] F. G. Monzon, H. X. Tang, and M. L. Roukes, "Magnetoelectronic phenomena at a ferromagnet-semiconductor interface", Physical Review Letters **84**, 5022 (2000).

[170] R Engel-Herbert and T Hesjedal, "Calculation of the magnetic stray field of a uniaxial magnetic domain", Journal of Applied Physics **97**, 074504 (2005).

[171] J. Park, S. B. Jo, Y.-J. Yu, Y. Kim, J. W. Yang, W. H. Lee, H. H. Kim, B. H. Hong, P. Kim, K. Cho, and K. S. Kim, "Single-Gate Bandgap Opening of Bilayer Graphene by Dual Molecular Doping", Advanced Materials **24**, 407–411 (2012).

[172] B. J. JoÌˆnsson-AÌŠkerman, R. Escudero, C. Leighton, S. Kim, I. K. Schuller, and D. A. Rabson, "Reliability of normal-state current-voltage characteristics as an indicator of tunnel-junction barrier quality", Applied Physics Letters **77**, 1870 (2000).

[173] S. Tang, G. Ding, X. Xie, J. Chen, C. Wang, X. Ding, F. Huang, W. Lu, and M. Jiang, "Nucleation and growth of single crystal graphene on hexagonal boron nitride", Carbon **50**, 329–331 (2012).

[174] S. Tang, H. Wang, H. S. Wang, Q. Sun, X. Zhang, C. Cong, H. Xie, X. Liu, X. Zhou, F. Huang, X. Chen, T. Yu, F. Ding, X. Xie, and M. Jiang, "Silane-catalysed fast growth of large single-crystalline graphene on hexagonal boron nitride", Nature Communications **6**, 6499 (2015).

[175] S. Tang, H. Wang, Y. Zhang, A. Li, H. Xie, X. Liu, L. Liu, T. Li, F. Huang, X. Xie, and M. Jiang, "Precisely aligned graphene grown on hexagonal boron nitride by catalyst free chemical vapor deposition", Scientific Reports **3**, 2666 (2013).

[176] V Carteaux, D Brunet, G Ouvrard, and G André, "Crystallographic, magnetic and electronic structures of a new layered ferromagnetic compound $Cr_2Ge_2Te_6$", Journal of Physics: Condensed Matter **7**, 69–87 (1995).

[177] B. Siberchicot, S. Jobic, V. Carteaux, P. Gressier, and G. Ouvrard, "Band structure calculations of ferromagnetic chromium tellurides CrSiTe3 and $CrGeTe_3$", Journal of Physical Chemistry **100**, 5863–5867 (1996).

[178] W. Xing, Y. Chen, P. M. Odenthal, X. Zhang, W. Yuan, T. Su, Q. Song, T. Wang, J. Zhong, S. Jia, X. C. Xie, Y. Li, and W. Han, "Electric field effect in multilayer $Cr_2Ge_2Te_6$: a ferromagnetic 2D material", 2D Materials **4**, 024009 (2017).

[179] W. Ge, K. Xu, W. Xia, Z. Yu, H. Wang, X. Liu, J. Zhao, X. Wang, N. Yu, Z. Zou, Z. Yan, L. Wang, M. Xu, and Y. Guo, "Raman spectroscopy and lattice dynamical stability study of 2D ferromagnetic semiconductor $Cr_2Ge_2Te_6$ under high pressure", Journal of Alloys and Compounds **819** (2020).

[180] G. T. Lin, H. L. Zhuang, X. Luo, B. J. Liu, F. C. Chen, J. Yan, Y. Sun, J. Zhou, W. J. Lu, P. Tong, Z. G. Sheng, Z. Qu, W. H. Song, X. B. Zhu, and Y. P. Sun, "Tricritical behavior of the two-dimensional intrinsically ferromagnetic semiconductor $CrGeTe_3$", Physical Review B **95**, 245212 (2017).

[181] Y. Tian, M. J. Gray, H. Ji, R. J. Cava, and K. S. Burch, "Magneto-elastic coupling in a potential ferromagnetic 2D atomic crystal", 2D Materials **3**, 025035 (2016).

[182] X. Zhang, Y. Zhao, Q. Song, S. Jia, J. Shi, and W. Han, "Magnetic anisotropy of the single-crystalline ferromagnetic insulator $Cr_2Ge_2Te_6$", Japanese Journal of Applied Physics **55**, 033001 (2016).

[183] Z. Lin, M. Lohmann, Z. A. Ali, C. Tang, J. Li, W. Xing, J. Zhong, S. Jia, W. Han, S. Coh, W. Beyermann, and J. Shi, "Pressure-induced spin reorientation transition in layered ferromagnetic insulator $Cr_2Ge_2Te_6$", Physical Review Materials **2**, 051004(R) (2018).

[184] Y. F. Li, W. Wang, W. Guo, C. Y. Gu, H. Y. Sun, L. He, J. Zhou, Z. B. Gu, Y. F. Nie, and X. Q. Pan, "Electronic structure of ferromagnetic semiconductor $CrGeTe_3$ by angle-resolved photoemission spectroscopy", Physical Review B **98**, 1–6 (2018).

[185] H. Ji, R. A. Stokes, L. D. Alegria, E. C. Blomberg, M. A. Tanatar, A. Reijnders, L. M. Schoop, T. Liang, R Prozorov, K. S. Burch, N. P. Ong, J. R. Petta, and R. J. Cava, "A ferromagnetic insulating substrate for the epitaxial growth of topological insulators Large anomalous Hall effect in ferromagnetic insulator-topological insulator heterostructures A ferromagnetic insulating substrate for the epitaxial growth of topologi", Journal of Applied Physics **114**, 114907 (2013).

[186] Z. Hao, H. Li, S. Zhang, X. Li, G. Lin, X. Luo, Y. Sun, Z. Liu, and Y. Wang, "Atomic scale electronic structure of the ferromagnetic semiconductor $Cr_2Ge_2Te_6$", Science Bulletin **63**, 825–830 (2018).

[187] Y. Sun, R. C. Xiao, G. T. Lin, R. R. Zhang, L. S. Ling, Z. W. Ma, X. Luo, W. J. Lu, Y. P. Sun, and Z. G. Sheng, "Effects of hydrostatic pressure on spin-lattice coupling in two-dimensional ferromagnetic $Cr_2Ge_2Te_6$", Applied Physics Letters **112** (2018).

[188] M. Mogi, A. Tsukazaki, Y. Kaneko, R. Yoshimi, K. S. Takahashi, M. Kawasaki, and Y. Tokura, "Ferromagnetic insulator $Cr_2Ge_2Te_6$thin films with perpendicular remanence", APL Materials **6**, 091104 (2018).

[189] R. Zhang and R. F. Willis, "Thickness-dependent curie temperatures of ultrathin magnetic films: Effect of the range of spin-spin interactions", Physical Review Letters **86**, 2665–2668 (2001).

[190] G. Menichetti, M. Calandra, and M. Polini, "Electronic structure and magnetic properties of few-layer $Cr_2Ge_2Te_6$: The key role of nonlocal electron-electron interaction effects", 2D Materials **6**, 045042 (2019).

[191] L. C. Peng, Y. Zhang, S. L. Zuo, M. He, J. W. Cai, S. G. Wang, H. X. Wei, J. Q. Li, T. Y. Zhao, and B. G. Shen, "Lorentz transmission electron microscopy studies on topological magnetic domains", Chinese Physics B **27**, 066802 (2018).

[192] M. G. Han, J. A. Garlow, Y. Liu, H. Zhang, J. Li, D. Dimarzio, M. W. Knight, C. Petrovic, D. Jariwala, and Y. Zhu, "Topological Magnetic-Spin Textures in Two-Dimensional van der Waals $Cr_2Ge_2Te_6$", Nano Letters **19**, 7859–7865 (2019).

[193] B. Ding, Z. Li, G. Xu, H. Li, Z. Hou, E. Liu, X. Xi, F. Xu, Y. Yao, and W. Wang, "Observation of Magnetic Skyrmion Bubbles in a van der Waals Ferromagnet Fe_3GeTe_2", Nano Letters **20**, 868–873 (2020).

[194] M Yang, Q Li, R. V. Chopdekar, R Dhall, J Turner, J. D. Carlström, C Ophus, C Klewe, P Shafer, A. T. N. Diaye, J. W. Choi, G Chen, Y. Z. Wu, C Hwang, F Wang, and Z. Q. Qiu, "Creation of skyrmions in van der Waals ferromagnet Fe_3GeTe_2 on (Co/Pd)n superlattice", Science Advances **6**, eabb5157 (2020).

[195] E. Dong, B. Liu, Q. Dong, X. Shi, X. Ma, R. Liu, X. Zhu, X. Luo, X. Li, Y. Li, Q. Li, and B. Liu, "Effects of pressure on the structure and properties of layered ferromagnetic $Cr_2Ge_2Te_6$", Physica B: Condensed Matter **595**, 412344 (2020).

[196] Z. Yu, W. Xia, K. Xu, M. Xu, H. Wang, X. Wang, N. Yu, Z. Zou, J. Zhao, L. Wang, X. Miao, and Y. Guo, "Pressure-Induced Structural Phase Transition and a Special Amorphization Phase of Two-Dimensional Ferromagnetic Semiconductor $Cr_2Ge_2Te_6$", Journal of Physical Chemistry C **123**, 13885–13891 (2019).

[197] J. Wang and S.-C. Zhang, "Topological states of condensed matter", Nature Materials **16**, 1062–1067 (2017).

[198] Q. L. He, L. Pan, A. L. Stern, E. C. Burks, X. Che, G. Yin, J. Wang, B. Lian, Q. Zhou, E. S. Choi, K. Murata, X. Kou, Z. Chen, T. Nie, Q. Shao, Y. Fan, S. C. Zhang, K. Liu, J. Xia, and K. L. Wang, "Chiral Majorana fermion modes in a quantum anomalous Hall insulator-superconductor structure", Science **357**, 294–299 (2017).

[199] Z. Qiao, W. Ren, H. Chen, L. Bellaiche, Z. Zhang, A. H. MacDonald, and Q. Niu, "Quantum anomalous Hall effect in graphene proximity coupled to an antiferromagnetic insulator", Physical Review Letters **112**, 116404 (2014).

[200] Z. Qiao, S. a. Yang, W. Feng, W.-K. Tse, J. Ding, Y. Yao, J. Wang, and Q. Niu, "Quantum Anomalous Hall Effect in Graphene from Rashba and Exchange Effects", Physical Review B **82**, 161414 (2010).

[201] H. X. Yang, A Hallal, D Terrade, X Waintal, S Roche, and M Chshiev, "Proximity Effects Induced in Graphene by Magnetic Insulators : First-Principles Calculations on Spin Filtering and Exchange-Splitting Gaps", Physical Review Letters **110**, 046603 (2013).

[202] A. Hallal, F. Ibrahim, H. Yang, S. Roche, and M. Chshiev, "Tailoring magnetic insulator proximity effects in graphene: first-principles calculations", 2D Materials **4**, 025074 (2017).

[203] P. K. Muduli, M. Kimata, Y. Omori, T. Wakamura, S. P. Dash, and Y. Otani, "Detection of the interfacial exchange field at a ferromagnetic insulator-nonmagnetic metal interface with pure spin currents", Physical Review B **98**, 024416 (2018).

[204] M. Piquemal-Banci, R. Galceran, S. M. Dubois, V. Zatko, M. Galbiati, F. Godel, M. B. Martin, R. S. Weatherup, F. Petroff, A. Fert, J. C. Charlier, J. Robertson, S. Hofmann, B. Dlubak, and P. Seneor, "Spin filtering by proximity effects at hybridized interfaces in spin-valves with 2D graphene barriers", Nature Communications **11**, 5670 (2020).

[205] J. B. Mendes, O. Alves Santos, L. M. Meireles, R. G. Lacerda, L. H. Vilela-Leão, F. L. Machado, R. L. Rodríguez-Suárez, A. Azevedo, and S. M. Rezende, "Spin-Current to Charge-Current Conversion and Magnetoresistance in a Hybrid Structure of Graphene and Yttrium Iron Garnet", Physical Review Letters **115**, 226601 (2015).

[206] J. Zhang, B. Zhao, Y. Yao, and Z. Yang, "Robust quantum anomalous Hall effect in graphene-based van der Waals heterostructures", Physical Review B **92**, 165418 (2015).

[207] K. Zollner, M. Gmitra, and J. Fabian, "Electrically tunable exchange splitting in bilayer graphene on monolayer $Cr_2X_2Te_6$ with X = Ge, Si, and Sn", New J. Phys. **20**, 073007 (2018).

[208] J. Zhang, B. Zhao, T. Zhou, Y. Xue, C. Ma, and Z. Yang, "Strong magnetization and Chern insulators in compressed graphene/CrI_3 van der Waals heterostructures", Physical Review B **97**, 085401 (2018).

[209] M. U. Farooq and J. Hong, "Switchable valley splitting by external electric field effect in graphene/CrI_3 heterostructures", npj 2D Materials and Applications **3**, 3 (2019).

[210] A. W. Cummings, "Probing magnetism via spin dynamics in graphene/2D-ferromagnet heterostructures", Journal of Physics: Materials **2**, 045007 (2019).

[211] Z. Wang et al., "Electric-field control of magnetism in a few-layered van der Waals ferromagnetic semiconductor", Nature Nanotechnology **13**, 554–559 (2018).

[212] E. L. Hahn and A. Abragam, *Pulsed Magnetic Resonance: NMR, ESR, and Optics*, Clarendon (Clarendon, New York, 1992), p. 550.

[213] J. Fabian, A. Matos-Abiaguea, C. Ertlera, P. Stano, and I. Zutic, "Semiconductor Spintronics", Acta Phys. Slovaca **57**, 565–907 (2007).

[214] L. D. Alegria, H Ji, N Yao, J. J. Clarke, R. J. Cava, and J. R. Petta, "Large anomalous Hall effect in ferromagnetic insulator-topological insulator heterostructures", Applied Physics Letters **105**, 053512 (2014).

[215] F. Katmis, V. Lauter, F. S. Nogueira, B. A. Assaf, M. E. Jamer, P. Wei, B. Satpati, J. W. Freeland, I. Eremin, D. Heiman, P. Jarillo-Herrero, and J. S. Moodera, "A high-temperature ferromagnetic topological insulating phase by proximity coupling", Nature **533**, 513–516 (2016).

[216] H. Idzuchi, A. E. Llacsahuanga Allcca, X. C. Pan, K. Tanigaki, and Y. P. Chen, "Increased Curie temperature and enhanced perpendicular magneto anisotropy of $Cr_2Ge_2Te_6$/NiO heterostructures", Applied Physics Letters **115**, 232403 (2019).

[217] L. Zhang, X. Huang, H. Dai, M. Wang, H. Cheng, L. Tong, Z. Li, X. Han, X. Wang, L. Ye, and J. Han, "Proximity-Coupling-Induced Significant Enhancement of Coercive Field and Curie Temperature in 2D van der Waals Heterostructures", Advanced Materials **32**, 2002032 (2020).

[218] Q. L. He et al., "Tailoring exchange couplings in magnetic topological-insulator/antiferromagnet heterostructures", Nature Materials **16**, 94–100 (2017).

[219] S. Ringer, S. Hartl, M. Rosenauer, T. Völkl, M. Kadur, F. Hopperdietzel, D. Weiss, and J. Eroms, "Measuring anisotropic spin relaxation in graphene", Physical Review B **97**, 205439 (2018).

[220] B. Raes, J. E. Scheerder, M. V. Costache, F. Bonell, J. F. Sierra, J. Cuppens, J. Van de Vondel, and S. O. Valenzuela, "Determination of the spin-lifetime anisotropy in graphene using oblique spin precession", Nature Communications **7**, 11444 (2016).

[221] A. W. Cummings, J. H. Garcia, J. Fabian, and S. Roche, "Giant Spin Lifetime Anisotropy in Graphene Induced by Proximity Effects", Physical Review Letters **119**, 206601 (2017).

[222] J. H. Garcia, M. Vila, A. W. Cummings, and S. Roche, "Spin transport in graphene/transition metal dichalcogenide heterostructures", Chemical Society Review **47**, 3359–3379 (2018).

[223] C. Tan, W.-Q. Xie, G. Zheng, N. Aloufi, S. Albarakati, M. Algarni, J. Song, J. Partridge, D. Culcer, X. Wang, J. Yi, Y. Xiong, M. Tian, Y.-J. Zhao, and L. Wang, "Gate-controlled magnetic phase transition in a van der Waals magnet Fe_5GeTe_2", arXiv:2012.00891 (2020).

[224] B. C. Hen, J. Y. Ang, H. W. Ang, M. I. Mai, H. O. Hta, C. M. Ichioka, K. Y. Oshimura, and M. F. Ang, "Magnetic Properties of Layered Itinerant Electron Ferromagnet Fe_3GeTe_2", Journal of the Physical Society of Japan **82**, 124711 (2013).

[225] A. F. May, C. A. Bridges, and M. A. McGuire, "Physical properties and thermal stability of $Fe_{5-x}GeTe_2$ single crystals", Physical Review Materials **3**, 104401 (2019).

[226] P. R. Jothi, J. P. Scheifers, Y. Zhang, M. Alghamdi, D. Stekovic, M. E. Itkis, J. Shi, and B. P. Fokwa, "$Fe_{5-x}Ge_2Te_2$ - a New Exfoliable Itinerant Ferromagnet with High Curie Temperature and Large Perpendicular Magnetic Anisotropy", Physica Status Solidi - Rapid Research Letters **14**, 1900666 (2020).

[227] H.-J. Deiseroth, K. Aleksandrov, C. Reiner, L. Kienle, and R. K. Kremer, "Fe_3GeTe_2 and Ni_3GeTe_2 - Two New Layered Transition-Metal Compounds: Crystal Structures, HRTEM Investigations, and Magnetic and Electrical Properties", European Journal of Inorganic Chemistry **2006**, 1561–1567 (2006).

[228] A. Milosavljević, A. Šolajić, S. Djurdjić-Mijin, J. Pešić, B. Višić, Y. Liu, C. Petrovic, N. Lazarević, and Z. V. Popović, "Lattice dynamics and phase transitions in $Fe_{3-x}GeTe_2$", Physical Review B **99**, 214304 (2019).

[229] A. M. Ziqan, A. F. Qasrawi, A. H. Mohammad, and N. M. Gasanly, "Thermally assisted variable range hopping in Tl_4S_3Se crystal", Bulletin of Materials Science **38**, 593–598 (2015).

[230] S. Liu, X. Yuan, Y. Zou, Y. Sheng, C. Huang, E. Zhang, J. Ling, Y. Liu, W. Wang, C. Zhang, J. Zou, K. Wang, and F. Xiu, "Wafer-scale two-dimensional ferromagnetic Fe_3GeTe_2 thin films grown by molecular beam epitaxy", npj 2D Materials and Applications **1**, 30 (2017).

[231] C. Tan, J. Lee, S.-G. Jung, T. Park, S. Albarakati, J. Partridge, M. Field, D. McCulloch, L. Wang, and C. Lee, "Hard magnetic properties in nanoflake van der Waals Fe_3GeTe_2", Nature Communications **9**, 1554 (2018).

[232] A. Roy, H. C. P. Movva, B. Satpati, K. Kim, R. Dey, A. Rai, T. Pramanik, S. Guchhait, E. Tutuc, and S. K. Banerjee, "Structural and Electrical Properties of $MoTe_2$ and $MoSe_2$ Grown by Molecular Beam Epitaxy", Applied Materials & Interfaces **8**, 7396–7402 (2016).

[233] L. Bao, W. Wang, N. Meyer, Y. Liu, C. Zhang, K. Wang, P. Ai, and F. Xiu, "Quantum Corrections Crossover and Ferromagnetism in Magnetic Topological Insulators", Scientific reports **3**, 2391 (2013).

[234] A. Arrott, "Criterion for Ferromagnetism from Observations of Magnetic Isotherias", Physical Review **108**, 1394 (1957).

[235] H. Ohno, D. Chiba, F. Matsukura, T. Omiya, E. Abe, T. Dietl, Y. Ohno, and K. Ohtani, "Electric-field control of ferromagnetism", Nature **408**, 944 (2000).

[236] I Stolichnov, S. W. E. Riester, H. J. Trodahl, N Setter, A. W. Rushforth, K. W. Edmonds, R. P. Campion, C. T. Foxon, B. L. Gallagher, and T Jungwirth, "Non-volatile ferroelectric control of ferromagnetism in (Ga, Mn)As", Nature materials **7**, 464 (2008).

[237] Y. Liu, V. N. Ivanovski, and C. Petrovic, "Critical behavior of the van der Waals bonded ferromagnet $Fe_{3-x}GeTe_2$", Physical Review B **96**, 144429 (2017).

[238] Z. Li, W. Xia, H. Su, Z. Yu, Y. Fu, L. Chen, X. Wang, N. Yu, Z. Zou, and Y. Guo, "Magnetic critical behavior of the van der Waals Fe_5GeTe_2 crystal with near room temperature ferromagnetism", Scientific Reports **10**, 15345 (2020).

[239] E. Stoner and E. P. Wohlfarth, "A mechanism of magnetic hysteresis in heterogeneous alloys", IEEE Transactions on Magnetics **27**, 3475 (1991).

[240] J Zeisner, A Alfonsov, S Selter, S Aswartham, M. P. Ghimire, M Richter, J. V. D. Brink, B Büchner, and V Kataev, "Magnetic anisotropy and spin-polarized two-dimensional electron gas in the van der Waals ferromagnet $Cr_2Ge_2Te_6$", Phys. Rev. B **99**, 165109 (2019).

[241] C. Tian, F. Pan, S. Xu, K. Ai, T. Xia, and P. Cheng, "Tunable magnetic properties in van der Waals crystals $(Fe_{1-x}Co_x)_5GeTe_2$", Applied Physics Letters **116**, 202402 (2020).

[242] H. Zhang, R. Chen, K. Zhai, X. Chen, L. Caretta, X. Huang, R. V. Chopdekar, J. Cao, J. Sun, J. Yao, R. Birgeneau, and R. Ramesh, "Itinerant ferromagnetism in van der Waals $Fe_{5-x}GeTe_2$ crystals above room temperature", Physical Review B **102**, 064417 (2020).

[243] T. Ohta, K. Sakai, H. Taniguchi, B. Driesen, Y. Okada, K. Kobayashi, and Y. Niimi, "Enhancement of coercive field in atomically-thin quenched Fe_5GeTe_2", Applied Physics Express **13**, 043005 (2020).

[244] "Tuning magnetic order in the van der Waals metal Fe_5GeTe_2 by cobalt substitution", Physical Review Materials **4**, 074008 (2020).

[245] G. Kimbell, P. M. Sass, B. Woltjes, E. K. Ko, T. W. Noh, W. Wu, and J. W. Robinson, "Two-channel anomalous Hall effect in $SrRuO_3$", Physical Review Materials **4**, 54414 (2020).

[246] P. Chongthanaphisut, S. K. Bac, S. Choi, K. J. Lee, J. Chang, S. Choi, S. Lee, M. Nnaji, X. Liu, M. Dobrowolska, and J. K. Furdyna, "Interlayer exchange coupling in ferromagnetic semiconductor trilayers with out-of-plane magnetic anisotropy", Scientific Reports **9**, 4740 (2019).

[247] D. A. Christian, K. S. Novoselov, and A. K. Geim, "Barkhausen statistics from a single domain wall in thin films studied with ballistic Hall magnetometry", Physical Review B **74**, 064403 (2006).

[248] M Kim, P Kumaravadivel, J Birkbeck, W Kuang, S. G. Xu, D. G. Hopkinson, J Knolle, P. A. Mcclarty, A. I. Berdyugin, M. B. Shalom, R. V. Gorbachev, S. J. Haigh, S Liu, J. H. Edgar, K. S. Novoselov, I. V. Grigorieva, and A. K. Geim, "Micromagnetometry of two-dimensional ferromagnets", Nature Electronics **2**, 457–463 (2019).

[249] A. Hirohata, K. Yamada, Y. Nakatani, L. Prejbeanu, B. Diény, P. Pirro, and B. Hillebrands, "Review on spintronics: Principles and device applications", Journal of Magnetism and Magnetic Materials **509**, 166711 (2020).

[250] M. Cosset-Chéneau, L. Vila, G. Zahnd, D. Gusakova, V. T. Pham, C. Grèzes, X. Waintal, A. Marty, H. Jaffrès, and J. P. Attané, "Measurement of the Spin Absorption Anisotropy in Lateral Spin Valves", Physical Review Letters **126**, 027201 (2021).

[251] A. Soluyanov, D. Gresch, Z. Wang, Q. Wu, M. Troyer, X. Dai, and B. A. Bernevig, "Type-II Weyl semimetals", Nature **527**, 495–498 (2015).

[252] L. Wang, I. Gutiérrez-lezama, C. Barreteau, N. Ubrig, E. Giannini, and A. F. Morpurgo, "Tuning Magnetotransport in a Compensated Semimetal at the Atomic Scale", Nature Communications **6**, 8892 (2015).

[253] X.-c. Pan, X. Wang, F. Song, and B. Wang, "The study on quantum material WTe_2", Advances in Physics: X **3**, 1468279 (2018).

[254] B. E. Brown, "The crystal structures of WTe_2 and high-temperature $MoTe_2$", Acta Crystallographica **20**, 268–274 (1966).

[255] S. Tang et al., "Quantum spin Hall state in monolayer 1T' -WTe_2", Nature Physics **13**, 683–688 (2017).

[256] P. Li, Y. Wen, X. He, Q. Zhang, C. Xia, Z.-m. Yu, Z. Zhu, H. N. Alshareef, and X.-x. Zhang, "Evidence for topological type-II Weyl semimetal WTe_2", Nature Communications **8**, 2150 (2017).

[257] Y. Wu, D. Mou, N. H. Jo, K. Sun, L. Huang, S. L. Bud, P. C. Canfield, and A. Kaminski, "Observation of Fermi arcs in the type-II Weyl semimetal candidate WTe_2", Physical Review B **94**, 121113(R) (2016).

[258] C. Wang et al., "Observation of Fermi arc and its connection with bulk states in the candidate type-II Weyl semimetal WTe_2", Physical Review B **94**, 241119(R) (2016).

[259] P. Gr, "Surface Fermi arc connectivity in the type-II Weyl semimetal candidate WTe_2", Physical Review B **94**, 161401(R) (2016).

[260] F. Y. Bruno, A Tamai, Q. S. Wu, I Cucchi, C Barreteau, A. D. Torre, S. M. Walker, S Ricc, Z Wang, T. K. Kim, M. Hoesch, M. Shi, N. C. Plumb, E. Giannini, A. A. Soluyanov, and F. Baumberger, "Observation of large topologically trivial Fermi arcs in the candidate type-II Weyl semimetal WTe_2", Physical Review B **94**, 121112(R) (2016).

[261] B. Q. Lv, S Muff, T Qian, Z. D. Song, S. M. Nie, N Xu, P Richard, C. E. Matt, N. C. Plumb, L. X. Zhao, G. F. Chen, Z Fang, X Dai, J. H. Dil, J Mesot, M Shi, H. M. Weng, and H. Ding, "Observation of Fermi-Arc Spin Texture in TaAs", Physical Review Letters **115**, 217601 (2015).

[262] Z. Zhu, X. Lin, J. Liu, B. Fauqué, Q. Tao, C. Yang, Y. Shi, and K. Behnia, "Quantum Oscillations , Thermoelectric Coefficients , and the Fermi Surface of Semimetallic WTe_2", Physical Review Letters **114**, 176601 (2015).

[263] A Kononov, O. O. Shvetsov, A. V. Timonina, N. N. Kolesnikov, and E. V. Deviatov, "Spin Wave Effects in Transport between a Ferromagnet and a Weyl Semimetal Surface", JETP Letters **109**, 180–184 (2019).

[264] B. Zhao, D. Khokhriakov, Y. Zhang, H. Fu, B. Karpiak, A. Hoque, X. Xu, Y. Jiang, B. Yan, and S. P. Dash, "Observation of charge to spin conversion in Weyl semimetal WTe_2 at room temperature", Physical Review Research **2**, 013286 (2020).

[265] D Rhodes, S Das, Q. R. Zhang, B Zeng, N. R. Pradhan, N Kikugawa, E Manousakis, and L Balicas, "Role of spin-orbit coupling and evolution of the electronic structure of WTe_2 under an external magnetic field", Physical Review B **92**, 125152 (2015).

[266] J Andzane, G Kunakova, S Charpentier, V Hrkac, L Kienle, M Baitimirova, T Bauch, F Lombardi, and D Erts, "Catalyst-free vapour-solid technique for deposition of Bi_2Te_3 and Bi_2Se_3 nanowires/nanobelts with topological insulator properties", Nanoscale **7**, 15935–44 (2015).

[267] F. Xiu, L. He, Y. Wang, L. Cheng, L. T. Chang, M. Lang, G. Huang, X. Kou, Y. Zhou, X. Jiang, Z. Chen, J. Zou, A. Shailos, and K. L. Wang, "Manipulating surface states in topological insulator nanoribbons", Nature Nanotechnology **6**, 216–221 (2011).

[268] L. R. Thoutam, Y. L. Wang, Z. L. Xiao, S Das, R Divan, G. W. Crabtree, and W. K. Kwok, "Temperature-Dependent Three-Dimensional Anisotropy of the Magnetoresistance in WTe_2", Physical Review Letters **115**, 046602 (2015).

[269] W.-D. Kong, S.-F. Wu, P. Richard, C.-S. Lian, J.-T Wang, C.-L. Yang, Y.-G. Shi, and H. Ding, "Raman scattering investigation of large positive magnetoresistance material WTe_2", Applied Physics Letters **106**, 081906 (2015).

[270] Y. Wu, N. H. Jo, M. Ochi, L. Huang, D. Mou, S. L. Bud'Ko, P. Canfield, N. Trivedi, R. Arita, and A. Kaminski, "Temperature-Induced Lifshitz Transition in WTe_2", Physical Review Letters **115**, 166602 (2015).

[271] L. Wang, I. Gutiérrez-lezama, C. Barreteau, D.-k. Ki, E. Giannini, and A. F. Morpurgo, "Direct Observation of a Long-Range Field Effect from Gate Tuning of Nonlocal Conductivity", Physical Review Letters **117**, 176601 (2016).

[272] B. Feng, Y. H. Chan, Y. Feng, R. Y. Liu, M. Y. Chou, K. Kuroda, K. Yaji, A. Harasawa, P. Moras, A. Barinov, W. Malaeb, C. Bareille, T. Kondo, S. Shin, F. Komori, T. C. Chiang, Y. Shi, and I. Matsuda, "Spin texture in type-II Weyl semimetal WTe_2", Physical Review B **94**, 195134 (2016).

[273] P. K. Das, D. Di Sante, I. Vobornik, J. Fujii, T. Okuda, E. Bruyer, A. Gyenis, B. E. Feldman, J. Tao, R. Ciancio, G. Rossi, M. N. Ali, S. Picozzi, A. Yadzani, G. Panaccione, and R. J. Cava, "Layer-dependent quantum cooperation of electron and hole states in the anomalous semimetal WTe_2", Nature Communications **7**, 10847 (2016).

[274] A. Johansson, J. Henk, and I. Mertig, "Edelstein effect in Weyl semimetals", Physical Review B **97**, 085417 (2018).

[275] D. Culcer and R. Winkler, "Generation of spin currents and spin densities in systems with reduced symmetry", Physical Review Letters **99**, 226601 (2007).

[276] K. Vaklinova, A. Hoyer, M. Burghard, and K. Kern, "Current-Induced Spin Polarization in Topological Insulator-Graphene Heterostructures", Nano Letters **16**, 2595–2602 (2016).

[277] J. A. Voerman, C. Li, Y. Huang, and A. Brinkman, "Spin-Momentum Locking in the Gate Tunable Topological Insulator $BiSbTeSe_2$ in Non-Local Transport Measurements", Advanced Electronic Materials **5**, 1900334 (2019).

[278] A. M. Hoque, D. Khokhriakov, B. Karpiak, and S. P. Dash, "All-electrical creation and control of giant spin-galvanic effect in $1T'$-$MoTe_2$/graphene heterostructures at room temperature", arXiv:1908.09367 (2019).

[279] L. Li, J. Zhang, G. Myeong, W. Shin, H. Lim, B. Kim, S. Kim, T. Jin, S. Cavill, B. S. Kim, C. Kim, J. Lischner, A. Ferreira, and S. Cho, "Gate-Tunable Reversible Rashba-Edelstein Effect in a Few-Layer Graphene/2H-TaS_2 Heterostructure at Room Temperature", ACS Nano **14**, 5251–5259 (2020).

[280] T. S. Ghiasi, A. A. Kaverzin, P. J. Blah, and B. J. Van Wees, "Charge-to-Spin Conversion by the Rashba-Edelstein Effect in Two-Dimensional van der Waals Heterostructures up to Room Temperature", Nano Letters **19**, 5959–5966 (2019).

[281] C. K. Safeer, J. Ingla-Aynés, F. Herling, J. H. Garcia, M. Vila, N. Ontoso, M. R. Calvo, S. Roche, L. E. Hueso, and F. Casanova, "Room-Temperature Spin Hall Effect in Graphene/MoS_2 van der Waals Heterostructures", Nano Letters **19**, 1074–1082 (2019).

[282] L. A. Benítez, W. Savero Torres, J. F. Sierra, M. Timmermans, J. H. Garcia, S. Roche, M. V. Costache, and S. O. Valenzuela, "Tunable room-temperature spin galvanic and spin Hall effects in van der Waals heterostructures", Nature Materials **19**, 170–175 (2020).

[283] M. H. Guimarães, G. M. Stiehl, D. MacNeill, N. D. Reynolds, and D. C. Ralph, "Spin-Orbit Torques in $NbSe_2$/Permalloy Bilayers", Nano Letters **18**, 1311–1316 (2018).

[284] C. K. Safeer, N. Ontoso, J. Ingla-Aynés, F. Herling, V. T. Pham, A. Kurzmann, K. Ensslin, A. Chuvilin, I. Robredo, M. G. Vergniory, F. De Juan, L. E. Hueso, M. R. Calvo, and F. Casanova, "Large Multidirectional Spin-to-Charge Conversion in Low-Symmetry Semimetal MoTe2 at Room Temperature", Nano Letters **19**, 8758–8766 (2019).

[285] G. N. Kamm, D. J. Gillespie, A. C. Ehrlich, T. J. Wieting, and F. Levy, "Fermi surface, effective masses, and Dingle temperatures of $ZrTe_5$ as derived from the Shubnikovde Haas effect", Physical Review B **31**, 7617–7623 (1985).

[286] S. Furuseth, L. Brattas, and A. Kjekshus, "The Crystal Structure of $HfTe_5$", Acta Chemica Scandinavica **27**, 2367–2374 (1973).

[287] T. E. Jones, W. W. Fuller, T. J. Wieting, and F. Levy, "Thermoelectric power of $HfTe_5$ and $ZrTe_5$", Solid State Communications **42**, 793–798 (1982).

[288] H. Weng, X. Dai, and Z. Fang, "Transition-metal pentatelluride $ZrTe_5$ and $HfTe_5$: A Paradigm for Large-Gap Quantum Spin Hall Insulators", Physical Review X **4**, 011002 (2014).

[289] Z. Fan, Q. F. Liang, Y. B. Chen, S. H. Yao, and J. Zhou, "Transition between strong and weak topological insulator in $ZrTe_5$ and $HfTe_5$", Scientific Reports **7**, 45667 (2017).

[290] Y. Choi, J. W. Villanova, and K. Park, "Zeeman-splitting-induced topological nodal structure and anomalous Hall conductivity in $ZrTe_5$", Physical Review B **101**, 035105 (2020).

[291] S. Sun, Z. Song, H. Weng, and X. Dai, "Topological metals induced by the Zeeman effect", Physical Review B **101**, 125118 (2020).

[292] Y. Liu, X. Yuan, C. Zhang, Z. Jin, A. Narayan, C. Luo, Z. Chen, L. Yang, J. Zou, X. Wu, S. Sanvito, Z. Xia, L. Li, Z. Wang, and F. Xiu, "Zeeman splitting and dynamical mass generation in Dirac semimetal $ZrTe_5$", Nature Communications **7**, 12516 (2016).

[293] J. Wang, J. Niu, B. Yan, X. Li, R. Bi, Y. Yao, D. Yu, and X. Wu, "Vanishing quantum oscillations in Dirac semimetal $ZrTe_5$", Proceedings of the National Academy of Sciences **115**, 9145–9150 (2018).

[294] X. Yuan, C. Zhang, Y. Liu, A. Narayan, C. Song, S. Shen, X. Sui, J. Xu, H. Yu, Z. An, J. Zhao, S. Sanvito, H. Yan, and F. Xiu, "Observation of quasi-two-dimensional Dirac fermions in $ZrTe_5$", NPG Asia Materials **8**, e325 (2016).

[295] Y. Jiang, J. Wang, T. Zhao, Z. L. Dun, Q. Huang, X. S. Wu, M. Mourigal, H. D. Zhou, W. Pan, M. Ozerov, D. Smirnov, and Z. Jiang, "Unraveling the Topological Phase of $ZrTe_5$ via Magnetoinfrared Spectroscopy", Physical Review Letters **125**, 046403 (2020).

[296] L. Moreschini, J. C. Johannsen, H. Berger, J. Denlinger, C. Jozwiack, E. Rotenberg, K. S. Kim, A. Bostwick, and M. Grioni, "Nature and topology of the low-energy states in $ZrTe_5$", Physical Review B **94**, 081101(R) (2016).

[297] H. Wang, H. Liu, Y. Li, Y. Liu, J. Wang, J. Liu, J. Dai, Y. Wang, L. Li, J. Yan, D. Mandrus, X. C. Xie, and J. Wang, "Discovery of log-periodic oscillations in ultra-quantum topological materials", Science Advances **4**, eaau5096 (2018).

[298] J. L. Zhang, C. Y. Guo, X. D. Zhu, L. Ma, G. L. Zheng, Y. Q. Wang, L. Pi, Y. Chen, H. Q. Yuan, and M. L. Tian, "Disruption of the Accidental Dirac Semimetal State in $ZrTe_5$ under Hydrostatic Pressure", Physical Review Letters **118**, 206601 (2017).

[299] Z. Sun, Z. Cao, J. Cui, C. Zhu, D. Ma, H. Wang, W. Zhuo, Z. Cheng, Z. Wang, X. Wan, and X. Chen, "Large Zeeman splitting induced anomalous Hall effect in $ZrTe_5$", npj Quantum Materials **5**, 36 (2020).

[300] J. Ge, D. Ma, Y. Liu, H. Wang, Y. Li, J. Luo, T. Luo, Y. Xing, J. Yan, D. Mandrus, H. Liu, X. C. Xie, and J. Wang, "Unconventional Hall effect induced by Berry curvature", National Science Review **7**, 1879–1885 (2020).

[301] R. Wu, J. Z. Ma, S. M. Nie, L. X. Zhao, X. Huang, J. X. Yin, B. B. Fu, P. Richard, G. F. Chen, Z. Fang, X. Dai, H. M. Weng, T. Qian, H. Ding, and S. H. Pan, "Evidence for topological edge states in a large energy gap near the step edges on the surface of $ZrTe_5$", Physical Review X **6**, 021017 (2016).

[302] Y. Jiang, Z. L. Dun, H. D. Zhou, Z. Lu, K. W. Chen, S. Moon, T. Besara, T. M. Siegrist, R. E. Baumbach, D. Smirnov, and Z. Jiang, "Landau-level spectroscopy of massive Dirac fermions in single-crystalline $ZrTe_5$ thin flakes", Physical Review B **96**, 041101(R) (2017).

[303] H. Xiong, J. A. Sobota, S. L. Yang, H. Soifer, A. Gauthier, M. H. Lu, Y. Y. Lv, S. H. Yao, D. Lu, M. Hashimoto, P. S. Kirchmann, Y. F. Chen, and Z. X. Shen, "Three-dimensional nature of the band structure of $ZrTe_5$ measured by high-momentum-resolution photoemission spectroscopy", Physical Review B **95**, 195119 (2017).

[304] X. B. Li, W. K. Huang, Y. Y. Lv, K. W. Zhang, C. L. Yang, B. B. Zhang, Y. B. Chen, S. H. Yao, J. Zhou, M. H. Lu, L. Sheng, S. C. Li, J. F. Jia, Q. K. Xue, Y. F. Chen, and D. Y. Xing, "Experimental Observation of Topological Edge States at the Surface Step Edge of the Topological Insulator $ZrTe_5$", Physical Review Letters **116**, 176803 (2016).

[305] J. L. Zhang, C. M. Wang, C. Y. Guo, X. D. Zhu, Y. Zhang, J. Y. Yang, Y. Q. Wang, Z. Qu, L. Pi, H. Z. Lu, and M. L. Tian, "Anomalous Thermoelectric Effects of $ZrTe_5$ in and beyond the Quantum Limit", Physical Review Letters **123**, 196602 (2019).

[306] L. Luo, D. Cheng, B. Song, L. L. Wang, C. Vaswani, P. M. Lozano, G. Gu, C. Huang, R. H. Kim, Z. Liu, J. M. Park, Y. Yao, K. Ho, I. E. Perakis, Q. Li, and J. Wang, "A light-induced phononic symmetry switch and giant dissipationless topological photocurrent in $ZrTe_5$", Nature Materials (2021).

[307] W. Wang, X. Zhang, H. Xu, Y. Zhao, W. Zou, L. He, and Y. Xu, "Evidence for Layered Quantized Transport in Dirac Semimetal $ZrTe_5$", Scientific Reports **8**, 5125 (2018).

[308] Q. Li, D. E. Kharzeev, C. Zhang, Y. Huang, I. Pletikosić, A. V. Fedorov, R. D. Zhong, J. A. Schneeloch, G. D. Gu, and T. Valla, "Chiral magnetic effect in ZrTe 5", Nature Physics **12**, 550–554 (2016).

[309] A. Pariari and P. Mandal, "Coexistence of topological Dirac fermions on the surface and three-dimensional Dirac cone state in the bulk of $ZrTe_5$ single crystal", Scientific Reports **7**, 40327 (2017).

[310] J. Niu, J. Wang, Z. He, C. Zhang, X. Li, T. Cai, X. Ma, S. Jia, D. Yu, and X. Wu, "Electrical transport in nanothick $ZrTe_5$ sheets: From three to two dimensions", Physical Review B **95**, 035420 (2017).

[311] H. Chi, C. Zhang, G. Gu, D. E. Kharzeev, X. Dai, and Q. Li, "Lifshitz transition mediated electronic transport anomaly in bulk $ZrTe_5$", New J. Phys. **19**, 015005 (2017).

[312] G. Zheng, J. Lu, X. Zhu, W. Ning, Y. Han, H. Zhang, J. Zhang, C. Xi, J. Yang, H. Du, K. Yang, Y. Zhang, and M. Tian, "Transport evidence for the three-dimensional Dirac semimetal phase in $ZrTe_5$", Physical Review B **93**, 115414 (2016).

[313] W. Yu, Y. Jiang, J. Yang, Z. L. Dun, H. D. Zhou, Z. Jiang, P. Lu, and W. Pan, "Quantum Oscillations at Integer and Fractional Landau Level Indices in Single-Crystalline $ZrTe_5$", Scientific Reports **6**, 35357 (2016).

[314] G. Manzoni, A. Crepaldi, G. Autès, A. Sterzi, F. Cilento, A. Akrap, I. Vobornik, L. Gragnaniello, P. Bugnon, M. Fonin, H. Berger, M. Zacchigna, O. V. Yazyev, and F. Parmigiani, "Temperature dependent non-monotonic bands shift in $ZrTe_5$", Journal of Electron Spectroscopy and Related Phenomena **219**, 9–15 (2017).

[315] G. Manzoni, A. Sterzi, A. Crepaldi, M. Diego, F. Cilento, M. Zacchigna, P. Bugnon, H. Berger, A. Magrez, M. Grioni, and F. Parmigiani, "Ultrafast Optical Control of the Electronic Properties of $ZrTe_5$", Physical Review Letters **115**, 207402 (2015).

[316] T. M. Tritt, N. D. Lowhorn, R. T. Littleton, A. Pope, C. R. Feger, and J. W. Kolis, "Large enhancement of the resistive anomaly in the pentatelluride materials $HfTe_5$ and $ZrTe_5$ with applied magnetic field", Physical Review B **60**, 7816–7819 (1999).

[317] G. Qiu, Y. Du, A. Charnas, H. Zhou, S. Jin, Z. Luo, D. Y. Zemlyanov, X. Xu, G. J. Cheng, and P. D. Ye, "Observation of Optical and Electrical In-Plane Anisotropy in High-Mobility Few-Layer $ZrTe_5$", Nano Letters **16**, 7364–7369 (2016).

[318] P. Shahi, D. J. Singh, J. P. Sun, L. X. Zhao, G. F. Chen, Y. Y. Lv, J. Li, J. Q. Yan, D. G. Mandrus, and J. G. Cheng, "Bipolar Conduction as the Possible Origin of the Electronic Transition in Pentatellurides: Metallic vs Semiconducting Behavior", Physical Review X **8**, 021055 (2018).

[319] B. Fu, H. W. Wang, and S. Q. Shen, "Dirac Polarons and Resistivity Anomaly in $ZrTe_5$ and $HfTe_5$", Physical Review Letters **125**, 256601 (2020).

[320] I. M. Lifshitz, "Anomalies of electron characteristics of a metal in the high pressure region", Soviet Physics JETP **11**, 1130–1135 (1960).

[321] G. E. Volovik, "Topological Lifshitz transitions", Low Temperature Physics **43**, 47–55 (2017).

[322] P. Zhang, R. Noguchi, K. Kuroda, C. Lin, K. Kawaguchi, K. Yaji, A. Harasawa, M. Lippmaa, S. Nie, H. Weng, V. Kandyba, A. Giampietri, A. Barinov, Q. Li, G. D. Gu, S. Shin, and T. Kondo, "Observation and control of the weak topological insulator state in $ZrTe_5$", Nature Communications **12**, 406 (2021).

[323] G. Manzoni, L. Gragnaniello, G. Autès, T. Kuhn, A. Sterzi, F. Cilento, M. Zacchigna, V. Enenkel, I. Vobornik, L. Barba, F. Bisti, P. Bugnon, A. Magrez, V. N. Strocov, H. Berger, O. V. Yazyev, M. Fonin, F. Parmigiani, and A. Crepaldi, "Evidence for a Strong Topological Insulator Phase in $ZrTe_5$", Physical Review Letters **117**, 237601 (2016).

[324] R. Y. Chen, S. J. Zhang, J. A. Schneeloch, C. Zhang, Q. Li, G. D. Gu, and N. L. Wang, "Optical spectroscopy study of the three-dimensional Dirac semimetal $ZrTe_5$", Physical Review B **92**, 075107 (2015).

[325] E. Martino, I. Crassee, G. Eguchi, D. Santos-Cottin, R. D. Zhong, G. D. Gu, H. Berger, Z. Rukelj, M. Orlita, C. C. Homes, and A. Akrap, "Two-Dimensional Conical Dispersion in $ZrTe_5$ Evidenced by Optical Spectroscopy", Physical Review Letters **122**, 217402 (2019).

[326] Y. Zhou, J. Wu, W. Ning, N. Li, Y. Du, X. Chen, R. Zhang, Z. Chi, X. Wang, X. Zhu, P. Lu, C. Ji, X. Wan, Z. Yang, J. Sun, W. Yang, M. Tian, Y. Zhang, and H.-k. Mao, "Pressure-induced superconductivity in a three-dimensional topological material $ZrTe_5$", Proceedings of the National Academy of Sciences **113**, 2904–2909 (2016).

[327] Y. Liu, H. Wang, H. Fu, J. Ge, Y. Li, C. Xi, J. Zhang, J. Yan, D. Mandrus, B. Yan, and J. Wang, "Induced anomalous hall effect of massive dirac fermions in $ZrTe_5$ and $HfTe_5$ thin flakes", arXiv:2012.08188 (2020).

[328] A. A. Burkov, "Anomalous Hall Effect in Weyl Metals", Physical Review Letters **113**, 187202 (2014).

[329] R. Y. Chen, Z. G. Chen, X. Y. Song, J. A. Schneeloch, G. D. Gu, F. Wang, and N. L. Wang, "Magnetoinfrared Spectroscopy of Landau Levels and Zeeman Splitting of Three-Dimensional Massless Dirac Fermions in $ZrTe_5$", Physical Review Letters **115**, 176404 (2015).

[330] J. Mutch, X. Ma, C. Wang, P. Malinowski, J. Ayres-Sims, Q. Jiang, Z. Liu, D. Xiao, M. Yankowitz, and J.-H. Chu, "Abrupt switching of the anomalous Hall effect by field-rotation in nonmagnetic $ZrTe_5$", arXiv:2101.02681 (2021).

[331] W. Han, Y. Otani, and S. Maekawa, "Quantum materials for spin and charge conversion", npj Quantum Materials **3**, 7570 (2018).

[332] J. Sinova, S. O. Valenzuela, J. Wunderlich, C. H. Back, and T. Jungwirth, "Spin Hall effects", Reviews of Modern Physics **87**, 1213–1260 (2015).

[333] N. Nagaosa, J. Sinova, S. Onoda, A. MacDonald, and N. Ong, "Anomalous Hall effect", Reviews of Modern Physics **82**, 1539–1592 (2010).

[334] A. Dankert, "Spin Transport in Two-Dimensional Material Heterostructures", PhD thesis (Chalmers University of Technology, 2015).

Appended Papers

Paper I

Gate-tunable Hall sensors on large area CVD graphene protected by h-BN with 1D edge contacts

Bogdan Karpiak, André Dankert,[a] and Saroj P. Dash[b]
Department of Microtechnology and Nanoscience, Chalmers University of Technology, SE-41296 Göteborg, Sweden

(Received 25 January 2017; accepted 22 July 2017; published online 4 August 2017)

Graphene is an excellent material for Hall sensors due to its atomically thin structure, high carrier mobility, and low carrier density. However, graphene devices need to be protected from the environment for reliable and durable performance in different environmental conditions. Here we present magnetic Hall sensors fabricated on large area commercially available chemical vapor deposited (CVD) graphene protected by exfoliated hexagonal boron nitride (h-BN). To connect the graphene active regions of Hall samples to the outputs, 1D edge contacts were utilized which show reliable and stable electrical properties. The operation of the Hall sensors shows the current-related sensitivity up to 345 V/(AT). By changing the carrier concentration and type in graphene by the application of gate voltage, we are able to tune the Hall sensitivity. *Published by AIP Publishing.*
[http://dx.doi.org/10.1063/1.4997463]

I. INTRODUCTION

As our society becomes more integrated with information technology, sensors are getting increasingly important as can be seen from the consistent global market growth.[1] A variety of different sensors based on magnetic field sensing are used,[2] more than 50% of which[3] exploit the Hall effect for their operation. These are utilized in many fields such as healthcare, automotive, industry, and consumer electronics for a broad spectrum of applications including position sensing, current monitoring, proximity detection, and others.[2,4,5] Si is the most commonly used material in active regions of Hall sensors as the technology is highly mature with relatively low manufacturing costs and reasonable current-related sensitivities $S_I \sim 100$ V/(AT).[4–7] For better sensitivity, Hall sensors based on high mobility compound semiconductor heterostructures are used, but yield an increased production price.[8–11]

Fostered by the constant strive for performance improvements and market price reduction, new materials are being considered for utilization in Hall sensors. Graphene is a highly promising material for Hall sensing applications due to its beneficial properties such as low charge carrier concentration and high mobility. Recent experimental reports[12–16,24,25] have already proven the feasibility of graphene Hall sensors with current-related sensitivity more than 60 times higher than in silicon-based sensors.[13] Furthermore, graphene's 2D nature allows its application in flexible and transparent electronics.

However, the high-performance proof-of-concept devices demonstrated so far either use exfoliated graphene flakes,[13] are made of a manually selected single crystal CVD graphene area,[15] or the graphene active layer is not protected from external influences required for robust device operation.[12,14,16,17,25] To harness the advantages of industrially compatible large area CVD graphene in Hall sensors, it is necessary to protect the graphene layer for reliable device performance in different environmental conditions.

Here we report magnetic Hall elements fabricated on large area CVD graphene covered by h-BN for protection against the environmental influences to ensure reliable operation and long lifetime. The insulating and two-dimensional nature of the h-BN capping layer is expected to have a good interface with graphene, containing fewer dangling bonds and charge traps.[19] Our devices incorporate 1D edge contacts to graphene/h-BN heterostructures, which circumvent the effects related to contact-induced doping. These factors are crucial for reliable performance of graphene Hall sensors in an ambient environment.

II. RESULTS AND DISCUSSIONS

The Hall sensor devices were fabricated on commercially available CVD graphene after it was transferred on a Si/SiO_2 substrate (Graphenea[20]). The schematic illustration and an optical image of the investigated Hall samples are shown in Figs. 1(a) and 1(b), respectively. The microfabrication process steps are depicted in Fig. 1(c). The h-BN was exfoliated from the bulk crystal on top of CVD graphene by means of a regular scotch-tape method. Then the unprotected graphene regions were etched away with oxygen plasma. 1D edge contacts[21] were fabricated by means of electron beam lithography and electron beam evaporation of metals (1 nm TiO_2/65 nm Co) followed by liftoff in acetone/isopropyl alcohol.

Figure 2 shows the characterization of the graphene/h-BN heterostructure and 1D edge contacts to graphene. The Raman spectra of CVD graphene and the graphene/h-BN heterostructure[22,23] are shown in Figs. 2(a) and 2(b), respectively. The absence of a band splitting of the 2D peak and its higher intensity compared to the G peak indicate that the graphene in the heterostructure is monolayer.[22] The CVD

[a]Electronic mail: andre.dankert@chalmers.se
[b]Electronic mail: saroj.dash@chalmers.se

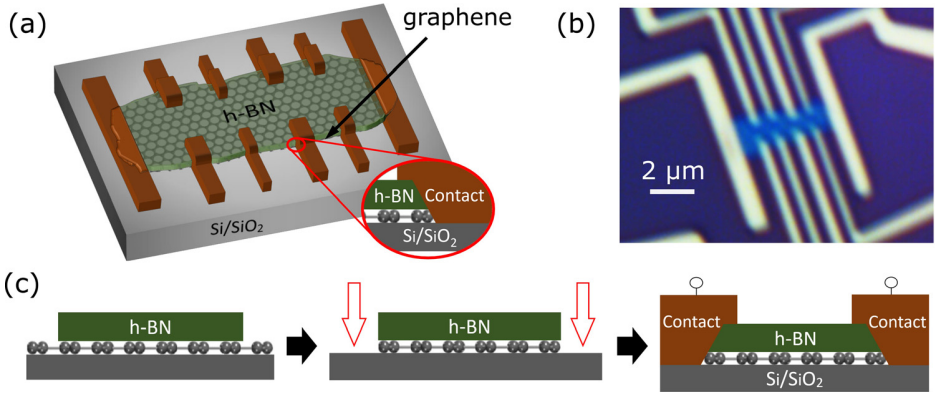

FIG. 1. Hall sensor fabrication with CVD graphene/h-BN heterostructures with 1D edge contacts. (a) Schematic representation and (b) optical microscope picture of the fabricated device. (c) Schematics of the fabrication process steps from left to right: the preparation of graphene/h-BN heterostructures; patterning by oxygen plasma; and deposition of 1D edge contacts. Dimensions in (a) and (c) are not to the scale.

graphene used here has grain sizes of 1–5 μm (Graphenea). The typical two-terminal current-voltage (I-V) characteristic at room temperature [Fig. 2(c)] shows a linear behaviour and the contact resistances, estimated from the analysis of data from local four- and two-terminal measurements, are reproducible in several devices. The field-effect mobility of the measured graphene at room temperature is found to be $\sim$133 cm^2/V s^{-1} and the sheet resistance is $\sim$17 k$\Omega/\square$.

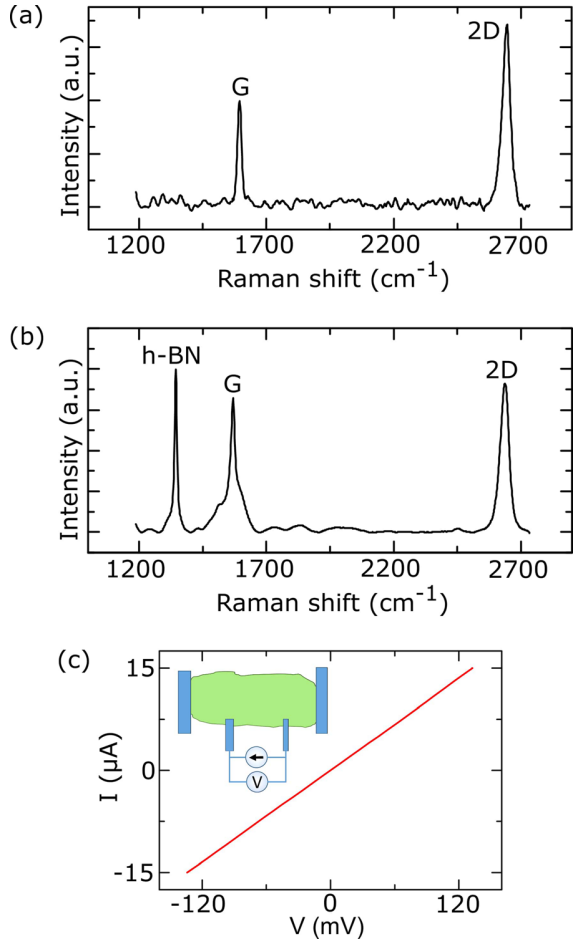

FIG. 2. Characterization of CVD graphene/h-BN heterostructures and 1D edge contacts. (a) Raman spectrum of CVD graphene and (b) graphene/h-BN heterostructure. (c) Typical two-terminal I-V characteristic of the 1D edge contacts to graphene at room temperature. Inset: two-terminal measurement configuration.

Figure 3(a) shows the Hall measurements performed using the measurement configuration depicted in the inset. The Hall voltage (V_H) response of the investigated samples obtained during the magnetic field (B) sweep at applied current bias $I = 15$ μA is fitted with[5,11]

$$\frac{\partial V_H}{\partial B} = \frac{1}{en_{2D}} I, \tag{1}$$

where e is the elementary electron charge and n_{2D} is the charge carrier density. Graphene was found to exhibit hole conduction at zero back gate voltage with a sheet charge carrier concentration of $n_{2D} = 1.75 \times 10^{12}$ cm^{-2} and a background voltage offset of 3 mV, which has been subtracted from the measured raw data. The linearity errors[5,9,12] were found to be within $\pm 3.1\%$ with an average absolute value of 1.3% over a large magnetic field range from –760 mT to 780 mT at room temperature. From the measured Hall voltage response as a function of time at different perpendicular magnetic fields [Fig. 3(b)], one can estimate the noise level and the minimum resolvable magnetic field of $\sim$20 mT at room temperature. From the Hall measurements, the calculated current-related Hall sensitivity

$$S_I = \frac{1}{I}\frac{\partial V_H}{\partial B}\bigg|_{I=const} \tag{2}$$

did not show significant bias-related change in the bias current range from 15 μA to 50 μA at room temperature [Fig. 3(c)].

Next, we investigated the Hall sensitivity of graphene for different carrier concentrations in electron- and hole-doped regimes at room temperature (Fig. 4). Graphene has the unique property that its charge carrier type and concentration can be tuned continuously by applying gate voltage. Figure 4(a) shows the Hall measurements with application of gate voltages $V_g = \pm 40$ V, where a sign change is observed in the slope of Hall response for electron- and hole-doped regimes. From the back gate dependence of the graphene resistance the charge neutrality point was found at $V_g = 26$ V. Such full gate-dependent Hall effect measurements were performed by sweeping the back gate voltages from electron to hole type of conduction across the Dirac point in the presence of different perpendicular magnetic fields [bottom panel of Fig. 4(b)]. To reduce the influence of

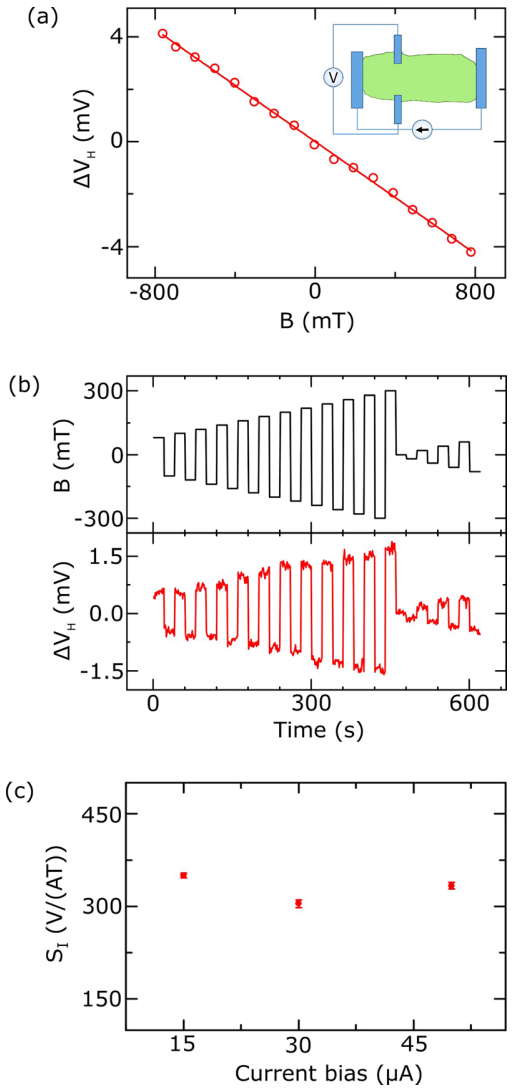

FIG. 3. Operation of CVD graphene/h-BN Hall elements. (a) Output Hall voltage as a function of perpendicular magnetic field measured at $I = 15\ \mu$A at room temperature (circles) with linear fitting (solid line) according to Eq. (1). Inset: Hall measurement configuration. (b) Output Hall voltage as a function of time at different applied magnetic fields measured at $I = 15\ \mu$A and at room temperature. (c) Current-related sensitivity as a function of current bias.

the device geometry, the Hall response at different magnetic fields ($V_H(B)$) is subtracted from measured response at 0 T magnetic field (V_{H0}): $\Delta V_H = V_H(B) - V_{H0}$.[13] Here, we observe a change in the amplitude and sign of ΔV_H by sweeping the gate voltage. Using Eq. (2), we extracted the current-related sensitivity by fitting the ΔV_H-B dependencies. It is plotted in Fig. 4(c) as a function of gate voltage at room temperature. This dependence reveals the gate tuning of the sensitivity with maxima (up to 345 V/(AT)) close to the graphene Dirac point. Such tunability of Hall response stems from gate voltage-induced change of the carrier concentration in the graphene sheet yielding a change of the current-related sensitivity and the output Hall voltage [Eqs. (1) and (2)].

These sensitivities of the large area CVD graphene/h-BN heterostructure-based Hall sensors are at least three times higher than current silicon-based devices.[4–7] Previous studies reported on the performance of unencapsulated graphene Hall sensors[12,14,17] with sensitivities up to 2093 V/(AT). Such unprotected devices are known to be extremely sensitive to environmental parameters and degrade rapidly. Consequently, an insulating barrier is required to protect the graphene layer. Even though recent studies on CVD graphene with Al_2O_3 encapsulation show very promising results on easily scalable and reproducible device fabrication techniques,[18] the 2D and atomically flat nature of insulating h-BN demonstrated outstanding electronic properties when encapsulating graphene.[19] Such exfoliated h-BN/graphene/h-BN heterostructure Hall devices were demonstrated with sensitivities 15 times higher than in our h-BN capped CVD graphene.[13] This can be attributed to the growth quality of CVD graphene, presence of grain boundaries, and charge doping from the SiO_2 substrate as well as contaminations introduced during wet transfer of CVD graphene. Contaminations and grain boundaries are also likely reasons behind the observed low mobility and high sheet resistance of graphene. The measured Hall sensitivities could be further increased by improving the CVD graphene mobility by reducing the SiO_2 substrate-induced doping and graphene-substrate interactions[12,26] by fully encapsulating CVD graphene in h-BN. Utilizing high-quality, large-grain graphene growth and Ohmic instead of tunnel contacts would also allow to significantly improve graphene characteristics and sensing

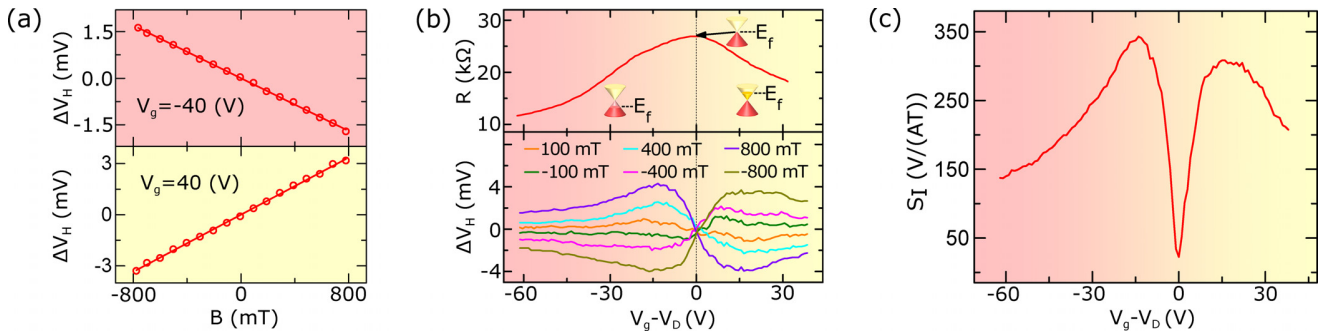

FIG. 4. Gate tunability of CVD graphene/h-BN Hall sensors at room temperature. (a) Output Hall voltage as a function of perpendicular magnetic field at gate voltages of ±40 V. (b) Back gate dependence of graphene resistance (top) and Hall voltage response at different perpendicular magnetic fields (bottom). V_D is the gate voltage corresponding to the Dirac point. (c) Absolute value of current-related sensitivity calculated from Hall voltage response as a function of gate voltage according to Eq. (2). The measurements at 75 K will be published elsewhere.

performance. Furthermore, as a next step forward a fully scalable fabrication approach should be considered with utilization of only all-CVD h-BN/graphene/h-BN stacks patterned on a large area.

III. CONCLUSIONS

In summary, we demonstrated the operation of graphene magnetic Hall elements fabricated on large area CVD graphene on a Si/SiO_2 substrate with h-BN capping and 1D edge contacts. Such heterostructure devices showed reliable contact properties and Hall sensor performance. The samples showed a constant bias dependence of the current-related sensitivity at room temperature. Gate voltage-induced tunability of the Hall response was observed with a maximum current-related sensitivity of 345 V/(AT) close to the Dirac point. These results obtained in graphene Hall sensors with h-BN protection are promising for operation in ambient conditions and for potential applications in transparent and flexible electronics.

ACKNOWLEDGMENTS

Authors are thankful for financial supports from European Union Graphene Flagship (No. 604391), FlagEra project (VR No. 2015-06813), Swedish Research Council (No. 2016-03658), Erasmus Mundus Masters Scholarship and Chalmers Innovation Center.

[1]Global Markets and Technologies for Sensors, BCC Research (2016).
[2]M. Diaz-Michelena, Sensors **9**, 2271 (2009).
[3]Magnetic Sensors Market Analysis by Technology (Hall Effect Sensing, AMR, GMR), by Application (Automotive, Consumer Electronics, Industrial) and Segment Forecasts to 2022, Grand View Research (2016).
[4]G. Boero, M. Demierre, P.-A. Besse, and R. S. Popovic, Sens. Actuators, A **106**, 314 (2003).
[5]R. S. Popovic, *Hall Effect Devices* (Institute of Physics, 2003).
[6]K. Vervaeke, E. Simoen, G. Borghs, and V. V. Moshchalkov, Rev. Sci. Instrum. **80**, 74701 (2009).
[7]P. Kejik, G. Boero, M. Demierre, and R. S. Popovic, Sens. Actuators, A **129**, 212 (2006).
[8]V. P. Kunets, W. T. Black, Y. I. Mazur, D. Guzun, G. J. Salamo, N. Goel, T. D. Mishima, D. A. Deen, S. Q. Murphy, and M. B. Santos, J. Appl. Phys. **98**, 014506 (2005).
[9]T. Hara, M. Mihara, N. Toyoda, and M. Zama, IEEE Trans. Electron Devices **ED-29**, 78 (1982).
[10]M. Bando, T. Ohashi, M. Dede, R. Akram, A. Oral, S. Y. Park, I. Shibasaki, H. Handa, and A. Sandhu, J. Appl. Phys. **105**, 07E909 (2009).
[11]J. Heremans, J. Phys. D: Appl. Phys. **26**, 1149 (1993).
[12]H. Xu, Z. Zhang, R. Shi, H. Liu, Z. Wang, S. Wang, and L.-M. Peng, Sci. Rep. **3**, 1207 (2013).
[13]J. Dauber, A. A. Sagade, M. Oellers, K. Watanabe, T. Taniguchi, D. Neumaier, and C. Stampfer, Appl. Phys. Lett. **106**, 193501 (2015).
[14]L. Huang, Z. Zhang, B. Chen, X. Ma, H. Zhong, and L.-M. Peng, Appl. Phys. Lett. **104**, 183106 (2014).
[15]Z. Wang, L. Banszerus, M. Otto, K. Watanabe, T. Taniguchi, C. Stampfer, and D. Neumaier, Phys. Status Solidi B **253**, 2316 (2016).
[16]M.-K. Joo, J. Kim, J.-H. Park, V. L. Nguyen, K. K. Kim, Y. H. Lee, and D. Suh, ACS Nano **10**, 8803 (2016).
[17]Z. Wang, M. Shaygan, M. Otto, D. Schall, and D. Neumaier, Nanoscale **8**, 7683 (2016).
[18]J. A. Alexander-Webber, A. A. Sagade, A. I. Aria, Z. A. Van Veldhoven, P. Braeuninger-Weimer, R. Wang, A. Cabrero-Vilatela, M.-B. Martin, J. Sui, M. R. Connolly, and S. Hofmann, 2D Mater. **4**, 011008 (2017).
[19]C. R. Dean, A. F. Young, I. Meric, C. Lee, L. Wang, S. Sorgenfrei, K. Watanabe, T. Taniguchi, P. Kim, K. L. Shepard, and J. Hone, Nat. Nanotechnol. **5**, 722 (2010).
[20]Graphenea, Inc., see http://www.graphenea.com for details on graphene characteristics.
[21]L. Wang, I. Meric, P. Y. Huang, Q. Gao, H. Tran, T. Taniguchi, K. Watanabe, L. M. Campos, D. A. Muller, J. Guo, P. Kim, J. Hone, K. L. Shepard, and C. R. Dean, Science **342**, 614 (2013).
[22]A. C. Ferrari, J. C. Meyer, V. Scardaci, C. Casiraghi, M. Lazerri, F. Mauri, S. Piscanec, D. Jiang, K. S. Novoselov, S. Roth, and A. K. Geim, Phys. Rev. Lett. **97**, 187401 (2006).
[23]R. V. Gorbachev, I. Riaz, R. R. Nair, R. Jalil, L. Britnell, B. D. Belle, E. W. Hill, K. S. Novoselov, K. Watanabe, T. Taniguchi, A. K. Geim, and P. Blake, Small **7**, 465 (2011).
[24]T. Ciuk, O. Petruk, A. Kowalik, I. Jozwik, A. Rychter, J. Szmidt, and W. Strupinski, Appl. Phys. Lett. **108**, 223504 (2016).
[25]H. Xu, L. Huang, Z. Zhang, B. Chen, H. Zhong, and L.-M. Peng, Appl. Phys. Lett. **103**, 112405 (2013).
[26]J. Park, S. B. Jo, Y.-J. Yu, Y. Kim, J.-W. Yang, W. H. Lee, H. H. Kim, B. H. Hong, P. Kim, K. Cho, and K. S. Kim, Adv. Mater. **24**, 407 (2012).

Paper II

2D Materials

PAPER

1D ferromagnetic edge contacts to 2D graphene/h-BN heterostructures

RECEIVED
3 January 2017

REVISED
6 September 2017

ACCEPTED FOR PUBLICATION
18 September 2017

PUBLISHED
3 October 2017

Bogdan Karpiak[1], André Dankert[1], Aron W Cummings[2], Stephen R Power[2], Stephan Roche[2,3] and Saroj P Dash[1]

[1] Department of Microtechnology and Nanoscience, Chalmers University of Technology, SE-41296, Göteborg, Sweden
[2] Catalan Institute of Nanoscience and Nanotechnology (ICN2), CSIC and The Barcelona Institute of Science and Technology, Campus UAB, Bellaterra, 08193 Barcelona, Spain
[3] ICREA—Institució Catalana de Recerca i Estudis Avançats, 08010 Barcelona, Spain

E-mail: saroj.dash@chalmers.se

Keywords: graphene, h-BN, CVD, spin-valve, stray field, 1D edge contact, spintronics

Supplementary material for this article is available online

Abstract

We report the fabrication of one-dimensional (1D) ferromagnetic edge contacts to two-dimensional (2D) graphene/h-BN heterostructures. While aiming to study spin injection/detection with 1D edge contacts, a spurious magnetoresistance signal was observed, which is found to originate from the local Hall effect in graphene due to fringe fields from ferromagnetic edge contacts and in the presence of charge current spreading in the nonlocal measurement configuration. Such behavior has been confirmed by the absence of a Hanle signal and gate-dependent magnetoresistance measurements that reveal a change in sign of the signal for the electron- and hole-doped regimes, which is in contrast to the expected behavior of the spin signal. Calculations show that the contact-induced fringe fields are typically on the order of hundreds of mT, but can be reduced below 100 mT with careful optimization of the contact geometry. There may be an additional contribution from magnetoresistance effects due to tunneling anisotropy in the contacts, which needs further investigation. These studies are useful for optimization of spin injection and detection in 2D material heterostructures through 1D edge contacts.

Introduction

Graphene has been shown to be a promising material for spin-polarized electron transport due to its low spin–orbit coupling and negligible hyperfine interactions [1–3]. Recently, long-distance spin transport and electrical control over spin signal and lifetimes have been achieved in graphene at room temperature [1, 2, 4–8]. These experiments have shown that the performance of graphene spintronic devices is significantly affected by the quality of the contacts to the graphene channel [1]. Conventional spin transport experiments use top ferromagnetic metal/tunnel barrier contacts of micrometer width on graphene channels for the purpose of spin injection and detection [1–3]. However, the fabrication of atomically smooth oxide tunnel barriers is challenging, as they usually contain pinholes, roughness, and defects [9–11]. The use of such wide contacts is known to limit the device performance due to inhomogeneous injection and detection of spins, and due to interface-induced spin dephasing under the contacts [9–11]. Additionally, at the nanoscale graphene edges can become important and are predicted to host spin-polarized edge states, giving rise to spin filtering [12, 13]. Such spintronic properties are also predicted to be tunable by external electric fields [12, 13]. If realized, this would add the spin degree of freedom to graphene-based devices and circuits, where spin currents can be generated and injected from zigzag nanoribbons to graphene without the need of ferromagnetic spin injectors.

Here we present the fabrication and characterization of a device that utilizes 1D ferromagnetic edge contacts to graphene/hexagonal boron nitride (h-BN) heterostructures. The non-local spin-valve measurements are found to show spurious magnetoresistance effects due to local Hall effects. Our detailed measurements in different geometries and gate voltages, as well as calculations show that the ferromagnetic contact-induced fringe fields give rise to such a signal.

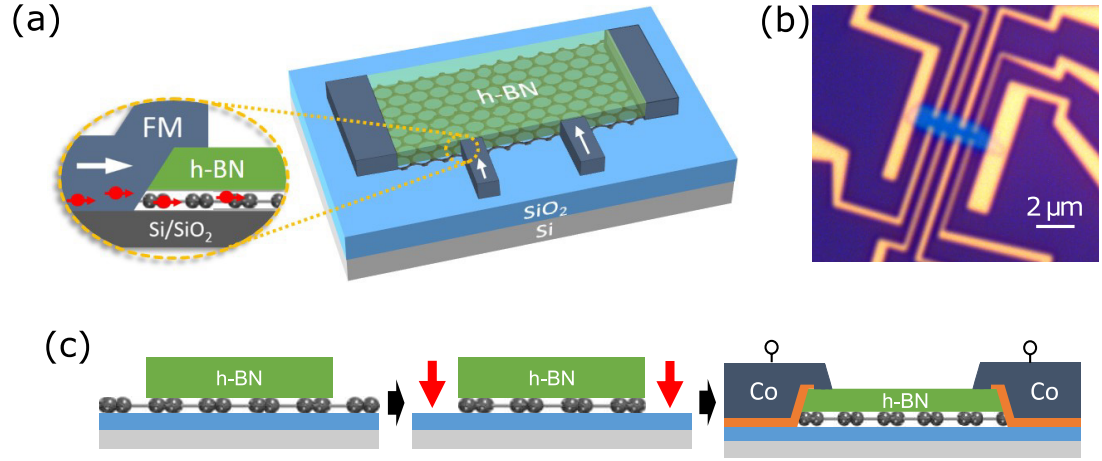

Figure 1. Fabrication of graphene/h-BN heterostructures with 1D ferromagnetic (TiO_2/Co) edge contacts. (a) Schematic representation and (b) optical microscopy picture of the fabricated device. (c) Schematics of the fabrication process steps including preparation of heterostructures, their patterning, and fabrication of contacts.

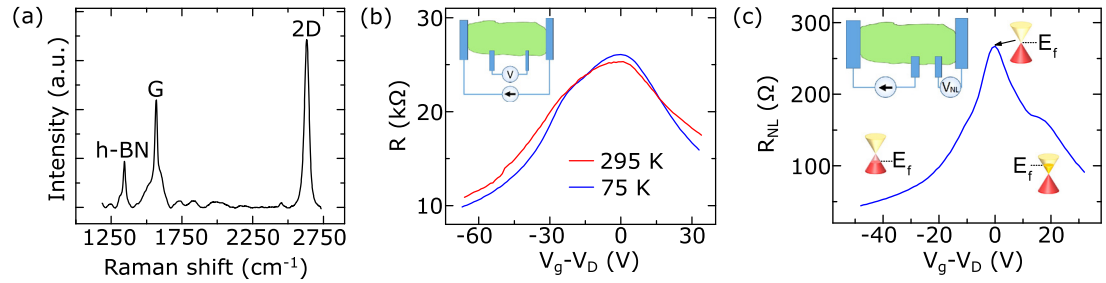

Figure 2. Characterization of graphene/h-BN heterostructures with 1D edge contacts. (a) Raman spectrum of the graphene/h-BN heterostructure. (b) Graphene channel resistance as a function of back gate voltage (V_g) at 295 K (red) and 75 K (blue) for a local measurement configuration (inset). (c) Nonlocal channel resistance ($R_{NL} = V_{NL}/I$) as a function of back gate voltage V_g at 75 K for the nonlocal measurement configuration (inset). The horizontal axes in (b) and (c) are plotted as V_g–V_D.

Results and discussion

A schematic representation and optical microscopy picture of the device are shown in figures 1(a) and (b), respectively. The devices with 1D edge contacts to graphene/h-BN heterostructures were fabricated using the process steps presented in figure 1(c). The shape anisotropy of the ferromagnetic contacts (different widths) was used to achieve different switching fields. The details about the fabrication steps of heterostructure and 1D edge contacts are described in Methods section.

The basic characterization of the fabricated graphene/h-BN heterostructure is depicted in figure 2. The Raman spectrum of the heterostructure is shown in figure 2(a), where the G and 2D peaks related to graphene [14] are visible at positions 1568 cm^{-1} and 2632 cm^{-1} respectively, and the h-BN peak [15] is at 1343 cm^{-1}. The 1D edge contact resistances to graphene were found to be in the range of 4–16 kΩ. The electrical properties of the graphene channel were characterized by gate voltage (V_g) dependence in both the local (figure 2(b)) and nonlocal ($R_{NL} = V_{NL}/I_{bias}$, figure 2(c)) configurations. The charge neutrality (Dirac) point of graphene was found to be in the range of $V_D \sim -5$ to +26 V for different channels measured in local or nonlocal configurations between different contacts due to variations of doping levels within the graphene sheet. The presence of a measurable nonlocal resistance R_{NL} in the detection circuit indicates a charge current spreading outside the bias current circuit, giving rise to an Ohmic resistance contribution $R_s \cdot e^{-\pi L/W}$, where R_s is graphene sheet resistance, and L and W are the length and width of the graphene channel, respectively [16].

Next, nonlocal magnetoresistance measurements were carried out in the 1D edge contact devices as shown in figure 3(a). We observed a nonlocal voltage V_{NL} with single switching and hysteresis behavior while sweeping the in-plane magnetic field aligned with the contacts at fixed bias currents (figure 3(b)). By changing the current direction, a similar switching signal with opposite sign was observed. The complete bias dependence of the signal is presented in figure 3(c), which shows a linear dependence in the measured bias range. The temperature dependence of the magnetoresistance signal V_{NL} was measured at a constant current bias of $I = +15$ μA (figure 4). We observed a decay of the switching amplitude of V_{NL} ($\Delta V_{\uparrow\downarrow}$) with increasing temperature, which could be measured up to 200 K.

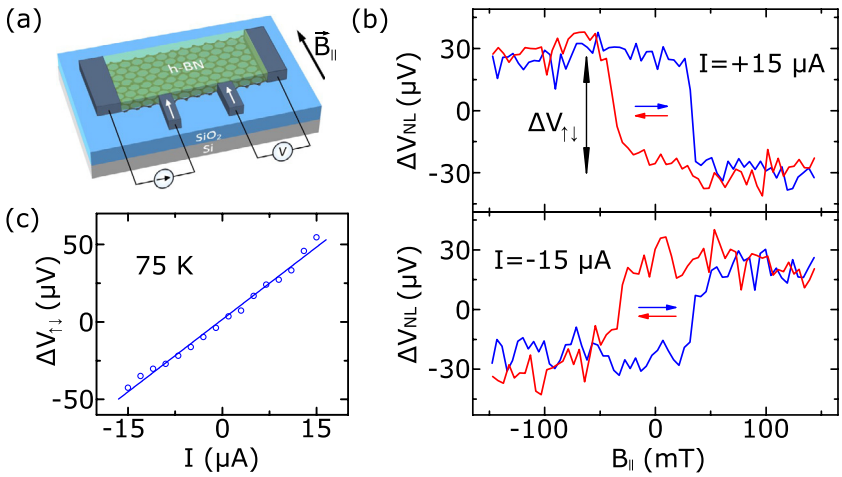

Figure 3. Magnetoresistance measurements and bias dependence of the spin valve device. (a) Schematic of the nonlocal measurement configuration. (b) Measured nonlocal voltage V_{NL} as a function of external in-plane magnetic field ($B_{||}$) at $I = \pm 15$ μA at 75 K. The $B_{||}$ sweep directions are indicated by red and blue arrows. A baseline linear background voltage is subtracted from the measured data. (c) Current bias dependence of the magnetoresistance switching amplitude $\Delta V_{\uparrow\downarrow}$ at 75 K.

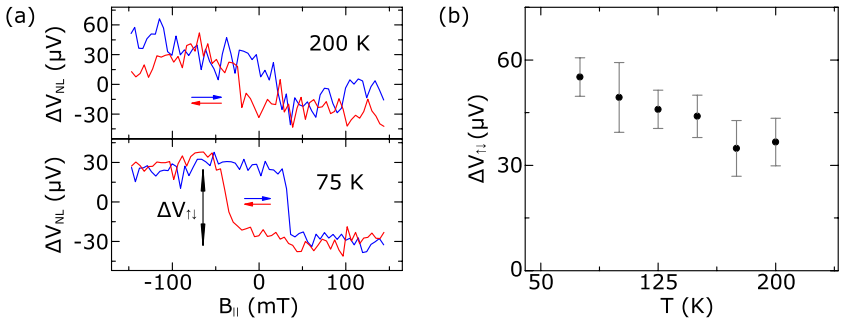

Figure 4. Temperature dependence of the magnetoresistance signal. (a) Nonlocal voltage as a function of applied external in-plane magnetic field at 200 K (top panel) and 75 K (bottom panel) at 15 μA current bias. The field sweep directions are indicated by arrows and a linear background voltage is subtracted from the measured data. (b) Temperature dependence of the switching amplitude ($\Delta V_{\uparrow\downarrow}$) at 15 μA current bias.

The presence of only one step of magnetoresistance for each sweep direction is not typical for spin signals that arise from spin injection and detection [6, 11, 17–20]. For comparison, a typical spin-valve signal for top ferromagnetic contacts to graphene is shown in supplementary figure S1(b) (stacks.iop.org/TDM/5/014001/mmedia). In the latter case, at least two steps are usually visible for each sweep direction, when both injector and detector contacts switch their magnetization direction [6, 11, 17–20]. The coercivity values of the ferromagnetic contacts used here are within the typical sweeping field range, which we have also verified with higher field sweep ranges (supplementary figure S2(b)). A single-step switching signal can arise if the graphene edge itself generates a spin current; however, such effects are only expected in graphene nanoribbons and not in the micrometer-scale devices used here [12, 13]. The quantum spin Hall effect is also unlikely to be responsible for the observed signal considering the negligible spin–orbit coupling in graphene. Additional confirmation of the absence of spin transport in our 1D contact devices comes from the out-of-plane field sweeps, where no Hanle spin precession signal is observed (supplementary figure S2(c)). The continuous linear change of magnetoresistance here (inset in supplementary figure S2(c)) could be due to Hall effect in the presence of continuous sweeps of external perpendicular magnetic field, in contrast to abrupt changes of stray fields as e.g. in figure 3. Therefore, the observed single-switching magnetoresistance with 1D ferromagnetic contacts could be due to the local Hall effect in the graphene in the presence of stray magnetic fields emanating from the edges of ferromagnetic contacts [10, 21–24].

In order to further clarify the origin of the magnetoresistance, gate-dependent measurements were carried out, where we tune the concentration and type of the charge carriers in graphene. Figure 5(a) shows the magnetoresistance switching with the application of $V_g = \pm 30$ V, where a change in the sign of the $\Delta V_{\uparrow\downarrow}$ is observed due to electron or hole conduction of the graphene channel. The complete gate dependence of $\Delta V_{\uparrow\downarrow}$, along with the channel resistance is shown in figure 5(b), revealing a correlation between the sign of $\Delta V_{\uparrow\downarrow}$ and type of charge carrier in graphene. The absolute value of $\Delta V_{\uparrow\downarrow}$ is found to have two maxima

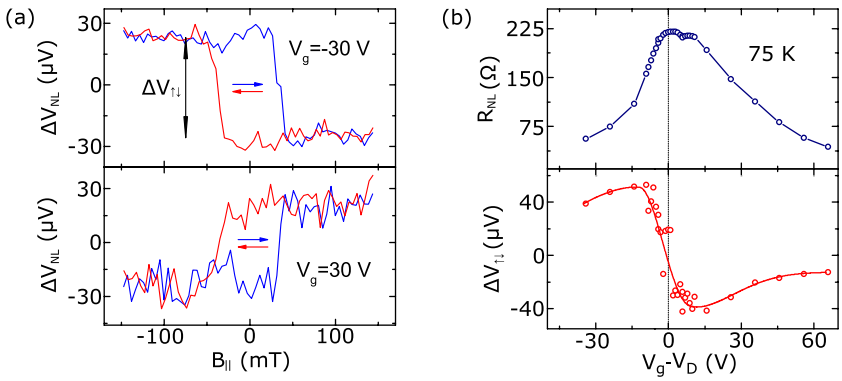

Figure 5. Gate dependence of the magnetoresistance signal. (a) V_{NL} as a function of in-plane external magnetic field sweeps at $V_g = -30$ V (top panel) and $V_g = 30$ V (bottom panel), measured with I = 15 μA at 75 K. A linear baseline offset voltage is subtracted from the raw data. (b) Dependence of the nonlocal graphene resistance $R_{NL} = \Delta V_{NL}/I$ on the back gate voltage V_g–V_D (top panel) and the nonlocal voltage step $\Delta V_{\uparrow\downarrow}$ (bottom panel). V_D is the Dirac point of graphene.

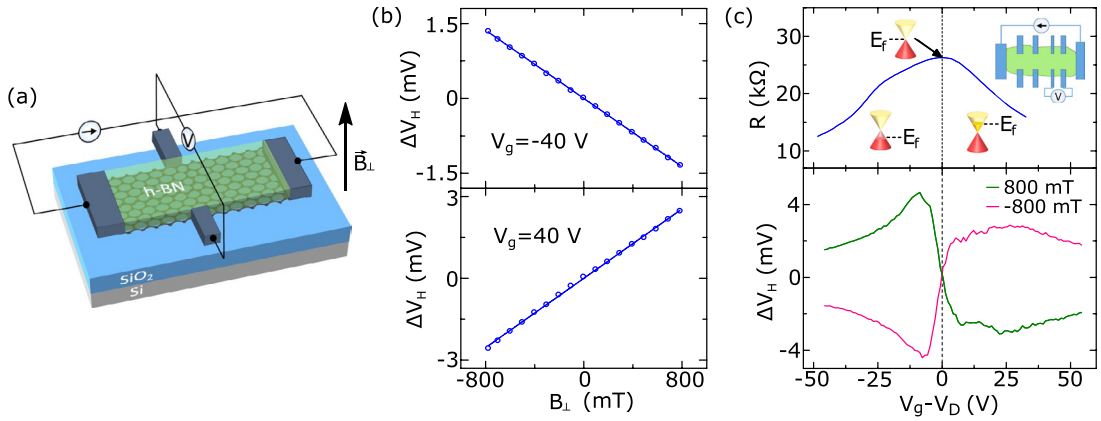

Figure 6. Hall effect in graphene. (a) Schematic of the Hall measurement configuration. (b) Hall voltage V_H as a function of the perpendicular magnetic field, measured with $V_g = \pm 40$ V at 75 K. (c) Gate dependence of the graphene resistance (top) and Hall voltage V_H (bottom) at 75 K for different perpendicular magnetic fields. The reference signal measured at a magnetic field of 0 T is subtracted from the Hall response at other magnetic fields. Measurements at room temperature for this device are reported elsewhere [25].

near the charge neutrality point in graphene, where the charge density n_{2D} is minimal. These results support the argument in favor of a local Hall effect-dominated magnetoresistance switching. At the same time, this gives additional evidence to rule out any spin-related nature of the observed switching, since the spin signal should not change sign with a change of charge carrier type [17].

Next, regular Hall measurements were performed (figure 6(a)) on the same device at 75 K to correlate with the magnetoresistance measurements. Figure 6(b) shows a change in the sign of the slope of the Hall response V_H in the graphene channel by the application of a gate voltage $V_g = \pm 40$ V, due to a change in conduction from electrons to holes. The full gate-dependent Hall measurements were performed by sweeping V_g from electron to hole conduction across the Dirac point in the presence of different perpendicular magnetic fields (figure 6(c)). We observe a change in the amplitude and sign of V_H with the applied V_g. A clear similarity is also observed between the V_g dependence of the magnetoresistance signal $\Delta V_{\uparrow\downarrow}$ (figure 5(b)) and the regular Hall voltage V_H (figure 6(c)). This similarity is justified due to the similar origin of the local Hall magnetoresistance and the regular Hall effects, which are due to stray magnetic fields from the ferromagnetic contacts, or the Lorentz force acting on moving charges in the presence of a perpendicular external magnetic field, respectively.

In order to quantify the impact of the local Hall effect on the magnetoresistance signal, we use the Biot–Savart law to numerically calculate the stray magnetic fields that can arise from the 1D edge contacts. The contact geometry we consider is shown in figure 7(a). To describe the contact we assume a surface current density given by the saturation magnetization of cobalt, $M_s = 1.42$ MA m^{-1}, which is parallel to the $+x$ ($-x$) axis on the top (bottom) surfaces of the side view, and parallel to the $+z$ ($-z$) axis on the left (right) surfaces of the top view. Away from the sloped region, this magnetizes the cobalt along the y-axis. In the sloped region, this surface current also yields an out-of-plane component to the polarization. For metal surfaces parallel to the principal axes, the stray magnetic field can

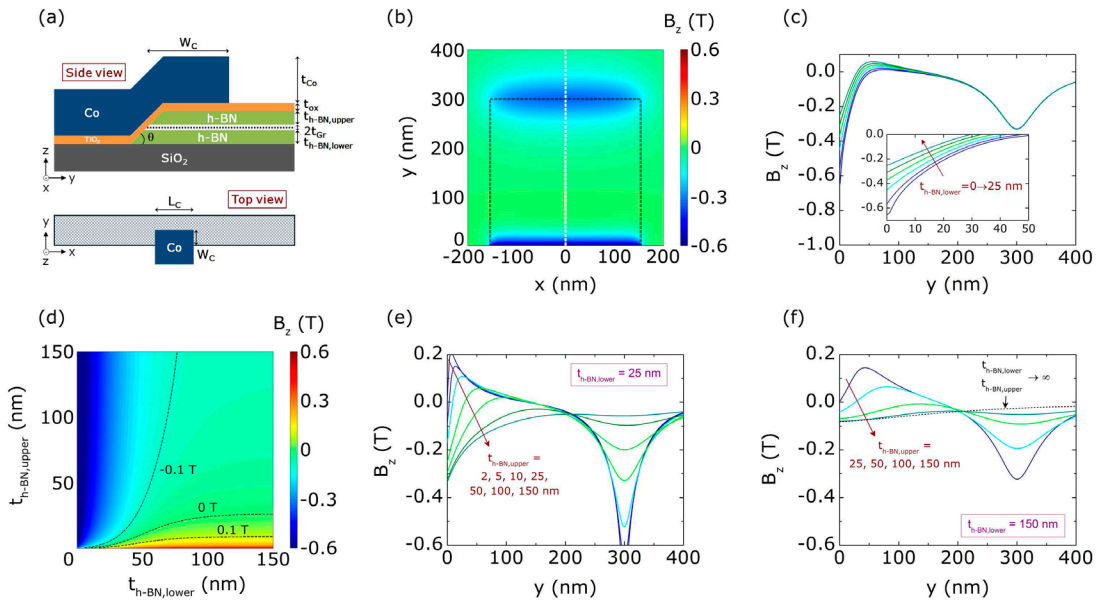

Figure 7. Stray magnetic fields from 1D ferromagnetic edge contacts. (a) Contact geometry considered for the stray field calculations. (b) Profile of the perpendicular stray field B_z within the graphene layer, assuming $L_C = 310$ nm, $W_C = 300$ nm, $t_{Co} = 65$ nm, $t_{ox} = 1$ nm, $t_{h\text{-}BN,upper} = 25$ nm, $t_{Gr} = 0.35$ nm, $t_{h\text{-}BN,lower} = 0$, and $\theta = 45°$. (c) Stray magnetic field along the center of the contact ($x = 0$) for different thicknesses of $t_{h\text{-}BN,lower}$, where the y-position is relative to the graphene edge. (d) Profile of B_z at different thicknesses of $t_{h\text{-}BN,lower}$ and $t_{h\text{-}BN,upper}$ at the graphene edge ($x = y = 0$). (e) B_z as a function of distance from the graphene edge for $t_{h\text{-}BN,lower} = 25$ nm and (f) 150 nm at different $t_{h\text{-}BN,upper}$.

be calculated analytically [26], while the sloped portion of the contact requires a numerical solution.

In figure 7(b) we show the spatial distribution of the perpendicular component of the stray magnetic field B_z within the graphene layer, using the experimental contact geometry (with $t_{h\text{-}BN,lower} = 0$ and the rest of the parameters listed in the caption of figure 7). The black dashed lines indicate the contact metal edges. Here we see that the stray field can be quite strong, reaching more than 600 mT at the graphene edge. In addition, the end of the top portion of the ferromagnetic contact also induces a strong perpendicular stray field on the order of 350 mT. Near the 1D edge contact to graphene, the stray field decays from 600 mT to zero over a distance of 50 nm. This average field of 300 mT corresponds to an average magnetic length of ~50 nm, indicating that the stray field can indeed induce a significant Hall effect at the charge injection/detection point.

In figure 7(c) we plot B_z along the middle of the contact, indicated by the white dashed line in figure 7(b). This plot shows that by increasing the thickness of the bottom h-BN layer, the magnitude of the stray field at the graphene edge can be reduced by nearly a factor of three for a typical set of experimental parameters. This reduction occurs because the stray fields due to the top and bottom surfaces of the contact tend to cancel one another as the vertical position of the graphene layer increases. While the perpendicular stray field at the injection edge is still relatively large, ~250 mT, further optimization of the contact geometry can reduce this. For example, tuning the ratio of $t_{h\text{-}BN,upper}/t_{h\text{-}BN,lower}$ can reduce B_z at the injection edge (figure 7(d)), but this can result in deeper penetration of stray fields into the graphene sheet, and in sign changes of B_z at different distances from the graphene edge (figure 7(e)). Generally, with thicker top and bottom h-BN layers, the stray field at the edge can be reduced to below 100 mT (figure 7(f) and supplementary figure S3(a)). A shallower etching angle θ could also reduce the stray fields at the graphene edge (supplementary figure S3(b)), but this is difficult to tune experimentally. Additionally, thicker top h-BN layer can significantly reduce the stray fields at the contact edge corresponding to y = 300 nm (supplementary figure S3(c)). It should also be noted that this calculation overestimates the stray field by a factor M_s/M_r, where M_r is the remanent magnetization of the contact.

A similar magnetoresistance switching effect can also arise due to tunneling anisotropic magnetoresistance (TAMR) [27–32]. In magnetic tunnel junctions, the TAMR signal strongly depends on the orientation of the magnetization with respect to the current direction, crystallographic axes, spin–orbit interaction (SOI) and density of states (DOS) anisotropies in the materials. In such devices, TAMR signals were measured at low temperatures and the magnitude is found to enhance in the presence of heavy elements. However, the TAMR signal is generally observed only at very low temperatures below 100 K due to sampling a wider region of the tunneling DOS at higher temperatures. In contrast, our magnetoresistance signal in graphene devices is persistent up to 200 K and vanishes only due to increased noise level of the junctions at higher temperatures. The TAMR effects in literature are also known to have a characteristic bias, temperature and angle dependence, and are strongly dependent on the interface SOI. Further detailed investigations are

required to identify the contribution of TAMR in the observed magnetoresistance signal (in addition to the stray Hall effect) in our graphene devices with 1D ferromagnetic contacts.

Conclusions

We have investigated the operation of a graphene device with 1D ferromagnetic edge contacts in a nonlocal configuration. The analysis of the measurements indicates a local Hall effect-dominated phenomenon in the presence of charge current spreading outside the injection circuit, resulting in a single-step magnetoresistance switching. This local Hall magnetoresistance can arise due to the Lorentz force acting on moving charges in the presence of ferromagnetic stray fields from the 1D edge contacts. This origin of the signal is also supported by the absence of a Hanle signal and the change in sign of the magnetoresistance with the change in carrier type from electron to hole in the graphene transport channel. Our calculations reveal that with proper optimization of the contact geometry, the magnitude of the perpendicular stray field can be reduced to below 100 mT at the contact edge. Further investigations are required to identify other contributions to the measured signal such as TAMR in our graphene devices. These findings provide insight into the phenomena that hinder the operation of nonlocal spin valve devices with 1D edge contacts, and they lay the foundation for further developments.

Methods

To fabricate h-BN encapsulated graphene devices, first CVD graphene was wet-transferred onto a Si/SiO_2 substrate (from Graphenea). After cleaning and annealing in Ar/H_2 atmosphere, h-BN flakes were dry-transferred using the scotch-tape method. The graphene was patterned by means of oxygen plasma etching where h-BN flakes were used as a mask. Electron beam lithography and electron beam evaporation of metals were utilized to fabricate the contacts (1 nm TiO_2/65 nm Co), which formed a 1D connection to encapsulated graphene. Electronic and magnetotransport measurements were performed in a cryostat by means of a Keithley 6221 current source and a Keithley 2182A nanovoltmeter. Gate voltage was applied using a Keithley 2612 source metre.

Acknowledgments

BK, AD and SPD acknowledge financial supports from EU Graphene Flagship (No. 604391), EU FlagEra project (No. 2015-06813), Swedish Research Council grants (No. 2012-04604 and No. 2016-03658), Graphene center and AoA Nano program at Chalmers University of Technology. BK acknowledges scholarship from EU Erasmus Mundus Master of Nanoscience and Nanotechnology. SRP acknowledges funding from the European Unions Horizon 2020 research and innovation programme under the Marie Sklodowska-Curie grant agreement No 665919. ICN2 is supported by the Severo Ochoa program from Spanish MINECO (Grant No. SEV-2013-0295) and funded by the CERCA Programme/Generalitat de Catalunya. AWC and SR acknowledge Funding from the Spanish Ministry of Economy and Competitiveness and the European Regional Development Fund (Project No. FIS2015-67767-P MINECO/FEDER), the Secretaría de Universidades e Investigación del Departamento de Economía y Conocimiento de la Generalidad de Catalunya (2014 SGR 58).

ORCID iDs

Bogdan Karpiak https://orcid.org/0000-0001-7462-8405
Stephen R Power https://orcid.org/0000-0003-4566-628X
Stephan Roche https://orcid.org/0000-0003-0323-4665
Saroj P Dash https://orcid.org/0000-0001-7931-4843

References

[1] Roche S *et al* 2015 Graphene spintronics: the European Flagship perspective *2D Mater.* **2** 30202
[2] Han W, Kawakami R K, Gmitra M and Fabian J 2014 Graphene spintronics *Nat. Nanotechnol.* **9** 794–807
[3] Ferrari A C *et al* 2015 Science and technology roadmap for graphene, related two-dimensional crystals, and hybrid systems *Nanoscale* **7** 4598–810
[4] Ingla-Aynés J, Guimarães M H D, Meijerink R J, Zomer P J and van Wees B J 2015 24 μm spin relaxation length in boron nitride encapsulated bilayer graphene *Phys. Rev.* B **92** 201410
[5] Drögeler M, Franzen C, Volmer F, Pohlmann T, Banszerus L, Wolter M, Watanabe K, Taniguchi T, Stampfer C and Beschoten B 2016 Spin lifetimes exceeding 12 ns in graphene nonlocal spin valve devices *Nano Lett.* **16** 3533–9
[6] Kamalakar V M, Groenveld C, Dankert A and Dash S P 2015 Long distance spin communication in chemical vapour deposited graphene *Nat. Commun.* **6** 6766
[7] Kamalakar V M, Dankert A, Kelly P J and Dash S P 2016 Inversion of spin signal and spin filtering in ferromagnet|hexagonal boron nitride-graphene van der Waals heterostructures *Sci. Rep.* **6** 21168
[8] Dankert A and Dash S P 2017 Electrical gate control of spin current in van der Waals heterostructures at room temperature *Nat. Commun.* **8** 16093
[9] Dash S P, Sharma S, Le Breton J C, Peiro J, Jaffrés H, George J-M, Lemaître A and Jansen R 2011 Spin precession and inverted Hanle effect in a semiconductor near a finite-roughness ferromagnetic interface *Phys. Rev.* B **84** 54410
[10] Muduli P K, Barzola-Quiquia J, Dusari S, Ballestar A, Bern F, Böhlmann W and Esquinazi P 2013 Large local Hall effect in pin-hole dominated multigraphene spin-valves *Nanotechnology* **24** 15703
[11] Han W, Pi K, McCreary K M, Li Y, Wong J J I, Swartz A G and Kawakami R K 2010 Tunneling spin injection into single layer graphene *Phys. Rev. Lett.* **105** 167202
[12] Son Y-W, Cohen M L and Louie S G 2006 Half-metallic graphene nanoribbons *Nature* **444** 347–2
[13] Wimmer M, Adagideli I, Berber S, Tománek D and Richter K 2008 Spin currents in rough graphene nanoribbons:

Universal fluctuations and spin injection *Phys. Rev. Lett.* **100** 177207
[14] Ferrari A, Meyer J C, Scardaci C, Casiraghi C and Lazzeri M 2006 Raman spectrum of graphene and graphene layers *Phys. Rev. Lett.* **97** 187401
[15] Gorbachev R V *et al* 2011 Hunting for monolayer boron nitride: optical and raman signatures *Small* **7** 465–8
[16] Johnson M and Silsbee R H 2007 Calculation of nonlocal baseline resistance in a quasi-one-dimensional wire *Phys. Rev.* B **76** 153107
[17] Tombros N, Jozsa C, Popinciuc M, Jonkman H T and van Wees B J 2007 Electronic spin transport and spin precession in single graphene layers at room temperature *Nature* **448** 571–4
[18] Kamalakar M V, Dankert A, Bergsten J, Ive T and Dash S P 2014 Enhanced tunnel spin injection into graphene using chemical vapor deposited hexagonal boron nitride *Sci. Rep.* **4** 6146
[19] Dankert A, Kamalakar M V, Bergsten J and Dash S P 2014 Spin transport and precession in graphene measured by nonlocal and three-terminal methods *Appl. Phys. Lett.* **104** 192403
[20] Dlubak B *et al* 2012 Highly efficient spin transport in epitaxial graphene on SiC *Nat. Phys.* **8** 557–61
[21] Monzon F G, Patterson D S and Roukes M L 1999 Characterization of individual nanomagnets by the local Hall effect *J. Magn. Magn. Mater.* **195** 19–25
[22] Monzon F G, Johnson M and Roukes M L 1997 Strong Hall voltage modulation in hybrid ferromagnet/semiconductor microstructures *Appl. Phys. Lett.* **71** 3087–9
[23] Hara M, Endo A, Katsumoto S and Iye Y 2004 Transport in ferromagnet/semiconductor 2DEG hybrid network structure *Physica* E **22** 345–8
[24] Monzon F G, Tang H X and Roukes M L 2000 Magnetoelectronic phenomena at a ferromagnet-semiconductor interface *Phys. Rev. Lett.* **84** 5022
[25] Karpiak B, Dankert A and Dash S P 2017 Gate-tunable Hall sensors on large area CVD graphene protected by h-BN with 1D edge contacts *J. Appl. Phys.* **122** 054506
[26] Engel-Herbert R and Hesjedal T 2005 Calculation of the magnetic stray field of a uniaxial magnetic domain *J. Appl. Phys.* **97** 74504
[27] Gould C, Rüster C, Jungwirth T, Girgis E, Schott G M, Giraud R, Brunner K, Schmidt G and Molenkamp L W 2004 Tunneling anisotropic magnetoresistance: A spin-valve-like tunnel magnetoresistance using a single magnetic layer *Phys. Rev. Lett.* **93** 117203
[28] Wang K, Sanderink J G M, Bolhuis T, van der Wiel W G and de Jong M P 2015 Tunnelling anisotropic magnetoresistance due to antiferromagnetic CoO tunnel barriers *Sci. Rep.* **5** 15498
[29] Liu R S, Michalak L, Canali C M, Samuelson L and Pettersson H 2008 Tunneling anisotropic magnetoresistance in Co/AlO_x/Au tunnel junctions *Nano Lett.* **8** 848–52
[30] Wang K, Tran T L A, Brinks P, Sanderink J G M, Bolhuis T, van der Weil W G and de Jong M P 2013 Tunneling anisotropic magnetoresistance in Co/AlO_x/Al tunnel junctions with fcc Co (1 1 1) electrodes *Phys. Rev.* B **88** 54407
[31] Wunderlich J *et al* 2006 Coulomb blockade anisotropic magnetoresistance effect in a (Ga, Mn)As single-electron transistor *Phys. Rev. Lett.* **97** 77201
[32] Park B G *et al* 2008 Tunneling anisotropic magnetoresistance in multilayer- (Co/Pt)/AlO_x/Pt structures *Phys. Rev. Lett.* **100** 87204

Paper III

SCIENTIFIC REPORTS

OPEN

Hall sensors batch-fabricated on all-CVD h-BN/graphene/h-BN heterostructures

Received: 18 January 2017
Accepted: 6 September 2017
Published online: 09 November 2017

André Dankert, Bogdan Karpiak & Saroj P. Dash

The two-dimensional (2D) material graphene is highly promising for Hall sensors due to its potential of having high charge carrier mobility and low carrier concentration at room temperature. Here, we report the scalable batch-fabrication of magnetic Hall sensors on graphene encapsulated in hexagonal boron nitride (h-BN) using commercially available large area CVD grown materials. The all-CVD grown h-BN/graphene/h-BN van der Waals heterostructures were prepared by layer transfer technique and Hall sensors were batch-fabricated with 1D edge metal contacts. The current-related Hall sensitivities up to 97 V/AT are measured at room temperature. The Hall sensors showed robust performance over the wafer scale with stable characteristics over six months in ambient environment. This work opens avenues for further development of growth and fabrication technologies of all-CVD 2D material heterostructures and allows further improvements in Hall sensor performance for practical applications.

Magnetic field sensors today represent a significant growing market, estimated to reach USD 4.16 billion in value terms by the year 2022[1]. The areas of application cover many fields, such as automotive, consumer electronics, healthcare and defense industry, where magnetic field sensors are used for position detection, current monitoring and angular sensing. Many different magnetic sensors based on a variety of effects have been realized for different applications[2]. Hall effect-based sensors constitute a significant part of the industry, with an estimated market share to be over 55% in 2014[3]. They are used for magnetic field detection in the field range from 10^{-7} T to 10^{2} T in a temperature range from −40 °C up to 150 °C. Today, the most ubiquitous sensors utilize an active region made of Si due to the low fabrication cost, highly developed processing technology, good integration into signal processing circuits and reasonable performance properties (current-normalized sensitivity S_I~100 V/AT)[4–7]. In comparison, Hall sensors based on III-V compound semiconductors provide better performances[8–11], but are expensive and more difficult to integrate in circuits.

Graphene is highly interesting material to be used as active region of magnetic Hall sensors, owing to its 2D nature, low carrier concentration n_{2D} and high carrier mobility μ. The previous reports on graphene Hall sensors demonstrated current-related sensitivities ($S_I \propto 1/n_{2D}$) up to 1200 V/AT on large area unprotected CVD graphene on SiO_2 substrate[12] and 1020 V/AT on epitaxial graphene on SiC substrates[13]. However, single layer graphene devices are prone to contaminations from environment and encapsulated structures are needed for reliable and durable performance for practical applications[14]. Recent studies on graphene encapsulation by Al_2O_3 grown by atomic layer deposition showed good results with low doping levels[15]. However, the encapsulated graphene with 2D insulating h-BN flakes provide superior interface, containing low amount of dangling bonds and charge traps and retaining the high electronic properties of graphene for high Hall sensor performance[16]. Moreover, the smoothness of h-BN allows using it as a high-quality substrate in addition to top encapsulation. Thus, current-related sensitivities S_I ~ 5700 V/AT were obtained on stacks of all-exfoliated h-BN/graphene/h-BN[17], S_I ~ 2270 V/AT on single crystal CVD graphene patches encapsulated between exfoliated h-BN[18], and S_I ~ 1986 V/AT with batch-fabricated CVD graphene on *in-situ* grown CVD h-BN substrate without top encapsulation[19]. In addition to increased sensitivities, high linearity[12,20] and low noise of the devices[20–22] combined with transparency and flexibility[18,23] generates a high interest in graphene for the use in magnetic Hall sensors. However, for practical utilization in ambient environment over longer period, there is a necessity to investigate graphene Hall sensors fabricated by a scalable process using all-CVD grown 2D material heterostructures with full encapsulation of graphene active region.

Department of Microtechnology and Nanoscience, Chalmers University of Technology, SE-41296, Göteborg, Sweden. André Dankert and Bogdan Karpiak contributed equally to this work. Correspondence and requests for materials should be addressed to A.D. (email: andre.dankert@chalmers.se) or S.P.D. (email: saroj.dash@chalmers.se)

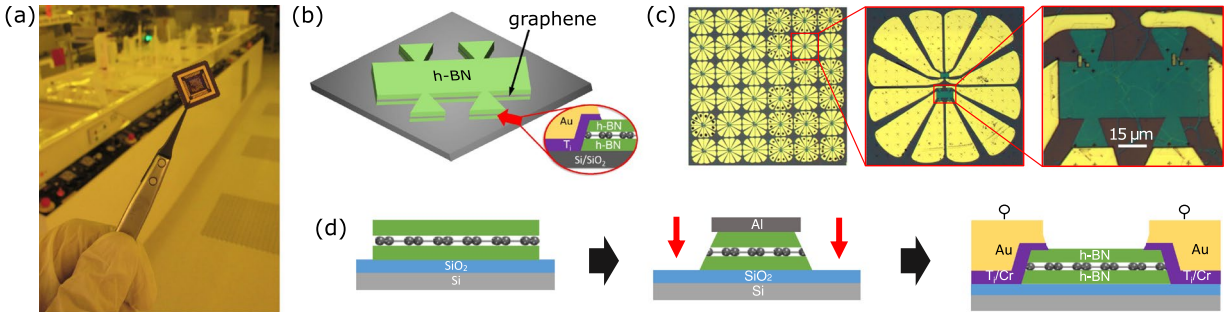

Figure 1. Fabrication of magnetic Hall elements based on large area CVD graphene encapsulated in CVD h-BN on Si/SiO_2 substrate. (**a**) Picture of the chip carrier with batch-fabricated graphene Hall elements. (**b**) The schematic representation of the fabricated Hall sensor devices with h-BN/graphene/h-BN heterostructure and 1D edge contacts. (**c**) Optical microscope picture of the batch-fabricated chip and individual graphene Hall element. (**d**) Schematic of the fabrication process steps involving the preparation of h-BN/graphene/h-BN heterostructures by layer transfer method, followed by patterning and formation of 1D edge metal contacts.

Here we report a scalable graphene Hall sensor fabrication process by using commercially available large area all-CVD grown 2D materials van der Waals heterostructures. The devices used here involve an active region consisting of CVD graphene, which is encapsulated with CVD grown multilayer h-BN. The 1D edge metal contacts are utilized to connect the graphene active region to the electronic circuit[24]. The Hall sensors exhibit stable performance over the wafer scale in ambient environmental conditions over a longer period of time. Although further improvements are required in the fabrication process, such large-scale batch fabrication of h-BN encapsulated graphene Hall elements can bring the technology closer to practical applications.

Results

The Hall sensors were prepared by using a scalable fabrication process. An optical picture of a chip-size batch-fabricated graphene Hall elements is shown in Fig. 1a. Figure 1b shows the schematic representation of the Hall bar devices with 1D edge contacts. Figure 1c presents an optical microscope picture of the chip and an individual graphene Hall element, which were fabricated through the micro-fabrication process as schematically shown in Fig. 1d. Each Hall element consists of CVD graphene (from Graphenea[25]) sandwiched between multilayer CVD h-BN (from Graphene Supermarket[26]). The 2D material heterostructure was prepared on a Si/SiO_2 wafer by large area PMMA-supported wet-transfer technique and Ar/H_2 annealing for each layer (service of Graphenea). Next, they were patterned to Hall bar structures by using an Al (20 nm) hard mask for etching with CHF_3 and O_2 gas. The Al hard mask was removed by wet chemical etching in Shipley Microposit MF-319. The 1D edge contacts were fabricated by means of photo-lithography and electron beam evaporation of metals followed by liftoff in acetone. More specifically, we investigated 1D edge metal contacts of Cr (5 nm)/Au (95 nm) and Ti (20 nm)/Au (60 nm) to 2D graphene channels.

Figure 2a shows the prepared all-CVD h-BN/graphene/h-BN heterostructures on a 4-inch SiO_2/Si wafer. The Raman spectrum of monolayer CVD graphene[27] on SiO_2/Si substrate show the G and 2D peaks at 1597 cm^{-1} and 2652 cm^{-1} respectively[28] with a small D peak (see Supplementary Fig. S1a). The grain size of the CVD graphene is mostly between 1–5 μm range. The Raman characterization of the h-BN film revealed a peak at 1357 cm^{-1} at selective places[29] (see Supplementary Figure S1b). The thickness of the CVD h-BN used in the heterostructures was measured by AFM (~10–13 nm, as shown in Fig. 2b). The rms roughness of the h-BN films were found to be 1–2 nm on Cu foil and SiO_2 substrate. Although we could get rid of organic contamination introduced on h-BN from the transfer and device fabrication process by annealing in Ar/H_2, the roughness remains at similar values (see Supplementary Fig. S2). Earlier, Kim *et al.* reported the multilayer CVD h-BN films to be polycrystalline in nature and indicated sp^2 bond coordination of B and N atoms[30].

The electrical characteristics of 1D edge contacts with Cr/Au and Ti/Au metals to graphene are shown in Fig. 2c–f. As observed from current-voltage (IV) characteristics, the Cr/Au contacts provide a low-resistive linear behavior, while Ti/Au contacts show a high-resistive non-linear tunneling behavior. The weak temperature dependence of the resistance for the Cr/Au contacts at zero bias and at 0.5 V bias (Fig. 2d) indicates high quality interfaces[31]. However, the high resistance and tunneling behavior of the Ti/Au edge contact to graphene (Fig. 2e and f) could be due to interfacial species, such as oxidation at the interfaces. The encapsulated CVD graphene is found to be hole-doped with sheet resistances R_S between 520–870 Ω/□.

First, we present the characterization of the h-BN/graphene/h-BN Hall sensors with Cr/Au edge contacts. The samples were measured at ambient conditions, i.e. at room temperature of 293 K, pressure of 750 Torr, relative humidity ~70%. Except for the cases where measurements were done at room temperature, pressure was 10^{-2} Torr. The Hall voltage V_H is measured at a constant applied current, while sweeping a perpendicular magnetic field (Fig. 3a). The Lorentz force acting on the moving charges in graphene resulted in a voltage difference in the transverse direction (Hall voltage V_H). The detected Hall voltage, measured as a function of applied perpendicular magnetic field $B_\perp$ at bias current I = 90 μA, is shown in Fig. 3b. A very weak temperature-dependent change is observed within the range of 75–293 K. A background voltage offset V_{offset}, due to a misalignment between Hall probe contacts, has been subtracted. Fitting the Hall response with $V_H = \frac{IB_\perp}{en_{2D}} + V_{offset}$, where e is the electron's

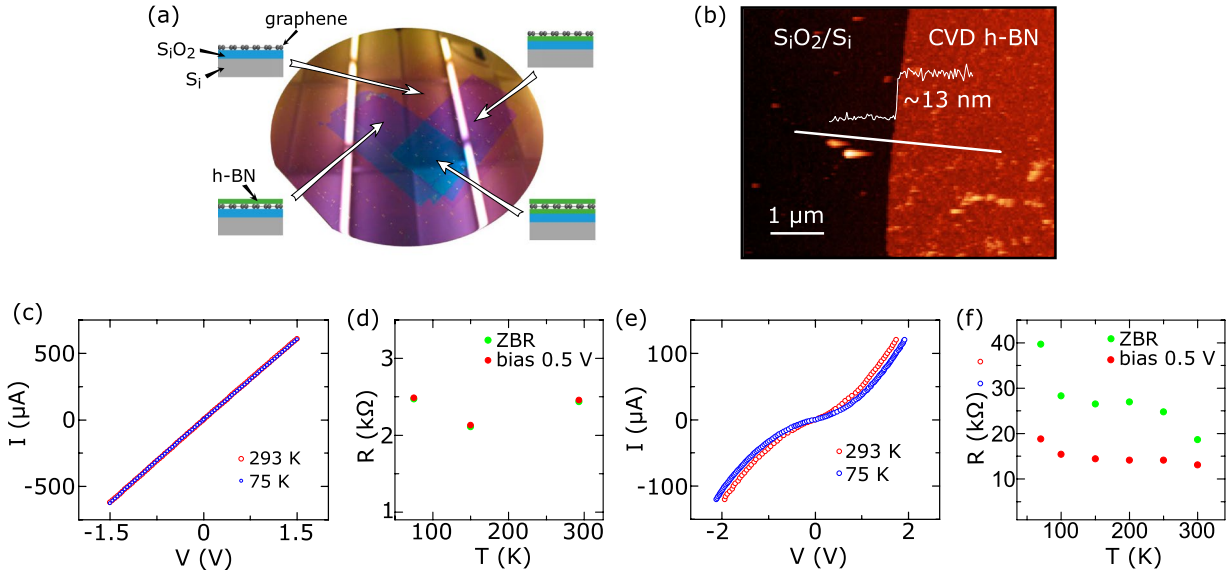

Figure 2. Characterization of the 2D heterostructures and 1D contacts. (**a**) The prepared h-BN/graphene/h-BN heterostructures using all-CVD grown 2D materials on a 4-inch SiO_2/Si wafer by layer transfer method. Different regions containing 2D layers and heterostructures are indicated by schematics. (**b**) AFM image and thickness profile of CVD h-BN on SiO_2/Si wafer. (**c**) Two-terminal IV characteristic of the device with Cr/Au edge contacts to graphene at 293 K and 75 K. (**d**) Cr/Au edge contact resistance at 0.5 V bias (red) and zero bias voltage (green) as a function of temperature. (**e**) 2-terminal IV characteristic of the device with Ti/Au edge contacts to graphene at 293 K (red) and 75 K (blue). (**f**) Ti/Au edge contact resistance at 0.5 V bias (red) and zero bias voltage (green) as a function of temperature.

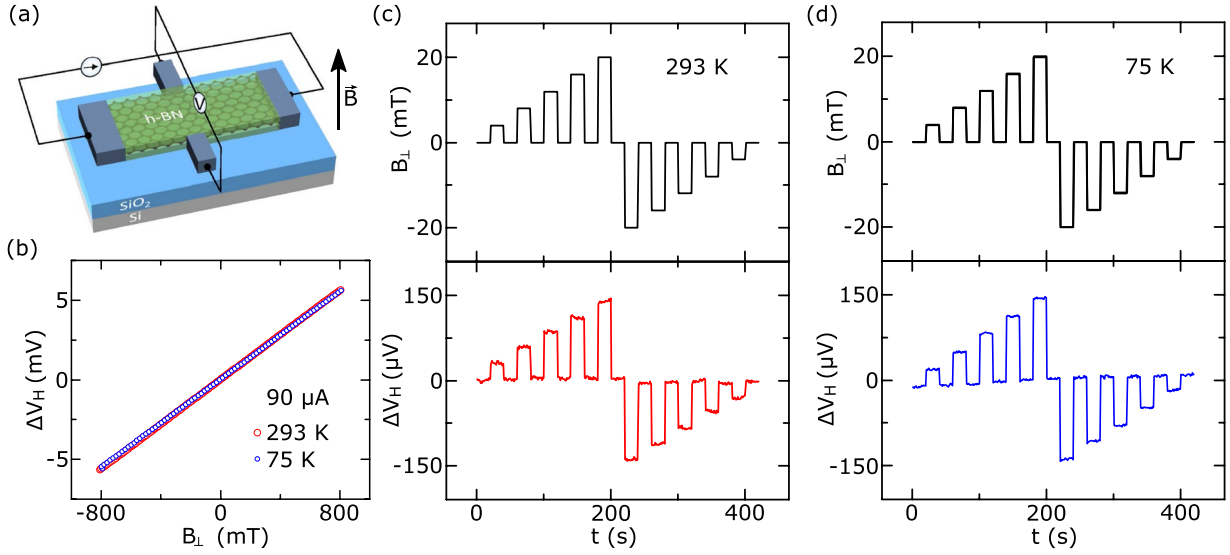

Figure 3. Characterization of the graphene Hall elements with Cr/Au 1D edge contacts. (**a**) The schematic of Hall measurements. (**b**) Hall voltage as a function of perpendicular magnetic field at 293 K and 75 K. (**c**) Hall voltage as a function of time at different applied magnetic fields at 293 K and (**d**) 75 K. Measurements are shown for a bias current of I = 90 μA and the background offset voltage is subtracted from the measured data.

elementary charge and n_{2D} is the sheet charge carrier concentration[4,11], we can extract the Hall mobilities $\mu = 1/(e|n_{2D}|R_S)$ around 1200 cm^2/Vs^{-1} with carrier concentrations around 8×10^{12} cm^{-2} at zero gate voltage. The high charge doping is most likely due to the wet transfer process that might have trapped impurities at the h-BN/graphene interfaces. The linearity error is found to be around 0.25% and independent of temperature. The Hall sensors also showed stable performance and good response to magnetic field changes in time (Fig. 3c and d).

In order to investigate the effect of the 1D edge contact material on Hall sensor performance, we also carried out measurements on devices with Ti/Au contacts. The output Hall voltage as a function of applied magnetic field

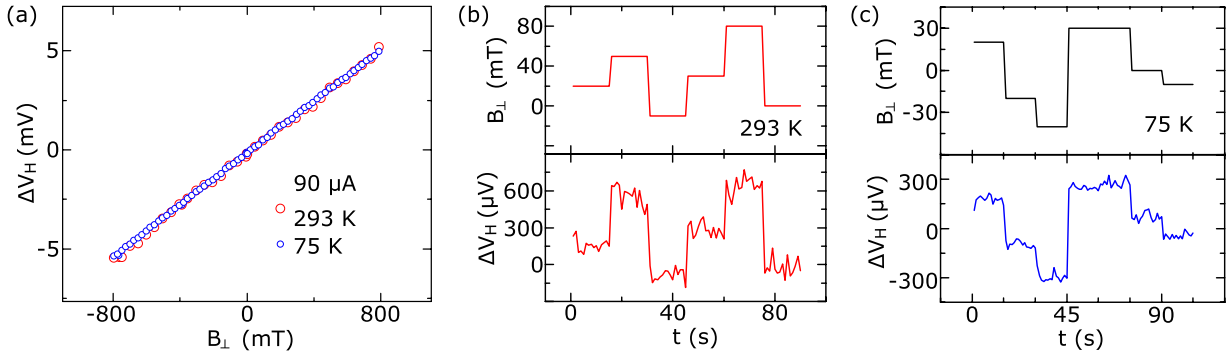

Figure 4. Characterization of the graphene Hall elements with Ti/Au 1D edge contacts. (**a**) Output Hall voltage as a function of perpendicular magnetic field strength at 293 K and 75 K. (**b**) Output Hall voltage as a function of time at different applied magnetic fields at 293 K and (**c**) 75 K. Measurements are shown at a bias current of 90 μA and the background voltage offset is subtracted from the data.

measured at 293 K and 75 K with a bias current of I = 90 μA is shown in Fig. 4a. Despite an order of magnitude higher contact resistance in Ti/Au devices, we observed a similar Hall sensitivity as in Cr/Au devices. The linearity errors in Hall measurements were found to be at an average level of ~2 % at 293 K down to ~0.4 % at 75 K, which is 2 to 8 times higher than for the Cr/Au device. Figure 4b and c show the Hall voltage responses measured as a function of time at different perpendicular magnetic fields at 293 K and 75 K, respectively. This shows that Cr/Au edge contacts perform better in terms of higher linearity of the Hall response and lower noise compared to Ti/Au. Noise spectral characterization of device with Cr/Au contacts (see Supplementary Fig. S3) revealed minimum magnetic resolution of 0.4 mT/Hz$^{0.5}$.

From the Hall measurements the current-related sensitivity $S_I = (\partial_B V_H)/I$ was extracted. Figure 5a shows the temperature dependence of S_I for the Cr/Au and Ti/Au contacts, which are found to be thermally stable with the values of $S_I \sim 75$ V/AT. The absence of temperature variation of S_I ($S_I \sim 1/n_{2D}$) is due to a stable carrier concentration (n_{2d}) in graphene. Figure 5b shows the current bias dependence with slight decrease of S_I at higher bias, which could be due to heating-related effects[19]. The more prominent bias-induced decrease of S_I with Ti/Au contacts compared to Cr/Au indicates more heating-related effects due to higher contact resistances. Comparing several different devices yields a narrow distribution of Hall sensitivity S_I (Fig. 5c) ranging from 60–97 V/AT. Furthermore, variations in geometry and size of the graphene Hall elements did not affect the sensitivity, with the S_I values ranging from 65–78 V/AT at room temperature (Fig. 5d). From the Hall measurement at constant voltage bias of 250 mV the voltage-related sensitivity for device with Cr/Au contacts was found to be 0.03 V/VT.

To compare the results of all-CVD h-BN/graphene/h-BN with differently prepared graphene Hall sensors, we have fabricated control samples of CVD graphene on SiO_2 substrate with and without exfoliated h-BN capping (see Supplementary Fig. S4). The CVD graphene devices on SiO_2 substrate without any encapsulation show S_I in the range of 100–200 V/AT at room temperature. However, we observed degradation in sensitivity with time showing values below 65 V/AT after few weeks of fabrication. The Hall sensors with exfoliated h-BN encapsulation show the current-related sensitivity up to 363 V/AT at room temperature, which is 3 to 4 times higher than the all-CVD heterostructure devices. For the control CVD graphene samples, the Hall mobility and carrier concentrations are found to be around 150 cm^2/Vs^{-1} and 2×10^{12} cm^{-2}, respectively, which is lower in comparison to all-CVD heterostructures prepared by wet transfer process. The higher carrier concentrations due to trapped impurities at the h-BN/graphene interfaces are supposed to give rise to lower Hall sensitivity in our all-CVD h-BN/graphene/h-BN Hall sensors.

In order to verify the stability of our all-CVD h-BN/graphene/h-BN Hall sensors over time in an ambient environment, we have carried out measurements up to 190 days after fabrication. The Hall voltages measured after 1, 22, 49 and 190 days from device fabrication are shown in Fig. 6a. The Hall sensors showed a good response to magnetic field changes even after 190 days (Fig. 6b) and a consistent Hall sensitivity S_I of 53–78 V/AT at room temperature (Fig. 6c), without much degradation of the contacts and the graphene channel over time. However, unencapsulated graphene showed fast degradation of sensitivity with time after fabrication of devices. The atomically thin graphene is known to degrade quickly in ambient conditions not only due to electronic doping, but also chemical and mechanical damages due to exposure to different environmental conditions[32,33]. Although the high doping of graphene in our devices can contribute to less degradation of Hall sensitivity over time, the utilized h-BN encapsulation is imperative step forward towards protection of graphene for practical applications in ambient environment.

Discussion

Our observed current-related Hall sensitivities in large area all-CVD h-BN encapsulated graphene devices are comparable to those in magnetic Hall sensors based on Si[4–7]. However, sensitivities were at least one order of magnitude below exfoliated graphene/h-BN structures[17], unprotected CVD graphene devices on Si/SiO_2 substrate[12] and on CVD h-BN substrate[19]. Also, our control experiment with CVD graphene on SiO_2 substrate with/without exfoliated h-BN capping showed 2–4 times higher sensitivity. However, the unprotected graphene showed faster

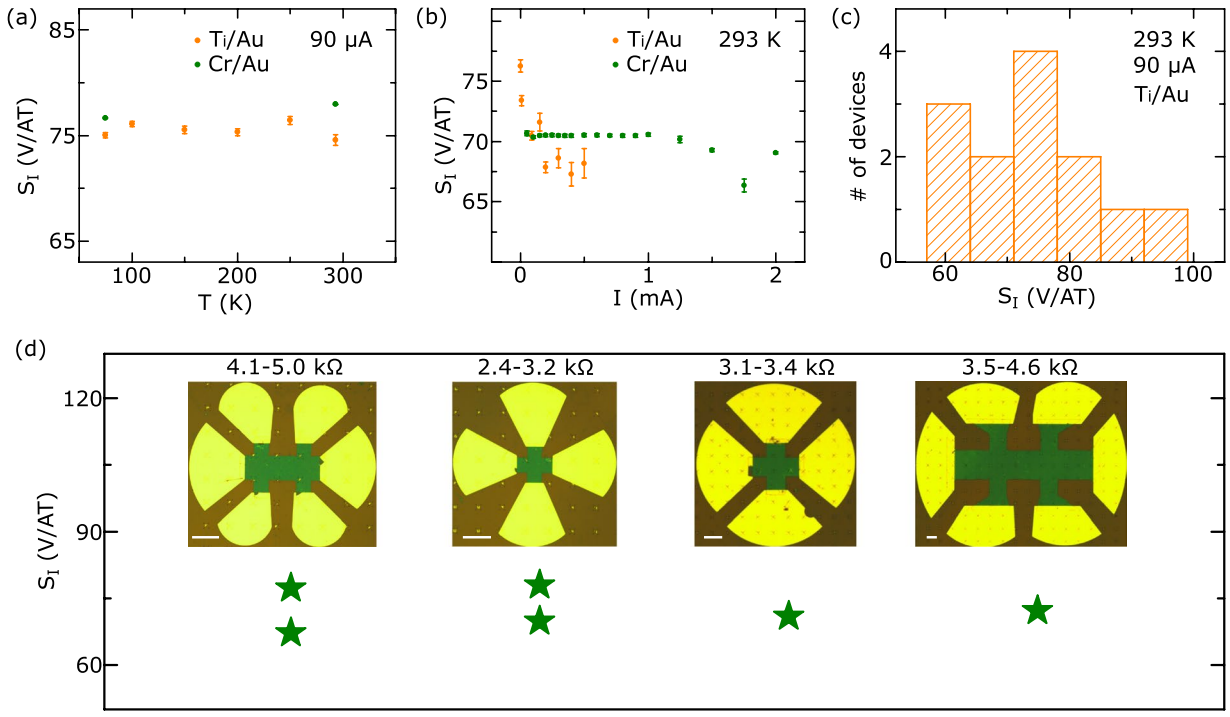

Figure 5. Current-related sensitivities (S_I) of graphene Hall elements. (**a**) Temperature dependence of S_I for Cr/Au and Ti/Au contacts measured at 90 μA current bias. (**b**) Current bias dependence of S_I for Cr/Au and Ti/Au contacts at room temperature. (**c**) Distribution of sensitivities S_I measured in 13 Hall elements with Ti/Au contacts at 90 μA current bias and at room temperature. The devices were selected from different parts of the wafer. (**d**) Sensitivities S_I for Hall sensors measured on devices with different size and geometry (Cr/Au contacts). Typical two-terminal resistances are shown with average resistivity value of ~75–100 kΩ·μm (graphene sheet concentration ~$8.5 \cdot 10^{12}$ cm^{-2}). Scale bars in the inset images are 60 μm.

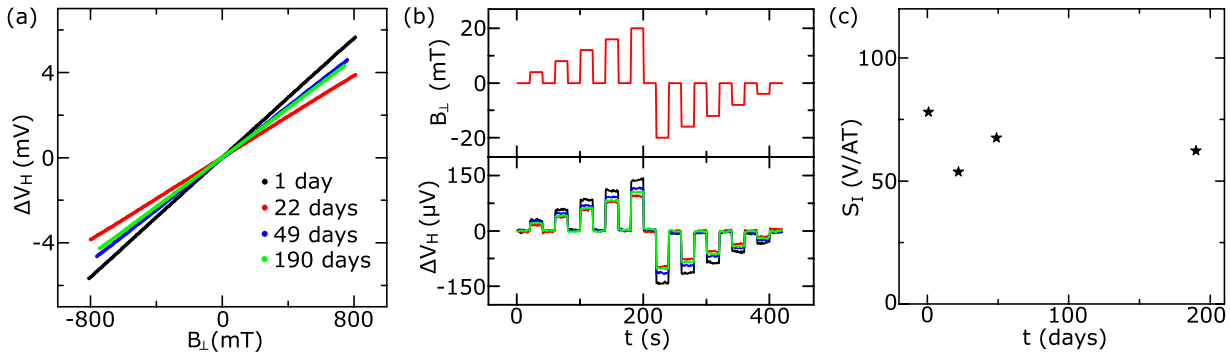

Figure 6. Stability of all-CVD h-BN/Graphene/h-BN Hall sensors over time in ambient environment. (**a**) Hall voltage as a function of magnetic field and (**b**) time at different applied magnetic fields at 293 K after keeping the device in ambient environment for 1 day (black), 22 days (red), 49 days (blue) and 190 days (green). (**c**) Current-related Hall sensitivity S_I over time.

degradation of sensitivity with time. The higher sensitivity of devices with exfoliated h-BN encapsulation can be due to introduction of roughness, ripples and wrinkles in the CVD graphene in all-CVDh-BN/graphene/h-BN heterostructures. The CVD grown multilayer h-BN films are known to be polycrystalline in nature and the c-axis of the crystallites points to random directions[30], giving rise to defects and roughness in the heterostructures. The significant doping of graphene in the all-CVD heterostructure devices is another major reason behind the reduced Hall sensitivities and it could be due to contaminations introduced during wet-transfer process of large area graphene and h-BN layers. This could explain also the significantly lower minimum magnetic field resolution of Hall sensors based on all-CVD h-BN/graphene/h-BN heterostructures compared to previous reports on graphene Hall sensors[17,19–22]. These are currently the practical challenges for the development of graphene and 2D materials science and technology.

Such Hall sensors would greatly benefit from improved CVD growth methods of graphene and multi-layer h-BN, and large area layer transfer techniques for fabrication of heterostructures. Furthermore, development of methods for *in-situ* growth[34–36] of high-quality h-BN/graphene/h-BN van der Waals heterostructures on large areas would by-pass fabrication-related problems and allow for higher Hall sensitivities with lower graphene doping levels. Additionally, the contacts resistance in 1D geometry can also play an important role on device performance. Our reported reduction in contact resistance by switching from Ti to Cr can be further improved by optimizing the fabrication process, in particular the etching angle and 1D edge contact deposition to eliminate incorporated species at the interfaces[24].

Conclusion

In summary, we demonstrated h-BN/graphene/h-BN van der Waals heterostructure Hall sensors using all-CVD 2D materials available on the market. The batch-fabricated Hall sensors with Cr/Au 1D edge contacts showed reproducible contact properties with low resistances. Hall measurements and time-dependent response at different applied magnetic fields revealed current-related Hall sensitivities in the range of 60–97 V/AT at room temperature. Such encapsulated Hall sensors also showed durable operations in ambient environmental conditions over six months. This study demonstrates proof-of-concept batch fabrication of fully encapsulated all-CVD graphene Hall elements allowing for further development towards practical applications.

References

1. Magnetic Field Sensors Market by Type (Hall Effect, Magnetoresistive (AMR, GMR, TMR), MEMS-based, SQUID, Fluxgate), Range (10 gauss), Application, End-User Industry - Global Forecasts to 2022. *Markets and Markets* (2016).
2. Díaz-Michelena, M. Small magnetic sensors for space applications. *Sensors* **9**, 2271–2288 (2009).
3. Magnetic Sensors Market Analysis By Technology (Hall Effect Sensing, AMR, GMR), By Application (Automotive, Consumer Electronics, Industrial) And Segment Forecasts To 2022. *Grand View Research* (2016).
4. Popovic, R. S. *Hall Effect Devices*. (Institute of Physics, 2003).
5. Boero, G., Demierre, M., Besse, P. A. & Popovic, R. S. Micro-Hall devices: Performance, technologies and applications. *Sensors Actuators A* **106**, 314–320 (2003).
6. Vervaeke, K., Simoen, E., Borghs, G. & Moshchalkov, V. V. Size dependence of microscopic Hall sensor detection limits. *Rev. Sci. Instrum.* **80**, 74701 (2009).
7. Kejik, P., Boero, G., Demierre, M. & Popovic, R. S. An integrated micro-Hall probe for scanning magnetic microscopy. *Sensors Actuators A* **129**, 212–215 (2006).
8. Kunets, V. P. *et al.* Highly sensitive micro-Hall devices based on Al0.12In0.88Sb/InSb heterostructures. *J. Appl. Phys.* **98**, 14506 (2005).
9. Hara, T., Mihara, M., Toyoda, N. & Zama, M. Highly Linear Gaas Hall Devices Fabricated By Ion Implantation. *IEEE Trans. Electron Devices* **ED-29**, 78–82 (1982).
10. Bando, M. *et al.* High sensitivity and multifunctional micro-Hall sensors fabricated using InAlSb/InAsSb/InAlSb heterostructures. *J. Appl. Phys.* **105**, 07E909 (2009).
11. Heremans, J. Solid state magnetic field sensors and applications. *J. Phys. D. Appl. Phys.* **26**, 1149–1168 (1993).
12. Xu, H. *et al.* Batch-fabricated high-performance graphene Hall elements. *Sci. Rep.* **3**, 1207 (2013).
13. Panchal, V. *et al.* Small epitaxial graphene devices for magnetosensing applications. *J. Appl. Phys.* **111**, 07E509 (2012).
14. Karpiak, B., Dankert, A. & Dash, S. P. Gate-tunable Hall sensors on large area CVD graphene protected by h-BN with 1D edge contacts. *J. Appl. Phys.* **122**, 54506 (2017).
15. Alexander-Webber, J. A. *et al.* Encapsulation of graphene transistors and vertical device integration by interface engineering with atomic layer deposited oxide. *2D Mater.* **4**, 11008 (2017).
16. Dean, C. R. *et al.* Boron nitride substrates for high-quality graphene electronics. *Nat. Nanotechnol.* **5**, 722–726 (2010).
17. Dauber, J. *et al.* Ultra-sensitive Hall sensors based on graphene encapsulated in hexagonal boron nitride. *Appl. Phys. Lett.* **106**, 193501 (2015).
18. Wang, Z. *et al.* Encapsulated graphene-based Hall sensors on foil with increased sensitivity. *Phys. Status Solidi B* **253**, 2316–2320 (2016).
19. Joo, M.-K. *et al.* Large-Scale Graphene on Hexagonal-BN Hall Elements: Prediction of Sensor Performance without Magnetic Field. *ACS Nano* **10**, 8803–8811 (2016).
20. Huang, L. *et al.* Ultra-sensitive graphene Hall elements. *Appl. Phys. Lett.* **104**, 183106 (2014).
21. Ciuk, T. *et al.* Low-noise epitaxial graphene on SiC Hall effect element for commercial applications. *Appl. Phys. Lett.* **108**, 223504 (2016).
22. Xu, H. *et al.* Flicker noise and magnetic resolution of graphene hall sensors at low frequency. *Appl. Phys. Lett.* **103**, 112405 (2013).
23. Wang, Z., Shaygan, M., Otto, M., Schall, D. & Neumaier, D. Flexible Hall sensors based on graphene. *Nanoscale* **8**, 7683–7687 (2016).
24. Wang, L. *et al.* One-dimensional electrical contact to a two-dimensional material. *Science* **342**, 614 (2013).
25. Graphenea Inc. Available at: http://www.graphenea.com.
26. Graphene Supermarket. Available at: https://graphene-supermarket.com.
27. Kamalakar, V. M., Groenveld, C., Dankert, A. & Dash, S. P. Long distance spin communication in chemical vapour deposited graphene. *Nat. Commun.* **6**, 6766 (2015).
28. Ferrari, A., Meyer, J. C., Scardaci, C., Casiraghi, C. & Lazzeri, M. Raman Spectrum of Graphene and Graphene Layers. *Phys. Rev. Lett.* **97**, 187401 (2006).
29. Gorbachev, R. V. *et al.* Hunting for monolayer boron nitride: Optical and raman signatures. *Small* **7**, 465–468 (2011).
30. Kim, K. K. *et al.* Synthesis and Characterization of Hexagonal Boron Nitride Film as a Dielectric Layer for Graphene Devices. *ACS Nano* **6**, 8583–8590 (2012).
31. Jönsson-Åkerman, B. J. *et al.* Reliability of normal-state current–voltage characteristics as an indicator of tunnel-junction barrier quality. *Appl. Phys. Lett.* **77**, 1870 (2000).
32. Roy, S. S., Safron, N. S., Wu, M. & Arnold, M. S. Evolution, kinetics, energetics, and environmental factors of graphene degradation on silicon dioxide. *Nanoscale* **7**, 6093–6103 (2015).
33. Yang, Y., Brenner, K. & Murali, R. The influence of atmosphere on electrical transport in graphene. *Carbon N. Y.* **50**, 1727–1733 (2012).
34. Tang, S. *et al.* Nucleation and growth of single crystal graphene on hexagonal boron nitride. *Carbon N. Y.* **50**, 329–331 (2012).
35. Tang, S. *et al.* Silane-catalysed fast growth of large single-crystalline graphene on hexagonal boron nitride. *Nat. Commun.* **6**, 6499 (2015).
36. Tang, S. *et al.* Precisely aligned graphene grown on hexagonal boron nitride by catalyst free chemical vapor deposition. *Sci. Rep.* **3**, 2666 (2013).

Acknowledgements

We acknowledge other financial support from EU Graphene Flagship (No. 604391), EU FlagEra project (No. 2015-06813), Swedish Research Council grants (No. 2012-04604 and No. 2016-03658), Graphene center and AoA Nano program at Chalmers University of Technology. AD acknowledges financial support from the Chalmers Innovation office. BK acknowledges scholarship from EU Erasmus Mundus Nanoscience and Nanotechnology master programme. We acknowledge the service by Graphenea for the layer transfer of 2D materials and support from Chalmers Nanofabrication facility.

Author Contributions

A.D. and B.K. carried out the device fabrication and measurements, and equally contributed. S.P.D. supervised the research. B.K. wrote the manuscript with input from all authors.

Additional Information

Supplementary information accompanies this paper at https://doi.org/10.1038/s41598-017-12277-8.

Competing Interests: The authors declare that they have no competing interests.

Publisher's note: Springer Nature remains neutral with regard to jurisdictional claims in published maps and institutional affiliations.

Paper IV

2D Materials

OPEN ACCESS

RECEIVED
15 August 2019

REVISED
23 October 2019

ACCEPTED FOR PUBLICATION
19 November 2019

PUBLISHED
11 December 2019

PAPER

Magnetic proximity in a van der Waals heterostructure of magnetic insulator and graphene

Bogdan Karpiak[1], Aron W Cummings[2], Klaus Zollner[3], Marc Vila[2,4], Dmitrii Khokhriakov[1], Anamul Md Hoque[1], André Dankert[1], Peter Svedlindh[5], Jaroslav Fabian[3], Stephan Roche[2,6] and Saroj P Dash[1,7,8]

[1] Department of Microtechnology and Nanoscience, Chalmers University of Technology, SE-41296, Göteborg, Sweden
[2] Catalan Institute of Nanoscience and Nanotechnology (ICN2), CSIC and The Barcelona Institute of Science and Technology, Campus UAB, Bellaterra, 08193 Barcelona, Spain
[3] Institute for Theoretical Physics, University of Regensburg, 93040 Regensburg, Germany
[4] Department of Physics, Universitat Autònoma de Barcelona, Campus UAB, Bellaterra, 08193 Barcelona, Spain
[5] Division of Solid-State Physics, Department of Engineering Science, Uppsala University, Box 534, SE-75121 Uppsala, Sweden
[6] ICREA—Institució Catalana de Recerca i Estudis Avançats, 08010 Barcelona, Spain
[7] Graphene Center, Chalmers University of Technology, SE-41296, Göteborg, Sweden
[8] Author to whom any correspondence should be addressed.

E-mail: saroj.dash@chalmers.se

Keywords: graphene, 2D ferromagnet, van der Waals heterostructures, $Cr_2Ge_2Te_6$, proximity effect, magnetism, spin anisotropy

Supplementary material for this article is available online

Abstract

Engineering 2D material heterostructures by combining the best of different materials in one ultimate unit can offer a plethora of opportunities in condensed matter physics. Here, in the van der Waals heterostructures of the ferromagnetic insulator $Cr_2Ge_2Te_6$ and graphene, our observations indicate an out-of-plane proximity-induced ferromagnetic exchange interaction in graphene. The perpendicular magnetic anisotropy of $Cr_2Ge_2Te_6$ results in significant modification of the spin transport and precession in graphene, which can be ascribed to the proximity-induced exchange interaction. Furthermore, the observation of a larger lifetime for perpendicular spins in comparison to the in-plane counterpart suggests the creation of a proximity-induced anisotropic spin texture in graphene. Our experimental results and density functional theory calculations open up opportunities for the realization of proximity-induced magnetic interactions and spin filters in 2D material heterostructures and can form the basic building blocks for future spintronic and topological quantum devices.

Introduction

Topological quantum states of matter and spintronics have considerable interest in the field of condensed matter physics for applications in low-power electronics without the application of an external magnetic field [1, 2]. The generation of magnetic exchange interaction and strong spin–orbit coupling in two-dimensional (2D) Dirac materials such as graphene is expected to result in the emergence of quantum anomalous Hall state and topologically protected chiral spin textures [3, 4]. Graphene, having excellent charge and spin transport properties, is a suitable atomically-thin 2D material to create proximity-induced effects when placed in heterostructures with other functional materials [5–7]. Proximity-induced magnetic effects have been investigated in 2D semiconductors on graphene in heterostructures with ferromagnetic semiconductors [8] and magnetic oxides [9–16]. However, there are severe challenges in producing a sizable out-of-plane exchange interaction in magnetic oxide-graphene structures due to the in-plane magnetic anisotropy of the oxide-based magnetic insulators used so far with graphene [13].

To create significant proximity-induced magnetic interaction in graphene, the use of a magnetic insulator with perpendicular magnetic anisotropy is desired. Additionally, for a good interface, atomically-flat layered 2D material-based van der Waals heterostructures (vdWh) are ideal [1–4]. Recently, 2D magnetic materials were successfully prepared

via exfoliation down to the monolayer limit, showing intrinsic long-range Heisenberg ferromagnetic order [17–19] that is tunable by application of a gate voltage [20–22]. Additionally, giant tunneling magnetoresistance, spin filtering and magnon-assisted tunneling phenomenon have been demonstrated using such 2D magnetic materials [23–27]. Recently, heterostructures of such 2D magnetic materials with 2D semiconductors [8], topological insulators [28], semimetals [29] and graphene [27] have also been investigated. Theoretical predictions indicate that heterostructures of 2D magnetic insulators with graphene are expected to produce a large exchange splitting in the graphene layer, enabling the emergence of a topological quantum phase [30–32].

Here, we use van der Waals heterostructures of graphene with the ferromagnetic insulator $Cr_2Ge_2Te_6$ (CGT) having a perpendicular magnetic anisotropy to demonstrate a proximity-induced magnetic exchange interaction, which is revealed by the temperature-dependent splitting of Hanle spin precession signals. The observed anisotropic spin relaxation indicates a possible nontrivial spin texture imprinted in graphene by proximity to CGT. The demonstration of out-of-plane proximity-induced magnetism induced in graphene is a crucial step towards realizing more exotic electronic states in 2D material heterostructures.

Results

The van der Waals heterostructures are prepared by dry-transferring CGT flakes (∼ 30 nm in thickness) onto chemical vapor deposited (CVD) graphene on a SiO_2/n-Si substrate in a cleanroom environment within one minute after exfoliation. The atomic structure of the CGT flakes consists of van der Waals layers of Cr atoms sandwiched by Te and Ge atoms with an interlayer distance of ∼ 6.9 Å (figure 1(a)) [33, 34]. The choice of CGT is motivated by its layered structure, insulating behavior [30, 35], and perpendicular magnetic anisotropy [17]. CGT is expected to induce a magnetic exchange interaction in graphene, splitting the spin-degenerate graphene bands by a characteristic exchange ΔE_{ex} (figure 1(b)). The Raman spectrum of the CGT flake in a heterostructure with graphene is shown in figure 1(c). It contains the phonon mode at 108 cm^{-1}, which is characteristic of a CGT flake with more than one layer [36]. We do not observe any broad peak at 121 cm^{-1}, characteristic of an oxidized CGT surface (supplement figure S1 (stacks.iop.org/TDM/7/015026/mmedia)) after long exposure to the ambient atmosphere, indicating absence of substantial oxidation in freshly cleaved CGT flakes. The Raman spectrum of the CVD deposited graphene channel (figure 1(c)) contains a 2D peak (2642 cm^{-1}) of stronger intensity than the G peak (1600 cm^{-1}), indicating monolayer thickness of graphene [37]. Magnetic characterization of the bulk CGT crystal by SQUID magnetometry shows perpendicular magnetic anisotropy of the material (figure 1(d)). From the temperature dependence of the magnetization of the bulk CGT crystal under a perpendicularly applied magnetic field of 100 mT (figure 1(e)), one can observe two magnetic ordering temperatures. By fitting the inverse magnetic susceptibility according to the Curie–Weiss law $\frac{1}{\chi} = \frac{(T-Tc)^{\gamma}}{C}$ (inset in figure 1(e)), values of the transition temperatures of ∼65 K ($\gamma = 1$) and ∼204 K ($\gamma \approx 1.6$) were obtained. The former shows a more distinct magnetization enhancement with deceasing temperature. The magnetic moment m of the high temperature ($T_c \sim 204$ K) phase is, however, two orders of magnitude smaller than that of the main magnetic phase ($T_c \sim 65$ K). The presence of a magnetic transition at higher temperature (figure 1(e) and supplement figure S2) could be due to imperfections in the lattice structure or an extra magnetic phase leading to a magnetic transition at higher temperature in the regions of the material with broken stoichiometry and lattice defects.

Magnetic proximity effect in graphene-$Cr_2Ge_2Te_6$ heterostructures

The device schematic and an optical microscope image of a nanofabricated device consisting of a graphene–CGT heterostructure channel are shown in figures 2(a) and (b) (see methods for details about the device fabrication process). The ferromagnetic tunnel contacts of Co/TiO_2 on graphene are used for injection and detection of the spin-polarized current in the heterostructure channel, with three-terminal contact resistances of 3–6 kΩ at room temperature (supplement figure S3). In such graphene-CGT heterostructure devices, we probe the proximity-induced exchange interaction by employing spin transport and Hanle precession measurements. The insulating behavior of CGT (two-terminal resistance ∼ 60 MΩ) allows charge carriers to flow mostly in the graphene layer with a field-effect mobility of ∼2400 cm^2 V^{-1} s^{-1} in the heterostructure channel (supplement figure S4).

First, spin-valve and Hanle precession measurements were carried out at room temperature (300 K), well above the T_c of CGT, to check the functionality of the heterostructure devices in a nonlocal (NL) configuration (see figure 2(a)). A NL spin resistance change $\Delta R_{NL} = \Delta V_{NL}/I \approx 5.5$ mΩ was measured at 300 K while sweeping the in-plane magnetic field ($B_{\parallel}$) along the easy axis of the Co contacts in a device with channel length $L = 6.9$ μm (figure 2(c)). Next, Hanle measurements were conducted in the NL configuration but with an out-of-plane applied magnetic field ($B_{\perp}$), which causes in-plane Larmor precession of spins as they propagate through the heterostructure channel. Such measurements at room temperature (figure 2(d)) for both up and down magnetic field sweeps showed conventional Hanle signals without any special features [38]. By fitting the data with the

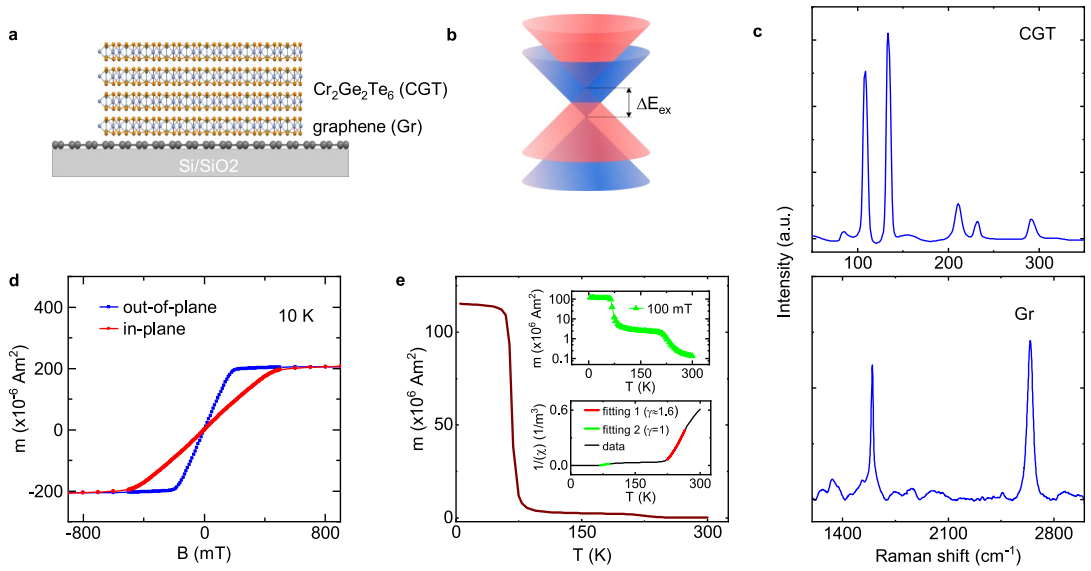

Figure 1. Characterization of $Cr_2Ge_2Te_6$ and its heterostructure with graphene. (a) Schematic of atomic structure of CGT/graphene heterostructure. (b) Schematic of graphene band structure in proximity with CGT in the vicinity of the Dirac point. Graphene can acquire magnetic order with a splitting of spin-degenerate bands by an exchange gap ΔE_{ex}. (c) Raman spectrum of CGT (top panel) and graphene (bottom panel) in the heterostructure. (d) Field dependence of magnetic moment (m) of bulk CGT crystal as a function of magnetic field at 10 K for both in-plane and out-of-plane magnetic field directions. (e) Temperature dependence of magnetic moment m of CGT under perpendicular magnetic field of 100 mT. Top inset shows the same data as in main panel but with log scale on vertical axis. Bottom inset shows inverse magnetic susceptibility as a function of temperature fitted with the Curie–Weiss law.

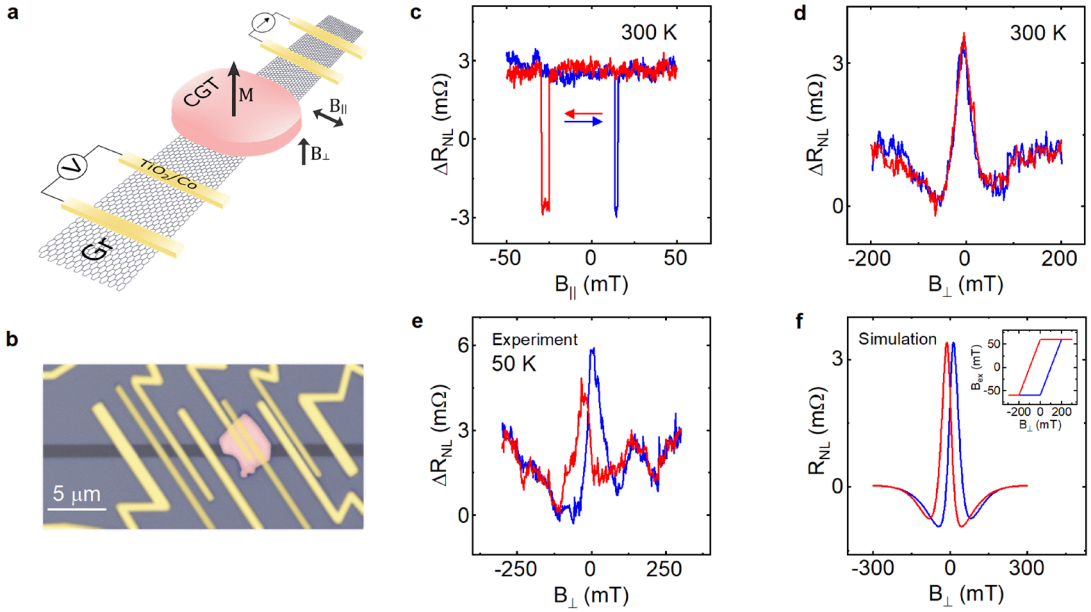

Figure 2. Magnetic proximity effect in graphene-$Cr_2Ge_2Te_6$ heterostructures. (a) and (b) Schematic and false-color optical microscope picture of graphene-CGT heterostructure with ferromagnetic tunnel contacts of TiO_2 (1 nm)/Co (60 nm). The scale bar is 5 μm. (c) and (d) Spin valve and Hanle spin precession signals measured in graphene-CGT heterostructure for in-plane and out-of-plane magnetic field directions, respectively, at 300 K, above the Curie temperature of CGT. The up and down magnetic field sweep directions are represented by blue and red colors. (e) The measured Hanle signal at 50 K, below the Curie temperature of CGT. (f) Simulated Hanle signal for typical channel parameters (see supplementary note 1 for details) with partial overlap of the graphene by CGT. The inset shows the assumed hysteresis for CGT flake in the simulations. The overlap area of the graphene-CGT heterostructure in the device channel is ~60%.

solution of the Bloch equation that describes spin dynamics in the channel with an applied $B_\perp$ [38], the spin lifetime $\tau_s = 244 \pm 32$ ps, diffusion coefficient $D_s = 0.019 \pm 0.005$ m^2 s^{-1} and diffusion length $\lambda = 2.1 \pm 0.4$ μm were obtained.

At low temperatures (50 K), below the Curie point of CGT (figure 2(e)), one can notice two distinctive features of the measured Hanle signal: a shift of the two Hanle peaks with respect to each other and asymmetry of the Hanle peak. Such observations are indicative of

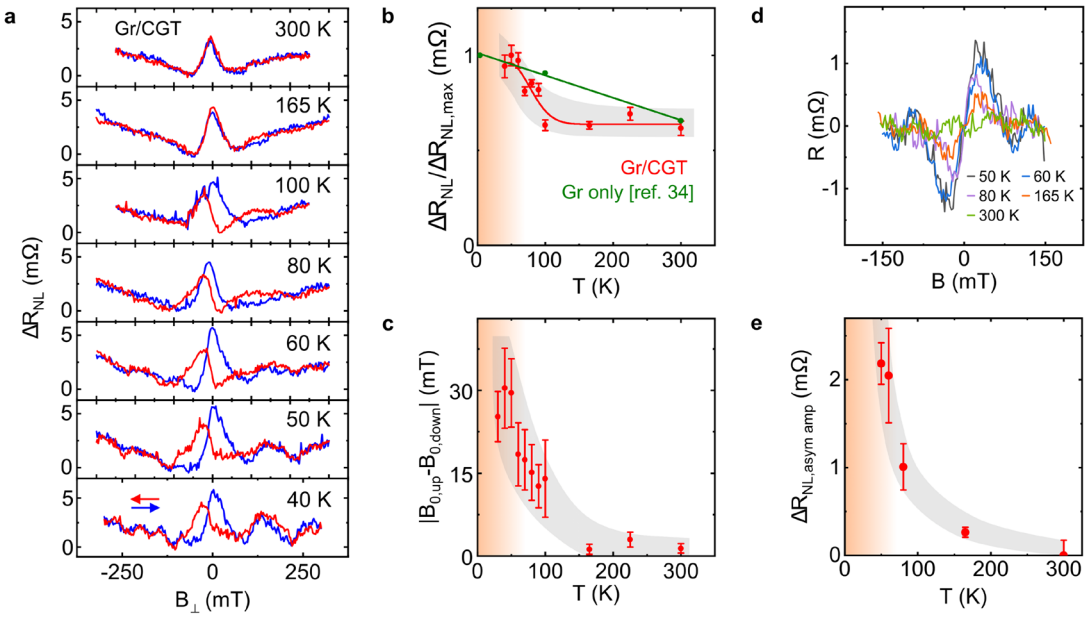

Figure 3. Temperature dependence of spin signal in graphene-$Cr_2Ge_2Te_6$ heterostructures. (a) Nonlocal Hanle spin precession measurements in the graphene-CGT heterostructure as a function of perpendicular magnetic field for up (blue) and down (red) sweeps at different temperatures. (b) Normalized nonlocal Hanle signal amplitudes (ΔR_{NL}) as a function of temperature for a graphene-CGT device and for a 4 μm CVD graphene channel [38] (green). (c) Magnitude of the horizontal separation between positions of nonlocal Hanle signal peaks for up ($B_{0,up}$) and down ($B_{0,down}$) sweeps as a function of temperature. (d) Asymmetric part of the measured Hanle signal at different temperatures. (e) Amplitude of the asymmetric signal from d as a function of temperature. The solid lines in b and grey regions in (b), (c) and (e) are guides to the eye.

an out-of-plane magnetism induced in the graphene by proximity to CGT. These features are also seen in simulations (figure 2(f) and supplementary note 1) obtained from the solution of the Bloch equation that considers a magnetic exchange interaction in graphene due to the influence of the CGT flake [39]. The CGT flake can induce ferromagnetism in the underlying graphene via the exchange field B_{ex}, which adds to the external magnetic field, $B_\perp \rightarrow B_\perp + B_{ex} + B_s$, and thus modifies the Hanle spin precession signal in the heterostructure channel. While the stray fields B_s do contribute to the spin precession in the channel in a similar way as B_{ex}, the observed Hanle signals are mainly shaped by the contributions from externally applied and exchange fields (see supplementary note 2). The peak splitting between the two Hanle sweeps can then originate from hysteretic behavior [20] of the proximity-induced magnetic exchange fields in graphene. This alters the position of the Hanle peak corresponding to zero total field, which, due to hysteresis, is obtained at different values of the applied magnetic field depending on the sweep direction.

Meanwhile, the asymmetry of the Hanle peak arises from the spatial inhomogeneity of the proximity-induced exchange field; a finite graphene-CGT interfacial region leads to an asymmetry, while CGT covering the entire graphene flake would result in a symmetric Hanle curve (see supplementary note 1). Since hysteresis gives opposite shifts of the exchange field depending on the sweep direction, this is reflected in the opposite asymmetry of the measured Hanle signals (figures 2(e) and (f)). The measurements in the two devices with different CGT/graphene channel overlaps by the CGT flake confirm decreased asymmetry with increased channel overlap (supplementary note 3), which is in agreement with simulation results (supplementary note 1).

To further elucidate the proximity-induced magnetic interaction in graphene-CGT heterostructures, the Hanle spin precession measurements were performed at several different temperatures in a systematic manner (figure 3(a)). The measured data reveal a rapid decrease of the nonlocal spin signal amplitude (R_{NL}) with increasing temperature in comparison to the temperature dependence of pristine graphene (figure 3(b)) [38], followed by a saturation of the signal above the curie temperature of the CGT. The rapid spin signal amplitude decay with temperature in the range of $T < T_c$, compared to pristine graphene [38], can be attributed to fluctuating proximity-induced magnetic exchange fields due to random fluctuations of the magnetization of the CGT flake, which become more pronounced approaching the magnetic ordering temperature of CGT [15]. Such fluctuations cause random changes of the proximity-induced exchange field and, hence, the effective field that acts on the propagating spins, leading to enhanced spin relaxation [40, 41]. Furthermore, the separation between the peaks for opposite Hanle sweeps vanishes at elevated temperatures (figure 3(c)).

The presence of Hanle peak shifts indicates that the proximity-induced exchange field in graphene persists above the Curie temperature for bulk CGT [28] ($\sim$ 65 K) up to at least 100 K. Additionally, one can deconvolute

the measured Hanle signal into symmetric and asymmetric components, where the latter contains information on additional rotation of spins in the channel [42] with respect to normal precession caused by the applied perpendicular magnetic field. Such rotation can originate e.g. from the modified spin texture of graphene under the CGT flake caused by the proximity to the latter. From figures 3(d) and (e) one can see that the asymmetric contribution to the signal also vanishes with increasing temperature in a comparable way as in figure 3(c). This suggests the same origin for peak splitting and asymmetry—both can arise from the proximity-induced exchange field in the graphene channel under the flake, which persists at $T > T_c$ of bulk CGT and decays with increasing temperature, while being completely absent at temperatures above 165 K. Fitting the symmetric component of the Hanle signal with the solution of the Bloch equation for spin diffusion in a homogeneous channel gives values of the in-plane spin lifetimes $\tau_\parallel$ in the range of 90–280 ps; the comparably large spread of values results due to a large number of free fitting parameters (see supplementary note 4). However, most fits resulting in reasonable spin transport parameters yielded an exchange field on the order of a few 10s of mT.

Anisotropic spin relaxation in graphene-CGT insulator heterostructures

The proximity-induced exchange interactions in the graphene-based heterostructures can also result in spin relaxation anisotropy. Here we observe spin relaxation anisotropy in graphene-CGT heterostructures by employing the same NL Hanle measurement configuration. However, here the field sweep range is broader, allowing the injection and detection of both in-plane and out-of-plane spins in different field ranges. In-plane spins are injected and detected at low field values when the contacts are magnetized in-plane at magnetic fields $B_\perp < 0.4$ T (figure 4(a)). With increasing out-of-plane field the magnetization of the contacts starts to rotate to the out-of-plane direction, reaching saturation at $B_\perp > 2$ T (figure 4(b)). When spins relax with different rates in the in-plane or out-of-plane direction, different amplitudes of the signal are observed for the corresponding magnetic field ranges (figure 4(c)). Therefore, the in-plane spin lifetime $\tau_{||}$ is estimated from low $B_\perp$-field Hanle data, while the out-of-plane spin lifetime $\tau_\perp$ is extracted from large out-of-plane $B_\perp$-field measurements. As shown in figure 4(d), in the graphene-CGT heterostructure the spin signal magnitudes at $B_\perp = 0$ for in-plane spins ($\Delta R_{\mathrm{NL}}^{||}$) and at $B_\perp = 2.5$ T for spins perpendicular to plane ($\Delta R_{\mathrm{NL}}^{\perp}$) show strong anisotropy, with $\Delta R_{\mathrm{NL}}^{\perp} > \Delta R_{\mathrm{NL}}^{||}$ and with a ratio $\Delta R_{\mathrm{NL}}^{\perp}/\Delta R_{\mathrm{NL}}^{||} \sim 10$. The spin lifetime anisotropy $r \equiv \tau_\perp/\tau_{||}$ is obtained from $\Delta R_{\mathrm{NL}}^{\perp}/\Delta R_{\mathrm{NL}}^{||} = \sqrt{r}e^{-(L/\lambda_{||})(\frac{1}{\sqrt{r}}-1)}$, where L is the channel length and $\lambda_{||}$ is the spin diffusion length for in-plane spins [43]. From this expression we find a strong anisotropy, with $\tau_\perp$ being 3.9 times the value of $\tau_{||} \sim 150$ ps (assuming homogeneous channel characteristics). Such observations are in contrast with the isotropic spin relaxation in pristine graphene channels, which have a value of r close to 1 (0.94 ± 0.01 in figure 4(e)).

The observed anisotropic spin relaxation in graphene-CGT heterostructures could occur, for example, if spin relaxation is dominated by the so-called valley-Zeeman spin–orbit coupling (SOC), similar to the case of graphene on transition metal dichalcogenides [44, 45]. Valley-Zeeman SOC (λ_{VZ}) generates an out-of-plane spin texture that, in the presence of strong inter-valley scattering (τ_{iv}), quickly relaxes the in-plane spins and results in large anisotropy. To determine the type and magnitude of SOC induced in graphene by CGT, we perform density functional theory (DFT) simulations of the graphene-CGT heterostructure (see methods and supplementary note 5). By evaluating the band splitting at both K and K' valleys, we obtain a Rashba SOC $\lambda_{\mathrm{R}} = 0.253$ meV and $\lambda_{\mathrm{VZ}} = 0.113$ meV. Assuming $\tau_{\mathrm{iv}} = (5-10)\,\tau_{\mathrm{p}}$, where τ_{p} is the momentum scattering time, we obtain an anisotropy of the order $r = (\lambda_{\mathrm{VZ}}/\lambda_{\mathrm{R}})^2\,(\tau_{\mathrm{iv}}/\tau_{\mathrm{p}}) + 1/2 = 1.5$–$2.5$.

While SOC can induce a spin lifetime anisotropy $r > 1$, the temperature dependence of the spin signal in figure 3(b) suggests that magnetic exchange fluctuations are playing a role in the spin relaxation. In this scenario, an apparent spin relaxation anisotropy can also emerge. In case of the exchange fluctuation mechanism the spins are dephased by the fluctuations, but if magnetic field is applied the fluctuations are suppressed. This is different for spins parallel and perpendicular to the applied magnetic field, which results in an increase of anisotropy with increasing out-of-plane magnetic field $B_\perp$. Assuming that exchange fluctuations are the sole source of spin relaxation in the graphene-CGT devices, we find that the spin relaxation is nearly completely isotropic ($r \approx 1.002$) at $B_\perp = 0$ and becomes anisotropic with increasing values of $B_\perp$ (see supplementary note 6). This analysis indicates that if the spin relaxation is dominated by exchange fluctuations, the large anisotropy seen in figure 4(d) can be driven by the external field $B_\perp$ and may not be intrinsic to the graphene/CGT interface. This is because the perpendicular proximity-induced exchange field B_{ex}, while sufficiently large to see in Hanle measurements, is not large enough to suppress exchange fluctuations in graphene. It is still unclear whether spin relaxation is dominated by SOC, exchange fluctuations, or a combination of the two. However, considering that according to DFT calculations the exchange splitting is expected to be an order of magnitude stronger than SOC (see discussion for supplement figure S10), one can expect the origin of the experimentally observed anisotropy of spin relaxation to be mainly caused by the exchange fluctuations. Figure 3(b) points to at least some contribution of exchange fluctuations, while

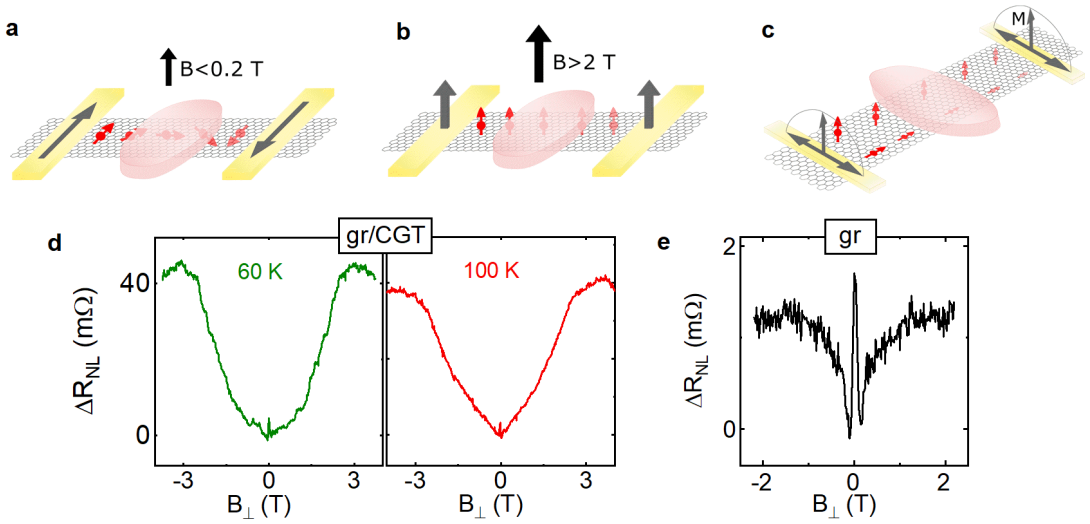

Figure 4. Anisotropic spin relaxation in graphene-$Cr_2Ge_2Te_6$ heterostructure. (a) Measurement geometry with small perpendicular magnetic field $B_\perp < 0.2$ T, where the magnetization of the ferromagnetic Co contacts and injected spin polarization are in-plane, resulting in Hanle spin precession. (b) Measurement geometry with large perpendicular magnetic field $B_\perp > 2$ T, where the magnetization of the ferromagnets and injected spin polarization are out of plane, resulting in no Hanle precession. (c) The measurements of graphene-CGT channels indicate anisotropic relaxation with faster rates of spin relaxation for in-plane spins, as demonstrated in the schematic and (d) experimental nonlocal measurements in a channel with ~60% flake overlap at 60 K and 100 K. A parabolic magnetoresistance background is subtracted from the measured data. (e) The reference measurement in pristine CVD graphene showing very low anisotropy with almost similar signal for in-plane and perpendicular spins.

the anisotropy measurement in figure 4(d) can be explained by either of the mechanisms.

Summary and outlook

In summary, the observed modulation of the spin transport signal demonstrates the existence of an exchange interaction in graphene proximity-coupled to the layered magnetic insulator CGT. This is revealed by the observation of nontrivial features in the measured nonlocal Hanle spin precession signals in the graphene-CGT channel. Namely, at low temperatures there is a hysteretic shift of the Hanle signal maxima for opposite magnetic field sweep directions, accompanied by a corresponding asymmetry in the Hanle signal. These features persist up to at least 100 K, above the T_c of bulk CGT. Supporting simulations reveal that these features can be explained by out-of-plane magnetism induced in the graphene layer by CGT. Additionally, measurements of large spin lifetime anisotropy indicate that proximity coupling of the graphene channel to CGT can modify its spin texture. This anisotropy can arise from the magnetic exchange induced in the graphene, while DFT simulations suggest that spin–orbit coupling could also be playing a role. Looking ahead, the proximity-induced effects can be further tuned by tailoring the van der Waals gap between graphene and CGT [30], and by placing it on both sides of the graphene layer. These achievements are important for the realization of quantum states of matter characterized by edge states which are topologically protected from backscattering without the application of an external magnetic field, namely, the quantum anomalous Hall effect [30–32]. This holds great potential for applications in spintronics and low-power quantum electronics.

Methods

Device fabrication and measurement

To fabricate the devices, CVD graphene was wet-transferred onto a Si/SiO_2 substrate (from Graphenea). After patterning the graphene into stripes of typical lateral width of 1–4 μm by photolithography and annealing in an Ar/H_2 atmosphere, 2D flakes (~30 nm thick) of the hexagonal ferromagnetic insulator $Cr_2Ge_2Te_6$ (from HQ Graphene), prepared by exfoliation method, were dry transferred immediately to reduce oxidation from air exposure. Suitable graphene-CGT heterostructure areas were chosen by optical microscope for further fabrication of ferromagnetic contacts by electron beam lithography and electron beam evaporation of metals (1 nm TiO_2/65 nm Co). The magnetic field sweeps at different temperatures were carried out in a Quantum Design Physical Property Measurement System while electrical biases were applied and measured by an external Keithley 6221 current source and a Keithley 2182A nanovoltmeter, respectively.

DFT simulations

For calculation of the electronic structure and structural relaxation of graphene on CGT density functional theory (DFT) [46] was used within Quantum ESPRESSO [47] using a previously developed model ([31]) with a k-point sampling of $6 \times 6 \times 1$, a Hubbard parameter of $U = 1$ eV [17], an energy cutoff for charge density of 500 Ry, and a

kinetic energy cutoff for wave functions of 60 Ry [48, 49]. When SOC is included, we used the relativistic versions of the pseudopotentials. For the relaxation of the heterostructures, we added van der Waals corrections [50, 51] and used a quasi-Newton algorithm based on a trust radius procedure. A vacuum gap of 20 Å was used to simulate quasi-2D systems. To determine the interlayer distances, the atoms of graphene were allowed to relax only in z direction (vertical to the layers) for determination of the interlayer distances, while the atoms of CGT were free to move in all directions until reaching a state when all components of all forces were reduced below 10^{-3} [Ry/a_0] (a_0 is the Bohr radius). For more details, see [31].

Acknowledgments

Authors from Chalmers, ICN2, and University of Regensburg acknowledge funding from the European Union's Horizon 2020 research and innovation programme under Grant agreement no. 785219 (Graphene Flagship Core 2). The authors at Chalmers acknowledge financial support from EU FlagEra project (from Swedish Research Council VR No. 2015-06813), Swedish Research Council VR project Grants (No. 2016-03658), Graphene center and the AoA Nano program at Chalmers University of Technology. We acknowledge Dr Ron Jansen for useful discussions about proximity-induced exchange and stray Hall effects in the heterostructures. We acknowledge help from Bing Zhao in our group and staff at Nanofabrication laboratory and Quantum device laboratory for useful discussions and help in fabrication and measurements of devices. ICN2 is funded by the CERCA Programme/Generalitat de Catalunya and is supported by the Severo Ochoa program from Spanish MINECO (Grant No. SEV-2017-0706). M. Vila acknowledges funding from 'La Caixa' Foundation.

Contributions

SPD and BK conceived the idea and designed the experiments. BK fabricated and measured the devices. AWC, MV, SR performed the simulations. KZ and JF performed the theoretical calculations. DK, AMH, AD helped in device fabrication and measurements. PS performed SQUID magnetic characterization of bulk CGT crystal. BK, AWC, MV, KZ, JF, SR, SPD contributed in analysis of the data, compiled the figures and wrote the manuscript. All authors gave input on interpretation of the data and contributed in writing of the manuscript. SPD supervised and managed the project.

Competing interests

The authors declare no competing financial interests.

ORCID iDs

Bogdan Karpiak https://orcid.org/0000-0001-7462-8405
Aron W Cummings https://orcid.org/0000-0003-2307-497X
Klaus Zollner https://orcid.org/0000-0002-6239-3271
Marc Vila https://orcid.org/0000-0001-9118-421X
Dmitrii Khokhriakov https://orcid.org/0000-0002-5515-9081
Anamul Md Hoque https://orcid.org/0000-0002-2117-7177
Peter Svedlindh https://orcid.org/0000-0002-3049-6831
Stephan Roche https://orcid.org/0000-0003-0323-4665
Saroj P Dash https://orcid.org/0000-0001-7931-4843

References

[1] Wang J and Zhang S-C 2017 Topological states of condensed matter *Nat. Mater.* **16** 1062–7
[2] He Q L *et al* 2017 Chiral Majorana fermion modes in a quantum anomalous Hall insulator–superconductor structure *Science* **357** 294–9
[3] Qiao Z *et al* 2014 Quantum anomalous Hall effect in graphene proximity coupled to an antiferromagnetic insulator *Phys. Rev. Lett.* **112** 116404
[4] Qiao Z *et al* 2010 Quantum anomalous Hall effect in graphene from rashba and exchange effects *Phys. Rev.* B **82** 161414
[5] Roche S *et al* 2015 Graphene spintronics: the European Flagship perspective *2D Mater.* **2** 030202
[6] Yang H X *et al* 2013 Proximity effects induced in graphene by magnetic insulators : first-principles calculations on spin filtering and exchange-splitting gaps *Phys. Rev. Lett.* **110** 046603
[7] Hallal A, Ibrahim F, Yang H, Roche S and Chshiev M 2017 Tailoring magnetic insulator proximity effects in graphene: first-principles calculations *2D Mater.* **4** 025074
[8] Zhong D *et al* 2017 Van der Waals engineering of ferromagnetic semiconductor heterostructures for spin and valleytronics *Sci. Adv.* **3** e1603113
[9] Haugen H, Huertas-Hernando D and Brataas A 2008 Spin transport in proximity-induced ferromagnetic graphene *Phys. Rev.* B **77** 115406
[10] Yang H *et al* 2018 Significant Dzyaloshinskii-Moriya interaction at graphene-ferromagnet interfaces due to Rashba effect *Nat. Mater.* **17** 605–9
[11] Dyrdał A and Barnaś J 2017 Anomalous, spin, and valley Hall effects in graphene deposited on ferromagnetic substrates *2D Mater.* **4** 034003
[12] Wang Z, Tang C, Sachs R, Barlas Y and Shi J 2015 Proximity-induced ferromagnetism in graphene revealed by the anomalous Hall effect *Phys. Rev. Lett.* **114** 016603
[13] Tang C *et al* 2018 Approaching quantum anomalous Hall effect in proximity-coupled YIG/graphene/h-BN sandwich structure *APL Mater.* **6** 026401
[14] Wei P *et al* 2016 Strong interfacial exchange field in the graphene/EuS heterostructure *Nat. Mater.* **15** 711–6
[15] Singh S *et al* 2017 Strong modulation of spin currents in bilayer graphene by static and fluctuating proximity exchange fields *Phys. Rev. Lett.* **118** 187201
[16] Leutenantsmeyer J C, Kaverzin A A, Wojtaszek M and Van Wees B J 2017 Proximity induced room temperature

ferromagnetism in graphene probed with spin currents *2D Mater.* **4** 014001
[17] Gong C *et al* 2017 Discovery of intrinsic ferromagnetism in two-dimensional van der Waals crystals *Nature* **546** 265–9
[18] Huang B *et al* 2017 Layer-dependent ferromagnetism in a van der Waals crystal down to the monolayer limit *Nature* **546** 270–3
[19] Tan C *et al* 2018 Hard magnetic properties in nanoflake van der Waals Fe_3GeTe_2 *Nat. Commun.* **9** 1554
[20] Wang Z *et al* 2018 Electric-field control of magnetism in a few-layered van der Waals ferromagnetic semiconductor *Nat. Nanotechnol.* **13** 554–9
[21] Huang B *et al* 2018 Electrical control of 2D magnetism in bilayer CrI_3 *Nat. Nanotechnol.* **13** 544–8
[22] Jiang S, Li L, Wang Z, Mak K F and Shan J 2018 Controlling magnetism in 2D CrI_3 by electrostatic doping *Nat. Nanotechnol.* **13** 549–53
[23] Klein D R *et al* 2018 Probing magnetism in 2D van der Waals crystalline insulators via electron tunneling *Science* **360** 1218–22
[24] Song T *et al* 2018 Giant tunneling magnetoresistance in spin-filter van der Waals heterostructures *Science* **360** 1214–8
[25] Wang Z *et al* 2018 Very large tunneling magnetoresistance in layered magnetic semiconductor CrI_3 *Nat. Commun.* **9** 2516
[26] Wang Z *et al* 2018 Tunneling spin valves based on Fe_3GeTe_2/hBN/Fe_3GeTe_2 van der Waals Heterostructures *Nano Lett.* **18** 4303–8
[27] Ghazaryan D *et al* 2018 Magnon-assisted tunnelling in van der Waals heterostructures based on $CrBr_3$ *Nat. Electron.* **1** 344–9
[28] Alegria L D *et al* 2014 Large anomalous Hall effect in ferromagnetic insulator-topological insulator heterostructures *Appl. Phys. Lett.* **105** 1–5
[29] Wu Y *et al* 2019 Néel-type skyrmion in WTe_2/Fe_3GeTe_2 van der Waals heterostructure (arXiv:1907.11349)
[30] Zhang J, Zhao B, Yao Y and Yang Z 2015 Robust quantum anomalous Hall effect in graphene-based van der Waals heterostructures *Phys. Rev.* B **92** 165418
[31] Zollner K, Gmitra M and Fabian J 2018 Electrically tunable exchange splitting in bilayer graphene on monolayer $Cr_2X_2Te_6$ with X = Ge, Si, and Sn *New J. Phys.* **20** 073007
[32] Zhang J *et al* 2017 Strong magnetization and Chern insulators in compressed graphene/CrI_3 van der Waals heterostructures *Phys. Rev.* B **97** 085401
[33] Xing W *et al* 2017 Electric field effect in multilayer $Cr_2Ge_2Te_6$: a ferromagnetic 2D material *2D Mater.* **4** 024009
[34] Carteaux V, Brunet D, Ouvrard G and André G 1995 Crystallographic, magnetic and electronic structures of a new layered ferromagnetic compound $Cr_2Ge_2Te_6$ *J. Phys.: Condens. Matter* **7** 69–87
[35] Li X and Yang J 2014 $CrXTe_3$ (X = Si, Ge) nanosheets: two dimensional intrinsic ferromagnetic semiconductors *J. Mater. Chem.* C **2** 7071–6
[36] Tian Y, Gray M J, Ji H, Cava R J and Burch K S 2016 Magneto-elastic coupling in a potential ferromagnetic 2D atomic crystal *2D Mater.* **3** 025035
[37] Ferrari A, Meyer J C, Scardaci C, Casiraghi C and Lazzeri M 2006 Raman spectrum of graphene and graphene layers *Phys. Rev. Lett.* **97** 187401
[38] Kamalakar V M, Groenveld C, Dankert A and Dash S P 2015 Long distance spin communication in chemical vapour deposited graphene *Nat. Commun.* **6** 6766
[39] Cummings A W 2019 Probing magnetism via spin dynamics in graphene/2D-ferromagnet heterostructures *J. Phys. Mater.* **2** 045007
[40] Hahn E L and Abragam A 1992 *Pulsed Magnetic Resonance: NMR, ESR, and Optics* (Oxford: Clarendon)
[41] Fabian J, Matos-Abiaguea A, Ertlera C, Stano P and Zutic I 2007 Semiconductor spintronics *Acta Phys. Slovaca* **57** 565–907
[42] Ringer S *et al* 2018 Measuring anisotropic spin relaxation in graphene *Phys. Rev.* B **97** 205439
[43] Raes B *et al* 2016 Determination of the spin-lifetime anisotropy in graphene using oblique spin precession *Nat. Commun.* **7** 11444
[44] Cummings A W, Garcia J H, Fabian J and Roche S 2017 Giant spin lifetime anisotropy in graphene induced by proximity effects *Phys. Rev. Lett.* **119** 206601
[45] Garcia J H, Vila M, Cummings A W and Roche S 2018 Spin transport in graphene/transition metal dichalcogenide heterostructures *Chem. Soc. Rev.* **47** 3359–79
[46] Honenberg P and Kohn W 1964 Inhomogeneous electron gas *Phys. Rev.* **136** B864–71
[47] Giannozzi P *et al* 2009 QUANTUM ESPRESSO : a modular and open-source software project for quantum simulations of materials *J. Phys.: Condens. Matter* **21** 395502
[48] Kresse G and Joubert D 1999 From ultrasoft pseudopotentials to the projector augmented-wave method *Phys. Rev.* B **59** 1758–75
[49] Perdew J P, Burke K and Ernzerhof M 1996 Generalized gradient approximation made simple *Phys. Rev. Lett.* **77** 3865–8
[50] Grimme S 2006 Semiempirical GGA-type density functional constructed with a long-range dispersion correction *J. Comput. Chem.* **27** 1787–99
[51] Barone V *et al* 2008 Role and effective treatment of dispersive forces in materials : polyethylene and graphite crystals as test cases *J. Comput. Chem.* **30** 934–9

Paper V

ADVANCED MATERIALS
www.advmat.de

Unconventional Charge–Spin Conversion in Weyl-Semimetal WTe_2

*Bing Zhao, Bogdan Karpiak, Dmitrii Khokhriakov, Annika Johansson, Anamul Md. Hoque, Xiaoguang Xu, Yong Jiang, Ingrid Mertig, and Saroj P. Dash**

An outstanding feature of topological quantum materials is their novel spin topology in the electronic band structures with an expected large charge-to-spin conversion efficiency. Here, a charge-current-induced spin polarization in the type-II Weyl semimetal candidate WTe_2 and efficient spin injection and detection in a graphene channel up to room temperature are reported. Contrary to the conventional spin Hall and Rashba–Edelstein effects, the measurements indicate an unconventional charge-to-spin conversion in WTe_2, which is primarily forbidden by the crystal symmetry of the system. Such a large spin polarization can be possible in WTe_2 due to a reduced crystal symmetry combined with its large spin Berry curvature, spin–orbit interaction with a novel spin-texture of the Fermi states. A robust and practical method is demonstrated for electrical creation and detection of such a spin polarization using both charge-to-spin conversion and its inverse phenomenon and utilized it for efficient spin injection and detection in the graphene channel up to room temperature. These findings open opportunities for utilizing topological Weyl materials as nonmagnetic spin sources in all-electrical van der Waals spintronic circuits and for low-power and high-performance nonvolatile spintronic technologies.

Topological quantum materials have attracted significant attention in condensed matter physics and spintronic technology because of their unique electronic bands with topologically protected spin textures.[1] After the realization of graphene, topological insulators (TIs), and semimetals with Dirac fermions, Weyl semimetals (WSMs) where the electrons behave as Weyl fermions have been discovered.[2] The WSMs constitute topologically secured Weyl nodes, which exist with opposite chirality in bulk with linear band dispersions in 3D momentum space forming the Weyl cones.[3] The fascinating revelation in a WSM is the presence of nontrivial Fermi-arc surface states that connect the projections of Weyl nodes on the surface Brillouin zone. In a recent breakthrough, WSMs of type-I and type-II are realized in TaAs and WTe_2 family of materials with symmetric and tilted Weyl cones, respectively.[4,5]

WTe_2 hosts unique transport phenomena such as chiral anomaly,[6,7] unconventional quantum oscillations,[8] colossal magnetoresistance,[9] spin–orbit torque,[10,11] substantial spin Hall effect[12] and quantum spin Hall states in monolayers,[13] which opens a new era for physics experiments. Most importantly, novel spin textures have been discovered in WSMs by photoemission experiments, showing spin polarization of Fermi pockets in bulk bands and Fermi arc surface states.[14,15] In such WSMs, the application of an electric field is expected to induce a macroscopic spin polarization, known as the Edelstein effect,[16] that can be utilized to generate and detect spin currents efficiently. Moreover, in crystals with lower or broken symmetry compared to conventional metals,[17] unconventional spin conductivity components can be existent.[18] Additionally, in the search for spin-polarized current sources in topological quantum materials, various experiments have been reported on TIs.[19] However, a reliable nonlocal measurement for spin polarization in TIs and its utilization for spin injection into non-magnetic materials are so far limited to cryogenic temperatures (below 20 K),[20,21] because of the interference from nontrivial bulk bands.[19] Therefore, finding a highly efficient spin-polarized topological material at room temperature is indispensable for practical applications in spintronics and quantum technologies.

Here, we report a highly efficient and unconventional charge-to-spin conversion (CSC) and its inverse phenomena (ICSC), in the type-II Weyl semimetal candidate WTe_2 up to

Dr. B. Zhao, Prof. X. Xu, Prof. Y. Jiang
Beijing Advanced Innovation Center for Materials Genome Engineering
School of Materials Science and Engineering
University of Science and Technology Beijing
Beijing 100083, China
Dr. B. Zhao, B. Karpiak, D. Khokhriakov, A. Md. Hoque, Prof. S. P. Dash
Department of Microtechnology and Nanoscience
Chalmers University of Technology
Göteborg SE-41296, Sweden
E-mail: saroj.dash@chalmers.se
Dr. A. Johansson, Prof. I. Mertig
Institute of Physics
Martin Luther University Halle-Wittenberg
Halle 06099, Germany
Dr. A. Johansson, Prof. I. Mertig
Max Planck Institute of Microstructure Physics
Weinberg 2, Halle 06120, Germany
Prof. S. P. Dash
Graphene Center
Chalmers University of Technology
Göteborg SE-41296, Sweden
The ORCID identification number(s) for the author(s) of this article can be found under https://doi.org/10.1002/adma.202000818.

DOI: 10.1002/adma.202000818

room temperature. Importantly, the detected spin polarization in WTe_2 is found to be different from the conventional spin Hall effect (SHE) and 2D Rashba–Edelstein effect (REE).[12] Furthermore, the detection of both the unconventional CSC and ICSC prove the robustness of spin polarization in WTe_2 obeying Onsager reciprocity relation and provides a new method for utilization of spin current in graphene for an all-electrical van der Waals spintronic device at room temperature.

The measurements of unconventional charge–spin conversion phenomena have been possible by employing a hybrid device structure of WTe_2 with graphene channel and ferromagnetic tunnel contacts (FM) in a reliable nonlocal (NL) device geometry. We fabricated van der Waals heterostructures of WTe_2 with graphene taking advantage of its layered structure. The schematics and the nanofabricated device picture are shown in **Figure 1**d, which consists of WTe_2–graphene heterostructure with ferromagnetic tunnel contacts (Co/TiO_2) (see the Experimental Section for details). The graphene (CVD monolayer[22] and exfoliated few layers) and the WTe_2 (20–70 nm in thickness) are exfoliated from single crystals (from Hq Graphene). The Raman spectroscopy characterization shows the T_d-bulk phase of WTe_2 at room temperature (see Figure S1a, Supporting Information). The crystal structure of WTe_2 has a nonsymmorphic symmetry, with the space group $Pmn2_1$ for bulk WTe_2 crystals with only one mirror plane M_a (*bc* plane), a glide mirror plane $\widetilde{M}_b$ (*ac* plane with translation of (**a**+**c**)/2), and a screw axis ‖ *c* (Figure 1a–c). Neither twofold rotational invariance nor inversion symmetry is present in this system.[17] In the measured devices, the heterostructures of WTe_2 with graphene show good contact properties with interface resistance in the range of 1–3 kΩ (see Figure S1b, Supporting

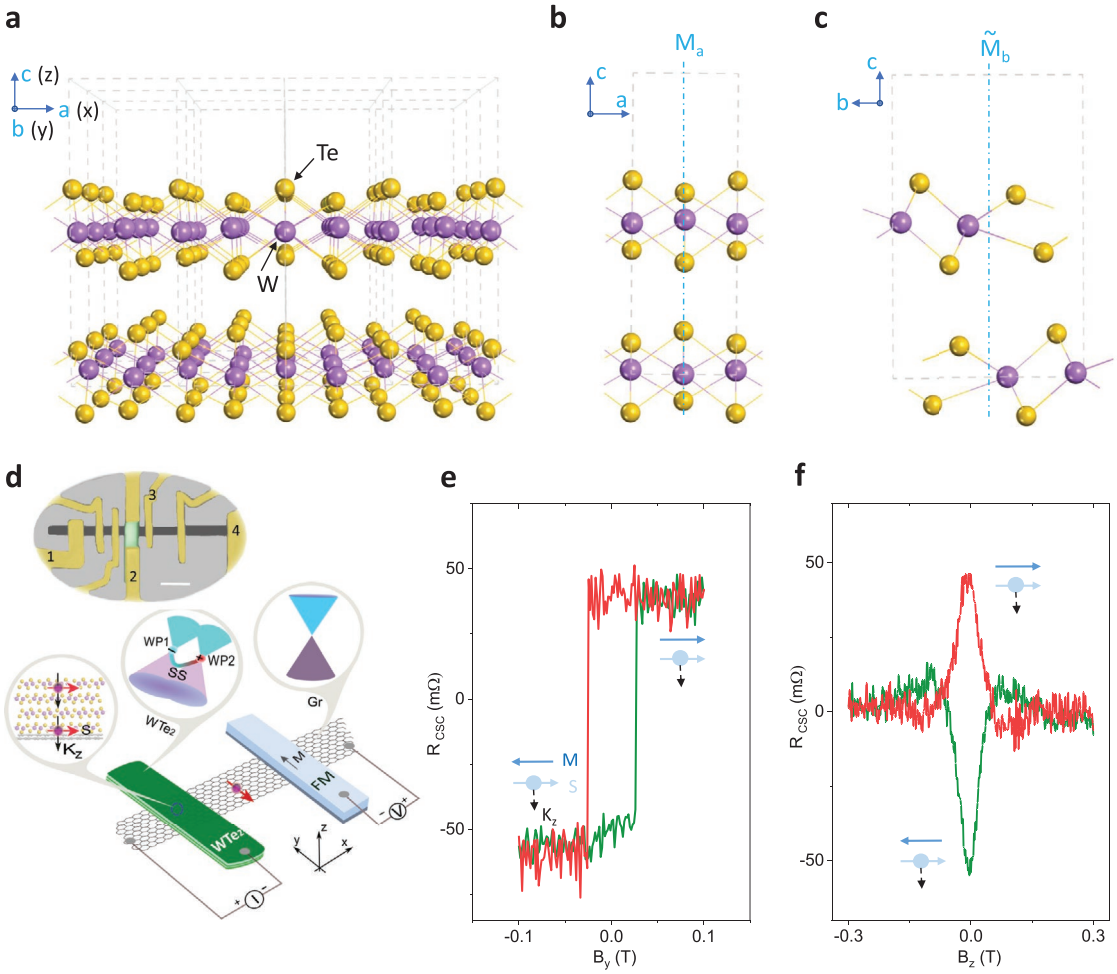

Figure 1. Unconventional charge-to-spin conversion in WTe_2 and efficient spin injection into graphene at room temperature. a–c) Crystal structure of T_d phase bulk WTe_2 with a mirror plane M_a (blue dot–dash line) and a glide mirror plane $\widetilde{M}_b$ with the translation of (**a**+**b**)/2 in the unit cell. d) Schematic of measurement geometry and colored device picture (the scale bar is 5 µm) for electrical detection of unconventional charge–spin conversion in WTe_2. The investigated device structure consists of a flake of WTe_2 (green) with a graphene channel (gray). The ferromagnetic tunnel contact (yellow) on graphene is used to detect the current-induced spin polarization of WTe_2. The insets in the schematics show the spin polarization due to perpendicular current component K_z, the simplified type-II Weyl semimetal band structure, and the Dirac band diagram of graphene. The upper inset is the optical microscopy image of the hybrid WTe_2/graphene van der Waals heterostructure device with a ferromagnetic Co detector contact. The contacts (1234) are used as $I_{12(34)}$ and $V_{34(12)}$ for the (I)CSC measurements. e,f) The nonlocal spin-valve measurement ($R_{CSC} = V_{CSC}/I$, I is the bias current across the WTe_2–graphene junction) and corresponding Hanle spin precession signal observed for parallel and anti-parallel orientation of the injected spin (s) from WTe_2 and magnetization of ferromagnet (M) with positive and negative magnetic field B sweep directions at $I = +50$ µA and 300 K in Device 1.

Information), which is an order of magnitude higher than used for detection of conventional CSC in WTe_2.[12] The standard spin injection and detection behavior of ferromagnetic tunnel contacts and spin transport properties of graphene was confirmed, as shown in Figure S2 (Supporting Information).

For the measurement of the unconventional charge–spin conversion effects, an electric current is applied vertically through the WTe_2 flake, which generates and injects a spin current into the graphene channel (Figure 1d). To be noted, here, we used a bias current across the WTe_2–graphene junction, which is different from the conventional CSC measurement configuration reported earlier[12] (see details in Note S1, Supporting Information). The injected spin polarization from WTe_2 is detected by a ferromagnetic contact (FM) after transport in a graphene channel by a NL measurement method. Figure 1d shows the NL spin-valve resistance ($R_{CSC} = V_{CSC}/I$) for bias current of $I = +50$ μA with an in-plane magnetic field (B_y) sweep at room temperature. The spin resistance R_{CSC} changes upon reversing the magnetization M direction of the FM detector with respect to the directions of the injected spins (s) from the WTe_2 (Figure 1e).

To prove that the origin of the signal is purely due to a spin current, the Hanle measurements were performed with a perpendicular magnetic field B_z sweep along the z-axis (Figure 1f). The Hanle effect induces precession of the spins injected from WTe_2 and transported in the graphene channel about the B_z field with Larmor frequency of $\omega_L = g\mu_B B_z/\hbar$ (where g is the Landé factor = 2, and μ_B is the Bohr magneton) as the projection of the spin current onto the magnetization of the detector ferromagnet change. The spin injection signal from WTe_2 into graphene is reproducibly observed in several devices (six devices were investigated) consisting of both monolayer and few-layer graphene channel with 20–70 nm thick WTe_2 flakes (Figures S3 and S4, Supporting Information). From these devices, we extracted spin parameters (with spin diffusion length 0.8–2.4 μm, spin lifetime in the range 100–400 ps) by fitting the Hanle signals (see Table S1, Supporting Information). The observation of both the spin valve and Hanle signal provide the direct and unambiguous evidence of the creation of current-induced spin polarization in WTe_2 and subsequent spin current injection and transport in the graphene channel at room temperature.

In a WTe_2–graphene hybrid device, the source of the spin polarization can have several origins, such as the spin Hall effect (SHE) and Edelstein effect (EE) from the bulk WTe_2, Rashba–Edelstein effect (REE) from the surface states,[12] and proximity-induced SHE and REE in graphene.[23–25] Moreover, some of these effects can induce the in-plane spin polarization and can be entangled with each other.[12] To distinguish different sources of the spin polarization, and to identify the origin of the induced spin current in our WTe_2 device, control experiments with geometrical dependence were performed.

We first examine the bias current direction dependence of the unconventional CSC signal (**Figure 2**a), where the direction

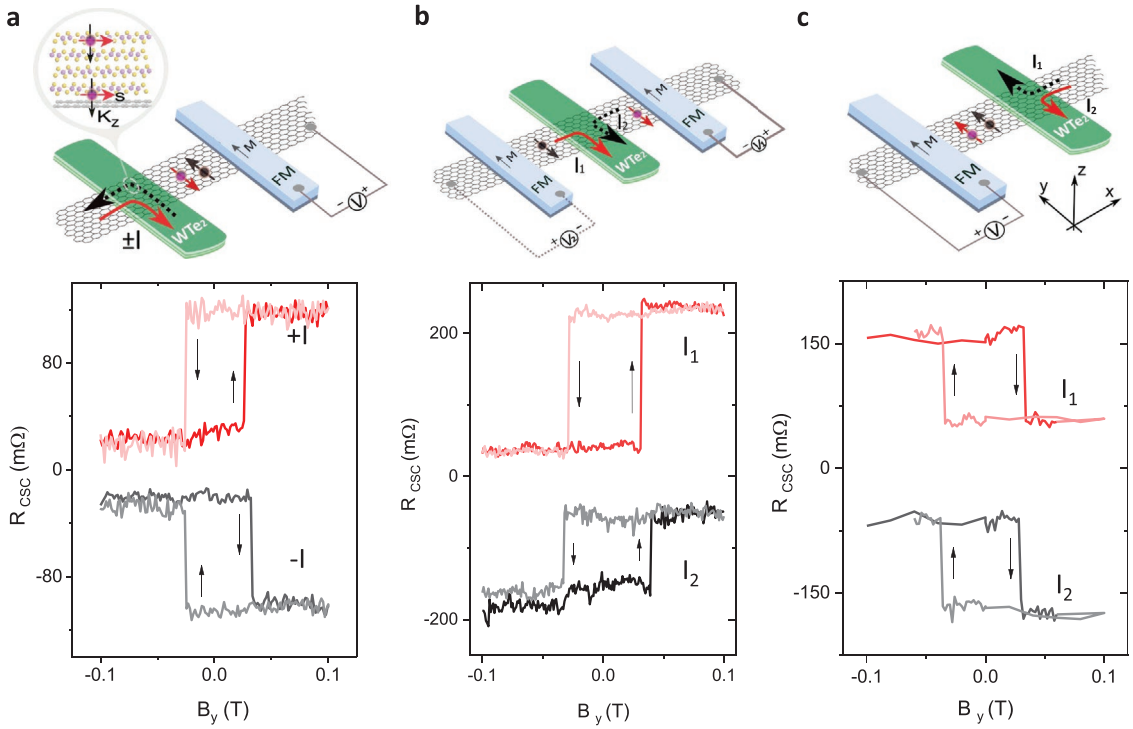

Figure 2. Geometrical dependence of the unconventional charge–spin conversion effect in WTe_2. a) Schematics of the measurement geometry (solid and dash arrows show the applied bias current directions) and the corresponding CSC signal with reversal of bias current polarity in Dev 1. The arrows show the switching direction of the signals. The inset shows the spin polarization due to an out-of-plane charge current component j_c. b) Schematics of the measurement with bias current applied at both sides of the WTe_2 flake and corresponding spin valve signals measured in Dev 2. This measurement creates a reversal of the component K_x of the bias current. c) Schematics of the measurement with bias current applied at both terminals of the WTe_2 flake and the corresponding spin valve signals measured in Dev 3. This measurement creates a reversal of the component K_y of the bias current. A shift in the Y-axis is added for the sake of clarity.

of the generated spins s in WTe_2 is found to be dependent on the polarity of the applied current bias. Reversing the bias current direction (I_{dc} = +/−50 μA) in WTe_2 results in an opposite spin polarization and hence an inverted hysteretic behavior of the measured spin-valve signal. These measurements show that the direction of spin polarization can be controlled by electrical means, and the spin density is observed to scale linearly with the applied bias current (see Figure S3, Supporting Information). The observation of linear bias dependence and a sign reversal behavior with bias current directions rule out the thermal contributions in the measured signal[26,27] (see detail discussion in Note S4, Supporting Information).

The charge current (I) applied in WTe_2 can have three components, i.e., K_x, K_y, and K_z, that can possibly induce the spin polarization (see schematics in Figure S5, Supporting Information). We performed control experiments by reversing the bias current polarity along different directions to check the polarity of unconventional CSC signals. As shown in Figure 2b, the switching directions of unconventional CSC signal (R_{CSC}) remain the same with the reversal of bias currents along both sides of the WTe_2 flake, i.e., the K_x and $-K_x$ directions. Therefore, the bias current component in K_x direction is not the source for the current-induced spin polarization. Consequently, we can rule out the origins of spin polarizations entangled to K_x-direction, like SHE and REE effect in WTe_2;[12] and also proximity-induced SHE and REE in graphene.[24,28–30] Second, when the bias current was applied either to one or the opposite terminal (K_y and $-K_y$ directions) of WTe_2 (Figure 2c), the R_{csc} signal switching directions remain the same. This rules out the contribution to the spin polarization from the current component in K_y direction. Both the control experiments in K_x and K_y directions were reproduced in other batches of devices (see Figures S6 and S7, Supporting Information). To be noted, the switching direction of the spin-switch signal is observed to be different for different devices (Dev 2 and 3 in Figure 2b,c). This can be due to the uncertainty in different crystal orientations (±a, ±b axis) of the exfoliated WTe_2 flakes relative to the detector FM.

All these control experiments indicate that the current component in K_z direction in WTe_2 is the primary source for the generation of spin polarization in the measurement geometry of WTe_2–graphene devices. Therefore, the origin of the spin signal can be attributed to the out-of-plane current-induced spin momentum locking of the spin-polarized Fermi states at room temperature.[14,15] Moreover, the out-of-plane current component along K_z can have two contributions: one ($K_{z,B}$) through the bulk states; and the other ($K_{z,S}$) via the surface states (see Figure 5c, Supporting Information). From the recent ARPES measurement on WTe_2,[31] it is clear that the surface states barely disperse with k_z over an entire Brillouin zone and can thus be considered fully 2D in the k_x–k_z plane, i.e., the Fermi lines are straight lines at the edge of the bulk electron and hole pockets. Therefore, the current in K_z direction is not accompanied by any significant transport originating from the surface states: nearly no surface states would contribute to the observed unconventional CSC signal (see details in Note S5, Supporting Information). Moreover, according to our control experiments (Figure 2), we know that it is the current along the z-axis that induces the spin polarization s, which are parallel to FM magnetic moments M, i.e., $s//M//y$. We also know that the spin current j_s is along the z-axis in our measurement geometry, i.e., j_s $//z//K_z$, which is also the direction of the charge current. However, in the conventional SHE measurements, charge current, spin current, and spin polarization should be mutually perpendicular, following the right-hand rule, i.e., $j_s \perp K_z \perp s$.[12,32] Therefore, the measured data in the present experimental configuration do not follow the conventional SHE rules (see Note S1, Supporting Information). Further, the unconventional CSC signal in this geometry can also neither originate from an unconventional spin conductivity nor the Edelstein effect of the spin-polarized Fermi states for symmetry reasons, as long as the symmetry operations of the space group $Pmn2_1$, in particular mirror and glide mirror symmetries, are present (see Note S5, Supporting Information). However, if the symmetry of WTe_2 is reduced, e.g., by strain,[33–35] magnetic field[36,37] or the interfaces[38] between WTe_2 and graphene, both unconventional spin Hall effect and Edelstein effect can give rise to the observed spin polarization (see details in Note S5, Supporting Information). However, our observation suggests that a magnetic field is less likely to be the origin of the unconventional CSC signal (see details in Note S3, Supporting Information). Strain can arise in the WTe_2 flakes due to fabrication of contacts and interfaces with different materials in the device, breaking both mirror M_a and glide mirror $\widetilde{M}_b$ symmetry. Furthermore, the interface between WTe_2 and graphene can as well break glide mirror and screw symmetries locally. This symmetry breaking leads to the occurrence of a y-polarized spin current and (or) a homogeneous spin density in the y direction, leading to a spin current $j_s \parallel K_z$ (here we name it j_s^y). Thus, although the symmetries of space group $Pmn2_1$ prohibit the generation of a spin current j_s^y by the spin Hall and Edelstein effects, breaking the crystal symmetries by strain or the occurring interface allows the emergence of the observed spin current.

To further confirm the orientation of spin polarization from WTe_2, we also performed angle-dependent measurements of the unconventional CSC signals both with in-plane and out-of-plane B field sweeps in Dev 4 (see Figure S8, Supporting Information). The measured unconventional CSC signal is observed to evolve from a step-like spin valve signal to a Hanle signal with changing the angle from 0° to 90°. Considering the direction of the spin current j_s, the spin polarization s, and bias current K_z, the contribution of the conventional CSC from WTe_2 can also be ruled out. These systematic measurements again support the observation of the unconventional CSC in bulk WTe_2. The unconventional CSC measurements in WTe_2 using both the spin valve and Hanle geometry were also performed as a function of gate voltage (V_g) in Dev 4 (see Figure S9, Supporting Information), where an enhancement of the unconventional CSC signal magnitude is observed close to the Dirac point of graphene. As the metallic WTe_2 channel resistance does not show any noticeable modulation with V_g (Figure S10, Supporting Information), the increase of unconventional CSC signal can be attributed to the increase in the graphene channel resistance in the heterostructure and conductivity matching issues at the interface (Figure S9c, Supporting Information). However, in the conventional spin valve signals with both FM injector and detector contacts on graphene, a small modulation of spin signal magnitude is observed (Figure S10, Supporting

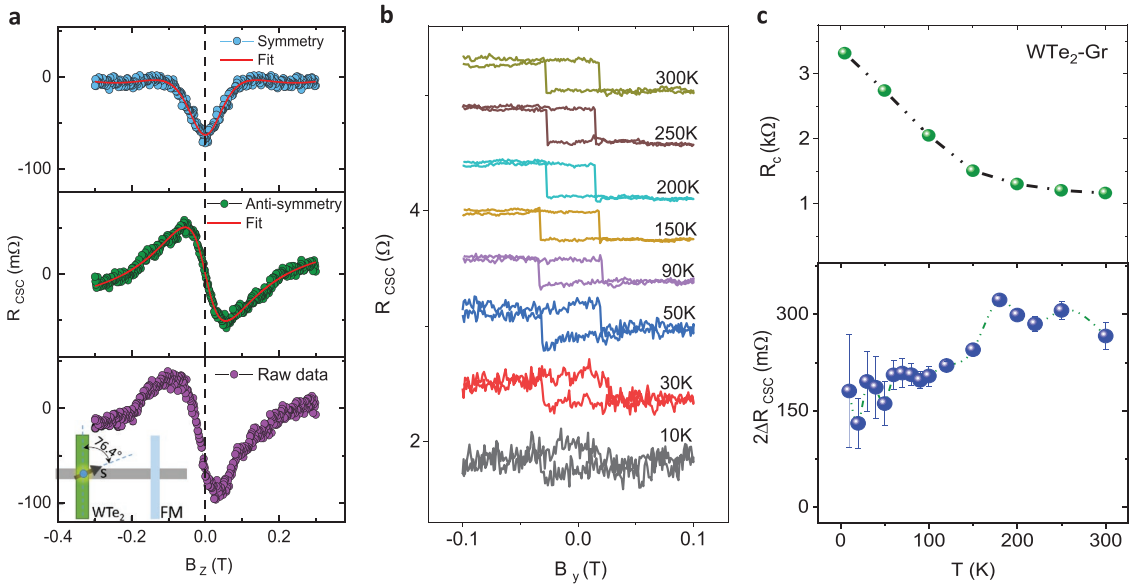

Figure 3. Observation of the in-plane asymmetric Hanle signal and temperature dependence of the unconventional charge–spin conversion in WTe_2. a) The measured asymmetric Hanle raw data (bottom panel) of the unconventional CSC signal in Device 2. The symmetric (top panel) and anti-symmetric (middle panel) components of the Hanle signal and the corresponding fittings. The inset shows the measurement geometry with charge current-induced spin polarization *s* in WTe_2 can be with an angle relative to the detector FM. b) Temperature dependence spin-switch signal of the unconventional CSC effect in WTe_2 for Device 2 ($R_{CSC} = V_{CSC}/I$, with $I = -50$ μA in the range of 10–300 K. c) Top panel: Temperature dependence of the WTe_2–graphene interface resistance. Bottom panel: Temperature dependence of the CSC signal magnitude. The error bars are estimated from the noise in the measured CSC signal.

Information).[39] This increasing trend of CSC signal with V_g suggests a possible enhancement of the spin injection efficiency from WTe_2 to graphene near the graphene Dirac point.

In comparison to the symmetric Hanle curves in other devices, Device 2 shows an in-plane asymmetric characteristic in the Hanle spin precession signal (**Figure 3**a). By decomposing the measured raw data mathematically, we obtained the symmetric and the anti-symmetric spin components, i.e., the spins along FM and the spins perpendicular to FM, respectively. Specifically, the magnitude of the symmetric (R_1) and the anti-symmetric (R_2) components are extracted by fitting the Hanle curves. Thus, the out-of-plane charge current generates a net spin polarization and/or a spin current, which is polarized with an angle of 76.4° (= arctan(R_1/R_2)) with respect to the FM. Such an asymmetric Hanle curve can be caused by the coexistence of spin polarization components parallel and perpendicular to the ferromagnet.[40] This can be explained by considering the simultaneously broken mirror symmetry M_a and glide symmetry $\widetilde{M}_b$ (see the symmetry analysis in Note S5, Supporting Information). We cannot distinguish the orientation of the samples in the present case, however, considering the randomly distributed *a*(*b*)-axis in the exfoliated WTe_2 flakes relative to the crystal boundary and presence of strain as well as the glide-symmetry ($\widetilde{M}_b$) -breaking interface in the devices, such an unconventional and asymmetric signal due to charge-to-spin convention is observed.

Next, the temperature-dependent measurements of the unconventional CSC in WTe_2 were carried out to correlate the basic characteristics of the Weyl materials and their spin polarization. The WTe_2 has been experimentally verified to be a type-II Weyl semimetal by observing the negative magnetoresistance[8,41] and the anomalous-quantum oscillation[8] at low temperatures. However, the verification of WTe_2 to be a type-II Weyl semimetal at room temperature is still under debate,[31,42,43] because the momentum difference for Weyl points (WPs) is beyond the resolution of ARPES measurement.[7,31,44] Hence, it is intriguing to check the temperature dependence of the signal and its relationship with the possible Weyl phase transition at a lower temperature.[8,41] Figure 3a shows the temperature dependence of the unconventional CSC signals from WTe_2, measured in Dev 2 in the temperature range of 10–300 K at a fixed bias current $I = -50$ μA. The switching direction of the measured unconventional CSC signal in WTe_2 remains the same throughout the temperature range, indicating that the origin of the spin polarization remains the same. The apparent slightly larger switching field observed for the signal at lower temperatures is due to an increase in the coercive field of the FM detector contact. The modulation of the magnitude of the unconventional CSC signal of WTe_2 is plotted with temperature in Figure 3b (lower panel), where two different regimes were observed. The signal magnitude is weakly temperature-dependent in the range 175–300 K, whereas a notable decrease is observed below 175 K. As spin transport parameters in graphene are known to weakly dependent on temperature,[45] we identified that the decrease in unconventional CSC magnitude could be due to the increase in WTe_2–graphene contact resistance at lower temperatures (Figure 3b upper panel). The increase in WTe_2–graphene contact resistance could cause a decrease in spin injection efficiency form WTe_2 into graphene, while the other parameters were very stable with temperature (see Figure S11, Supporting Information). The increased noise level in the unconventional

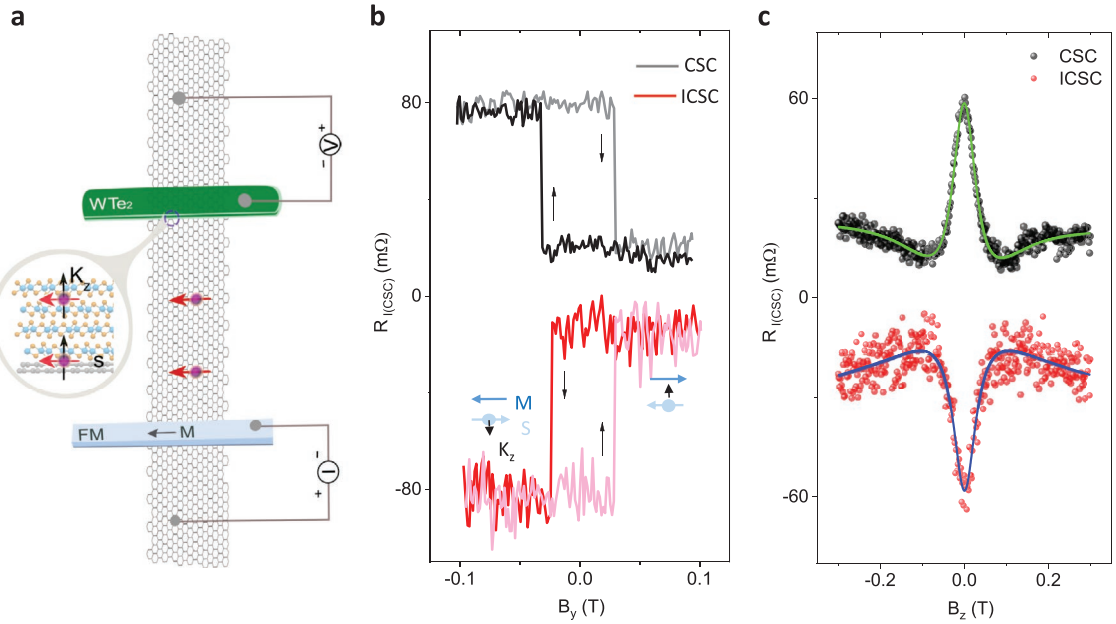

Figure 4. Inverse charge–spin conversion in WTe_2 at room temperature. a) Schematics of the inverse charge–spin conversion (ICSC) measurement configuration with spin current injected into the WTe_2 from the FM/graphene structure. b,c) Measured data of both spin valve and corresponding *z* Hanle signal with the fitting curve for both CSC and ICSC in Device 1 with an application of $I = -70$ μA at room temperature. The Hanle signal of the (I)CSC is defined by $R_{(I)CSC} = (V_{(I)CSC}(P) - V_{(I)CSC}(AP))/(2 \times I)$.

CSC signal at the lower temperature can also be due to the larger WTe_2–graphene contact resistances. All these measurements suggest that the observed unconventional CSC effect is robust from 10 K to room temperature, and the spin-polarized bulk Fermi states in WTe_2 should be present through all the measured temperature range.

To check the reciprocity[46] of the unconventional charge–spin conversion effect in WTe_2, the inverse charge–spin conversion (ICSC)[47,48] measurements were also performed at room temperature (see **Figure 4**a). Here, the spin current is injected from an FM tunnel contact into a graphene channel and subsequently detected by the WTe_2 due to the ICSC effect in a NL measurement geometry. The spin current with spin polarization *s* along the *y*-axis is absorbed into the WTe_2, resulting in a net charge current in the K_z direction due to the inverse charge–spin conversion. By reversing the FM magnetic moments by an external in-plane magnetic field sweep, the opposite spins $-s$ are injected into the graphene channel and subsequently absorbed by the WTe_2, which induces a charge current $-K_z$. An apparent hysteric switching behavior of the measured voltage signal is observed with B_y magnetic field sweep, with the switching fields corresponding to the magnetization switching of the spin injector FM electrode (Figure 4b). Importantly, both the ICSC and CSC signals measured in the same device show a good Onsager reciprocity with comparable signal magnitude and opposite switching directions, i.e., $R_{CSC}(B) = R_{ICSC}(-B)$ (Figure 4b). The ICSC effect is reproducibly observed in different devices and the magnitude of the signal is also found to scale linearly with spin injection bias current and changes sign with the bias polarity (see Figure S12 in the Supporting Information for data on Dev 2). As a confirmatory test for the observed ICSC effect, corresponding Hanle spin precession measurements were also performed with application of an out-of-plane magnetic field B_z in the same NL measurement geometry. Figure 4c shows the measured modulation of signal $R_{ICSC} = V_{ICSC}/I$ as detected by ICSC in WTe_2 due to spin diffusion and precession in the graphene channel.

We estimate the unconventional CSC efficiency α_{CSC} ($= j_s/j_c$) in WTe_2 to be up to 9% at room temperature by fitting the Hanle curves of (I)CSC signals (see details in Note S2, Supporting Information). The calculated lower limit of Edelstein length is $\lambda_{EE} = \alpha_{CSC}\lambda_{WTe_2} \approx 0.72$ nm (considering spin diffusion length of WTe_2 $\lambda_{WTe_2} = 8$ nm[12]). The observed large charge–spin conversion efficiency in WTe_2 is believed to be due to the spin polarization of Fermi states, broken space inversion symmetry, and a significant influence of SOI in WTe_2 as known from the band structure calculations and spin-resolved ARPES results.[15] Interestingly, our measurements show that the charge–spin conversion is not restricted to the 2D surface but originates in the bulk Weyl semimetal WTe_2. From our control experiments, we could rule out the origins of the observed spin polarization related to conventional SHE and REE in WTe_2,[12] and also proximity induced SHE and REE in graphene.[24,28–30] These observations of the unconventional CSC are fundamentally different from the conventional REE, which is an interface phenomenon where the spins and current density are confined in the 2D plane[48,49] as measured in the heterostructures of metals[48] and oxides,[50] topological insulator,[51,52] Transition metal dichalcogenides (TMDCs)[53] and in graphene heterostructures with MoS_2,[28] WS_2,[23,30] TaS_2,[25] $MoTe_2$[24] and topological insulator $(Bi_{0.15}Sb_{0.85})_2Te_3$.[54] This unconventional charge–spin conversion phenomenon in WTe_2, however, is shown to be useful for injection and detection of spin polarization in graphene at room temperature, avoiding problems existing in topological insulators,[20,21] and open ways for spintronic devices without the use of traditional ferromagnets. The WTe_2 based van der Waals

heterostructure devices also provide the advantage that their operating temperature is not restricted by a Curie temperature (T_c), such as recently discovered 2D ferromagnets have T_c much below the room temperature.[55] Other advantages are that the direction of spin polarization in WTe_2 can be controlled by using an electric bias current, instead of using an external magnetic field in case of FMs to switch the magnetic moments. From the application point of view, spin–orbit torque (SOT) studies[10,11] show that WTe_2 can be more efficient and energy-saving in SOT technologies compared to traditional heavy metals.

In summary, we demonstrated the electrical creation, detection, and control of the unconventional charge–spin conversion and its inverse phenomenon in type-II Weyl semimetal candidate WTe_2 up to room temperature. Contrary to conventional bulk spin Hall effect and surface states dominated Rashba–Edelstein effect, the charge–spin conversion is shown here to be created in WTe_2 due to unconventional spin Hall effect or (and) Edelstein effect. The unconventional spin conductivities in WTe_2 are allowed by considering strain as well as the WTe_2/graphene interface to break the crystal symmetry. The spin polarization created in WTe_2 is shown to be utilized for spin injection and detection in a graphene channel in an all-electrical van der Waals heterostructure spintronic device at room temperature, which circumvents the problem existing in topological insulators for spin injection into graphene below 20 K.[20,21] Such unique spin-polarized electronic states in Weyl semimetal candidates with novel spin topologies can be further tuned by tailoring their electronic band structure through enhancing their spin–orbit interaction strength, increasing the separation between the Weyl nodes through Berry curvature design, and controlling strain to break the crystal symmetry. These findings in Weyl semimetal WTe_2 for efficiently transforming the electric current into a spin polarization at room temperature is highly desirable for energy-efficient spintronic memory and information processing technologies.[56]

After submission of our manuscript, we noticed two very recent papers on the multidirectional and unconventional charge–spin conversion in $MoTe_2$.[35,38] Our results on Weyl semimetal candidate WTe_2 show an efficient and unconventional charge–spin conversion, which is different from conventional SHE and REE and demonstrates a practical approach for efficient generation and injection of spin polarization into graphene channel up to room temperature.

Experimental Section

The devices with monolayer CVD graphene on Si/SiO_2 substrate (from Groltex) were patterned by electron beam lithography (EBL) followed by an O_2 plasma etching. The WTe_2 (from Hq Graphene) flakes were exfoliated and dry transferred on to the CVD graphene in the N_2 atmosphere inside a glovebox. The few layers graphene devices were mechanically transferred onto the n-doped Si substrate with 300 nm SiO_2. The WTe_2 flakes were exfoliated and dry transferred on to the few-layer graphene in by a transfer stage in a class 100 cleanroom environment. For the preparation of ferromagnetic tunnel contacts to graphene, a two-step deposition and oxidation process was adopted, 0.4 nm Ti was deposited, followed by a 30 Torr O_2 oxidation for 10 min each, followed by 100 nm Co deposition. Measurements were performed inside a vacuum cryostat and a PPMS measurement system in the temperature range of 10–300 K with a magnetic field and a sample rotation stage. The electronic measurements were carried out using current source Keithley 6221, nanometer 2182A, and dual-channel source meter Keithley 2612B.

Supporting Information

Supporting Information is available from the Wiley Online Library or from the author.

Acknowledgements

The authors at Chalmers University of Technology, Sweden acknowledge financial supports from EU Graphene Flagship (Core 1 No. 604391, Core 2 No. 785219, and Core 3 No. 881603), Swedish Research Council VR project grants (No. 2016–03658), EU FlagEra project (from Swedish Research Council VR No. 2015–06813), 2D Tech VINNOVA competence Center, Graphene center and the AoA Nano program at Chalmers University of Technology. The authors from the University of Science and Technology, Beijing, China, acknowledge financial supports from the National Basic Research Program of China (Grant No. 2015CB921502) and the National Natural Science Foundation of China (Grant Nos. 51731003, 51471029). Bing Zhao would like to thank the financial support from the program of China Scholarships Council (File No. 201706460036) for his two years of research at Chalmers. The authors from Martin Luther University Halle-Wittenberg acknowledge support by CRC/TRR 227 of Deutsche Forschungsgemeinschaft (DFG). The authors would like to thank Binghai Yan, Marcos Guimaraes, C. K. Safeer and Felix Casanova for useful discussions. The data that support the findings of this study are available from the corresponding authors on reasonable request.

Conflict of Interest

The authors declare no conflict of interest.

Author Contributions

S.P.D. and B.Z. conceived the idea and designed the experiments. B.Z., B.K., D.K., A.M.H., S.P.D. fabricated and measured the devices at the Chalmers University of Technology. B.Z. and S.P.D. analyzed, interpreted the experimental data, compiled the figures, and wrote the manuscript. A.J. and I.M. performed theoretical calculations. B.K., D.K., A.M.H., X.X., Y.J. discussed the results and provided feedback on the manuscript. S.P.D. supervised the research.

Keywords

current-induced spin polarization, Edelstein effect, graphene, spin-momentum locking, type-II, unconventional charge–spin conversion, van der Waals heterostructures, Weyl-semimetals, WTe_2

Received: February 5, 2020
Revised: July 8, 2020
Published online: August 9, 2020

[1] Y. Tokura, M. Kawasaki, N. Nagaosa, *Nat. Phys.* **2017**, *13*, 1056.
[2] S.-Y. Xu, I. Belopolski, N. Alidoust, M. Neupane, G. Bian, C. Zhang, R. Sankar, G. Chang, Z. Yuan, C.-C. Lee, S.-M. Huang, H. Zheng, J. Ma, D. S. Sanchez, B. Wang, A. Bansil, F. Chou, P. P. Shibayev, H. Lin, S. Jia, M. Z. Hasan, *Science* **2015**, *349*, 613.

[3] N. P. Armitage, E. J. Mele, A. Vishwanath, *Rev. Mod. Phys.* **2018**, *90*, 15001.
[4] H. Zheng, M. Zahid Hasan, *Adv. Phys.: X* **2018**, *3*, 1466661.
[5] B. Yan, C. Felser, *Annu. Rev. Condens. Matter Phys.* **2017**, *8*, 337.
[6] H. B. Nielsen, M. Ninomiya, *Phys. Lett. B* **1983**, *130*, 389.
[7] A. A. Soluyanov, D. Gresch, Z. Wang, Q. Wu, M. Troyer, X. Dai, B. A. Bernevig, *Nature* **2015**, *527*, 495.
[8] P. Li, Y. Wen, X. He, Q. Zhang, C. Xia, Z.-M. Yu, S. A. Yang, Z. Zhu, H. N. Alshareef, X.-X. Zhang, *Nat. Commun.* **2017**, *8*, 2150.
[9] M. N. Ali, J. Xiong, S. Flynn, J. Tao, Q. D. Gibson, L. M. Schoop, T. Liang, N. Haldolaarachchige, M. Hirschberger, N. P. Ong, R. J. Cava, *Nature* **2014**, *514*, 205.
[10] D. MacNeill, G. M. Stiehl, M. H. D. Guimaraes, R. A. Buhrman, J. Park, D. C. Ralph, *Nat. Phys.* **2017**, *13*, 300.
[11] S. Shi, S. Liang, Z. Zhu, K. Cai, S. D. Pollard, Y. Wang, J. Wang, Q. Wang, P. He, J. Yu, G. Eda, G. Liang, H. Yang, *Nat. Nanotechnol.* **2019**, *14*, 945.
[12] B. Zhao, D. Khokhriakov, Y. Zhang, H. Fu, B. Karpiak, A. M. Hoque, X. Xu, Y. Jiang, B. Yan, S. P. Dash, *Phys. Rev. Res.* **2020**, *2*, 013286.
[13] S. Tang, C. Zhang, D. i. Wong, Z. Pedramrazi, H.-Z. Tsai, C. Jia, B. Moritz, M. Claassen, H. Ryu, S. Kahn, J. Jiang, H. Yan, M. Hashimoto, D. Lu, R. G. Moore, C.-C. Hwang, C. Hwang, Z. Hussain, Y. Chen, M. M. Ugeda, Z. Liu, X. Xie, T. P. Devereaux, M. F. Crommie, S.-K. Mo, Z.-X. Shen, *Nat. Phys.* **2017**, *13*, 683.
[14] B. Feng, Y.-H. Chan, Y. Feng, R.-Y. Liu, M.-Y. Chou, K. Kuroda, K. Yaji, A. Harasawa, P. Moras, A. Barinov, W. Malaeb, C. Bareille, T. Kondo, S. Shin, F. Komori, T.-C. Chiang, Y. Shi, I. Matsuda, *Phys. Rev. B* **2016**, *94*, 195134.
[15] P. K. Das, D. Di Sante, I. Vobornik, J. Fujii, T. Okuda, E. Bruyer, A. Gyenis, B. E. Feldman, J. Tao, R. Ciancio, G. Rossi, M. N. Ali, S. Picozzi, A. Yadzani, G. Panaccione, R. J. Cava, *Nat. Commun.* **2016**, *7*, 10847.
[16] A. Johansson, J. Henk, I. Mertig, *Phys. Rev. B* **2018**, *97*, 085417.
[17] B. E. Brown, *Acta Crystallogr.* **1966**, *20*, 268.
[18] D. Culcer, R. Winkler, *Phys. Rev. Lett.* **2007**, *99*, 226601.
[19] M. Z. Hasan, C. L. Kane, *Rev. Mod. Phys.* **2010**, *82*, 3045.
[20] K. Vaklinova, A. Hoyer, M. Burghard, K. Kern, *Nano Lett.* **2016**, *16*, 2595.
[21] J. A. Voerman, C. Li, Y. Huang, A. Brinkman, *Adv. Electron. Mater.* **2019**, *5*, 1900334.
[22] D. Khokhriakov, B. Karpiak, A. M. Hoque, S. P. Dash, *Carbon* **2020**, *161*, 892.
[23] T. S. Ghiasi, A. A. Kaverzin, P. J. Blah, B. J. van Wees, *Nano Lett.* **2019**, *19*, 5959.
[24] A. M. Hoque, D. Khokhriakov, B. Karpiak, S. P. Dash, arXiv: 1908.09367v2, **2019**.
[25] L. Li, J. Zhang, G. Myeong, W. Shin, H. Lim, B. Kim, S. Kim, T. Jin, S. Cavill, B. S. Kim, C. Kim, J. Lischner, A. Ferreira, S. Cho, *ACS Nano* **2020**, *14*, 5251.
[26] A. Slachter, F. L. Bakker, J.-P. Adam, B. J. van Wees, *Nat. Phys.* **2010**, *6*, 879.
[27] J. F. Sierra, I. Neumann, J. Cuppens, B. Raes, M. V. Costache, S. O. Valenzuela, *Nat. Nanotechnol.* **2018**, *13*, 107.
[28] C. K. Safeer, J. Ingla-Aynés, F. Herling, J. H. Garcia, M. Vila, N. Ontoso, M. R. Calvo, S. Roche, L. E. Hueso, F. Casanova, *Nano Lett.* **2019**, *19*, 1074.
[29] L. Li, J. Zhang, G. Myeong, W. Shin, H. Lim, B. Kim, S. Kim, T. Jin, B. Kim, C. Kim, J. Lischner, A. Ferreira, S. Cho, arXiv: 1906.10702, **2019**.
[30] L. A. Benítez, W. Savero Torres, J. F. Sierra, M. Timmermans, J. H. Garcia, S. Roche, M. V. Costache, S. O. Valenzuela, *Nat. Mater.* **2020**, *19*, 170.
[31] F. Y. Bruno, A. Tamai, Q. S. Wu, I. Cucchi, C. Barreteau, A. de la Torre, S. M. Walker, S. Riccò, Z. Wang, T. K. Kim, M. Hoesch, M. Shi, N. C. Plumb, E. Giannini, A. A. Soluyanov, F. Baumberger, *Phys. Rev. B* **2016**, *94*, 121112.
[32] J. Sinova, S. O. Valenzuela, J. Wunderlich, C. H. Back, T. Jungwirth, *Rev. Mod. Phys.* **2015**, *87*, 1213.
[33] M. H. D. Guimarães, G. M. Stiehl, D. MacNeill, N. D. Reynolds, D. C. Ralph, *Nano Lett.* **2018**, *18*, 1311.
[34] J. Lee, Z. Wang, H. Xie, K. F. Mak, J. Shan, *Nat. Mater.* **2017**, *16*, 887.
[35] C. K. Safeer, N. Ontoso, J. Ingla-Aynés, F. Herling, V. T. Pham, A. Kurzmann, K. Ensslin, A. Chuvilin, I. Robredo, M. G. Vergniory, F. de Juan, L. E. Hueso, M. R. Calvo, F. Casanova, *Nano Lett.* **2019**, *19*, 8758.
[36] Y. Chen, Y.-M. Lu, H.-Y. Kee, *Nat. Commun.* **2015**, *6*, 6593.
[37] Y. Chen, H.-S. Kim, H.-Y. Kee, *Phys. Rev. B* **2016**, *93*, 155140.
[38] P. Song, C.-H. Hsu, G. Vignale, M. Zhao, J. Liu, Y. Deng, W. Fu, Y. Liu, Y. Zhang, H. Lin, V. M. Pereira, K. P. Loh, *Nat. Mater.* **2020**, *19*, 292.
[39] W. Han, K. Pi, K. M. Mccreary, Y. Li, J. J. I. Wong, A. G. Swartz, R. K. Kawakami, *Phys. Rev. Lett.* **2010**, *105*, 167202.
[40] B. Zhao, D. Khokhriakov, B. Karpiak, A. M. Hoque, L. Xu, L. Shen, Y. P. Feng, X. Xu, Y. Jiang, S. P. Dash, *2D Mater.* **2019**, *6*, 035042.
[41] Y. Wang, E. Liu, H. Liu, Y. Pan, L. Zhang, J. Zeng, Y. Fu, M. Wang, K. Xu, Z. Huang, Z. Wang, H. Z. Lu, D. Xing, B. Wang, X. Wan, F. Miao, *Nat. Commun.* **2016**, *7*, 13142.
[42] W. Zhang, Q. Wu, L. Zhang, S.-W. Cheong, A. A. Soluyanov, W. Wu, *Phys. Rev. B* **2017**, *96*, 165125.
[43] P. Rüßmann, A. P. Weber, F. Glott, N. Xu, M. Fanciulli, S. Muff, A. Magrez, P. Bugnon, H. Berger, M. Bode, J. H. Dil, S. Blügel, P. Mavropoulos, P. Sessi, *Phys. Rev. B* **2018**, *97*, 075106.
[44] C. Wang, Y. Zhang, J. Huang, S. Nie, G. Liu, A. Liang, Y. Zhang, B. Shen, J. Liu, C. Hu, Y. Ding, D. Liu, Y. Hu, S. He, L. Zhao, L. Yu, J. Hu, J. Wei, Z. Mao, Y. Shi, X. Jia, F. Zhang, S. Zhang, F. Yang, Z. Wang, Q. Peng, H. Weng, X. Dai, Z. Fang, Z. Xu, C. Chen, X. J. Zhou, *Phys. Rev. B* **2016**, *94*, 241119.
[45] M. V. Kamalakar, C. Groenveld, A. Dankert, S. P. Dash, *Nat. Commun.* **2015**, *6*, 6766.
[46] L. Onsager, *Phys. Rev.* **1931**, *37*, 405.
[47] K. Shen, G. Vignale, R. Raimondi, *Phys. Rev. Lett.* **2014**, *112*, 096601.
[48] J. C. R. Sánchez, L. Vila, G. Desfonds, S. Gambarelli, J. P. Attané, J. M. De Teresa, C. Magén, A. Fert, *Nat. Commun.* **2013**, *4*, 2944.
[49] V. M. Edelstein, *Solid State Commun.* **1990**, *73*, 233.
[50] Q. Song, H. Zhang, T. Su, W. Yuan, Y. Chen, W. Xing, J. Shi, J. Sun, W. Han, *Sci. Adv.* **2017**, *3*, 1602312.
[51] H. Wang, J. Kally, J. S. Lee, T. Liu, H. Chang, D. R. Hickey, K. A. Mkhoyan, M. Wu, A. Richardella, N. Samarth, *Phys. Rev. Lett.* **2016**, *117*, 076601.
[52] J.-C. Rojas-Sánchez, S. Oyarzún, Y. Fu, A. Marty, C. Vergnaud, S. Gambarelli, L. Vila, M. Jamet, Y. Ohtsubo, A. Taleb-Ibrahimi, P. Le Fèvre, F. Bertran, N. Reyren, J.-M. George, A. Fert, *Phys. Rev. Lett.* **2016**, *116*, 096602.
[53] Q. Shao, G. Yu, Y.-W. Lan, Y. Shi, M.-Y. Li, C. Zheng, X. Zhu, L.-J. Li, P. K. Amiri, K. L. Wang, *Nano Lett.* **2016**, *16*, 7514.
[54] D. Khokhriakov, A. M. Hoque, B. Karpiak, S. P. Dash, *Nat. Commun.* **2020**, *11*, 3657.
[55] M. Gibertini, M. Koperski, A. F. Morpurgo, K. S. Novoselov, *Nat. Nanotechnol.* **2019**, *14*, 408.
[56] S. Manipatruni, D. E. Nikonov, C.-C. Lin, T. A. Gosavi, H. Liu, B. Prasad, Y.-L. Huang, E. Bonturim, R. Ramesh, I. A. Young, *Nature* **2019**, *565*, 35.